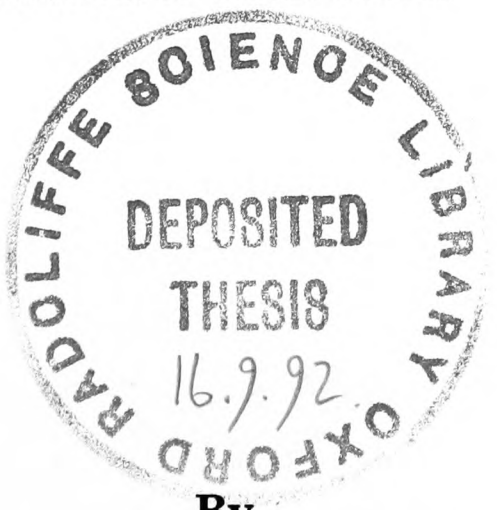
CRACK INITIATION UNDER SHOCK LOADING

VALIDATION OF A NEW TESTING TECHNIQUE

A THESIS
SUBMITTED TO THE DEPARTMENT OF ENGINEERING SCIENCE
OF OXFORD UNIVERSITY
IN PARTIAL FULFILMENT OF THE REQUIREMENTS
FOR THE DEGREE OF
DOCTOR OF PHILOSOPHY



By

Luis Héctor Hernández-Gómez

Exeter College

Oxford

Hilary Term, 1992

Abstract

CRACK INITIATION UNDER SHOCK LOADING

VALIDATION OF A NEW TESTING TECHNIQUE

Luis Héctor Hernández-Gómez — D. Phil.

Exeter College — Hilary Term 1992

The evaluation of the dynamic fracture properties with the current impact testing techniques is subject of some controversy, because the crack initiation conditions cannot be established with accuracy. Besides, some of them are limited to low loading velocities and the evaluations are made following a static approach. In consequence, a fundamental study is required with two aims, namely, a development of a new impact testing technique and the analysis of the extension of the fracture mechanics concepts to crack initiation under dynamic loading. These are the objectives of this research project.

The impact testing technique proposed is based on the shock tube technique and is capable to test the specimens, which are central cracked circular plates, under static and dynamic conditions. The findings show that the specimens are loaded uniformly with blast waves, which have an initial ramp that increases steadily without oscillations. The magnitude of the load is controllable and reproducible and the fracture analysis should be based on a dynamic calibration.

This technique has been applied to the evaluation of the dynamic fracture toughness of PMMA following an experimental-numerical procedure. The crack initiation load and the strain rate were measured experimentally and the fracture toughness was calculated numerically with standard solutions and with numerical calculations of the J-Integral with the finite element code ABAQUS.

The problem of crack initiation under pressure load has not been completely solved. Consequently, the significance of the static and dynamic test results was established with the findings of additional experimental and numerical work, which showed that the modulus of elasticity and fracture stress increases with the strain rate, that there is plastic deformation at the crack tip of those specimens tested under static conditions and that the dynamic calculations with ABAQUS involves the interaction of the stress waves with the boundaries. Furthermore, it has to be noticed that the crack tip is under bending stresses. Thus, this test is not a standard plane strain material dynamic test. Finally, conclusions are drawn on the use of the this experimental-numerical technique and its further application.

Preface

This thesis is an account of work carried out by the author in the Department of Engineering Science at Oxford University. The work was carried out under the supervision of Dr. Carlos Ruiz.

The research described here is original, although the work of others has been drawn upon freely, with due acknowledgment in the text. No part of this thesis has been submitted for a degree at any other university.

Acknowledgments

I wish to thank to my supervisor, Dr. Carlos Ruiz, for his continuous guidance and advice through the entire research project.

The scholarship that supported this research project has been granted by Imperial Chemical Industries and was coordinated by the British Council, to whom grateful acknowledgment is made. Also, I would like to thank the following institutions, which granted complementary support for the development of this research programme, namely, Banco de México, Consejo Nacional de Ciencia y Tecnología, Instituto de Investigaciones Eléctricas, Escuela Superior de Ingeniería Mecánica y Eléctrica of the Instituto Politécnico Nacional and the Overseas Research Students Award Scheme.

My thanks go to Messrs. P. Webb, P. Hardy, R. Duffin and R. Stone for their invaluable technical assistance and experience during the experimental work.

I would like to express my appreciations to Dr. F. Salvatorelli, for his help at the beginning of this project, Dr. Xia, for his advice, and all my colleagues in the impact group for the interesting discussions we had.

My gratitude extends to the Academic and Technical staff and specially to Mr. H. Fearnley and Mr. C. Curran for their help during the numerical work with the CONVEX computer and Mr. D. Wingent.

Finally, I would like to thank my wife, Laura, and my son, Luis H. Jr., for their support, encouragement and, most important, their love.

A Laura y Luis H. Jr. por todo lo que
significa mi vida a su lado.

Elizabeth, el camino que tu seguiste está marcado de gratos recuerdos y enseñanzas. Nunca dejaste de luchar aunque tu cruz fué pesada, siempre amaste ala vida y caminaste con la frente en alto. Siempre te recordaré con alegría.

Q. E. P. D.

CONTENTS

Abstract ii
Preface iii
Acknowledgments iv
Nomenclature xii

CHAPTER 1 **INTRODUCTION** 1
1.1 Background 1
1.2 Dynamic Fracture of Polymers 3
1.2.1 Impact Testing Methods with Pendulum Machines 4
1.2.2 Impact Testing Methods with the Optical Method of Caustics 6
1.2.3 Impact Testing Methods with Shock Tubes 9
1.3 Mechanical Behaviour of Polymers 14
1.4 Aim and Outline of the Thesis 16
References 17

CHAPTER 2 **DEVELOPMENT OF THE IMPACT TESTING PROCEDURE** 24
2.1 Introduction 24
2.2 Description of the Experimental Rig 28

2.2.1 Operational Procedure of the Impact Test Apparatus for Dynamic Tests 33
2.2.2 Operational Procedure of the Impact Test Apparatus for Static Tests 34
2.3 Calibration of the Impact Test Apparatus 34
2.3.1 Calibration of the Pressure Transducers 34
2.3.2 Pressure-Time Analysis: Open Tube 36
2.3.3 Pressure-Time Analysis: Closed Tube 43
2.3.4 Pressure-Time Analysis: Gap Between Tube and End Plate 44
2.3.5 Analysis of the Pressure Front 48
2.4 Strain Distribution in the Specimen 49
2.4.1 Analysis of the Strain History 49
2.4.2 Analysis of the Bending Strain History 52
2.4.3 Analysis of the Elastic Response of the Specimens with the Loading Cases Selected 55
2.5 Summary 57
References 61

CHAPTER 3 **EXPERIMENTAL ANALYSIS OF CRACK INITIATION UNDER DYNAMIC LOADING** 63
3.1 Introduction 63
3.2 Characteristics of Polymethylmethacrylate 64
3.3 Fabrication of the Specimens 65
3.4 Effect of the Notch Shape in the Evaluation of the Stress Intensity Factor 69
3.5 Description of the Crack Initiation Tests under Dynamic Loading Pressure 70
3.6 Experimental Analysis of Crack Initiation under Dynamic Loading Pressure 71
3.7 Description of Crack Initiation Tests under Static Loading Pressure 77
3.8 Experimental Results of Crack Initiation under Static Loading Pressure 78
3.9 Discussion of the Results 80
3.10 Summary 82

References 82

CHAPTER 4 **NUMERICAL ANALYSIS OF CRACK INITIATION UNDER DYNAMIC PRESSURE LOADING** 85

4.1 Introduction 85

4.2 Evaluation of the Fracture Toughness 87

4.2.1 The J-Integral Concept 87

4.2.2 The $\hat{J}$-Integral Concept 90

4.2.3 Numerical Evaluation of the J-Integral 91

4.2.3.1 Basic Principles of Finite Element Method 91

4.2.3.2 Evaluation of the J-Integral with ABAQUS 96

4.3 Analysis of the Standard Solutions to the Problem of a Central Cracked Plate under Uniform Bending 103

4.3.1 Evaluation of the Stress Intensity Factor with the Theory of Kirchhoff 103

4.3.2 Evaluation of the Stress Intensity Factor with the Theory of Reissner 107

4.4 Application to the Problem in Hand 111

4.4.1 Analysis of a Plate without a Crack 111

4.4.1.1 Characteristics of the Finite Element Mesh 113

4.4.1.2 Selection of the Boundary Conditions of the Finite Element Model 115

4.4.1.2.1 Experimental Evaluation of the Natural Frequency of the Specimens (115)

4.4.1.2.2 Numerical Evaluation of the Natural Frequency of the Specimens (116)

4.4.1.3 Results Obtained 116

4.4.1.4 Evaluation of the Stress Intensity Factor 121

4.4.2 Analysis of Cracked Plates 124

4.4.2.1 Characteristics of the Finite Element Mesh for the Evaluation of the J-Integral 125

4.4.2.2 Fracture Toughness Evaluation of the Dynamic Tests . 125

4.4.2.3 Fracture Toughness Evaluation of the Static Tests . . . 130

4.5 Discussion of the Results 132

4.6 Summary 135

References 137

CHAPTER 5 **INTERPRETATION OF THE RESULTS** 141

5.1 Introduction 141

5.2 Evaluation of the Mechanical Properties of PMMA at Different Strain Rates 142

5.2.1 Description of the Testing Rig 142

5.2.2 Fabrication of the Specimens 143

5.2.3 Description of the Test 145

5.2.4 Results Obtained 147

5.3 Analysis of the Crack Surfaces 153

5.3.1 Description of the Procedure of Analysis 154

5.3.2 Analysis of the Crack Surfaces of the Specimens Tested under Dynamic Loading 154

5.3.3 Analysis of the Crack Surfaces of the Specimens Tested under Static Loading 158

5.4 Analysis of the Numerical Results 161

5.5 Conclusions 166

References 168

CHAPTER 6 **GENERAL CONCLUSIONS AND PROPOSAL FOR FUTURE WORK** 171

6.1 Research Objectives 171

6.2 Conclusions 172

6.2.1 Design of the Impact Testing Rig 172

6.2.2 Crack initiation Analysis under Dynamic Pressure Loading 174

6.3 Proposal for Future Work 179

APPENDIX A **EVALUATION OF THE CRACK PROPAGATION VELOCITY** 181

A.1 Description of the Experimental Technique 181

A.2 Results Obtained 182

A.3 Discussion of the Results 184

References 187

APPENDIX B **CRACK INITIATION ANALYSIS WITH SPECIMENS WITH A TRIANGULAR NOTCH FRONT** 188

B.1 Experimental Work 188

B.1.1 Fabrication of the Specimens 188

B.1.2 Dynamic Tests 189

B.1.3 Static Tests 190

B.2 Analysis of the Crack Surfaces 191

B.3 Discussion of the Results 194

Nomenclature

a Half crack length.

E Modulus of elasticity.

G Energy release rate.

h Thickness.

{i} Inertial vector.

I Moment of inertia.

I_m Impulse.

J J-Integral.

$\hat{J}$ $\hat{J}$-Integral.

K Stress intensity factor.

[K] Stifness matrix.

K_c Fracture toughness under bending stresses.

K_{Ic} Fracture toughness under plane strain conditions.

$\dot{K}_I$ Rate of change of the stress intensity factor.

M Bending moment.

[N] General function of position.

P Pressure.

{p} Column vector of distributed loads per unit of volume.

{P} Column vector of external forces.

PA Polyamide.

PMMA Poly-methylmethacrylate.

PVC Poly-vinyl chloride.

PP Polypropylene.

PTFE Poly-tetrafluoroethylene.

Q Shear force.

r Root radius of a notch.

{R} Column vector of concentrated loads.

S Surface energy.

T Traction vector perpendicular to the path of integration of the J-Integral or the $\hat{J}$-Integral.

U Strain energy.

V_T Maximum velocity of crack propagation.

W Strain energy density in the J-Integral calculation or external work in the evaluation of the potential energy.

W_p Energy due to distributed loads per unit of volume.

W_e Elastic strain energy..

SIF Stress intensity factor.

γ Surface energy density per unit of area.

Γ Integration path of the J-integral.

$\{\delta\}$ Nodal displacements.

$\dot{\varepsilon}$ Strain rate.

$\{\varepsilon\}$ Strain vector.

$\{\varepsilon_o\}$ Initial strain vector.

K Bulk modulus.

μ Shear modulus.

ν Poisson ratio.

Π Potential energy of a cracked body.

ρ Density of the material.

$\{\sigma\}$ Stress vector.

σ_x, σ_y, σ_z Tensile stresseses in the direction x, y and z respectively.

τ_{xy}, τ_{yz}, τ_{zy} Shear stresses in the directions xy, yz and zy respectively.

ϕ Potential energy of the system.

$\Phi(1)$ Solution to the first Fredholm integral equation at the crack tip.

CHAPTER 1

INTRODUCTION

1.1 Background.

The assessment of the structural integrity of cracked structures under dynamic loading is an important problem which remains open. Of the two main areas of interest, namely crack initiation under shock loading and rapid crack growth under quasi-static loading, only the second has been studied in depth. Typical structural examples of these two cases are fracture due to explosions and running cracks in pipelines respectively.

Crack propagation in pipelines is developed by a sudden release of energy, which is converted into fracture, elastic strain, plastic deformation and kinetic energies, as the cracks extend over long distances. This problem has been solved following an empirical approach, by means of full scale burst tests of large diameter pipes [1-7]. However, the specimens have several manufacturing limitations. They are not perfect cylinders and the welded seams must be made carefully. Otherwise, the risk to induce a certain degree of brittleness is increased. The main interest of these tests is to establish the crack arrest conditions by correlating the observed fracture conditions with Charpy test results, manufacturing processes and existing imperfections. The problem has also been analyzed with a similar approach, using scale models [8-14]. In these tests,

the conditions observed in the full scale tests have been reproduced with specimens made of a wide range of materials. The observations have helped to get an insight into the problem, because fracture can be observed under controlled conditions. In some cases, crack propagation is promoted with a falling weight technique or the specimen is impacted with a hammer, using in some instances pregrooved specimens. All these conditions generate a complex stress field at the crack and make the interpretation of the test data rather uncertain.

Considering the findings on the full scale tests and the results of the scale analysis, several models have been proposed [15-29]. They are based upon stress analysis under very simplified considerations or considering energy balance during fracture. It is found that the energy required to deform plastically the wall of the cylinder is a predominant parameter. In consequence, the evaluation of the fracture energy and the energy required for plastic deformation at the crack tip, which are much lower, is inaccurate. As a result, the effect of the crack tip process zone is lost in the analysis. The published solutions can also be criticised because structural dynamic effects and strain rate properties are often ignored.

A rational alternative, that may be proposed to analyze this problem, is provided by fracture mechanics. Its main assumption is that the elastic material is a uniform mechanical continuum, which reacts in a predictable way to stresses and strains. Considering the material isotropic and homogeneous, the strength of a cracked body depends on its mechanical properties and the dimensions of the actual flaw. Rather than attempting to describe the actual process of fracture, as the growing crack tears the structure apart, failure is deemed to occur at the onset of crack growth. Fracture initiation rather than fracture propagation is then the focus of interest and the objective of the study becomes to identify the critical conditions when the crack starts.

Two fracture criteria have been established. The first, which is derived from the analysis of Griffith [30] and Orowan [31], is the critical strain energy release rate criterion. It establishes that fracture occurs when elastic or potential energy of the loading system is released by growth of the crack, supplying the energy requirements for the creation of new crack surfaces. Alternatively, the fracture toughness criterion, which was stated by Irwin [32], establishes that the stress field around a sharp crack in a linear elastic material could be uniquely defined by a parameter named stress intensity factor (SIF) K. Hence, the fracture occurs when K equals the fracture toughness

K_{Ic} which is a measure of a material property [33]. Although both criteria are, in fact, equivalent, they have generated slightly different formulations for the evaluation of the crack initiation conditions, namely, the energy balance and the evaluation of the stress intensity factor.

The fracture mechanics principles have been fully developed only for static loading conditions. Consequently, they have to be extended to dynamic loading conditions, if they are used for the study of crack initiation under a suddenly applied loading as occurs in the case of an explosion, pressure blast, etc. Two issues are raised: the first is related with the evaluation of the SIF under dynamic conditions and the second is associated with the significance of the fracture toughness under dynamic loading.

1.2 Dynamic Fracture of Polymers.

The strain rate sensitivity, that casts some doubt on the accuracy of the solution of dynamic fracture problems when dealing with metals, is even more important in the case of polymers. The use of polymers as "model materials" is preferable to metals for a fundamental study of dynamic fracture -be it crack initiation or crack propagation- for several reasons:

1. The high strain rate sensitivity, even at moderately low strain rates of 10-100 s^{-1}, helps to distinguish between static and dynamic failure conditions.

2. Because the strength is relatively low, the fracture process requires lower loads and energies than when dealing with metals, reducing the cost of the apparatus and the hazard of operation.

3. The specimens are relatively easy to make and cheap.

Besides the interest in obtaining actual material data for design, the above reasons explain the abundant literature on dynamic fracture of polymers using techniques that involve impact tests with pendulum machines or shock tubes, dynamic photoelasticity, caustics, etc. A review of these techniques is presented in the following sections.

1.2.1 Impact Testing Methods with Pendulum Machines.

The simplest interpretation of the impact tests using a pendulum is based on an energy balance in which it is assumed that the loss of potential energy of the pendulum is equal to the energy of fracture. Defining the strain energy release rate, G, as the energy released per unit area as the crack grows, Marshall et. al. [34] proposed that,

$$G = \frac{U}{BW\phi} \qquad 1.1$$

where B and W are the thickness and width of the specimen respectively, U is the potential energy lost by the pendulum and ϕ is a calibration constant to account for the specimen shape and for loading. From a series of tests, with specimens loaded in 3-point bending, the diagram of figure 1.1 was obtained. It shows that U is indeed proportional to $BW\phi$ but that the straight line does not pass through the origin. The reason was ascribed to the need to take into account the kinetic energy imparted to the specimen. When this was included, the corrected straight line passed through the origin. Its slope was the critical strain energy release rate G_c.

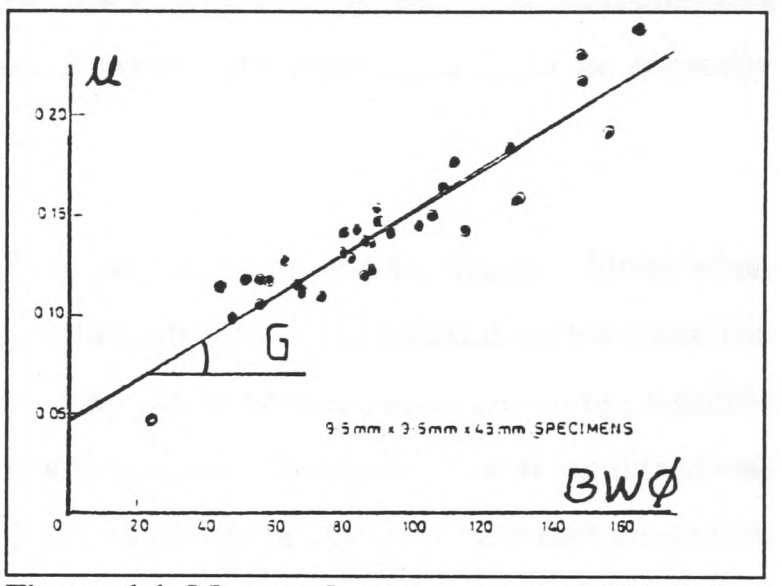


Figure 1.1 Measured energy u vs. $BW\phi$. After Marshal et. al. [34].

With a similar approach, Brown [35] has proposed a model, which establishes that the energy lost by the pendulum is the energy required to start the crack moving. These conclusions were based on experimental results obtained with glassy homopolymer, which is a polymer resulting from polymerization of a single monomer.

Plati and Williams [36] extended the work in [34], evaluating the critical strain energy release rate for a range of polymers and deriving calibration factors ϕ for Charpy and Izod tests. These researchers observed that this method is acceptable for brittle polymers, while a fully plastic

analysis had to be applied to highly ductile materials.

Birch and Williams [37] evaluated the critical energy release rate in ductile materials, namely medium density polyethylene (MOPE) and polytetrafluoroethylene (PTFE), following the method described in [36]. A plastic zone and a slow crack correction factor were introduced in the calculations. Furthermore, the rate of the test was changed by varying the specimen dimensions. The results showed that the rate effect is associated with crazing and yielding

Clutton et. al. [38] followed the same technique to study the impact performance of polyethylene. The findings showed that the evaluation of the fracture energy is improved with instrumented Charpy tests at impact speeds lower than 3.5 m/s. However, the specimens must be carefully balanced to minimise oscillations of the load signal.

McMillan and Tesh [39] studied the limitations of the pendulum impact testing machines when testing specimens of brittle materials. The findings established that the inertial forces make the interpretation of the results difficult. In consequence, the instrumented pendulum is not suitable for evaluating the effect of fast loading rates on crack propagation because of the irregular stress pulses generated. Further work was recommended on the design of the instrumented pendulum in order to make accurate evaluations of the absorbed energy.

This problem was also analyzed by Ruiz et. al. [40], who observed, in unfiltered traces from Charpy tests, that the variation of the load P(t) through the time is a ramp with decaying inertial oscillations superimposed as shown in figure 1.2. A solution to this problem was proposed by means of the Hopkinson pressure bar apparatus. A diagrammatic

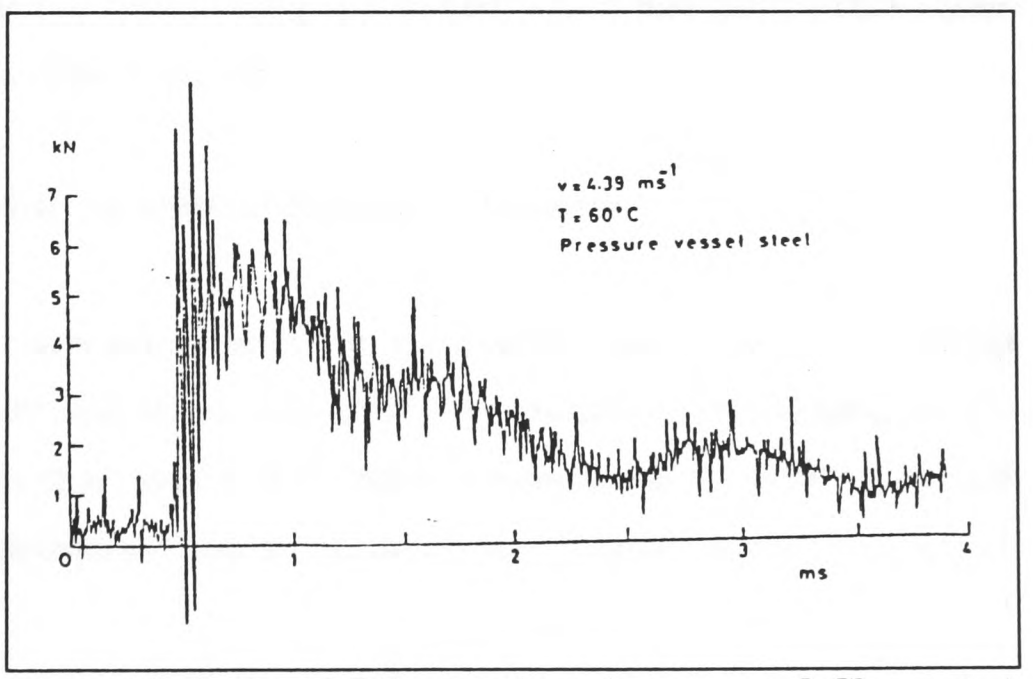


Figure 1.2 Unfiltered P(t) trace from instrumented Charpy test. After Ruiz et. al. [40].

arrangement is shown in figure 1.3. Experimental evidence was gathered testing steel specimens. The authors claim that the load is measured accurately, because the load trace is free from oscillations. Moreover, the specimen fracture occurs before the stress waves are reflected at the free ends of the bar. In addition, the energy absorbed is obtained more accurately and the bouncing of the specimen on its anvil is unlikely.

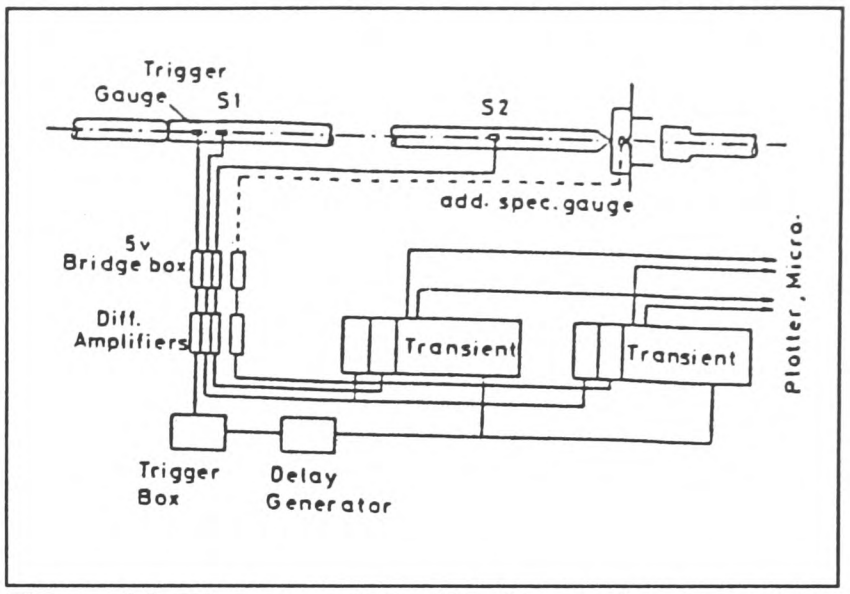


Figure 1.3 Diagram of the Hopkinson bar apparatus and instrumentation. After Ruiz et. al. [40].

A totally different approach for the interpretation of the impact data consists in using the SIF/K_{Ic} approach. It can be argued that once the SIF is known, as a function of the specimen geometry, crack size and applied load, all that is needed is to measure the load at fracture to find the fracture toughness K_{Ic}. Charpy-type specimens, notched or notched and precracked, tested in a pendulum machine instrumented with a dynamometer are often interpreted in this manner. It is often assumed that the state of stress can be predicted accurately by a static analysis. This introduces a limitation that may invalidate tests of very brittle materials or at very high strain rates, when the crack starts before static equilibrium has been reached. It also assumes that fracture occurs at the same time as the peak loading is recorded, which may not be true under dynamic conditions where inertia is important [40].

1.2.2 Impact Testing Methods with the Optical Method of Caustics.

Many attempts have been made to characterise the SIF in specimens subjected to impact loading using full-field methods such as Moiré and photoelasticity. The poor sensitivity of the first and the limitations to transparent materials that become birefringent under stress of the latter method have, however, prevented their widespread use to the study of dynamic crack initiation or propagation

Kalthoff [41-45] has used the optical method of caustics, which was introduced by Mannog [46],

for investigating dynamic fracture. Its physical principle, when applied to transparent specimens, is illustrated in figure 1.4. The crack tip of a loaded specimen is illuminated by a parallel light beam. Due to the stress gradient, the thickness of the specimen is reduced local to the crack tip. Hence, the surrounding area of the crack tip diffracts the light rays that cross the section deflecting outwards. The caustic, which is a shadow area surrounded by a luminous arc, is observed on a screen. Its dimensions have a unique relation with the SIF. The shadow pattern under dynamic conditions is photographed with a Cranz-Schardyn camera at regular intervals of time.

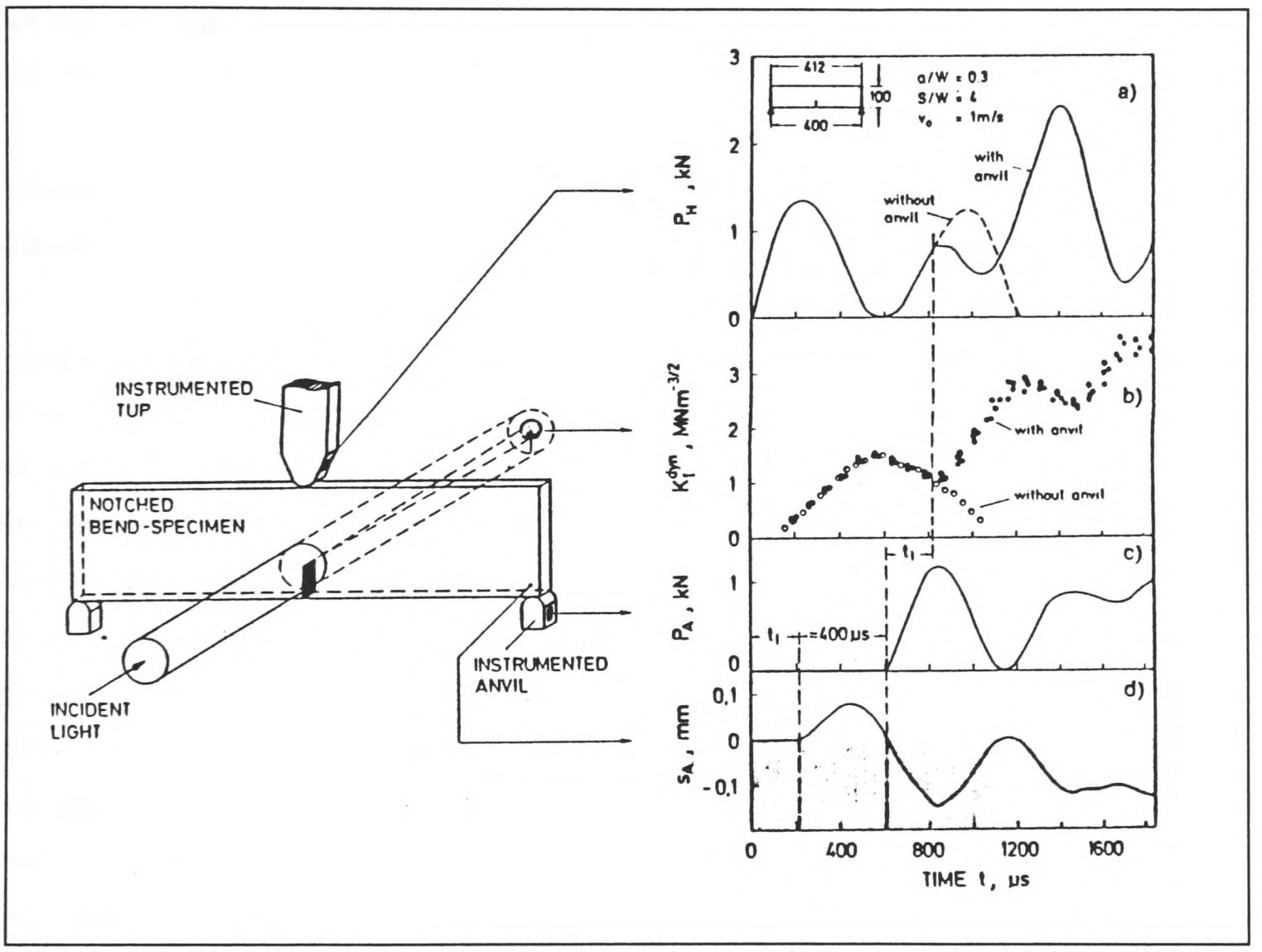


Figure 1.4 Application of the caustic method to the drop weight impact method. After Kalthoff et. al. [44].

In the testing arrangement of figure 1.4, a strain gauge measures the load applied by the tup, P_H. From the radius of the caustics, the dynamic SIF, K_I^{dyn}, is obtained. The anvils are also strain gauged to provide a measure of the reaction force, P_A and the deflection S_A is also measured. A glance at figure 1.4 shows that there is an out-of phase between P_H and P_A, indicating that the

static equilibrium is only reached after a number of stress wave reflections have taken place. Ergo, a calibration based on static stress analysis is therefore unacceptable. The specimens were made of epoxy (Araldite B) and tested at impact velocities of around 1 m/s, very modest in comparison with the impact speeds found in many practical situations. It will also be noticed that K_I^{dyn} increases more steadily -albeit with some oscillations- than P_H, which exhibits violent oscillations. This adds further proof to the inadmissibility of the static calibration approach, in which the SIF is assumed to be proportional to the applied load. The conclusion is that to interpret an impact test, it is necessary to know the SIF at the time of fracture. One way to do this is to obtain experimentally a dynamic calibration curve (SIF-time) and find the time to fracture in the actual test which should reproduce as closely as possible the conditions under which the calibration curve was obtained.

Following a similar line, Theocaris et. al. [47] studied the dynamic behaviour of PMMA notched specimens under stress pulses. A series of tests were carried out with plates of dimensions 300 mm x 400 mm. Their thickness is 4 mm and their notches were 4, 6 and 10 mm long. The specimens were held horizontal by thin filaments as shown in figure 1.5 and they were impacted at one of their ends by a steel sphere of 10 mm diameter, which was accelerated by an air gun. The findings showed that the crack propagated by steps, when it was loaded by tensile stresses. The dynamic SIF was measured with caustics, assuming that the static and dynamic stress fields are analogous. The crack propagation velocity was also evaluated.

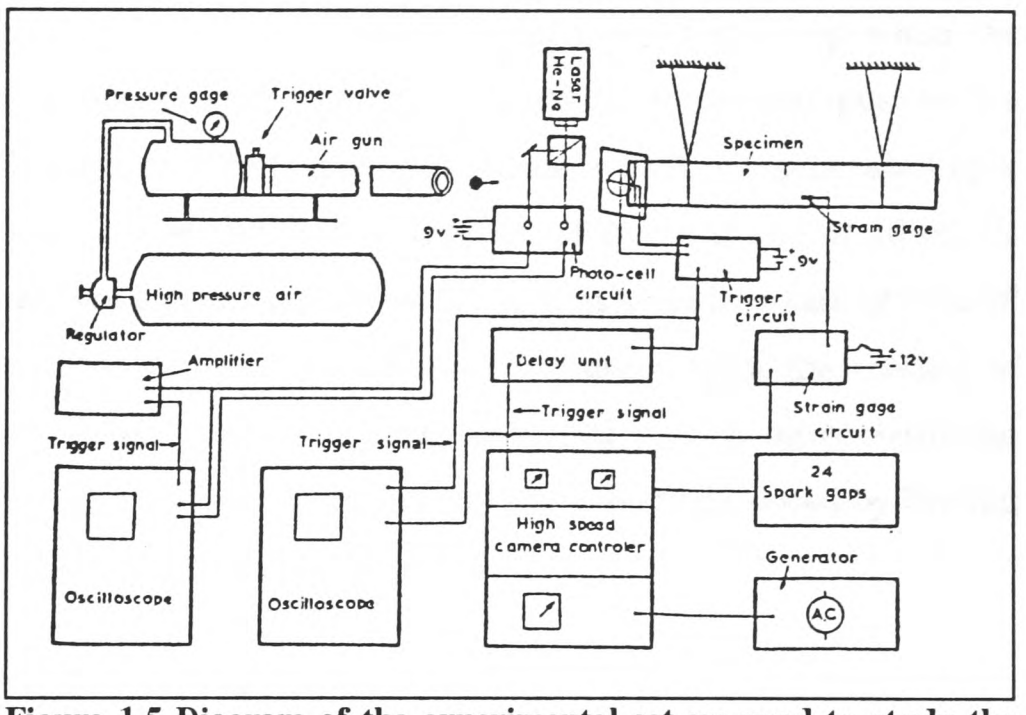


Figure 1.5 Diagram of the experimental set up used to study the dynamic behaviour of notched specimens under stress pulses. After Theocaris et. al. [47].

This experimental technique was also followed by Katsamanis et. al. [48], who tested PMMA notched specimens 40 mm wide and 300 mm long. They also observed that the crack propagates

in steps. Thus, the dynamic SIF and the energy release rate were calculated after Griffith [30] with the crack onset at the second step, because the authors judged that the notch front is unblunted after it has propagated in the first step. In this evaluation, a correction factor, which accounts for the error made by using static analysis, was introduced.

Ravi-Chandar et al. [49] proposed a technique to study the problem of a plane wave impinging on a crack parallel to its front. Homalite-100 plates of 500 mm x 300 mm and 4.76 mm thick were tested with the stress wave generator shown in figure 1.6. It consists of a doubled up conductor inserted into the crack. The space in between is filled with a "Mylar" strip for a dielectric. A magnetic field is generated on each leg of the loop when the current flows. Then, the field interaction produces an electromagnetic force that pushes the conductors apart, loading the crack surfaces. The trapezoidal pulses, which are generated by a discharge from a capacitor bank, have a rise time and a duration of 25×10^{-6}s and of 160×10^{-6}s respectively. The maximum pressure that can be obtained is 62 MPa at a loading rate of 2.5×10^{6} MPa/s. Crack initiation was analyzed in [50] and the SIF was evaluated with the method of caustics in conjunction with a high speed camera. The experimental results agree with the analytical solution of a step wave that loads a crack in an infinite plane body proposed by Freund [51,52]. Clearly, the results are valid for two dimensional problems.

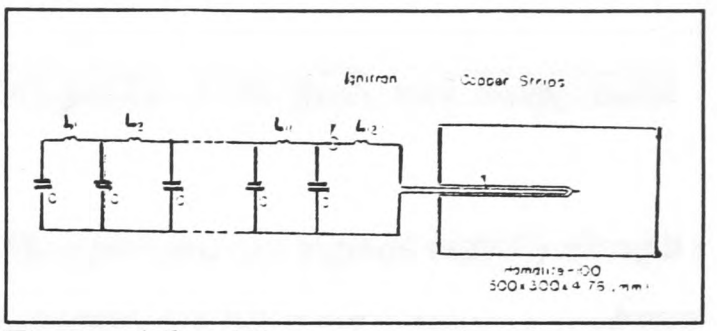


Figure 1.6 Electromagnetic stress wave generator. After Ravi-Chandar et. al. [50].

1.2.3 Impact Testing Methods with Shock Tubes.

Reed and coworkers [53] developed a shock tube for impact testing. It consists of three main parts, namely the driver, the driven and the test sections. A schematic arrangement is shown in figure 1.7. The driver section is filled with high pressure gas and is sealed with a thin diaphragm. On bursting, the gas expands in the driven section, generating a shock wave that travels at a constant speed. The test section is at the end of the driven section, inside a dump tank which collects the gases and the specimen fragments after impact testing.

The cylindrical specimens, which are machined from extruded tubes, are mounted to form an extension of the driven section. They are axially clamped between two end plates to prevent them from falling under their own weight as shown in figure 1.8. The authors claim that the specimen can expand radially along its entire length with minimal end restraints. Besides, controllable step loads are obtained with strain rates as high as 10^3 s^{-1}.

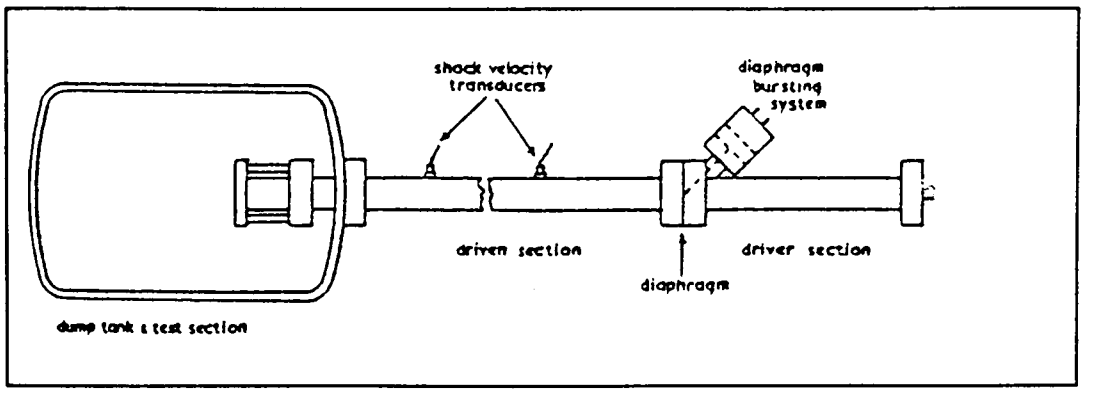


Figure 1.7 Schematic arrengement of the shock tube testing facility. After Reed et. al. [53].

The shock pressure is measured with pressure transducers mounted at the ends of the specimen. The specimen hoop strain was measured with a strain gauge bonded to the specimen. The resultant load-deformation data was synchronized with the shock wave.

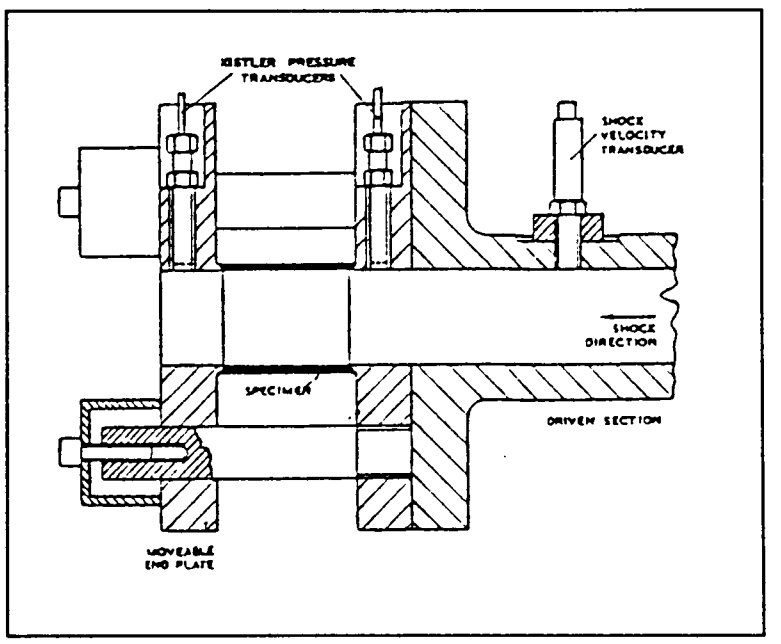


Figure 1.8 Method of mounting the cylindrical specimens and the location of the transducers. After Reed et. al. [53].

Thin walled cylindrical specimens of PMMA containing artificial flaws along the axial direction were analyzed in [54]. The specimens were 50.8 mm long, with a wall thickness of 0.762 mm and an internal diameter of 42.4 mm. The length of their centrally located cracks varied between 0.76 and 38 mm. Each specimen was subjected to a series of shock pulses of steadily increasing pressure until fracture occurred. As result, the minimum pressure required to cause fracture was ascertained.

The fracture hoop stress was obtained from the quasi-static relation between the internal pressure and stresses in thin cylinders, considering the shock pressure that was calculated from measurements of the pressures of the driver and driven gases. A linear relationship between the minimum hoop stress required for fracture and the inverse square root of the crack length, which

does not extrapolate to the origin, was observed over a range of crack length between 16 and 38 mm. The fracture occurred along the axial direction. It was concluded that a Griffith type relationship can be applied, which has the following form.

$$\sigma_\theta = \sqrt{\frac{2E\gamma}{\pi a}} - \sigma_0 = \frac{PR}{t} \qquad 1.2$$

However, the specimens with cracks smaller than 16 mm fragmented. The authors argued that the failure was probably initiated at numerous points throughout the specimen and not at the crack tip.

Following the same technique, the effects of wall thickness and tube length on the fracture strength were analyzed with four series of tests [55]. In three series, the specimens were 50.8 mm long and 0.38, 0.762 and 1.525 mm thick respectively. In the fourth series, the specimens were 25.4 mm long and 0.762 mm thick. The crack size was varied to give a crack length-to-specimen width ratio in the range between 0.015 and 0.75.

The fracture stresses were calculated from the quasi-static model for thick cylinders, that relates the internal pressure with the hoop stress. A linear relationship was obtained between the square root of the inverse of the crack length and fracture stress, when the crack length is over 3.5 mm. The resultant straight line did not intersect the origin. Moreover, it was observed that the fracture stress was independent of the flaw size, when the crack size was below 3.5 mm. The authors explained that the fracture initiated probably in different points which are not close to the crack tip. In the range where the linear relation was observed, the following relation between crack length and fracture stress was suggested, in which A and B are empirical constants.

$$\sigma_\theta = Aa^{-1/2} - B \qquad 1.3$$

The authors argue that a geometrical crack factor Y for finite width flawed tubes is not available. They considered that the crack is predominantly loaded with uniaxial stresses. Therefore, very

similar to that in a flat plate. Provided the tube diameter is sufficiently large, the finite corrections will be similar to those for flat plates. Thus, the fracture toughness in infinitely wide plate is given by

$$K_{Ic} = \sigma_c (\pi a)^{1/2} \qquad 1.4$$

Besides, the same parameter for a plate of finite width W is

$$K_{Ic} = Y\sigma_f a^{1/2} \qquad 1.5$$

where $Y = \pi^{1/2} + 0.227(2a/W) - 0.51(2a/W)^2 + 2.7(2a/W)^3$. From the last two equations, the factor $Y/\pi^{1/2}$ was obtained and the fracture stress was increased in this proportion. Consequently, the constant B was reduced 40%. The authors argue that the bending corrections are not applicable under dynamic loading, because the short time scale of the fracture event does not permit the bending deflections to reach the values predicted from equilibrium conditions. Besides, a correction factor for dynamic conditions must be considered, because the expression is derived from equilibrium considerations.

Jamarani et. al. [57,58] extended this research, testing unplasticized polyvinyl chloride (PVC) specimens, which were notched and unnotched. In the case of the notched specimens, the nominal crack lengths were 1, 2, 3, 4, 5, 6, 8 and 10 mm, which were produced along the generator of the cylinder. The specimens were loaded under incident and reflected modes of step load. The resultant step load was followed by a slow pressure rise just prior to the specimen collapse. However, a more complicated pattern is obtained in the reflected conditions, because the gas expands in a closed volume.

The numerical factor $(\pi a)^{-1/2}$, that involves the crack length, was plotted against the fracture stress, which was evaluated with the quasi-static relation for thin cylinders between the internal pressure and hoop stress. A linear relationship, that does not extrapolate to the origin, was obtained for various load rates up to 10^3 MPa/s. The Folias factor [56] was adjusted to account for

the initial bending effects and crack configuration. When it was applied to the results, the lines were shifted to the origin. Then, the fracture energy release rate G was obtained, following the method described by Marshall et. al. [34]. In this case, a geometrical factor which considers the notch and the geometry effects for this sort of specimen was derived and the energy release rate and stress intensity factor were calculated.

The results showed that in the case of PVC the fracture toughness decreased as the loading rate was increased. Although this material is ductile, the fracture of the notched specimens was brittle. The dimension of the plastic zone was evaluated using the models of Dugdale and Irwin and it was argued that the extent of the plastic zone at the crack tip decreases continuously with increasing strain rate.

Summarising, several impact testing techniques have been developed, which evaluate the dynamic fracture toughness in plastics with fracture mechanics, assuming quasi-static considerations. In the case of the pendulum, the falling weight and the impacting sphere tests, the first and foremost problem is the effect of the inertia forces, which are developed after the impact, over the elastic response of the specimen. In consequence, the load evaluation at crack initiation is inaccurate. Moreover, a complex stress field is developed at the crack tip due to stress waves, and at the same time, the interaction between the specimen and the testing rig generates structural vibrations. These factors complicate even more the evaluation of the fracture parameters.

The interaction between the specimen and the testing rig in the shock tubing tests has been minimized. However, the specimen geometry introduces some problems, because it is not possible to consider the proper crack geometry factor Y. Besides, a controversy has been raised related with the influence of the bending stresses over the crack initiation. With regard to the loading conditions, the specimen is not loaded uniformly, although its dimensions are small. Furthermore, in the reflection mode, the load pattern is complex. As a result, a complex stress field may be developed in the specimen.

An accurate calculation of the fracture toughness and an evaluation of the fracture process with the available impact testing techniques is not possible. Consequently, the development of a new impact method is required.

1.3 Mechanical Behaviour of Polymers.

In mechanical creep experiments [59], a sudden stress is applied to a polymeric specimen at time t_0 and then held constant until some time later t_1, when it is totally removed. In this case, the strain commonly increases gradually until a maximum value at t_1. After the stress removal, the strain returns slowly with time to zero. This situation is illustrated in figure 1.9. The time-dependent compliance may be defined

$$Compliance = D(t) = \frac{\varepsilon(t)}{\sigma_0} \qquad 1.6$$

where $\varepsilon(t)$ is the time dependant strain and that for small strains ($\varepsilon(t) < 0.001$), D(t) is found to be independent of the magnitude of σ_0.

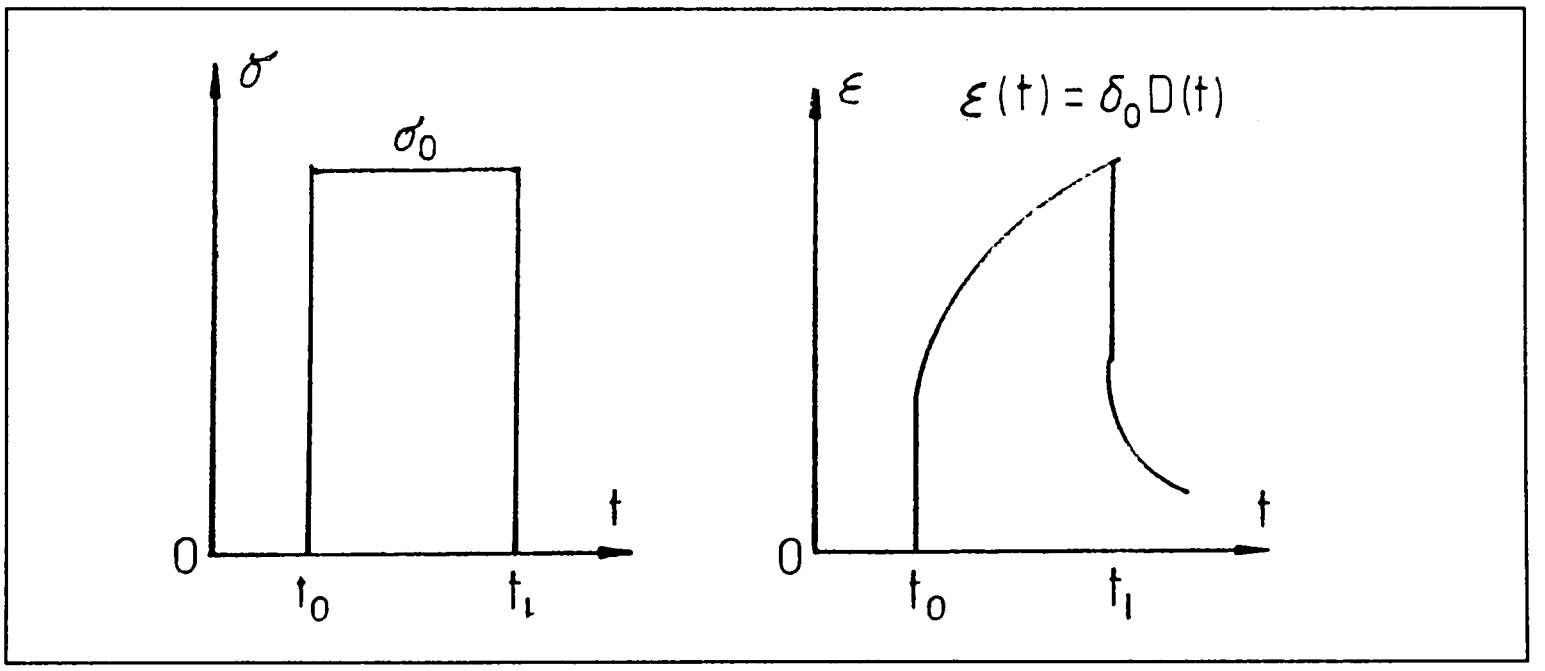


Figure 1.9 Results of a typical creep experiment.

Similarly, in the stress relaxation experiments [59], the strain ε_0 is held constant during the time t_1-t_0. Then, it is removed. In this instance, the stress $\sigma(t)$ is time dependent and diminishes from its maximum value at t_0 to a certain value $\sigma(t)$ at t_1, when it shows a sudden drop. Eventually, it recovers to zero as illustrated in figure 1.10. The time-dependant modulus is defined by

$$\textit{Time-Dependant Modulus} = E(t) = \frac{\sigma(t)}{\epsilon_0} \qquad 1.7$$

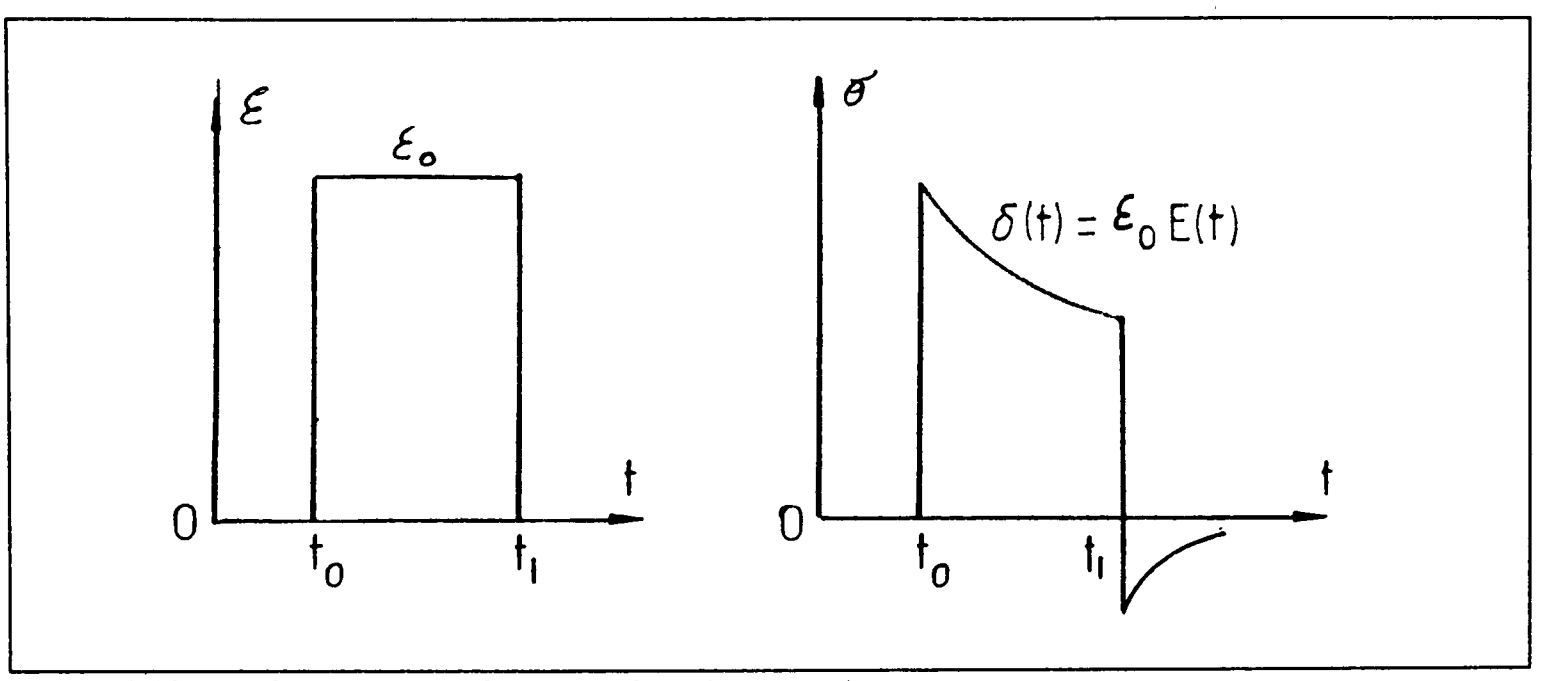


Figure 1.10 Results of a typical stress relaxation experiment.

These results suggest that polymers have a viscoelastic behaviour. In other words, they do not only have elastic characteristics, but also they share some features with the viscous fluids.

With respect to the findings in the dynamic response analysis, the viscoelastic material behaves like a viscous fluid, when a extremely slow sinusoidal strain is applied. On the contrary, when the cyclic strain rate is very rapid the material behaves as purely elastic. Thus, at elevated strain rates, the behaviour of the material may be considered elastic. This situation has been corroborated with the findings of the research reported in the last sections and is, indeed, fundamental to all the work published on dynamic fracture.

In the case of metallic materials, the experimental evidence has shown that most metals and alloys exhibit an increase in yield point and tensile strength with strain rate. In consequence, the elastic range is wider. The rate sensitivity depends chiefly in the temperature and the internal structure of the material [60].

Summarising, metals and polymers have different behaviour when they are loaded with quasi-

static loads. Nevertheless, their response is elastic at high strain rates. Accordingly, the fracture problems at elevated rates may be treated using a linear fracture mechanics approach in both cases. In particular, the conclusions drawn from the impact analysis in plastics, may be used to establish a background for a complete explanation of the dynamic fracture phenomenon in metals.

1.4 Aim and Outline of the Thesis.

The main aim of this thesis is the development of an impact testing method, improving the current techniques. It shall be rigorously analyzed and will be used in the evaluation of the dynamic fracture toughness of PMMA specimens under dynamic pressure loading, by means of a numerical-experimental analysis.

In the following chapter, the new impact testing technique, which tests circular plates, is presented. Initially, the experimental rig and the operational procedures for dynamic and static tests are described. Then, the calibration of the set up and the characterization of the dynamic pressure load is discussed. With the analysis of the experimental findings, the loading cases for the crack initiation tests are selected. In the last part, the elastic response of the specimens to the dynamic pressure load is analyzed experimentally. With this background, the advantages over other impact testing techniques are established and an experimental-numerical technique is proposed for the analysis of crack initiation under dynamic pressure loading.

In Chapter Three, the experimental crack initiation analysis under dynamic and static load is reported. In the case of the dynamic tests, the average strain rate before crack initiation is evaluated and the crack initiation load is evaluated, considering a dynamic calibration. These results are compared with the findings of the quasi-static tests.

In Chapter Four, the numerical evaluation of the dynamic fracture toughness is reported. In the case of the dynamic tests, three different procedures are followed. In the first, this parameter is evaluated with standard solutions in conjunction with a dynamic stress analysis of an uncracked specimen. Furthermore, an assessment of the factors involved in the formulation of the equation of these solutions is made. In the second, a quasi-static evaluation is performed with the J-Integral method, in which only the crack initiation load is taken into account. In the third, the dynamic

fracture toughness is evaluated with the J-Integral method following a dynamic approach. In the case of the static cases, the fracture toughness is evaluated with the J-Integral method and standard solutions. The stress analysis and the calculations of the J-Integral were carried out with the finite element code ABAQUS.

In Chapter Five, the interpretation of the experimental and numerical results is carried on. Thus, the mechanical properties of the material at the observed strain rates are evaluated and the results of microscopical analysis of the crack surfaces are reported. Likewise, ABAQUS evaluation of the J-Integral under dynamic loading is assessed with benchmark results. All the experimental and numerical findings are linked and a criterion for the acceptance and validity of the results is established. Finally, the main conclusions are drawn in Chapter Six and suggestions are made for further work.

REFERENCES

1. McClure, G. M., Duffy, A. R. and Eiber, R. J. Fracture Resistance in Line Pipe, *Trans. ASME J. of Eng. for Industry*, Vol. 87, Series B, Number 3 (1965)265-278.

2. Fearnehough, G. D., Jude, D. W. and Weiner, R. T. The arrest of brittle fracture in pipelines, *Practical Applications of Fracture Mechanics in Pressure Vessels Technology*, Proc. Inst. Mech. Engr. London (1971)156-162.

3. Ives, K. D., Shoemaker, A. K. and McCartney, R. F. Pipe deformation during a running shear fracture, *Trans. ASME J. of Eng. Mat. and Tech.* October (1974)309-317.

4. Shoemaker, A. K. and McCartney, R. F. Displacement considerations for a ductile propagating fracture in line pipe, *Trans. ASME J. of Eng. Mat. and Tech.* October (1974)318-322.

5. Bonomo, F., Bramante, M. and Spedaletti M. Ductile fracture propagation in pipelines: Results of instrumented full scale burst tests on 48" and 56" diameter pipes for gas transmission, *Analytical and Experimental Fracture Mechanics*, (ed.) G. C. Sih and Mirabik, Sijthoff-

Noordhoof (1981)567-578.

6. Sugie, E., Matsuoka, M., Akiyama, T., Mimura, H. and Kawaguchi, Y. A study of shear crack propagation in gas-pressurized pipelines. *Trans. ASME J. of Press. Vessels Tech.* 104(1982)338-343.

7. Demofonti, G., Maresca, A., and Buzzichelli, G. Ductile fracture propagation and arrest in offshore pipelines, *Appl. Mech. Rev.* No. 2 41(1988)85-95.

8. Almond, A. E., Petch, N. J., Wraith, A. E. and Wright, E. S. The fracture of pressurized laminated cylinders, *J. of The Iron and Steel Institute*, October(1969)1319-1323.

9. Poyton, W. A. and Christian, J. R. An experimental study of shear fracture propagation using small scale models. Paper 5, *Crack Propagation in Pipelines*, The Inst. of Gas Engr. & British Gas, Newcastle upon Tyne, England. 26th and 27th March 1974.

10. Hood, J. E. and Jamieson, R. M. Ductile Fracture in large-diameter pipe, *J. of The Iron and Steel Institute*, May(1973)369-373.

11. Shannon, R. W. E. and Wells, A. A. Brittle crack propagation in gas filled pipelines-A model study using thin walled unplasticised PVC pipe, *Int. Journ. of Fracture*, 10(1974)471-486.

12. Baum, M. R. The development of the Breach generated by axial rupture of a gas-pressurized steel pipe, *Trans. ASME J. of Press. Vessel Tech.*, 104(1982)253-261.

13. Emery, A. F., Kobayashi, A. S., Love, W. J., Place, B. W., Lee, C. and Chao, Y. H. An experimental and analytical investigation of axial crack propagation in long pipes, *Engng. Fracture Mech.*, No. 1, 23(1986)215-226.

14. Kobayashi, A. S., Emery, A. F., Love, W. J. and Chao, Y. -H. Subsize experiments and numerical modelling of axial rupture of gas transmission lines, *Trans. ASME J. of Press. Vessel*

Tech. May 110(1988)155-160.

15. Hahn, G. T., Sarrate, M., Kanninen, M. F. and Rosenfield, A. R. A model for unstable shear crack propagation in pipes containing gas pressure, *Int. Journ. of Fracture*, 9(1973)209-222.

16. Poynton, W. A., Shannon, R. W. E. and Fearnehough, G. D. The design and application of shear fracture propagation studies, *Trans. ASME J. of Eng. Mat. and Tech.* October (1974)323-329.

17. Emery, A. F., Love, W. J. and Kobayashi, A. S. Elastic crack propagation along a pressurized pipe, *Second National Congress on Pressure Vessels and Piping*, San Francisco Calif., June 23-27, 1975, ASME, Paper 75-PVP-15.

18. Kanninen, M. F., Sampath, S. G. and Popelar, C. Steady-state crack propagation in pressurized pipelines without backfill, *Second National Congress on Pressure Vessels and Piping*, San Francisco Calif., June 23-27, 1975, ASME, Paper 75-PVP-39.

19. Emery, A. F., Love, W. J. and Kobayashi, A. S. Fracture in straight pipes under large deflection conditions-Part I, Structural deformations, *Petroleum Mechanical Engineering and Pressure Vessels and Piping Conference*, Mexico City, Mexico, September 19-24, 1976, ASME, Paper 76-PVP-9.

20. Love, W. J., Emery, A. F. and Kobayashi, A. S. Fracture in straight pipes under large deflection conditions-Part II, Pipe Pressures, *Petroleum Mechanical Engineering and Pressure Vessels and Piping Conference*, Mexico City, Mexico, September 19-24, 1976, ASME, Paper 76-PVP-14.

21. Freund, L. B., Parks, D. M. and Rice J. R. Running ductile fracture in pressurized line pipe, *Mechanics of Crack Growth ASTM STP 590*, American Society for Testing and Materials (1976)243-262.

22. Owen, D. R. J. and Shantaram, D. Numerical study of dynamic crack growth by the finite element method, *Int. Journ. of Fracture*, 13(1977)821-837.

23. Freund, L. B., Li, V. C. F. and Parks, D. M. An analysis of a wire-wrapped mechanical crack arrester for pressurized pipelines, *Trans. ASME J. of Press. Vessel Tech.*, 101(1979)51-58.

24. Emery, A. F., Perl, M., Kobayashi, A. S. and Love, W. J. The use of the split ring in modelling ductile axial crack extensions in pipes, *Trans. ASME J. of Press. Vessel Tech.*, 103(1981)151-154.

25. Emery, A. F., Perl, M., Love, W. J. and Kobayashi, A. S. On the motion of an axial crack through crack in a pipe, *Trans. ASME J. of Press. Vessel Tech.*, 103(1981)281-286.

26. Maxey, W. A. Dynamic crack propagation in line pipe, *Analytical and Experimental Fracture Mechanics*, (ed.) G. C. Sih and M. Mirabik, Sitjhoff Noordhoff (1981)109-123.

27. Ramulu, M., Kobayashi, A. S. and Kang, B. S. -J. Dynamic crack curving and branching in line-pipe, *Trans. ASME J. of Press. Vessel Tech.*, 104(1982)317-322.

28. Alpa, G., Bozzo, E. and Gambarotta L. A theoretical evaluation of the backfill effect in fracture of gas pressurized pipelines, *Trans. ASME J. Press. Vessel Tech.*, 106(1984)47-53.

29. Abbassian, F. and Calladine, C. R. On the deformation of the pipe wall during propagation of ductile crack in high-pressure gas pipeline, *Trans. ASME J. Press. Vessel Tech.*, 111(1989)47-56.

30. Griffith A. A. The phenomena of rupture and flow in solids, *Phil. Trans. Roy. Soc.*, A221(1921)163-197.

31. Orowan, E. *Repts. Prog. Phys.* 12(1948)185.

32. Irwin, G. R. Structural aspects of brittle fracture, *Appl. Mats. Res.* 3(1964)65-81.

33. Kinloch, A. J. and Young, R. J. *Fracture Behaviour of Polymers*, Elsevier Applied Science, London and New York, (1990).

34. Marshall, G. P., Williams, J. G. and Turner, C. E. Fracture toughness and absorbed energy measurements in impact tests on brittle materials. *J. Mater. Sci.*, 8(1973)949-956.

35. Brown, H. R. A Critical examination of the impact test for glassy polymers. *J. Mater. Sci.* 8(1973)941-948.

36. Plati, E. and Williams, J. G. The determination of the fracture parameters for polymers in impact. *Polym. Eng. and Sci.* 15(1975)470-477.

37. Birch, M. W. and Williams, J. G. The effect of rate on the impact fracture toughness of polymers. *Int. Journ. of Fracture*, 14 (1978)69-84.

38. Clutton, E. Q., Hemingway, A. J., Channell, A. D. Instrumented Charpy impact testing of polyethylene. *Impact Testing of Plastics Conference*, The Plastics and Rubber Institute, Sept. 1990.

39. McMillan, P. W. and Tesh, J. R. Dynamic effects in the impact testing of brittle materials, *J. Mater. Sci.* 10(1975)621-632.

40. Ruiz, C. and Mines, R. A. W. The Hopkinson pressure bar: an alternative to the instrumented pendulum for Charpy tests. *Int. Journ. of Fracture*, 29(1985)101-109.

41. Kalthoff, J. F., Winkler, S. and Beinert, J. The influence of dynamic effects in impact testing. *Int. Journ. of Fracture*, 13(1977) RCR 528-531.

42. Kalthoff, J. F., Böhme, W., Winkler, S. and Klemm, W. *Proceedings CSNI Specialist Meeting on Instrumented Precracked Charpy Testing,* EPRI, Palo Alto, California (1980) II 1-16.

43. Kalthoff, J. F., Böhme, W. and Winkler, S. *Proceedings VIIth International Conference on Experimental Stress Analysis*, Society for Experimental Stress Analysis, Haifa, Israel (1982)148-160.

44. Böhme, W. and Kalthoff, J. F. The behaviour of notched bend specimens in impact testing. *Int. Journ. of Fracture*, 20(1982) R139-143.

45. Kalthoff, J. F., Winkler, S., Böhme, W. and Klemm, W. *Proceedings of International Conference on Dynamical Mechanical Properties and Fracture Dynamics of Engineering Materials*, Czechoslovak Academy of Science, Institute of Physical Metallurgy, Brno-Valtice, CSSR (1983) 1-16

46. Manogg, P. Anwendung der schattenoptik zur untersuchung des zerreissvorgangs von platten. Dissertation, Universität Freiburg, West Germany (1964).

47. Theocaris, P. S. and Katsamanis, F. Response of cracks to impact by caustics. *Engng. Fracture Mech.*, 10(1978)197-210.

48. Katsamanis, F. G. and Delies, C. G. Fracture surface energy measurements of PMMA: A new experimental approach. *J. Phys. D: Appl. Phys.* 21(1988)79-86.

49. Ravi-Chandar, K. and Knauss, W. G. Dynamic crack-tip stresses under wave loading - a comparison of theory and experiments. *Int. Journ. of Fracture* 20(1982)209-222.

50. Ravi-Chandar, K. and Knauss, W. G. An experimental investigation into dynamic fracture: I. Crack initiation and arrest. *Int. Journ. of Fracture* 25(1984)247-262.

51. Freund, L. B. Crack propagation in an elastic solid subjected to general loading - I. Constant rate of extension. *J. Mech. Phys.* 20(1972)129-140.

52. Freund, L. B. Crack propagation in an elastic solid subjected to general loading - II. Non-

uniform rate of extension. *J. Mech. Phys.* 20(1972)141-152.

53. Reed, P. E., Nurse, P. J. and Andrews, E. H. High strain rate testing of plastics. Part 1. Shock tube technique. *J. Mater. Sci.* 9(1974)1977-1986.

54. Reed, P. E. and Squires, H. V. Application of fracture mechanics to plastics deformed at high strain-rates. *J. Mater. Sci.* 9(1974)129-135.

55. Squires, H. V. and Reed, P. E. Application of fracture mechanics to plastics deformed at high strain-rates. Part 2 Geometrical factors. *J. Mater. Sci.* 10(1975)1465-1471.

56. Folias, E. S. An axial crack in a pressurized cylindrical shell. *Int. J. Fracture Mech.* 1(1965)104.

57. Jamarani, M. B., Reed, P. E. and Davies, W. R. Fracture behaviour of UPVC thin tubes at high loading rates. *J. Mater. Sci.* 23(1988)4437-4444.

58. Jamarani, M. B., Reed, P. E. and Davies, W. R. Fracture behaviour of UPVC thin tubes at high loading rates. Part 2 Validity of fracture toughness tests and the effects of rate. *J. Mater. Sci.* 24(1989)2917-2922.

59. McCrum, N. G., Read, B. E. and Williams, G. *Anelastic and dielectric effects in polymeric solids*, John Wiley & Sons (1967).

60. Harding, J. The effect of high strain rate on materials properties. *Materials at high strain rates*, Ed. T. Z. Blazynski, Elsevier Applied Science, London, (1987).

CHAPTER 2

DEVELOPMENT OF THE IMPACT TESTING PROCEDURE

2.1 Introduction.

A new impact testing procedure must satisfy several requirements. The first and foremost is that the elastic response of the specimen should be affected as little as possible by the inertia forces. Besides, the loading must increase steadily without violent oscillations, so that it may be evaluated accurately. With respect to the specimens, their geometry should be simple to facilitate their fabrication and the numerical analysis of the problem. Regarding the testing apparatus, it should be capable to perform static tests as well, so as to compare the static and dynamic results with the same approach and, thus, derive a criterion for the evaluation of the dynamic test results. Lastly, the test procedure must be simple.

These considerations are satisfied if the tests are performed with the impact testing apparatus based on shock tube, shown in figure 2.1, in which a circular plate, fixed at its top end, is subject to a uniform pressure. The apparatus produces pressure-rises in a short period by bursting a thin membrane, loading the specimens perpendicularly with a uniform pressure wave and developing a field of tensile and bending stresses with its maximum point at the specimen centre. Hence, the interaction between the specimen and the testing rig is diminished, because the samples are not

loaded with mechanical devices and the dynamic structural effects are minimized.

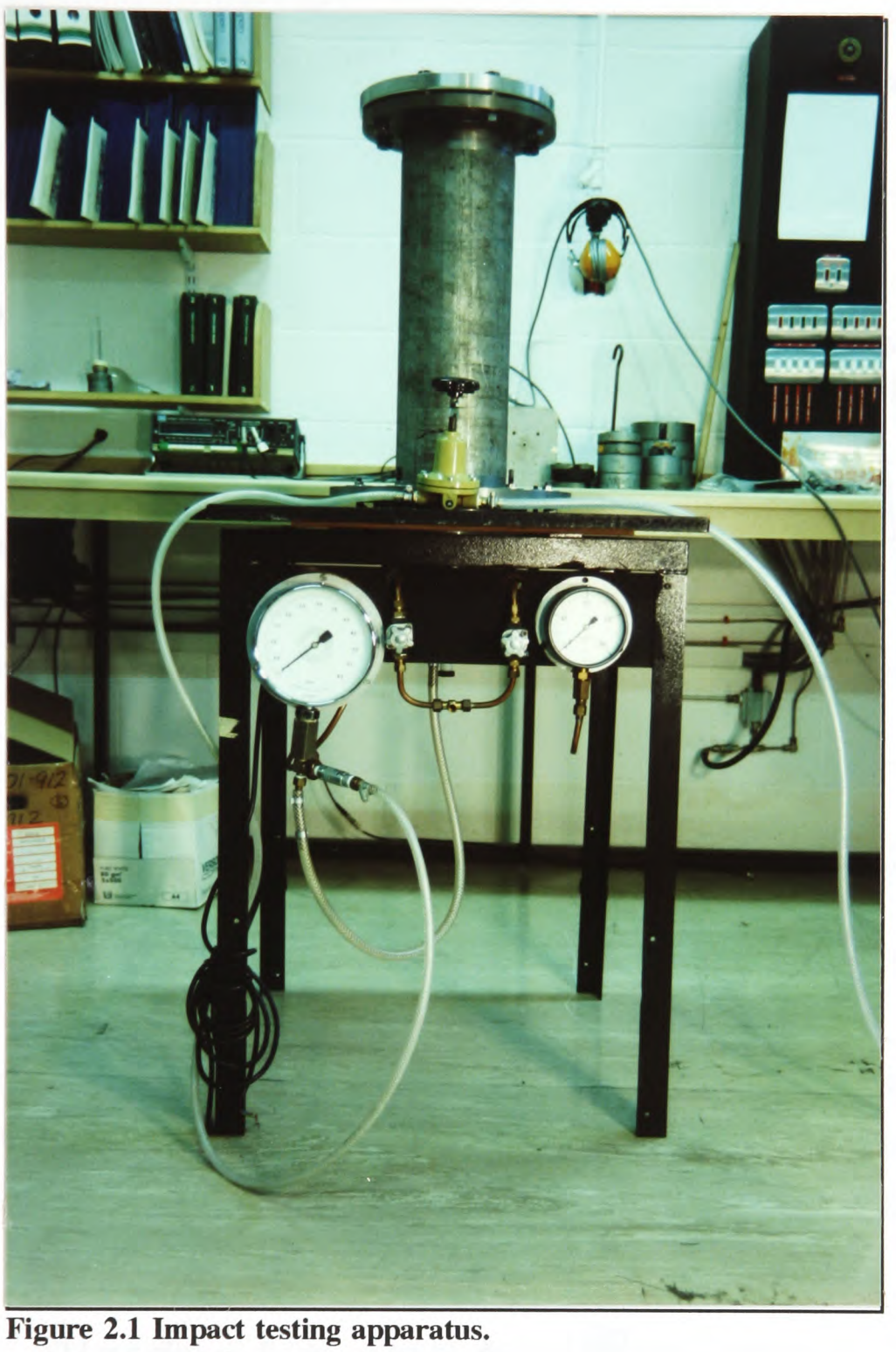


Figure 2.1 Impact testing apparatus.

In this research, the proposed impact technique will be used in the analysis of crack initiation under dynamic loading, testing centrally cracked specimens. In addition, the impact test apparatus can perform static tests without substantial changes. In that case, the recording technique and the rig calibration are very simple.

In relation with the dynamic test, there are three questions that have to be answered before it is

applied to dynamic fracture analysis. The first one is related with the evaluation of the characteristics of the pressure pulse. The second is associated with the shape of the pressure wave front and the third is linked with the elastic response of the specimens to these impulsive loads.

With respect to the last issue, the theoretical analysis of bending waves on plates has shown that the displacement of each point, along a direction perpendicular to their principal plane, is in function of the bending and shear stresses. In particular, consider a flat plate of thickness h, whose mid-plane is on the xy plane, when it is in equilibrium, and remains unstrained, when it is bent under the pressure loading P(t). The material is linear elastic and it is subjected to small deflections.

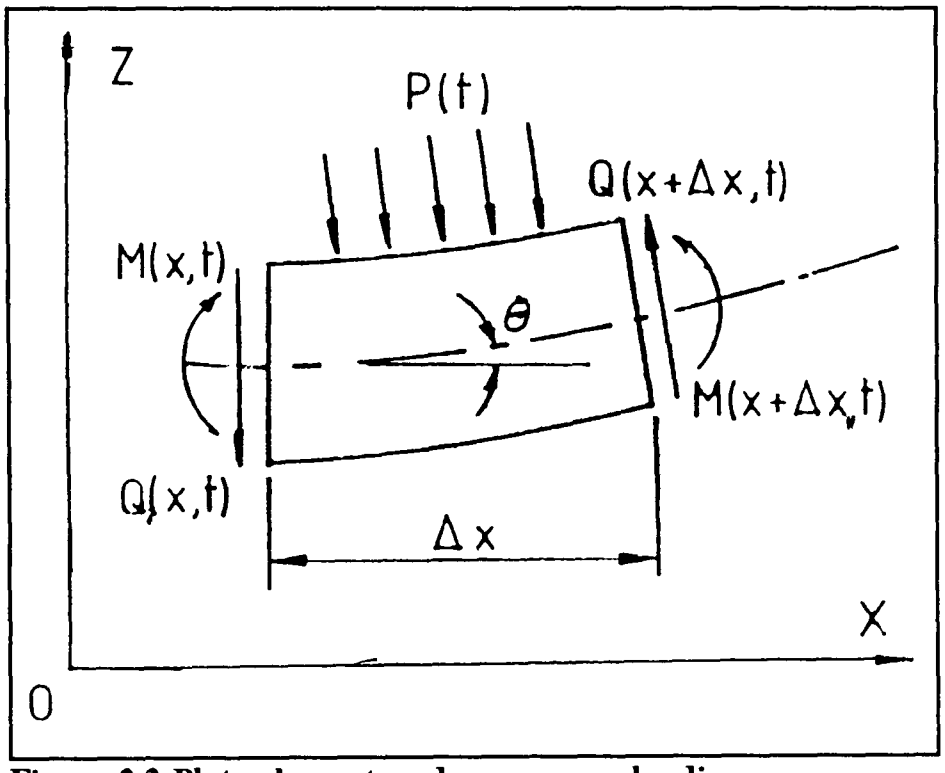


Figure 2.2 Plate element under pressure loading.

Now, take a plate element between x and x + dx, as illustrated in figure 2.2, of unit width and thickness h, which is under the pressure load P(t). Moreover, the shear forces Q(x,t) and Q(x+dx,t) and the moments M(x,t) and M(x+dx,t) act at its ends. Then, the net vertical force is

$$Q(x+dx) - Q(x) - P(t)\,dx = \left(\frac{\partial Q}{\partial x}\right)dx - P(t)\,dx$$

The resultant equation of translational motion, in which the mass density of the plate ρ and the displacement of each point of the plate along the vertical direction ξ are considered, has the following form

$$\rho h \frac{\partial^2 \xi}{\partial t^2} = \frac{\partial Q}{\partial x} - P(t)$$

In addition, the rotational motion is expressed in terms of the angle θ. Thus, the total couple on the element is

$$M(x+dx, t) - M(x, t) + Q dx + P(t)\frac{d^2x}{2} = \left(\frac{\partial M}{\partial x}\right)dx + Q dx + P(t)\frac{d^2x}{2}$$

The moment of inertia ρIdx of the element about the centre of mass axis is Idx = (h^3/12)dx. Hence, the equation of motion is

$$\rho I \frac{\partial^2 \theta}{\partial t^2} = \frac{\partial M}{\partial x} + \frac{P(t)}{2} dx + Q$$

In the case of the proposed impact technique, the flexural waves are generated from the centre of the specimen, which is the point of maximum displacement and symmetry centre. They take the generated loads to the plate ends. So, the elastic response is influenced by the stresses and the inertia.

Although inertial loads cannot be ignored, their importance is still likely to be less than in the case, for example, of a plate or a beam under point loading. In that case, typified by the Charpy test, the only distributed load is due to the inertial term and the specimen inertia will therefore play an essential role in determining the state of stress. In the plate under uniformly distributed pressure, the pressure term might conceivably overwhelm the inertial load.

The theoretical analysis of the structural response to impulsive loads has demonstrated that in the case of short duration loads, when the ratio of the load duration to the period of vibration of the structure (t_1/T) is less than 0.25, the maximum displacement depends principally upon the magnitude of the applied impulse

$$I_m = \int_0^{t_1} p(t)\, dt$$

and is not strongly influenced by the form of the loading impulse. Besides, the maximum response is likely to occur after the interval of load application. On the other hand, for long-duration

loading, when the ratio $t_1/T > 1$, the maximum response occurs during the loading interval [1].

All these considerations suggest that the answers to the questions mentioned above are not straightforward. So, a series of experiments have been performed. Their description and results are discussed in the following sections of this chapter.

2.2 Description of the Experimental Rig.

The experimental rig has four main parts, namely the pressure chamber, the expansion chamber, the specimen and the recording system, which includes transducers, recording devices, oscilloscopes, software and a personal computer, for processing the experimental data. The equipment used is shown in figure 2.3 and figure 2.4 illustrates a schematic diagram of this arrangement.

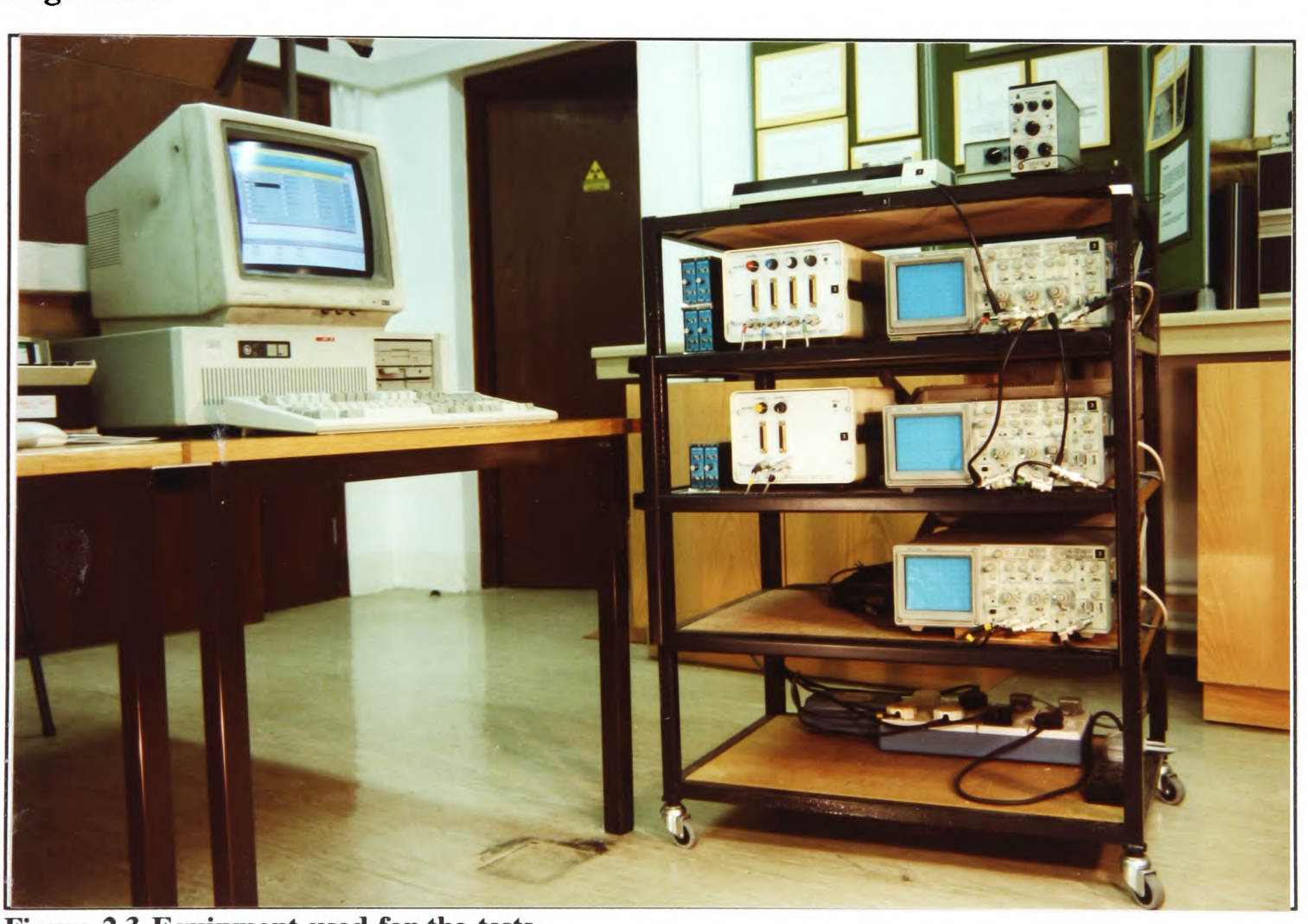


Figure 2.3 Equipment used for the tests.

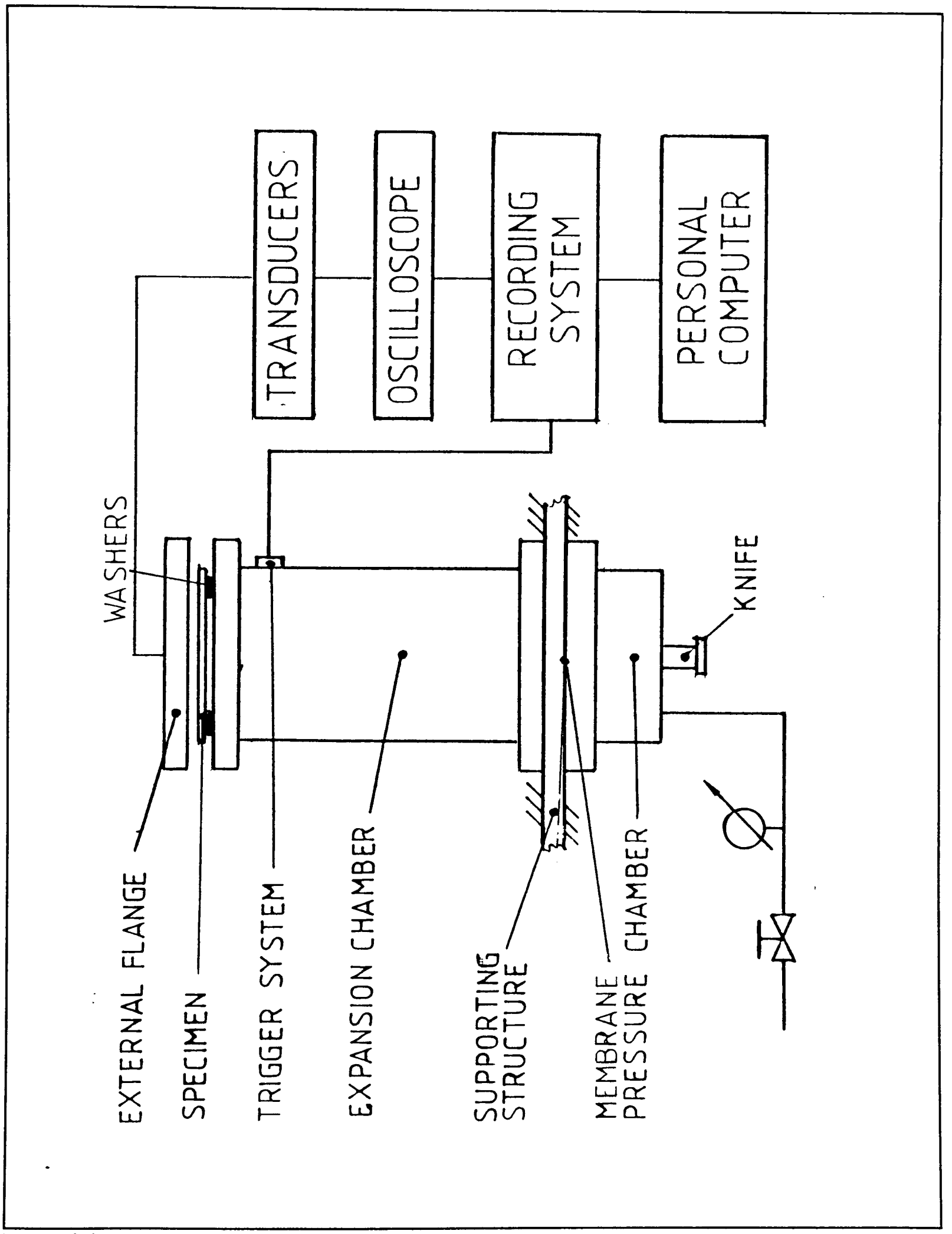


Figure 2.4 Schematic arrangement of the testing rig.

The pressure chamber, as shown in figure 2.5, is an open vessel made of aluminium, whose diameter and height are 200 mm and 110 mm respectively. A spring-loaded knife with a cross-shaped end and an air inlet are fixed at the bottom. Its upper end is threaded and joined to the chamber flange, which is clamped onto the supporting structure (figure 2.6). The open end is closed with a circular MELINEX[a] membrane 0.1 mm thick and 205 mm diameter, which is clamped between the top end of the open vessel and the flange of the supporting structure.



Figure 2.5 Pressure chamber.

The membrane material is a polyester film, which is transparent and flexible. It is produced from polyethylene terephthalate and its tensile strength is 160 MPa. Furthermore, the effect of the temperature on the physical and isotropic mechanical properties is small between -20°c and 80°c and no embrittlement occurs in this temperature range. Its impact strength and bursting strength are high [2,3].

The pressure is measured with a bourdon manometer made by Budenberg Gauge Co. Ltd. Its

[a] Melinex is a trade mark of ICI.

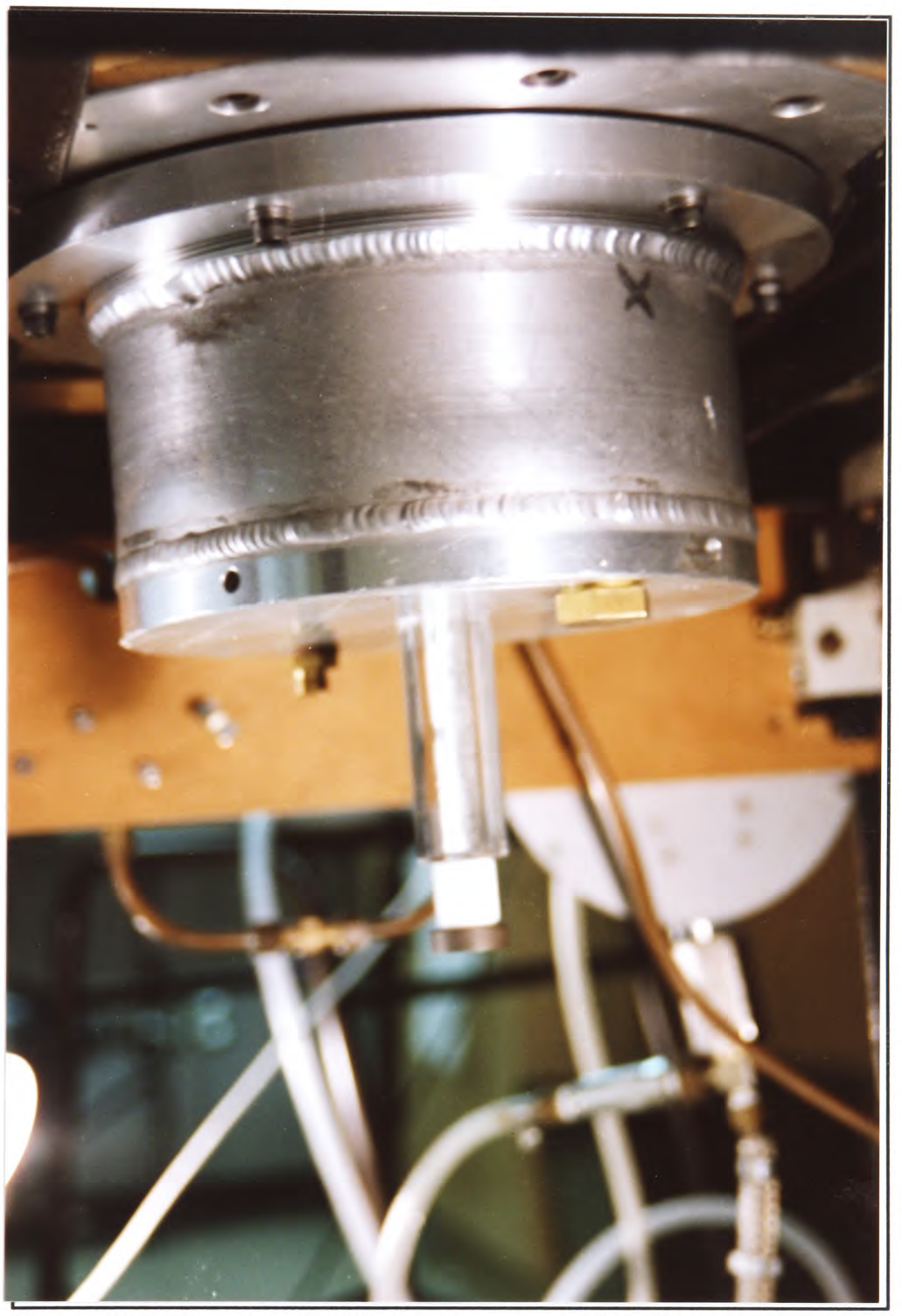


Figure 2.6 Clamping detail of the pressure chamber.

reading range is between 0.10 bar and 6 bar, with a minimum scale division of 0.05 bar and it is installed between the pressure chamber air inlet and the pressure regulator valve, which controls the air flow from the compressor. This valve has been manufactured by Norgren and its maximum output pressure is 2 bar.

The expansion chamber, which directs the resultant pressure wave to the specimen, is a steel cylinder with constant cross section and flanged ends. The one at the bottom connects with the

flange of the supporting structure, while the top flange fastens the specimen with an external flange. Its internal diameter and length are 155 mm and 550 mm respectively.

The analysis of the pressure waves was done with piezoelectric pressure transducers of high mechanical input impedance (stiffness), which means that their natural frequency is high and thus causes only a small distortion to dynamic signals. Their disadvantage is the need for low-noise cables of low capacitance, because the output signal normally represents a high electrical impedance [4].

The transducers are mounted on a circular steel plate whose thickness and diameter are 9 mm and 280 mm respectively. It also has 8 holes of 15 mm on the perimeter of a circle which coincides with the bolt circle of the clamping flanges. Hence, the whole set up is self-aligned with the principal axis of the expansion chamber. This stiff arrangement was chosen because it is advisable to avoid vibrations which may affect the output signal [5].

The strain and crack initiation analyses were done with PMMA specimens, which were cut from the same sheets. Their diameter and thickness are 280 mm and 3 mm respectively and they also have 8 holes of 15 mm, which coincide with the bolt circle of the clamping flanges. In the case of the instrumented tests, strain gauges were bonded on the specimens. They have been chosen because in dynamic conditions their small volume and mass do not affect the phenomenon studied [6].

In all the dynamic tests, the information is logged in a Tektronix 2211 oscilloscope, which is a combination of an analog and digital storage portable oscilloscope. Its vertical input channels are dual with an analog bandwidth of DC to 50 MHz and a digital bandwidth of DC to 10 MHz. Moreover, it has a CRT readout and a cursor measurement display. With regard to the calibrated sweep speeds, the range of the horizontal deflection system is from 0.5 to 5 x 10^{-8} s and the data is recorded with 4096 points per channel.

The data plotted on the oscilloscope screens allows an immediate assessment of the quality of tests. If the results are considered good, they are saved in an IBM personal computer AT with the

GRABBER software package [7]. This code transfers the waveforms displayed on the oscilloscope to a personal computer, stores the captured data on disk, displays the waveforms on the computer screen, converts the plot data to binary and other formats and print the captured information. Finally, the experimental data is processed for later analysis with Lotus software release 2.2 [8].

The recording system is triggered with a 4344 accelerometer produced by Brüel & Kjær. Its undamped natural frequency is 122 kHz and its voltage and charge sensitivities are 2.21 mV/g[b] and 2.42 pC/g respectively. All these values are referred to 50 Hz and 22°c. This instrument is fixed 20 mm below the top flange of the expansion chamber on the external surface of the cylinder.

2.2.1 Operational Procedure of the Impact Test Apparatus for Dynamic Tests.

The dynamic tests that can be performed with the experimental rig are the analysis of the pressure waves, the dynamic strain response and the crack initiation analyses. In all these cases, the operational procedure is described in the following.

Initially, the specimen is fixed between the external and top expansion chamber flanges. The flange bolts are tightened evenly with a torque wrench. Afterwards, the pressure chamber is removed from the testing rig. Then, the spring-loaded knife is put in its trigger position and the MELINEX membrane is installed on the open side. The resultant closed chamber is fixed to the pressure chamber flange, avoiding any distortion of the membrane. The sliding of the membrane is restrained by griping the pressure chamber flange with the flange of the supporting structure.

The air line supply is connected to the inlet of the pressure chamber. Subsequently, the chamber is pressurized to the required level within the range 0.25 bar to 2.0 bar. This operation is controlled with the pressure regulation valve and the manometer.

A pressure wave is generated when the membrane, which is broken along two perpendicular diameters, is burst by releasing the spring-loaded knife. The resultant blast wave is directed

---

[b] 1 g = 980.6 cm s^{-2}

perpendicularly to the plane of the specimen. As the wave moves towards the top end, a small vibration is induced in the expansion chamber which is picked up by the accelerometer, triggering the recording system. The signals of the transducers are registered with the transient recorders and the resultant traces are displayed on the oscilloscope screen and transferred to the memory of a personal computer with the GRABBER code for a later analysis.

2.2.2 Operational Procedure of the Impact Test Apparatus for Static Tests.

Two types of tests are done under static conditions, namely, calibration of the pressure transducers and crack initiation tests in quasi-static conditions. In both cases, the specimens are prepared for the required test, fixed to the testing rig and the pressure chamber is not sealed with a membrane. As a result, the pressure and expansion chambers constitute a single vessel which is closed with a specimen on its open side. Besides, the static events develop during relative long periods. So, the transient recording system is not used.

In the calibration of the pressure transducers, an initial reading of the atmospheric pressure is taken as a reference from the oscilloscope. Then, the pressure is increased slowly until a preestablished level is reached. When the pressure has stabilized, readings are taken from the manometer and the oscilloscope. This process is repeated until the maximum test pressure has been reached. In order to check the reproducibility of the results, a similar procedure is followed during depressurization. After sufficient information has been gathered, the calibration factor is obtained.

In the case of crack initiation analysis under static pressure, the pressure is increased very slowly or in small steps. This process is regulated with the control pressure valve and the pressure chamber manometer. This procedure continues until the crack initiates, which is detected by the "pop" sound and the crack initiation pressure is registered.

2.3 Calibration of the Impact Test Apparatus.

2.3.1 Calibration of the Pressure Transducers.

The variation of the pressure is registered as a voltage increment by the piezoelectric pressure transducers. Consequently, a calibration factor, which relates voltage and pressure increments, is required for each one. Thus, a series of tests have been performed with the impact testing apparatus operated in static conditions, following the procedure described in section 2.2.2.

The pressure transducers are model LX1603A, produced by SenSym and their charge sensitivity and natural frequency are 21.6 mV/bar and 50 kHz respectively. They are fully conditioned hybrid pressure transducers with temperature compensation and high level output voltage. Each transducer is provided in a compact ceramic package with pressure ports suitable for attachment to flexible tubing, whose external diameter and length are 5 mm and 9 mm respectively. The sensor chip has been attached with a stress-relieving mount to minimize stress transfer, but the stressing of the ceramic package during its installation must be avoided.

For the purpose of the calibration, the transducers have been identified with colours and each one was installed on the centre of a carrier plate, in which a 5 mm hole was drilled on its centre. They were back supported with an aluminium brace, as shown in figure 2.7, just to keep the instrument in position during the test and were connected to the oscilloscope of the recording system, at a sensitivity of 1 V/div. Readings at every 0.25 bar were taken, until a maximum pressure of 1.25 bar was reached. The calibration factors for each transducer are given in table 2.1.

TABLE 2.1
CALIBRATION FACTORS OF THE PRESSURE TRANSDUCERS

PRESSURE TRANSDUCER	CALIBRITION FACTOR (V/bar)
BLACK	4.68
YELLOW	4.64
WHITE	4.32
BLUE	4.48
RED	4.48
GREY	4.76



Figure 2.7 Transducers mounted on the steel plate.

2.3.2 Pressure-Time analysis: Open Tube.

Initially, the atmospheric expansion of the pressure waves was studied with several tests, following the procedure described in 2.2.1. Hence, the top end of the pressure chamber was left open and six transducers were installed on its cylindrical surface, along the axial direction. They were connected to three transient recorders and were triggered simultaneously. Thus, the variation of pressure along the pressure chamber was analyzed. Figure 2.8 indicates the position of the transducers relative to the membrane and their identification label.

The membrane was burst at pressures ranging from 0.25 bar to 2.0 bar, to obtain a data bank for calibration. The results were all entirely consistent and repeatable and only one will be described in detail, which corresponds to a bursting pressure of 1.5 bar. Its pressure history is shown in figure 2.9.

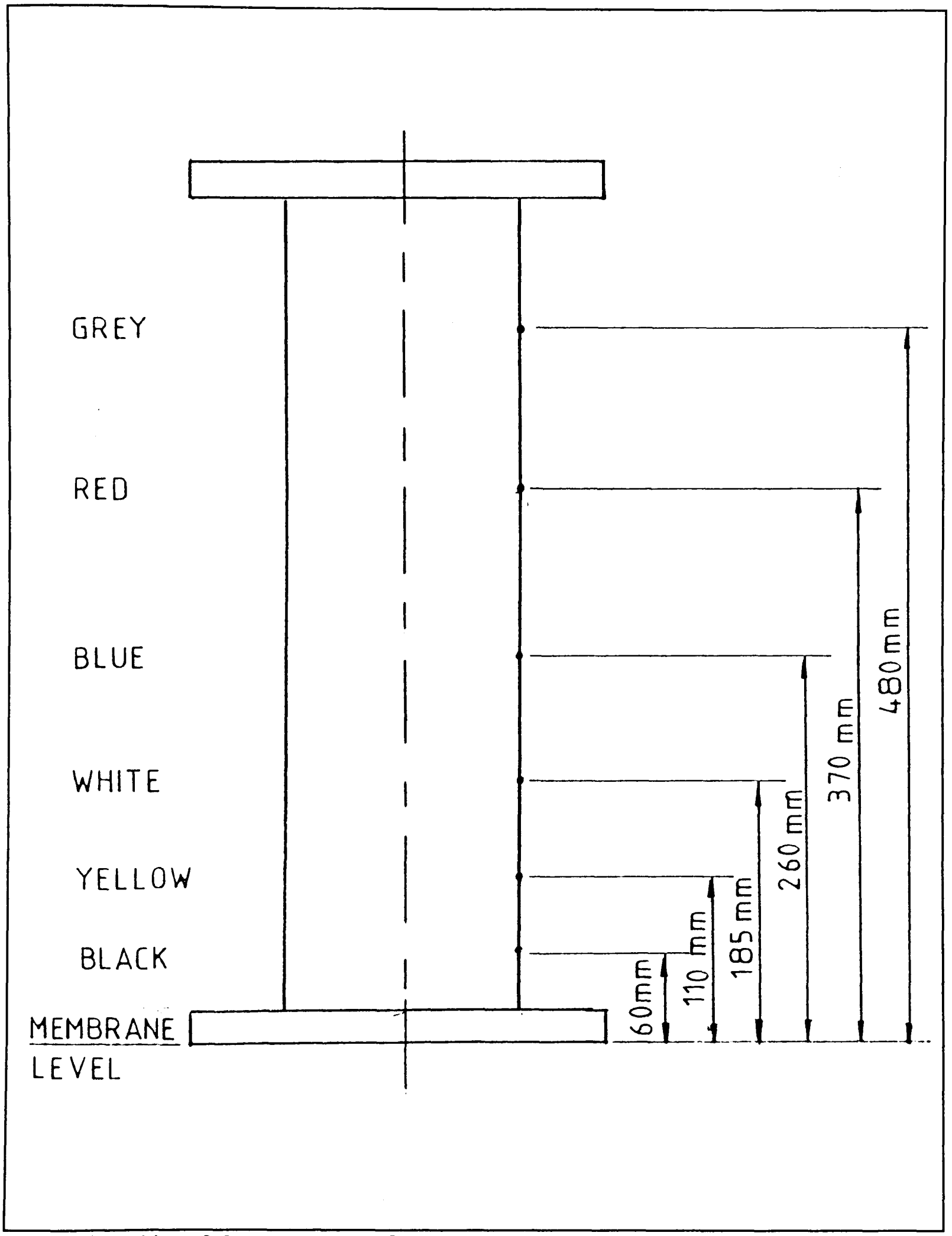


Figure 2.8 Position of the pressure transducers for the propagation analysis of the blast wave in the expansion chamber.

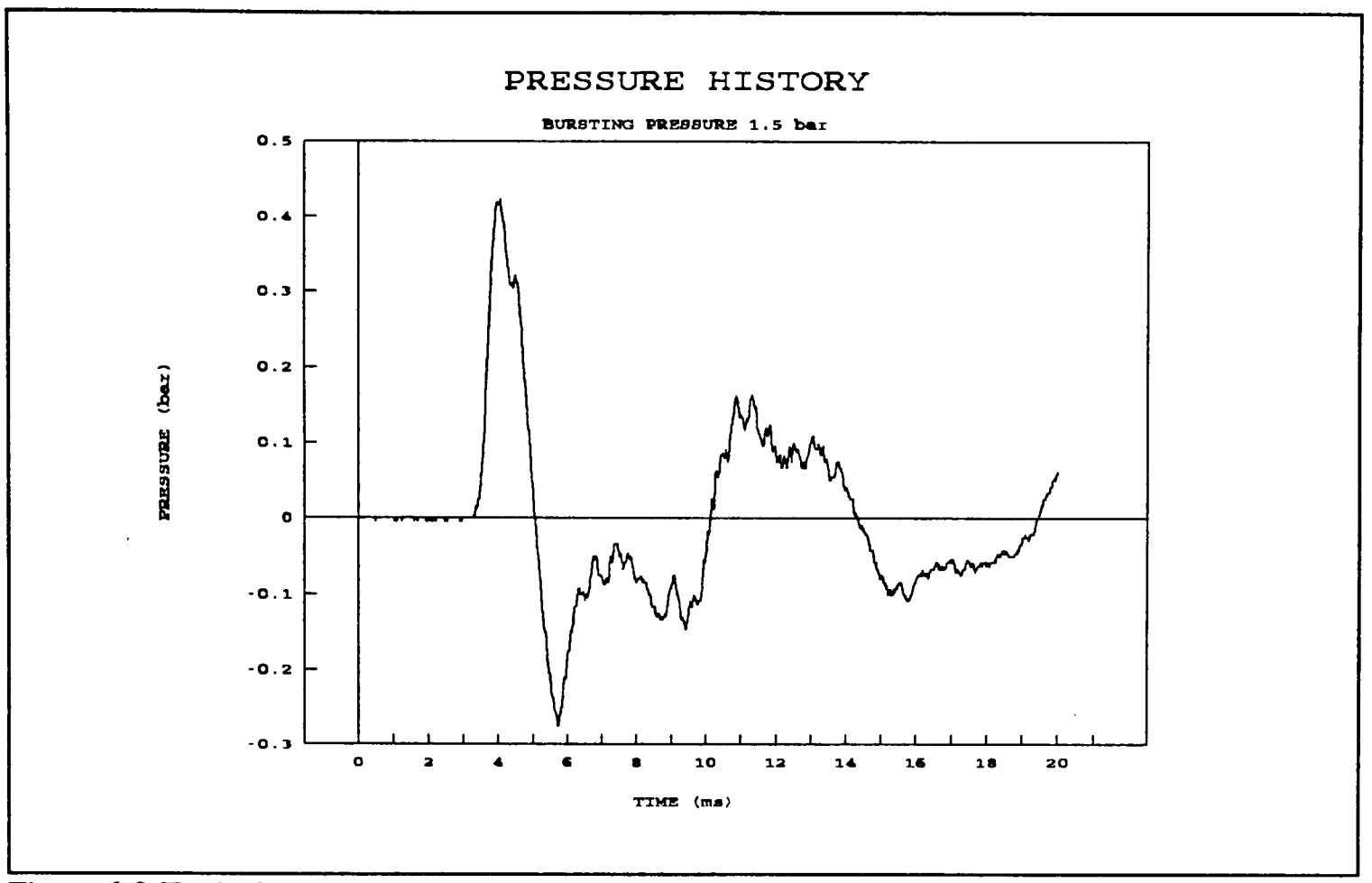


Figure 2.9 Typical pressure history.

The graph shows that as soon as the membrane bursts a damped pressure wave is generated which oscillates around the atmospheric pressure. The first peak is triangular with a well defined rapid rise. After the maximum pressure has been reached, it drops over a longer time interval to a partial vacuum. Eventually, it returns to the atmospheric pressure, completing the first cycle. This process is repeated, but the absolute values of the maximum and minimum peak pressures are lower in the subsequent cycles.

The resultant blast wave can be explained with the theoretical model proposed by Baker et. al. [9], illustrated in figure 2.10. In this case, the ambient pressure is P_0, before the blast wave is generated. At the arrival time t_a, the pressure rises abruptly to a peak value $P_s^+ + P_0$. Afterwards, the pressure decays to the ambient pressure P_0 in a total time $t_a + T^+$ and then drops to a partial vacuum of amplitude P_s^-.

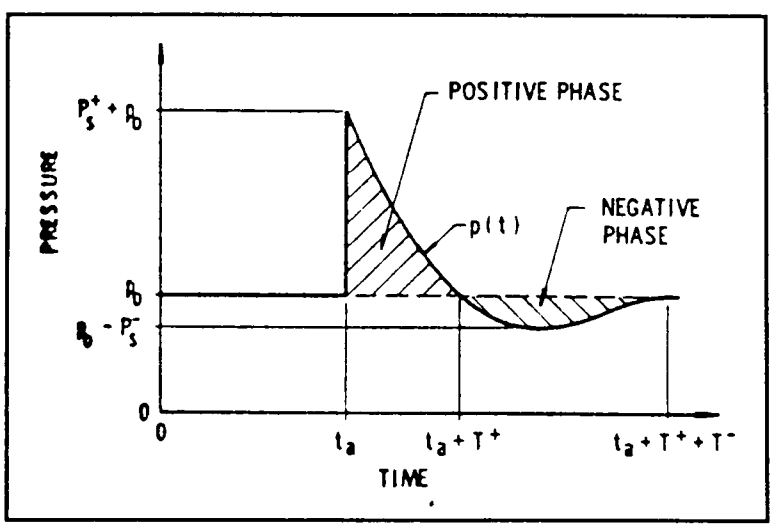


Figure 2.10 Ideal blast wave. After Baker et. al. [9].

Finally, it returns to the ambient pressure in a total time $t_a + T^+ + T^-$.

P_s^+ is usually termed the peak overpressure and the positive phase is the area between the ambient pressure and the segment of the curve which represents the overpressure values. Its duration is T^+. By contrast, the negative or suction phase, whose interval time is T^-, is the area enclosed by the suction phase, which is the segment of the curve that represents the partial vacuum, and the straight line that represents the ambient pressure.

Figures 2.11, 2.12 and 2.13 provide a comparison between pairs of transducers. The blue and white transducers, located near the central region of the expansion chamber give virtually identical signals (figure 2.11). Nonetheless, the traces of the transducers at the ends -grey and black- differ significantly, as shown in figure 2.12 since the pressure wave changes as it progresses along the expansion chamber. The difference becomes less pronounced for the yellow and red transducers - figure 2.13- and, as the transducers get closer together, the differences obviously disappear.

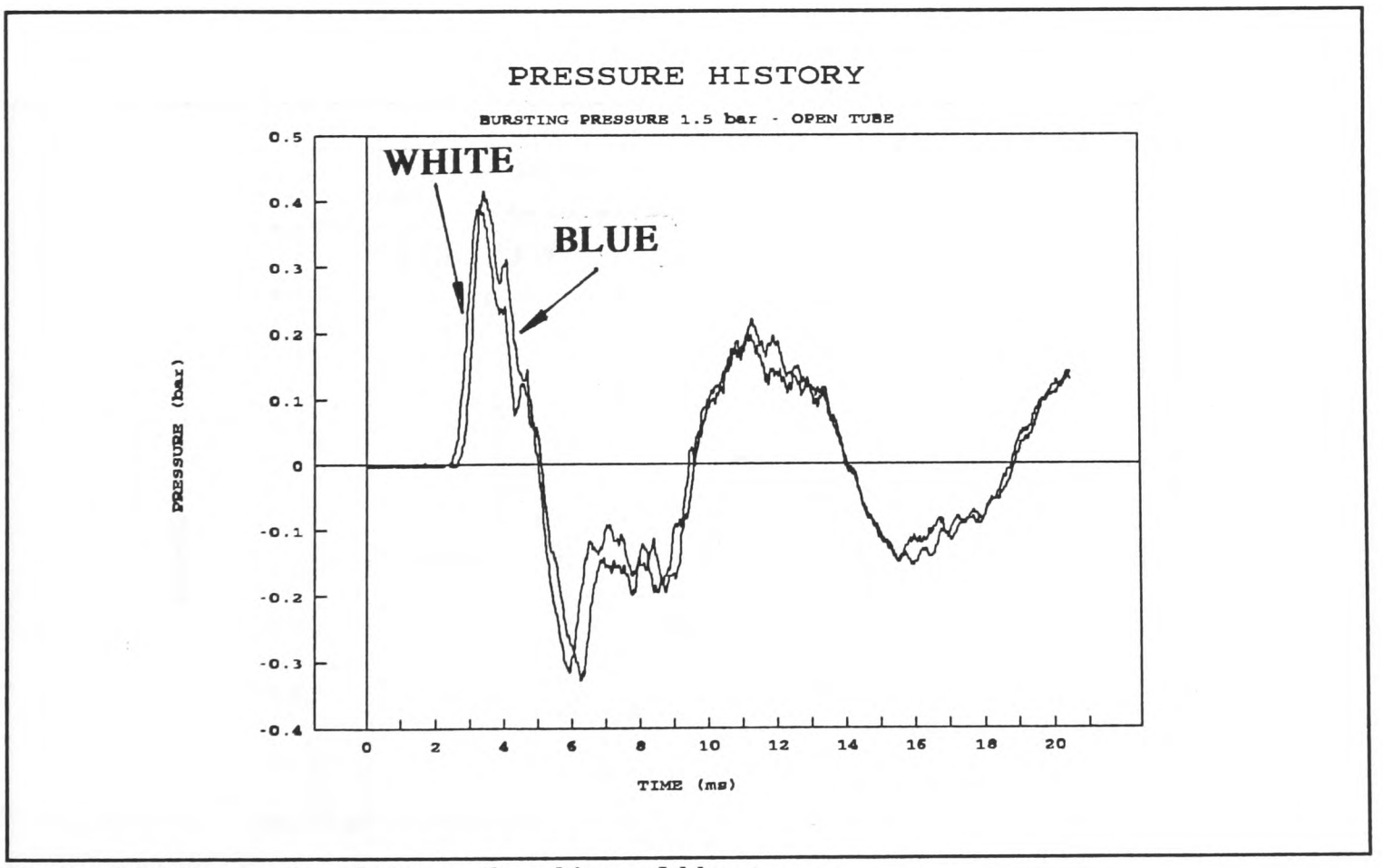


Figure 2.11 Comparison between the white and blue traces.

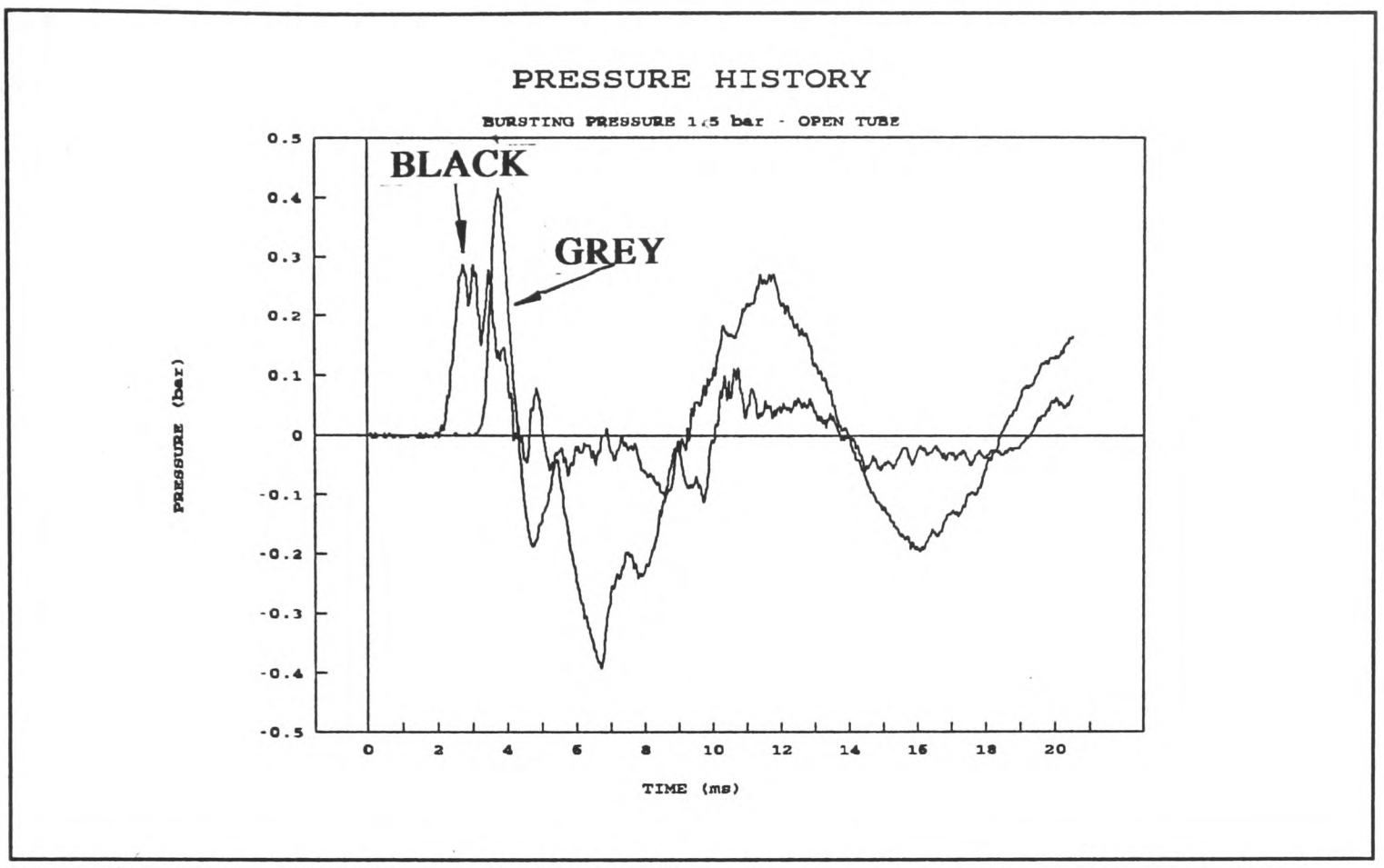


Figure 2.12 Comparison between the black and grey traces.

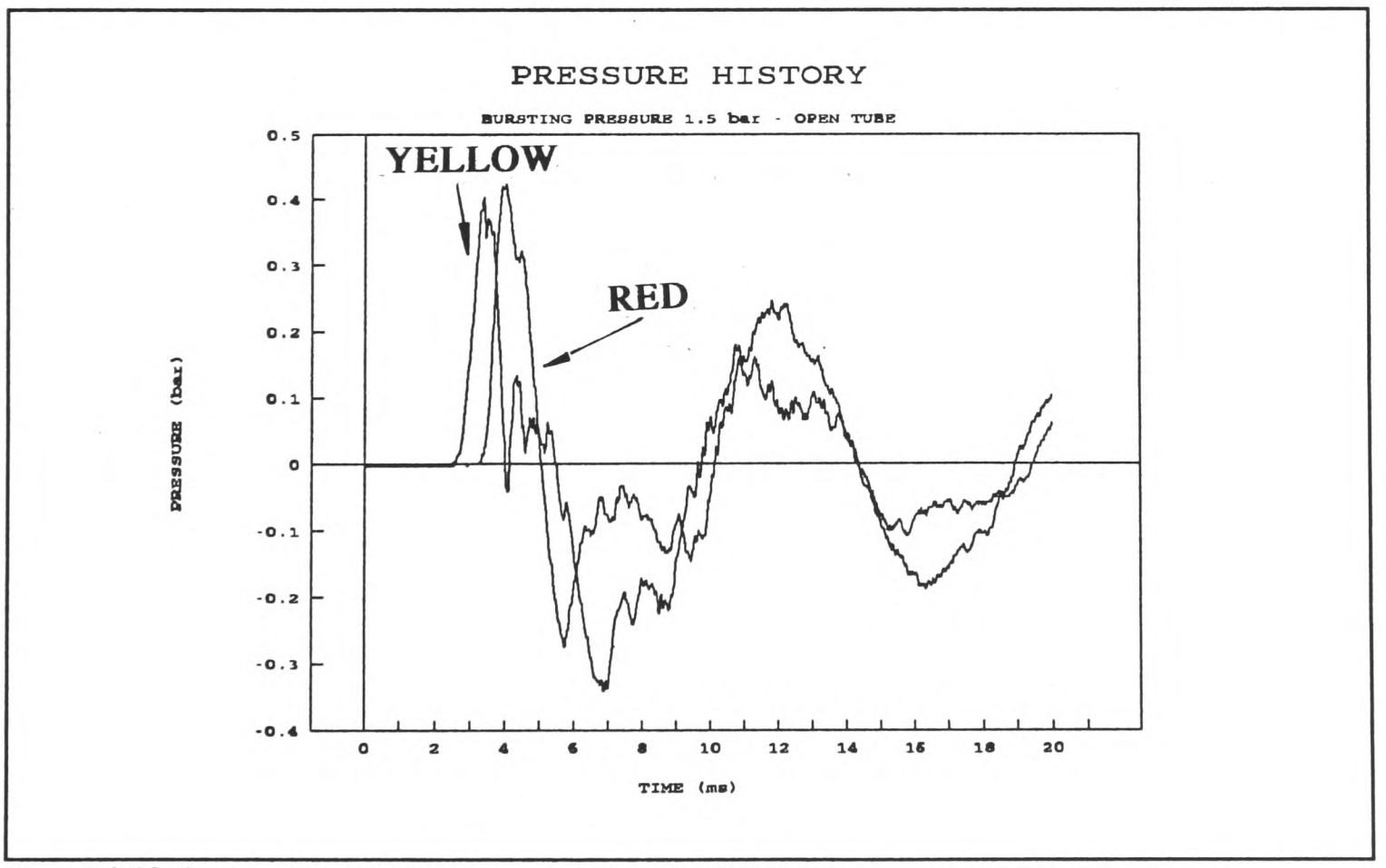


Figure 2.13 Comparison between the yellow and red traces.

In order to make an analysis of the development of the pressure wave along the expansion chamber, figure 2.14 shows the traces combined in a single graph of the black, white, blue and grey transducers, which are arranged from the left to the right respectively. It will be noted that, as the pressure wave front progresses, from the position of the black to the white, the magnitude of initial pressure pulse increases and becomes well defined. This difference can be explained by the fact that the wave is generated at a point and, during this initial stage, there are reflections with the internal wall of the expansion chamber, making the pressure pulse unstable. The pressure wave develops along this interval and its velocity is 285 m/s, as measured from the initiation points of each wave.

Theoretically, the velocity of a sound pressure wave in a gas is equal to the velocity of the sound in such gas [10]. Accordingly, the velocity of the pressure wave generated by the impact testing rig should be 342 m/s, which is the velocity of the sound in air at 20°c. This value is larger than the one measured in the interval of formation of the pressure wave. The difference is due to frictional effects, viscosity, reflections at the walls, variation of pressure including decompression, etc.

The comparison between the traces of the white and blue transducers shows that the magnitude of the pulse has an small increase and the shape of two waves are similar. Besides, the velocity measured along this interval is 313 m/s. Clearly, the wave is stabilizing and accelerating in the central part of the expansion chamber.

Finally, the trace of the grey transducer indicates that, in the top part of the expansion chamber, the initial ramp of the triangular pulse has stabilized and, virtually, it can be considered constant. However, the minimum of the depressurization ramp is reached quicker. This may be explained on the fact that, at this point, the expansion takes place in the atmosphere and there is no air mass ahead that has to be accelerated.

Another aspect that deserves attention is the development of the initial points of the pressure wave. As it can be observed, after the shape of the pressure wave is practically stabilized -signal of the white transducer- the transition between the state of equilibrium and the loading ramp is

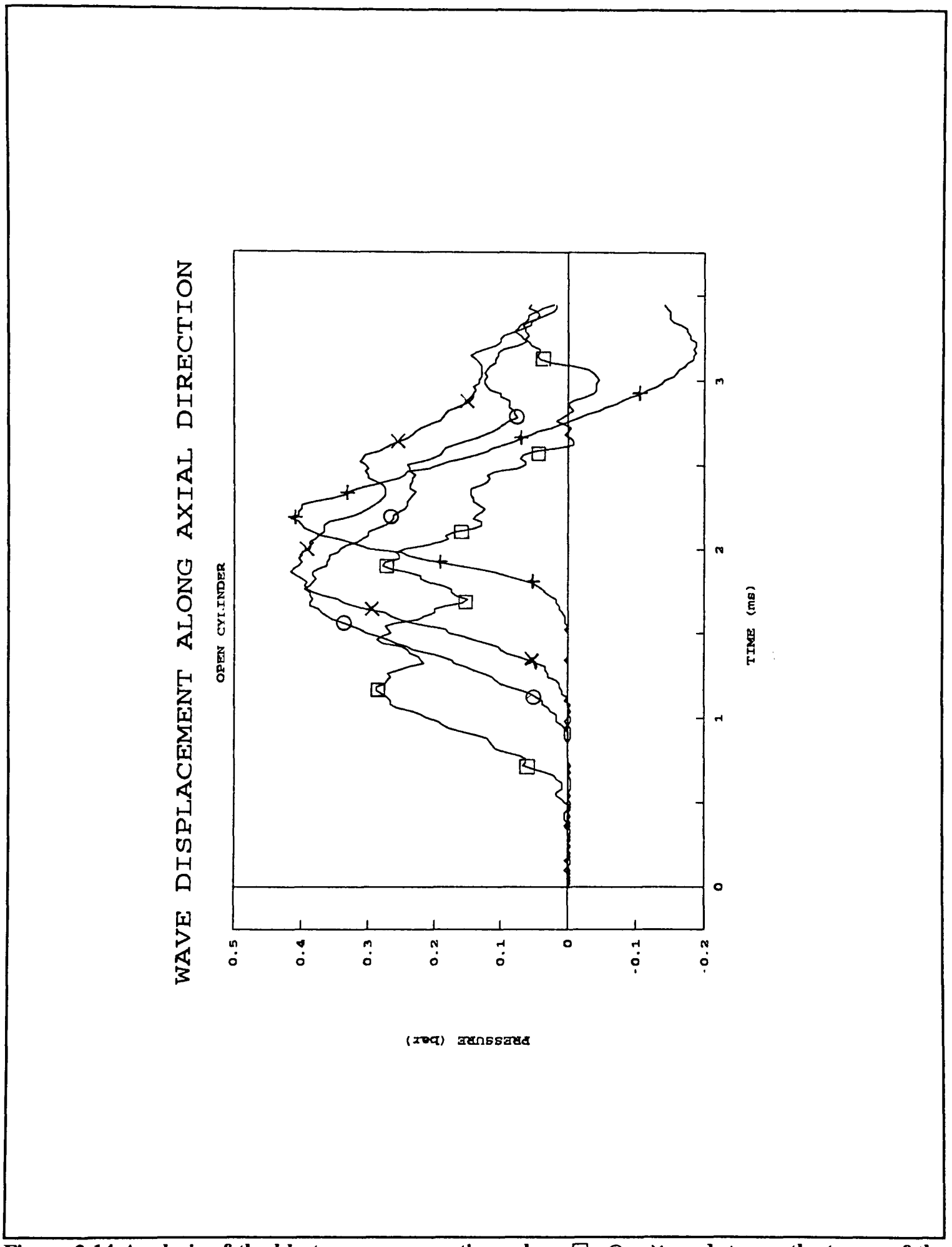


Figure 2.14 Analysis of the blast wave propagation, where □ , ○ , × and + are the traces of the black, white, blue and grey transducers respectively.

smoother for the wave registered at the end of the expansion chamber. This can be explained by the fact that, during the early stages of the expansion, the accelerated air mass is increasing. In consequence, the grey transducer is logging this early activity. Hence, the average speed was measured with the initial point of the trace of the blue transducer and the intersection of the average slope of the ramp of the grey transducer signal with the horizontal axis. The resulting wave speed is 352 m/s, which compares well with the velocity of the sound in air.

2.3.3 Pressure-Time analysis: Closed Tube.

In these series of tests, the expansion chamber was closed and all the transducers were in the position shown in figure 2.8. They were connected to three transient recorders which were triggered simultaneously. As before, the membrane was burst at pressures ranging between 0.25 and 2.0 bar. Only the case of 1.5 bar bursting pressure will be described.

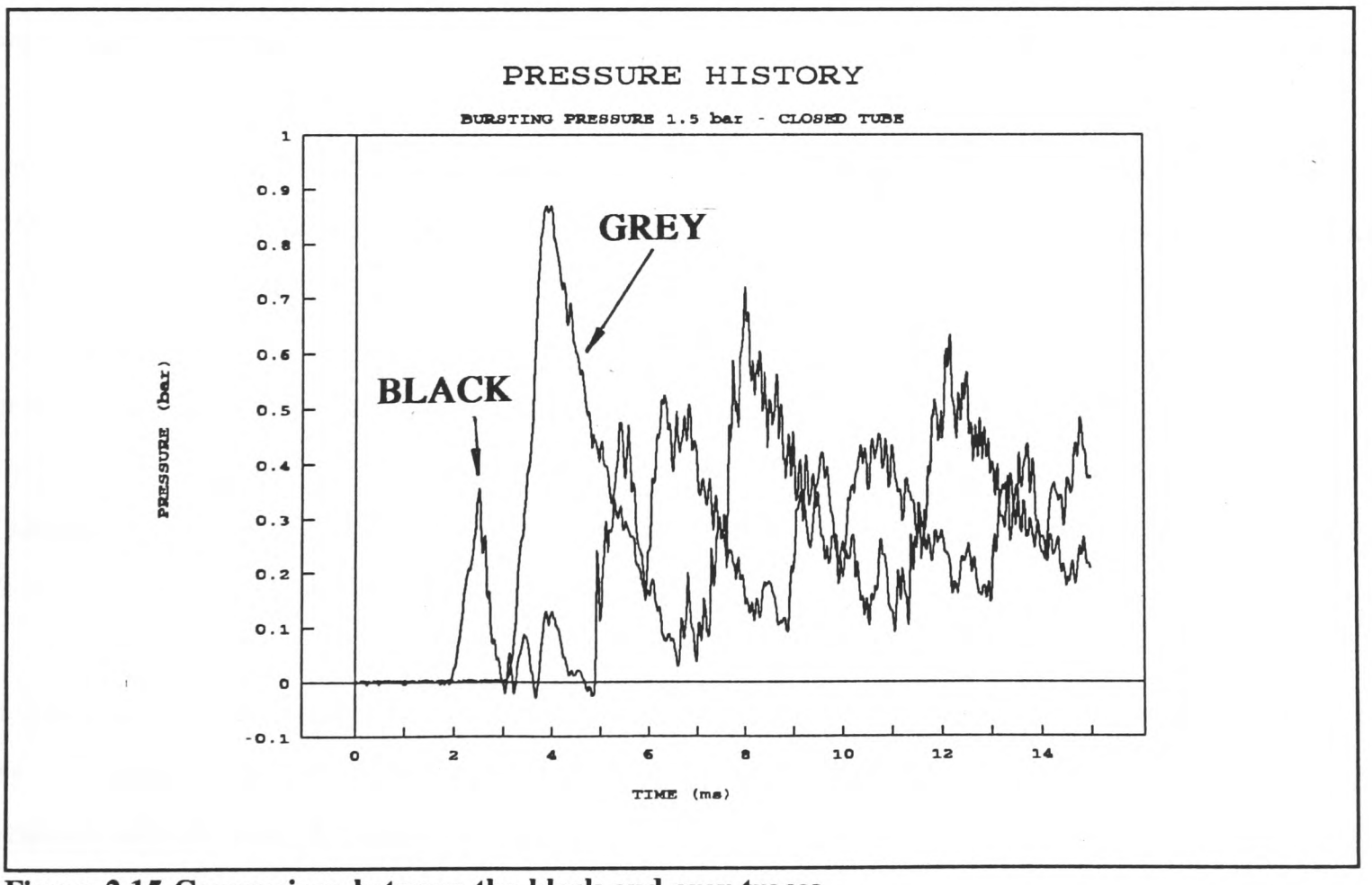


Figure 2.15 Comparison between the black and grey traces.

The pressure-history is similar to the case of an open tube. Nonetheless, it oscillates around the

resultant static pressure. In general terms, the pressure history can also be explained with the ideal model for blast waves proposed by Baker [9].

The comparison of the black and grey transducer traces in figure 2.15 reveals that the magnitude of the reflected peak pressure is more than double the peak registered close to the membrane. This pattern is unwanted, because the reflection on the end plate complicates the evaluation of the pressure wave.

2.3.4 Pressure-Time Analysis: Gap Between Tube and End Plate.

The conclusion from these experiments is that the specimen must be fixed in such way that the pressure wave is expanded in the atmosphere, because the shape of the pulse is stabilized quickly. This situation is achieved by leaving a gap between the top flange of the expansion chamber and the specimen bottom face, fixing both elements with washers in between. The thickness of each washer is 1.4 mm. Hence, the gaps obtained are 1.4 mm, 2.8 mm, 4.2 mm and 5.6 mm when one, two, three or four washers are used respectively with each bolt.

The next step consists in establishing the variation of the pressure that is applied to the specimen with time and with position. To find first the pressure history, a pressure transducer was fixed at the centre of a blank steel plate which was clamped to the top flange leaving a gap. Accordingly with the possible washers combinations, four series of tests were carried out. In each one, the pressure histories were generated with a burst pressure equal to 0.5 bar, 0.75 bar, 1.0 bar, 1.25 bar and 1.5 bar. For this purpose, the pressure transducer was connected to the first channel of a transient recorder, setting the vertical input to 1 V/div and each point was registered every 12.5×10^{-6} s, following the dynamic test procedure, explained in 2.2.1.

In the four series of tests, well defined traces were obtained when the membrane was burst at 1.0 bar, 1.25 bar and 1.5 bar. The traces of the blast waves generated with 0.5 bar and 0.75 bar burst pressure are not well defined and, in some cases, no data was registered. In all these cases, the pressure histories have similar characteristics to those observed when the blast wave expands in the atmosphere.

The qualitative analysis is summarized in table 2.2 and figures 2.16, 2.17, 2.18 and 2.19 illustrate typical results. They correspond to the pressure histories of the waves, which expand through a 4.2 mm gap and were generated with 0.75 bar, 1.0 bar, 1.25 bar and 1.5 bar respectively.

TABLE 2.2
TRACE QUALITY OF THE PRESSURE HISTORIES

GAP (mm)	BURST PRESSURE (bar)				
	0.50	**0.75**	**1.00**	**1.25**	**1.50**
1.4	P. D.	P. D.	W. D.	W. D.	W. D.
2.8	P. D.	P. D.	W. D.	W. D.	W. D.
4.2	N. D.	P. D.	W. D.	W. D.	W. D.
5.6	N. D.	P. D.	W. D.	W. D.	W. D.

N. D. not detectable
P. D. poorly defined
W. D. well defined

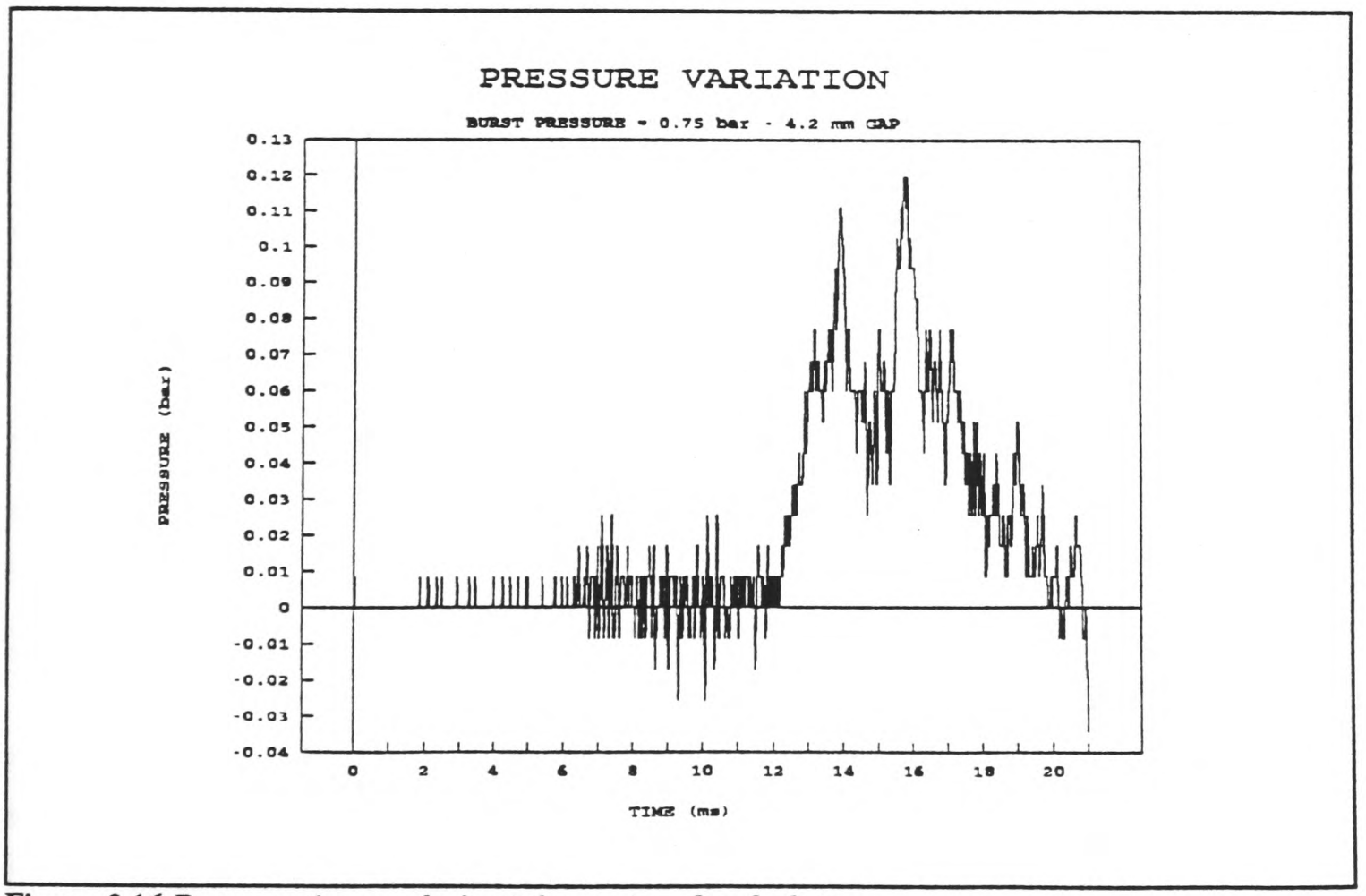


Figure 2.16 Pressure-time analysis at the centre of end plate.

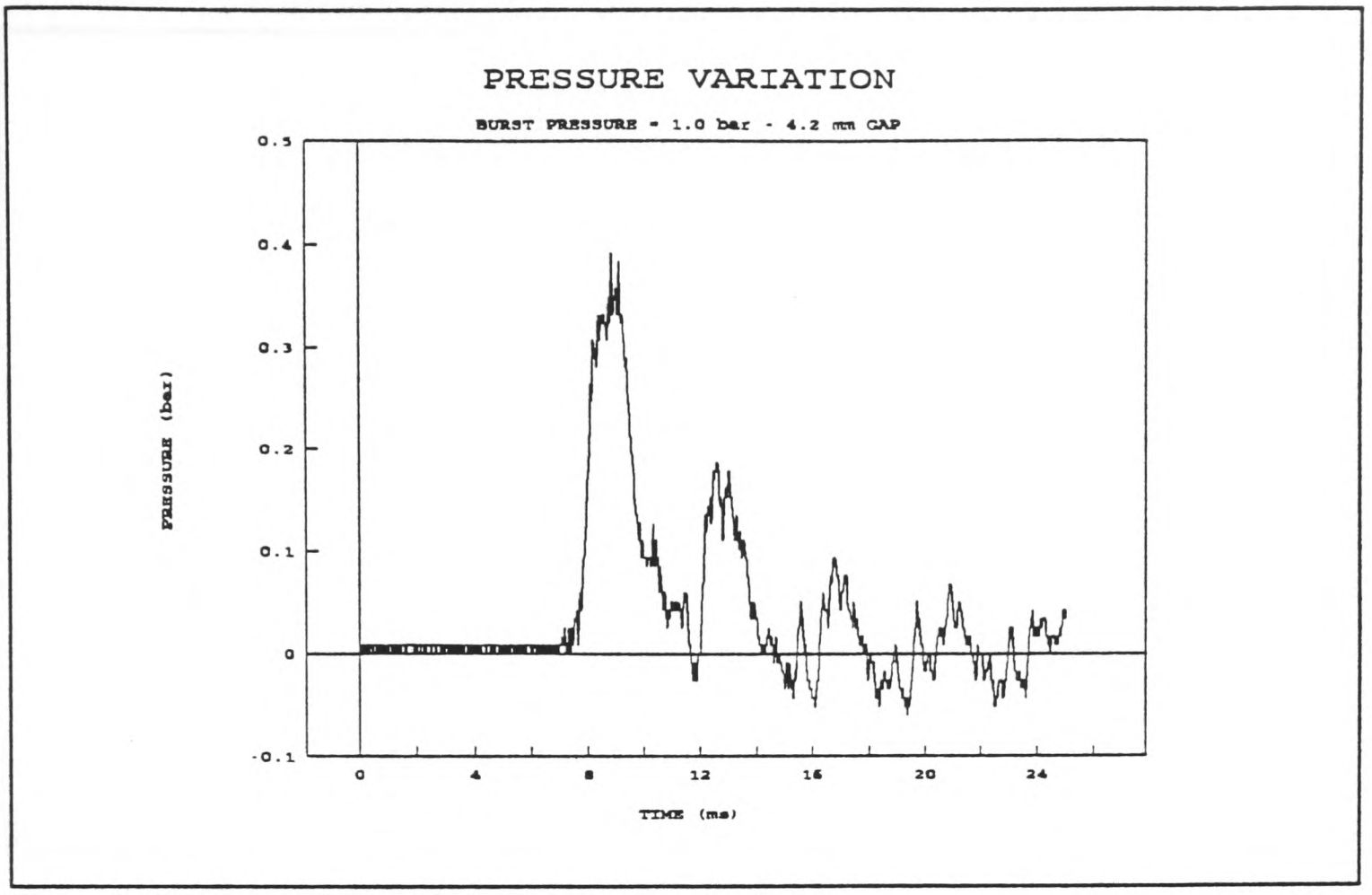


Figure 2.17 Pressure-time analysis at the centre of end plate.

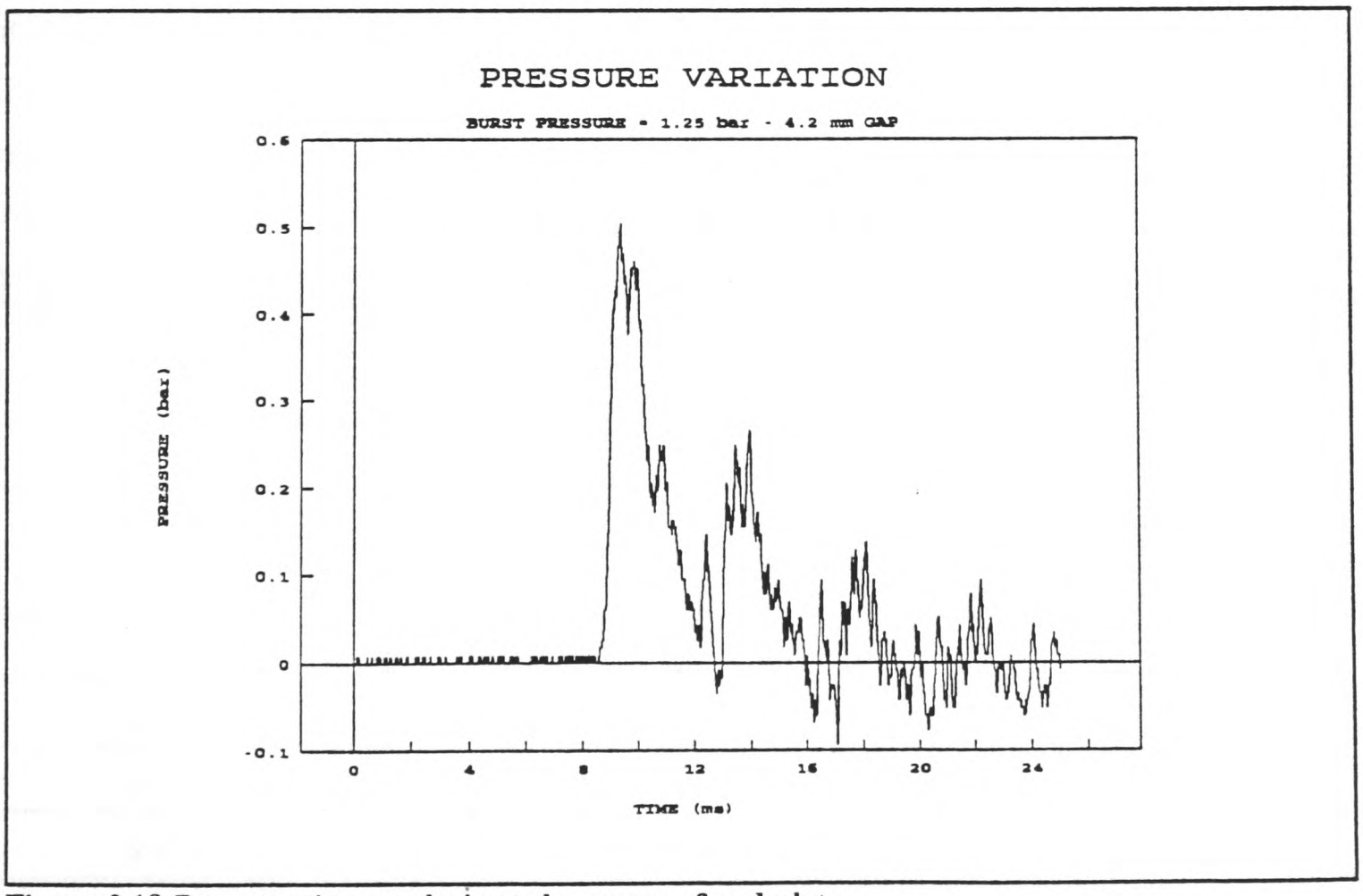


Figure 2.18 Pressure-time analysis at the centre of end plate.

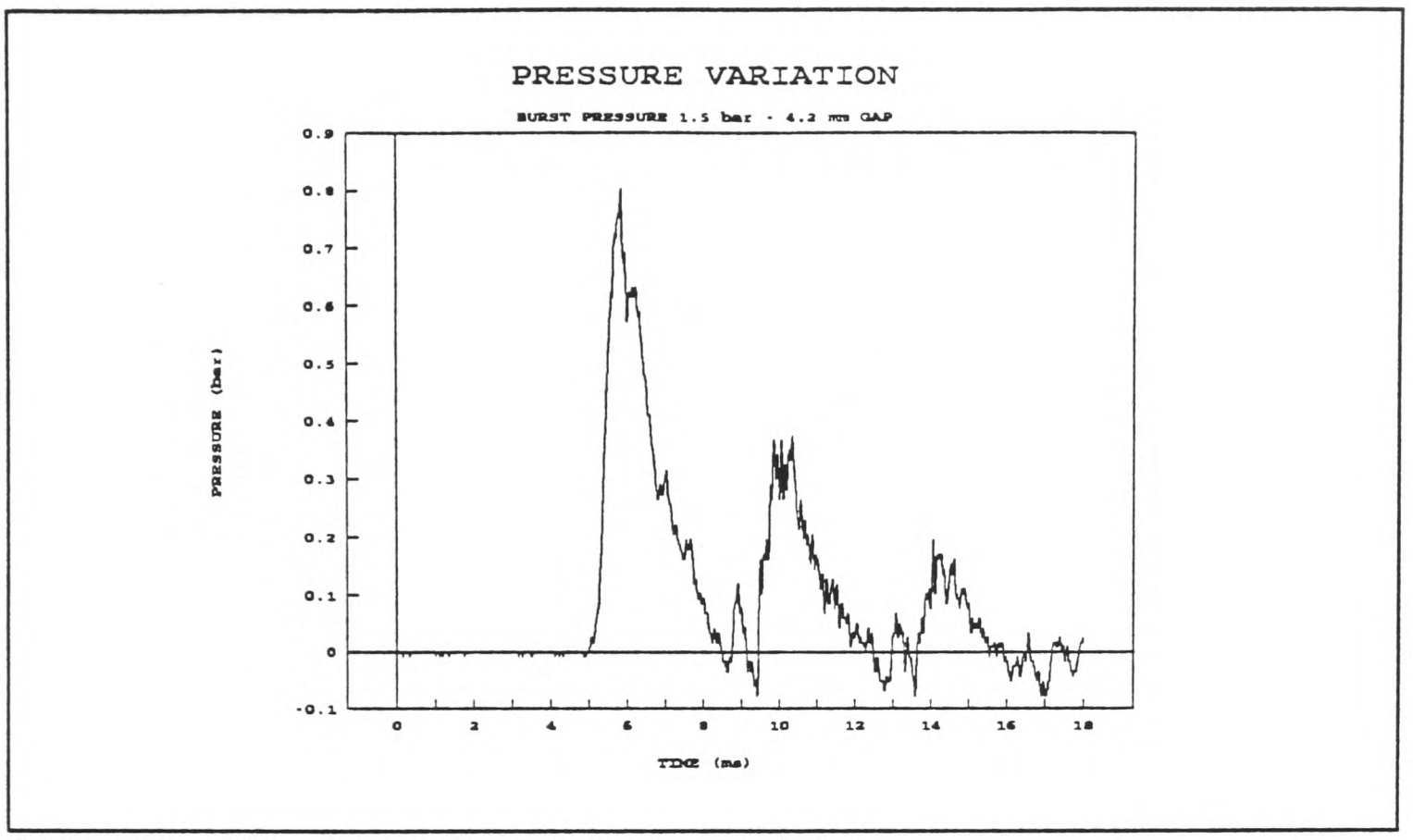


Figure 2.19 Pressure time analysis at the centre of end plate.

In a similar way, the initial points of each pressure history were analyzed and it was observed, that in some of them, there was a relative long transition period between the state of equilibrium and the loading process. Hence, it was not easy to say when the loading process began. They were considered as not well defined. On the other hand, there are traces in which the instant of load initiation can be established easily and they were considered as well defined. This analysis is summarized in table 2.3. and figures 2.17 and 2.19 illustrate typical results of each case.

TABLE 2.3
INITIAL POINT OF THE PRESSURE HISTORIES

GAP (mm)	PRESSURE (bar)		
	1.0	**1.25**	**1.5**
1.4	N. W.	N. W.	W. D.
2.8	N. W.	W. D.	W. D.
4.2	N. W.	W. D.	W. D.
5.6	N. W.	N. W.	W. D.

W. D. well defined
N. W. not well defined

2.3.5 Analysis of the Pressure Front.

Once the pressure variation with time has been established, it is necessary to find how the applied pressure varies over the specimen. It has already been shown that the transducers at the centre of the plate and on the wall of the expansion chamber adjacent to the top flange give the same signals. Thus, as a next step, it remains to prove that the pressure is uniformly distributed all over the specimen. This has been achieved by means of two series of tests. In each case, three pressure histories, which correspond to 1.0 bar, 1.25 bar and 1.5 bar burst pressure, were obtained with an expansion gap of 4.2 mm. The vertical input of the transient recorder was set to 1 V/div and each point was recorded every $5x10^{-6}$ s in all the tests.

In the first series of tests, two transducers were installed in a supporting plate, one of them on the centre, while the other was 45 mm away. They were back supported, connected to the recording system and triggered simultaneously. In the second series, the second transducer was put 65 mm from the plate centre, which is a position that is close to the internal surface of the expansion chamber. The rest of the testing conditions were unchanged.

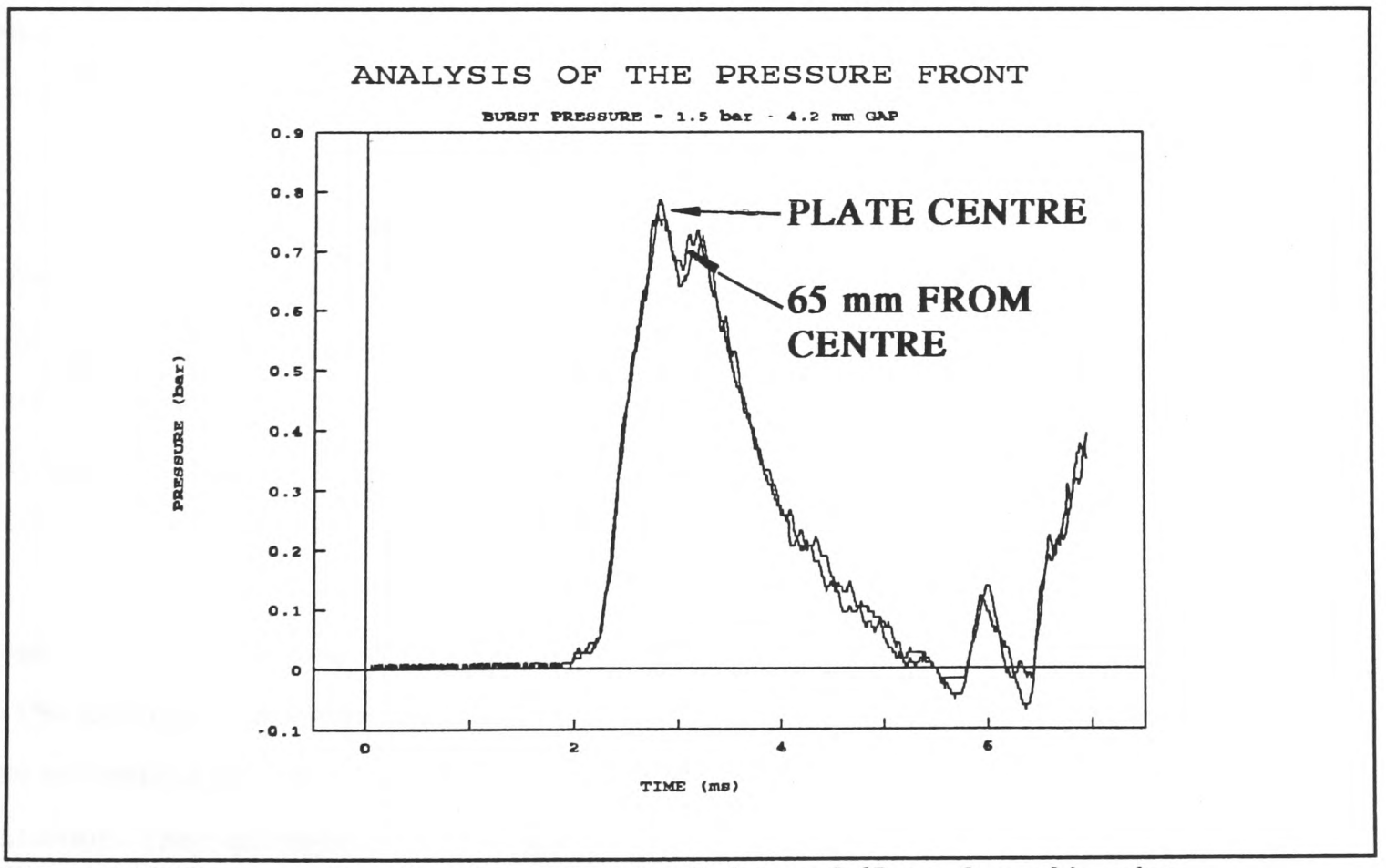


Figure 2.20 Traces registered at the centre of end plate and 65 mm from this point.

The three pairs of traces for each series of tests were almost identical. Additionally, the transducer, which was close to the internal surface of the expansion chamber, did not show any interference from the wall. Undoubtedly, the pressure front is plane. A typical result is shown in figure 2.20.

2.4 Strain Distribution in the Specimen.

2.4.1 Analysis of the Strain History.

In order to make a complete analysis of the loading characteristics of the impact testing apparatus, the assessment of the elastic response of the specimen is required. For this reason, the strain (membrane+bending) history has been obtained for the clamping and loading conditions proposed in section 2.3.4. Accordingly, four series of tests were performed.

A 1 mm strain gauge was bonded to the centre of the specimen and another similar gauge was fixed to a rectangular PMMA plate, which was unstressed. The type FLE-I-23 of Tokyo Sokki Kenkyujo was selected. They were connected to a temperature compensated bridge circuit, in which an active and a live dummy gauges are connected to adjacent arms. The vertical input of the oscilloscope was set at 2 V/div and each point was registered every $5x10^{-6}$ s.

The strain histories registered in the four series of tests have similar characteristics. In particular, when the burst pressure is 0.5 bar no strain was detected. In the case of tests conducted with a 0.75 bar burst pressure, small strains were registered. The traces of those tests produced with a burst pressure equal to 1.0 bar, 1.25 bar and 1.5 bar are well defined. Their initial peak is triangular and increases steadily and their range is between 0.0018 and 0.0045. Table 2.4 summarizes the results and typical strain-histories are illustrated in figures 2.21, 2.22 and 2.23.

Regarding the initial points in the strain histories, the transition period from the equilibrium state to the loading ramp is small in the tests conducted with 1.0 bar and 1.25 bar burst pressure with two exceptions, in which this event is longer and it is not easy to establish the instant of load initiation. They correspond to the expansion of the pressure wave generated with 1.0 bar burst

pressure through 1.4 mm and 2.8 mm gap. Furthermore, negative strains are observed at the beginning of the traces generated with a 1.5 bar burst pressure. This analysis is summarized in table 2.5.

TABLE 2.4
TRACE QUALITY OF THE STRAIN HISTORIES

GAP (mm)	BURST PRESSURE (bar)				
	0.50	**0.75**	**1.00**	**1.25**	**1.50**
1.4	N. D.	P. D.	W. D.	W. D.	W. D.
2.8	N. D.	P. D.	W. D.	W. D.	W. D.
4.2	N. D.	P. D.	W. D.	W. D.	W. D.
5.6	N. D.	P. D.	W. D.	W. D.	W. D.

N. D. not detectable
P. D. poorly defined
W. D. well defined

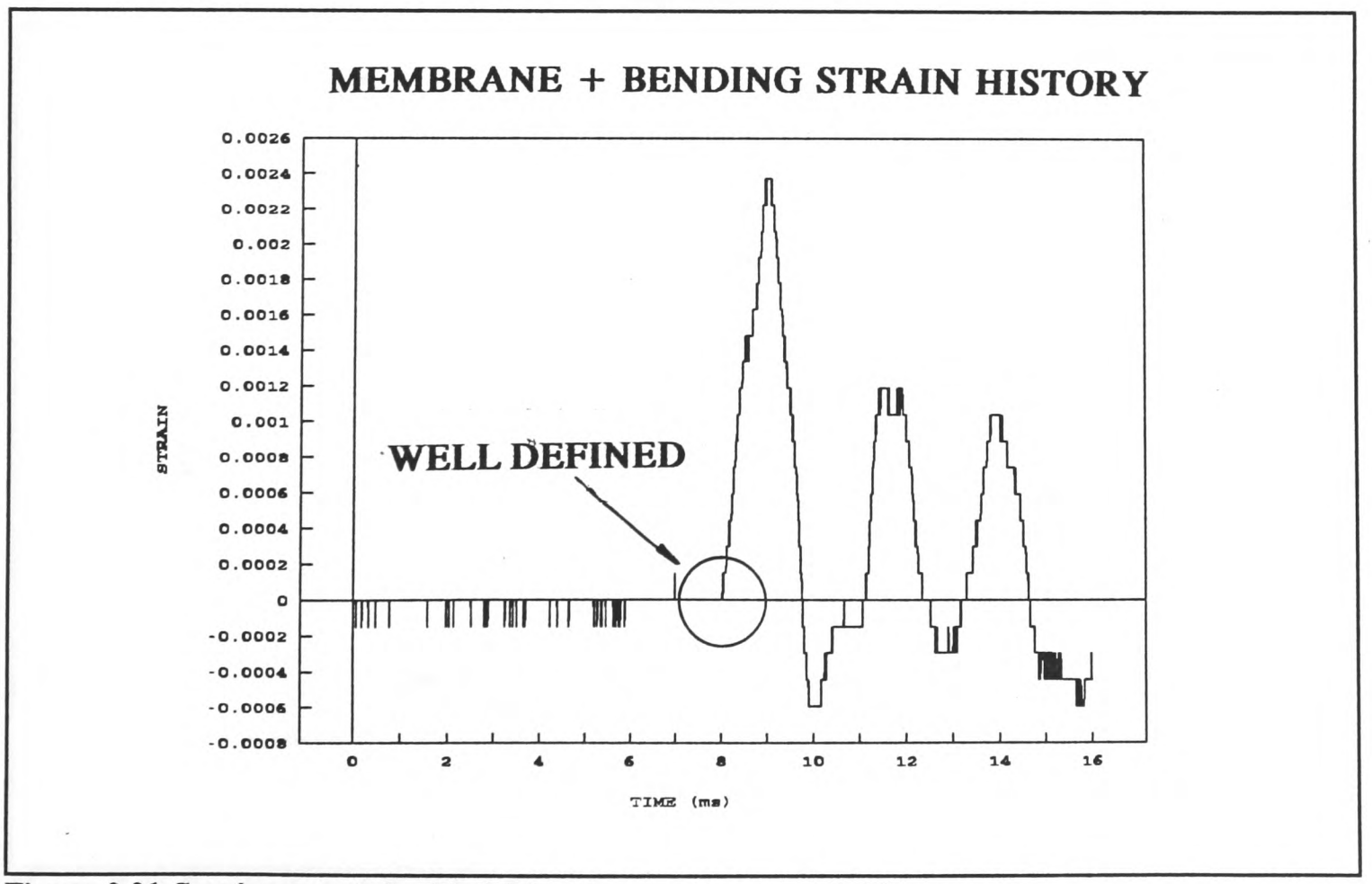


Figure 2.21 Specimen tested with 1.0 bar burst pressure and 4.2 mm gap.

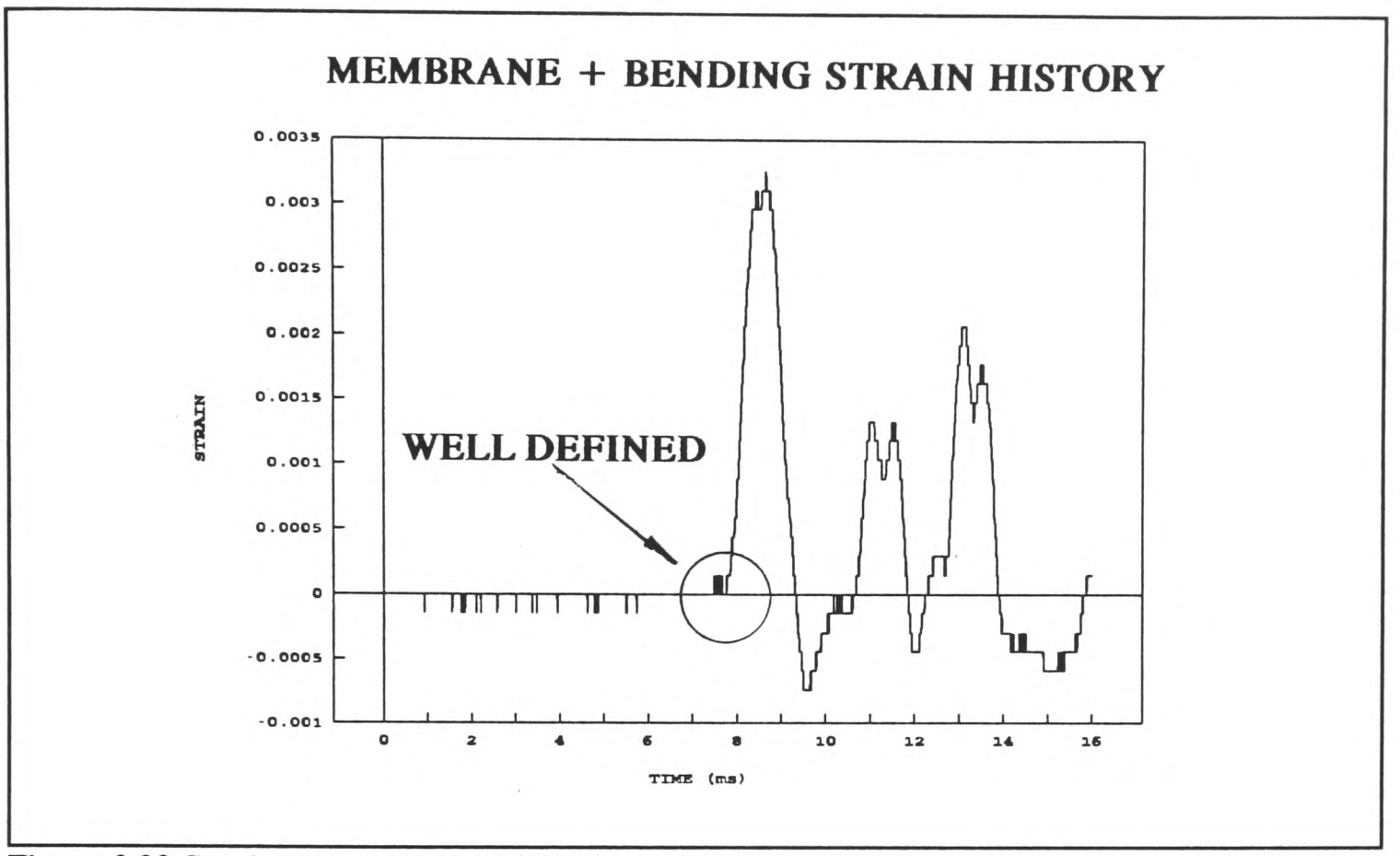


Figure 2.22 Specimen tested with 1.25 bar burst pressure and 4.2 mm gap.

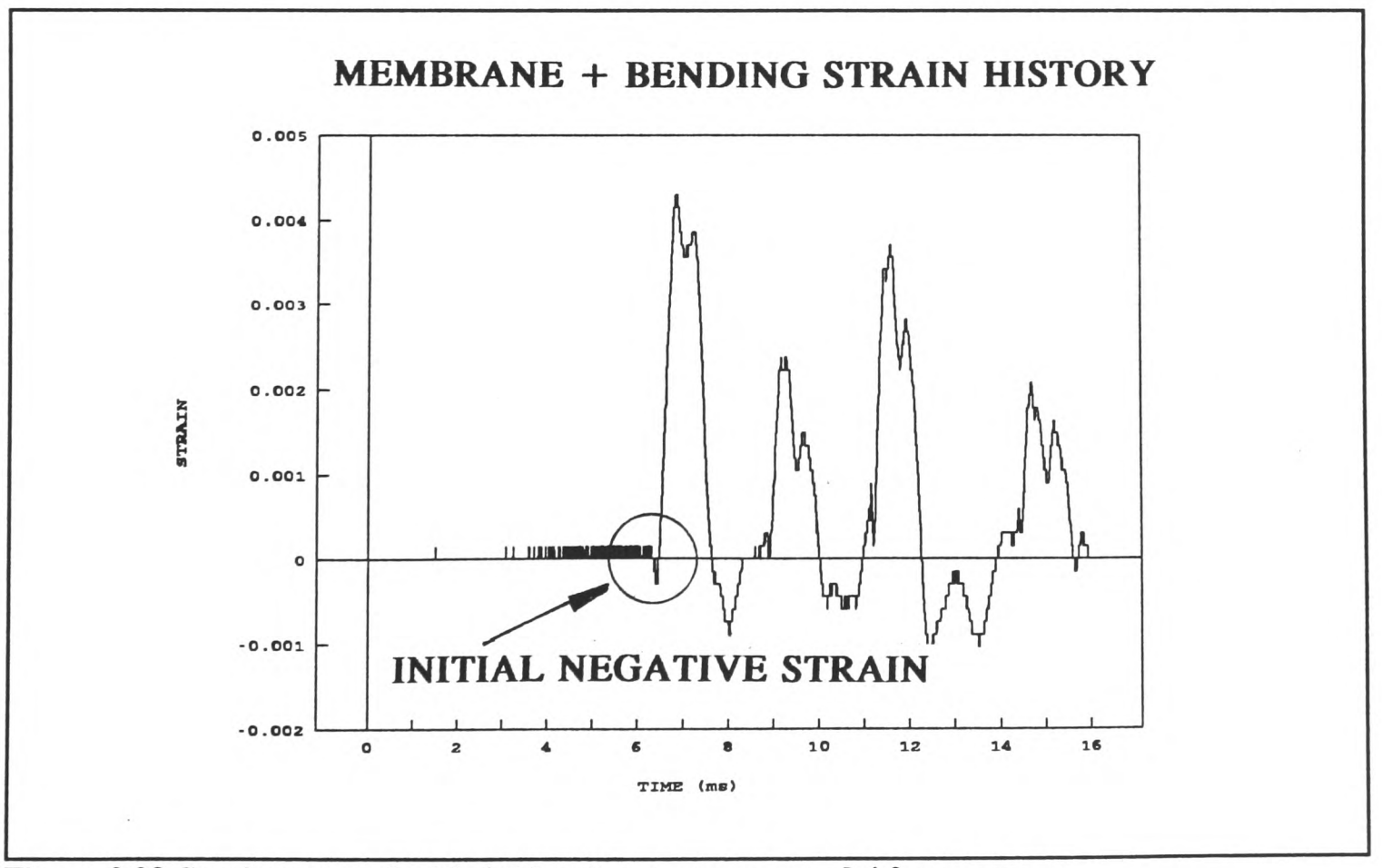


Figure 2.23 Specimen tested with 1.5 bar burst pressure and 4.2 mm gap.

TABLE 2.5
INITIAL POINT OF THE STRAIN HISTORIES

GAP (mm)	BURST PRESSURE (bar)		
	1.00	**1.25**	**1.50**
1.4	P. D.	W. D.	N. S.
2.8	P. D.	W. D.	N. S.
4.2	W. D.	W. D.	N. S.
5.6	W. D.	W. D.	N. S.

P. D. poorly defined
W. D. well defined
N. S. initial negative strain

2.4.2 Analysis of the Bending Strain History.

The aim of these tests is the evaluation of the magnitude of the bending strains. Thus, the same types of specimens, used in the strain analysis, were tested with the loading and clamping conditions proposed in section 2.3.4. For this purpose, two strain gauges of 1 mm length were bonded at the centre of the plate. One of them was at the top surface, while the other was at the bottom. They were connected to the same bridge circuit and the settings of the recording system, which were used in the strain analysis tests, were employed in these tests too.

The findings show that in all cases bending strains were registered. Particularly, the traces corresponding to 1.0 bar, 1.25 bar and 1.5 bar are well defined. In addition, the comparison of the bending and resultant (membrane+bending) strain histories, show that the former are smaller. The peak values of the bending strains, generated with 1.0 bar, 1.25 bar and 1.50 bar burst pressure, are in the range between 0.0015 and 0.003, which, in average, are 20% smaller than the total strain. Typical bending strain-histories are shown in figures 2.24, 2.25 and 2.26 and the results are summarized in table 2.6.

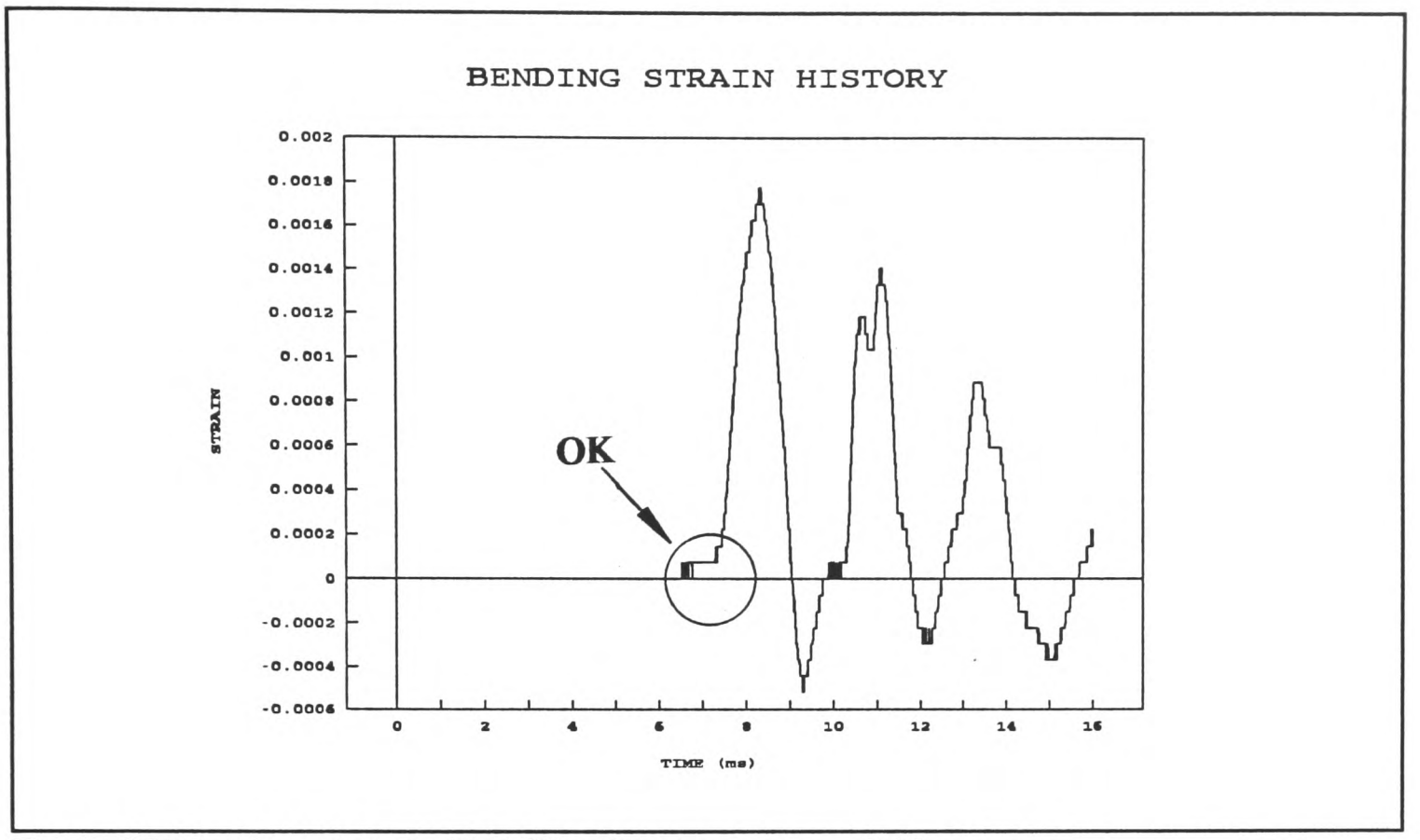


Figure 2.24 Specimen tested with 1.0 bar burst pressure and 4.2 mm gap.

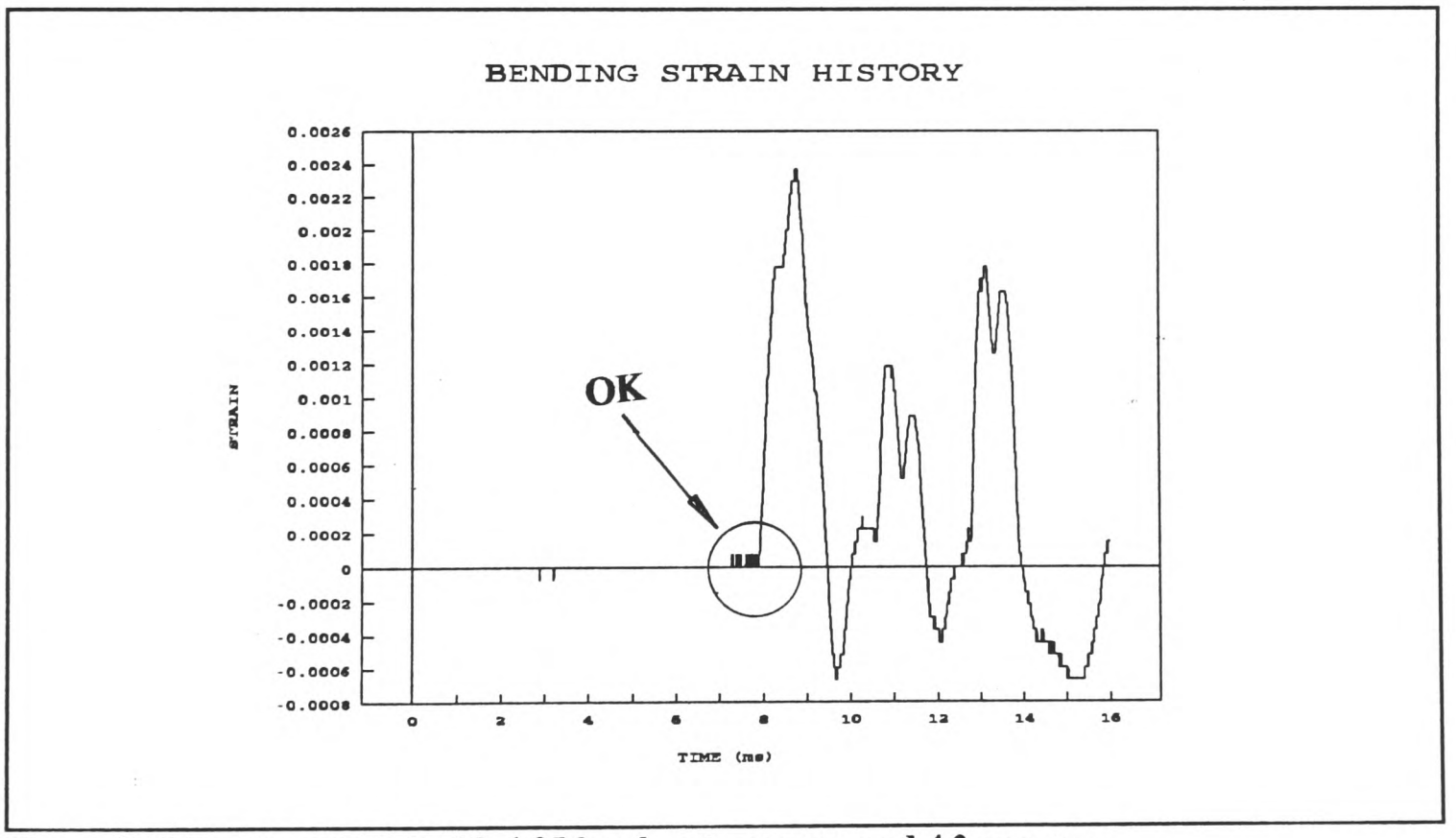


Figure 2.25 Specimen tested with 1.25 bar burst pressure and 4.2 mm gap.

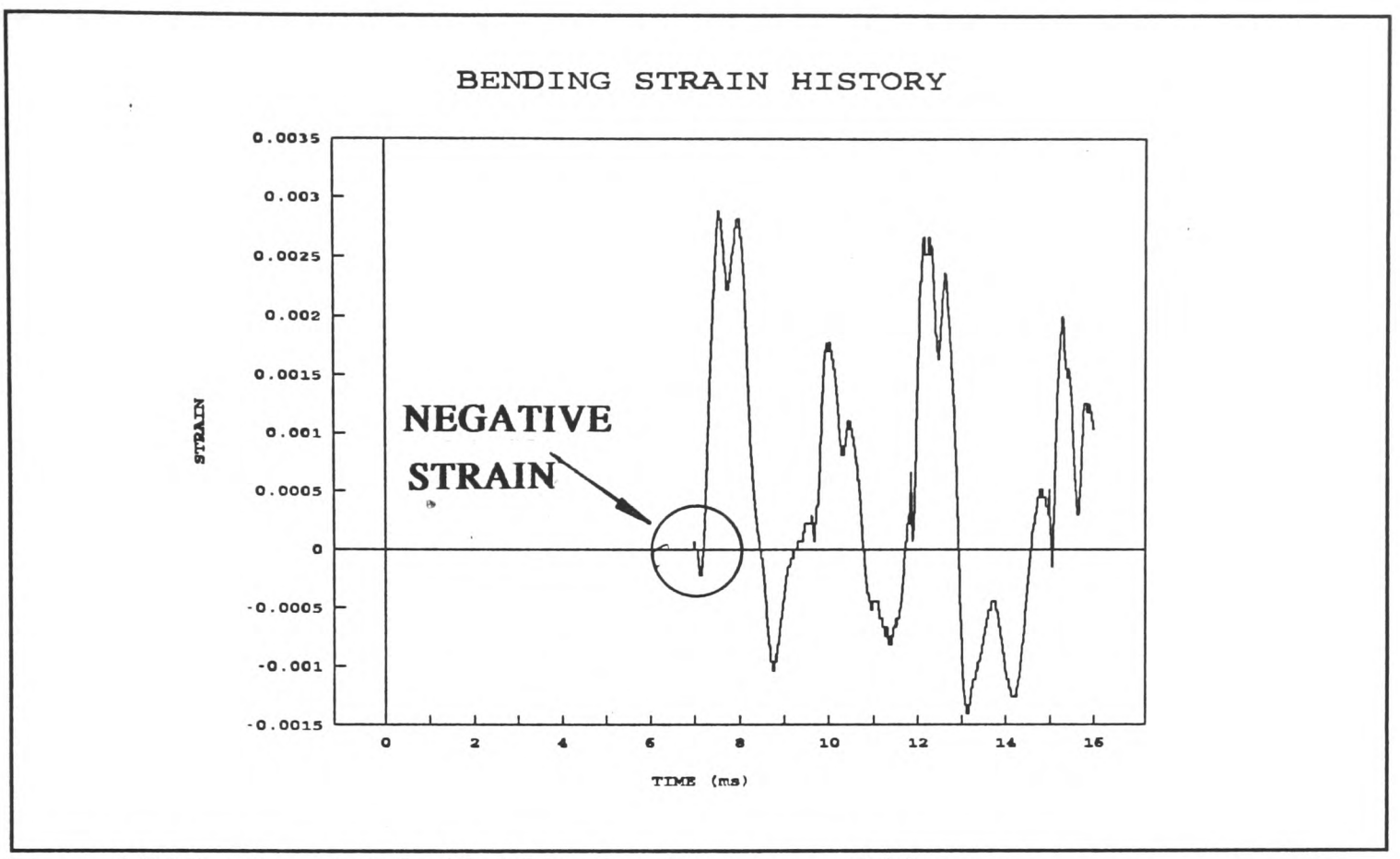


Figure 2.26 Specimen tested with 1.5 bar burst pressure and 4.2 mm gap.

TABLE 2.6
TRACE QUALITY OF THE BENDING STRAINS

GAP (mm)	PRESSURE (bar)				
	0.50	**0.75**	**1.00**	**1.25**	**1.50**
1.4	P. D.	W. D.	W. D.	W. D.	W. D.
2.8	P. D.	P. D.	W. D.	W. D.	W. D.
4.2	P. D.	P. D.	W. D.	W. D.	W. D.
5.6	P. D.	P. D.	W. D.	W. D.	W. D.

P. D. poorly defined
W. D. well defined

Similarly, the analysis of the definition of the initial point of the bending strain history is presented in table 2.7 for those cases in which good traces have been obtained. The series of tests which shows the best definition of the initial point correspond to the expansion through a 4.2 mm gap.

TABLE 2.7
INITIAL POINT OF THE BENDING STRAIN HISTORIES

GAP (mm)	PRESSURE (bar)		
	1.0	**1.25**	**1.5**
1.4	P. D.	N. S.	N. S.
2.8	P. D.	W. D.	N. S.
4.2	W. D.	W. D.	N. S.
5.6	W. D.	N. S.	N. S.

P. D. poorly defined
W. D. well defined
N. S. initial negative strain

Finally, the selection of the loading cases involves the analysis of the findings in all the tests. In this instance, table 2.2 shows that the pressure histories obtained with burst pressures equal to 1.0 bar, 1.25 bar and 1.50 bar in the four series of tests have traces well defined. In consequence, this evaluation is going to be focused on these cases. With regard to the quality of the initial points of these pressure histories, table 2.3 indicates that the best results are obtained when the blast wave expands through a gap between 2.8 mm and 4.2 mm.

Similarly, the quality of the membrane+bending strain traces (table 2.4) is analogous with that of the pressure histories. Nevertheless, the definition of the initial points (table 2.5) of the 4.2 and 5.6 gap cases are good. Moreover, the bending strain history (table 2.6) is well defined for the same cases discussed above and the initial points of the 4.2 mm and 5.6 mm cases are the best (table 2.7). In brief, the expansion of the pressure wave through a 4.2 mm gap has shown a good consistency through all the tests. In consequence, this is selected as the standard configuration for the crack analysis tests.

2.4.3 Analysis of the Elastic Response of the Specimens with the Loading Cases Selected.

In the final part of the development of the impact testing procedure, the elastic response of the specimens, under the dynamic pressure loading pattern selected in the last section, was analyzed. For this purpose a series of tests was designed, in which the resultant strain and the pressure load were measured simultaneously.

A PMMA plate, 3 mm thick, was instrumented with a 1 mm strain gauge bonded at its centre and was connected to temperature compensate circuit. The plate was mounted onto the impact testing rig, leaving a 4.2 mm gap. Additionally, a pressure transducer was mounted as close as possible to the plate centre by means of a steel strip 20 mm x 280 mm and 1 mm thick. This set up was fixed between the expansion chamber flange and the specimen, in front of the bottom plate centre, as shown in figure 2.27. Therefore, the distance between the bottom surface of the specimen and the sensor element of the pressure transducer is around 8 mm. Considering the wave velocity (section 2.3.2), the lag time between both signals is 22×10^{-6}s. Thus, the measurement of both parameters is virtually at the same point and time. Care was taken to avoid the vibration of the pressure transducer and its contact with the bottom face of the specimen.

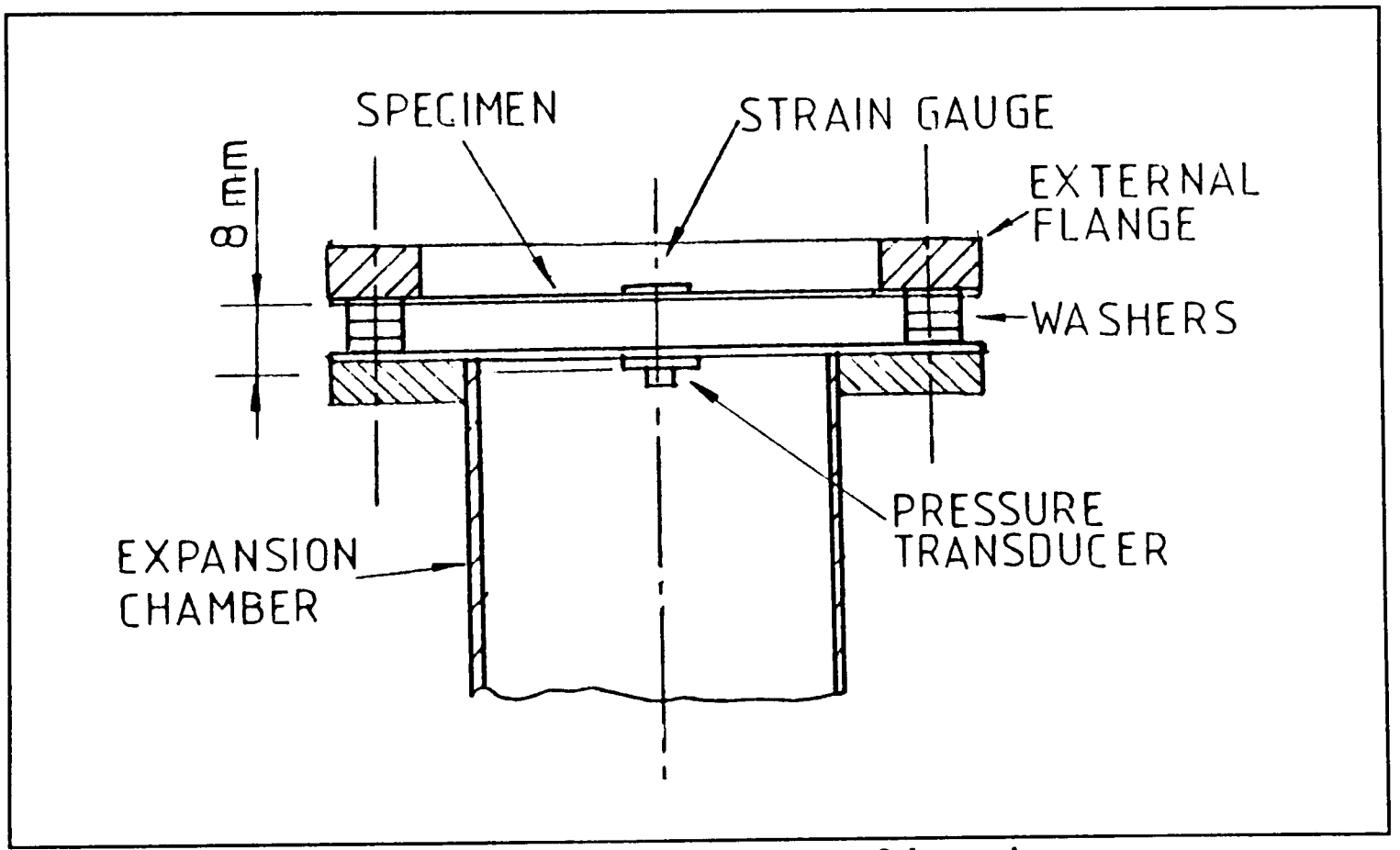


Figure 2.27 Set-up for the analysis of the dynamic response of the specimen.

Both transducers were triggered simultaneously and the data was registered with the recording system described in section 2.2. Tests were done with bursting pressure equal to 1.0 bar, 1.25 bar and 1.50 bar. The results are presented in figures 2.28, 2.29 and 2.30. It is important to observe that the pressure and strain traces are compared in terms of Volts, which is the common parameter registered by both transducers. The pattern in all the graphs is consistent and shows that the elastic response occurs after the pressure load has been applied. In general terms, the elastic response occurs 0.6 ms later than the pressure history, when a burst pressure of 1.0 bar and 1.25 bar is applied. This gap is reduced to 0.5 ms for the case of 1.5 bar.

With regard to the occurrence of the maximum values of the pressure and strain histories, the results show that the peak value of the strain history occurs later than the peak of the pressure history, when the pressure is generated with a burst pressure equal to 1.0 bar. On the contrary, both peak values occur around the same instant on the other two cases. Likewise, a negative phase is observed before the principal ramp in the strain history of the cases of 1.25 bar and 1.5 bar.

It is clear from these results that the inertia forces are important because they cause the out-of phase between the pressure and strain. In consequence, the evaluation of the crack initiation load has to take into consideration the observed time lag between the pressure and strain histories.

2.5 Summary.

The experimental findings show that the impact test apparatus is adequate for the study of crack initiation under dynamic pressure loading, because the elastic response of the specimen and the dynamic loading have a similar rate of change. Consequently, the crack tip is loaded with a regular stress pattern.

The magnitude of the blast wave produced is controlled by varying the bursting pressure. In particular, the blast waves, which are generated with 1.0 bar, 1.25 bar and 1.5 bar bursting pressure, have been selected as loading cases. The range of the peak pressure is between 0.30 bar and 0.8 bar and the load has an initial ramp, which last less than 1 ms. The loading conditions and the strain field have to be evaluated separately and the results obtained must be synchronized

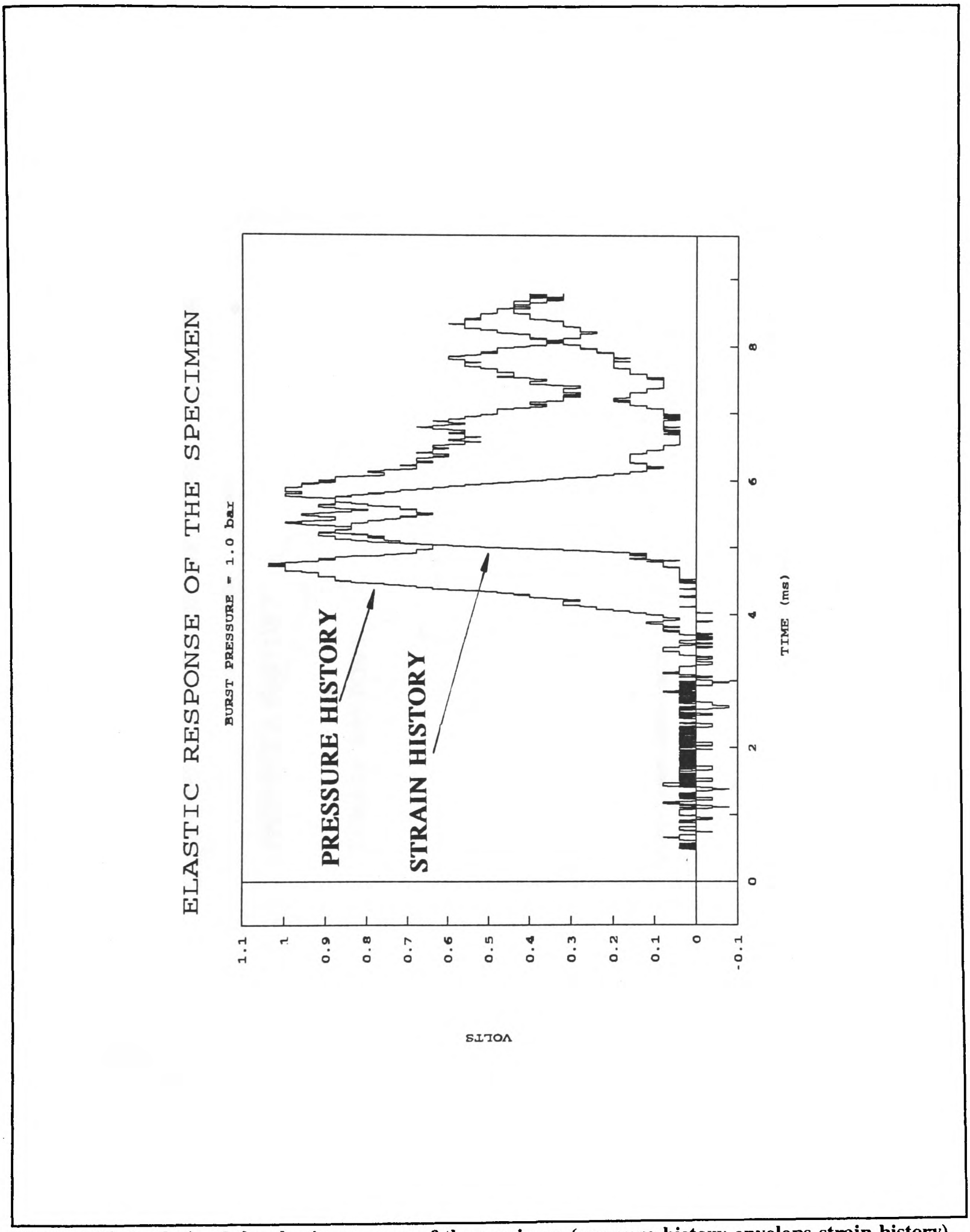


Figure 2.28 Analysis of the elastic response of the specimen (pressure history envelops strain history).

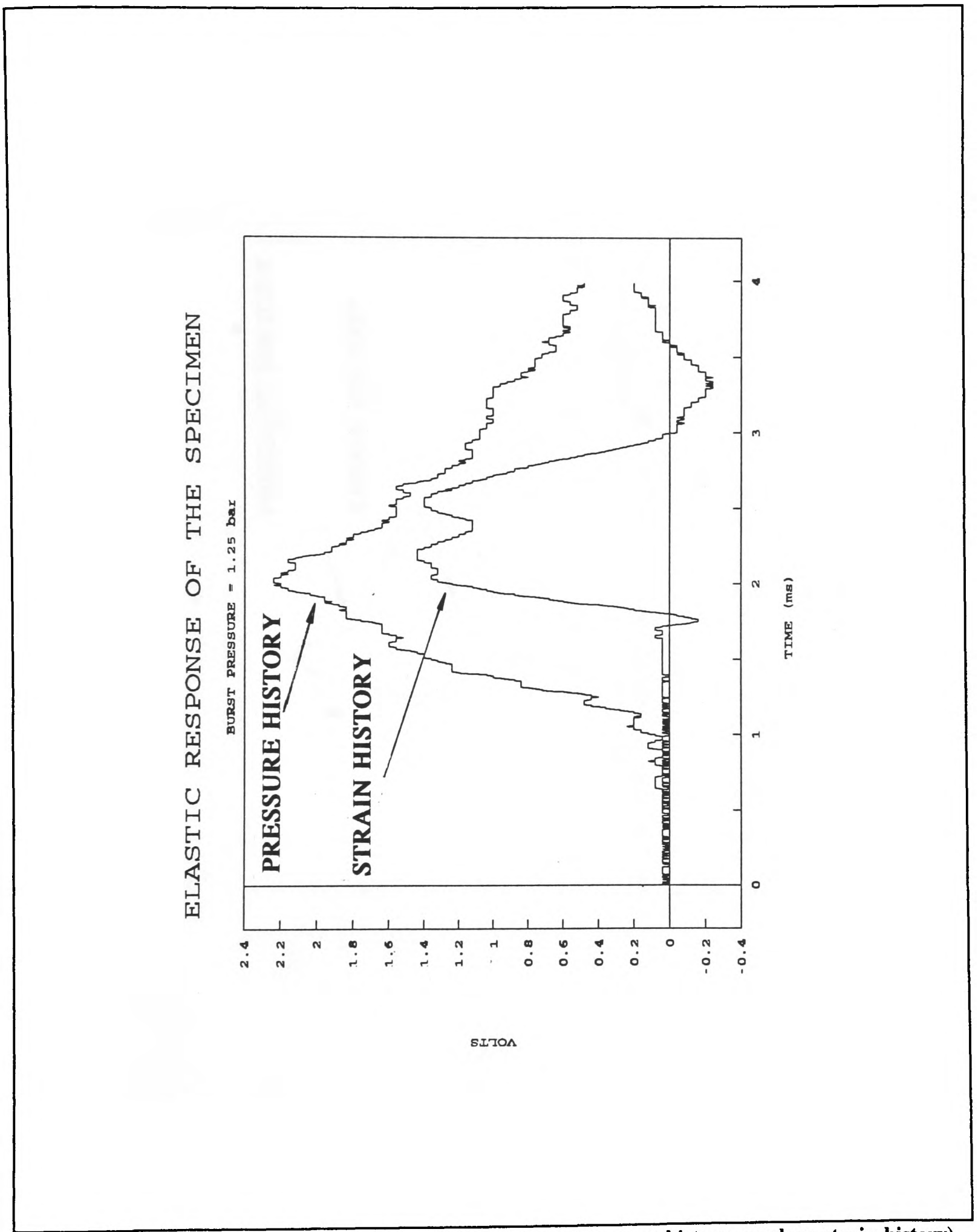


Figure 2.29 Analysis of the elastic response of the specimen (pressure history envelops strain history).

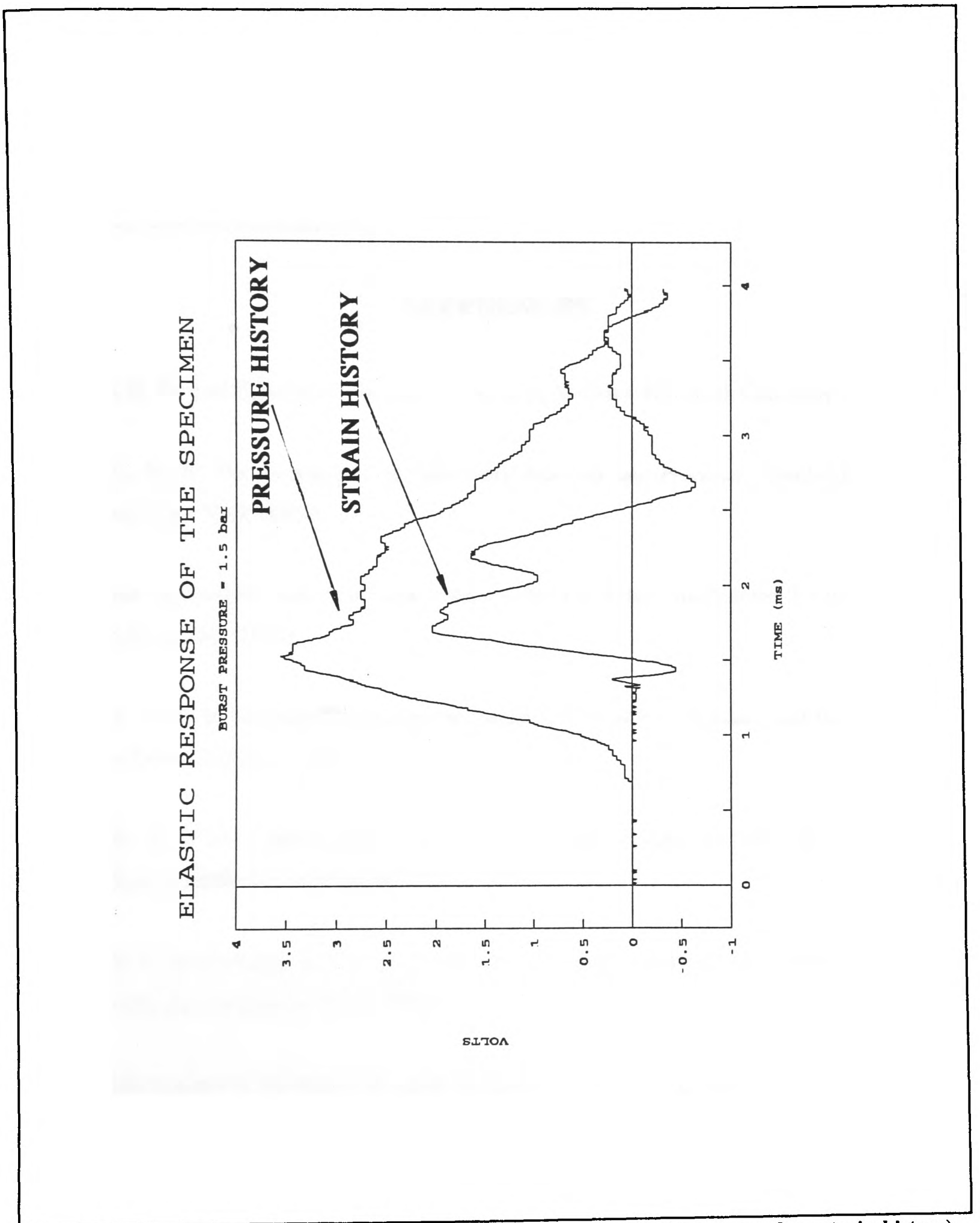


Figure 2.30 Analysis of the elastic response of the specimen (pressure history envelops strain history).

later, with a dynamic calibration, in which the delay time observed between the pressure and strain histories is considered.

All these conclusions suggest that the problem of crack initiation may be studied with a experimental-numerical approach based on a fracture mechanics approach, in which the loading conditions at crack initiation are evaluated experimentally and the fracture toughness is calculated numerically from the dynamic SIF.

REFERENCES

1. Clough, R. W. and Penzien, J. *Dynamic of Structures*, McGraw-Hill Book Company (1975).

2. Clauser, H. R. *The Encyclopedia of Engineering Materials and Processes*, Reinhold Publishing Corporation, New York (1963).

3. Billmeyer Jr., Fred W. *Textbook of Polymer Science*, 2nd Ed. Wiley Interscience, A Division of John Wiley and Sons, Inc. (1971).

4. Neubert, H. K. P. *Instrument Transducers-An Introduction to their Performance and Design.* 2nd Ed. Clarendon Press. Oxford (1975).

5. Doebelin, E. O. *Measurement Systems-Application and Design*, 3rd ed. McGraw-Hill International Book Company, International Student Edition (1983).

6. Dove, R. C. and Adams, P. H., *Experimental Stress Analysis and Motion Measurement*, Charles E. Merrill Books, Inc. Columbus, Ohio, (1964).

7. Tektronix. *Grabber II*, Waveform Transfer Software for the Tek 2201/2211/2214 (1989).

8. Lotus Development Corporation. *Reference Manual, Lotus 1-2-3 Release 2.2* (1989).

9. Baker, W. E., Cox, P. A., Westine, P. S., Kulesz, J. J. and Strehlow, R. A. *Explosion Hazards and Evaluation*, Fundamental Studies in Engineering 5, Elsevier Scientific Publishing Company (1983).

10. Ingard, K. U. *Fundamentals of Waves and Oscillations*, Cambridge University Press, Cambridge (1988).

CHAPTER 3

EXPERIMENTAL ANALYSIS OF CRACK INITIATION UNDER DYNAMIC PRESSURE LOADING

3.1 Introduction.

The experimental results of the last chapter have demonstrated that the analysis of crack initiation under dynamic pressure loading with the proposed impact testing rig is feasible, following an experimental-numerical approach. The aim of the experimental work is the evaluation of the crack initiation conditions. Thus, it has been divided in two parts. Firstly, cracked PMMA specimens have been tested with the loading and clamping conditions selected in the last chapter, establishing the instant of crack initiation for each specimen with the rapid variation of the membrane strain history traces. These are monitored with a strain gauge bonded close to the crack tip and, from this data, the strain rate is obtained. Secondly, the load and strain histories are plotted in a single graph, considering the dynamic calibration obtained in the analysis of the elastic response of the specimens. From this graph, the crack initiation load is inferred. Furthermore, quasi-static tests have been developed in order to establish the background for the interpretation of the results.

The experimental data will be used in the numerical analysis, in which the fracture surface energy is evaluated following the J-integral method, which is implemented within the finite element method code ABAQUS. Nevertheless, there are some points that have to be studied before, namely, the range of application of this impact technique and the development of brittle

fracture under quasi-static and dynamic loading. These concepts will be discussed jointly with the experimental results.

3.2 Characteristics of Polymethylmethacrylate.

Polymethylmethacrylate (PMMA) is also known by the trade name "Perspex"[a]. It is formed by the polymerization of methyl-methacrylate, which is a clear organic liquid of boiling point 100°c. According to Williams [1], this material has a brittle fracture behaviour under normal testing conditions below 85°c and its mechanical properties are constant. In addition, the production of cracks, using razor blades, is easy, because the craze stress is slightly lower than the shear yield stress at room temperature.

Kinloch et. al. [2] state that the fracture stress in PMMA at room temperature becomes independent of the flaw size when the length of the crack is lower than 0.07 mm. Hence, the material behaves as if it contains natural flaws. Besides, Fraser et. al. [3] have observed that, in cracked specimens, very small plastic zones are developed at the crack tip, which is an important condition in fracture mechanics analysis.

This material is easy to machine and commercially available. Its mechanical properties are not dependent upon fabrication conditions and exhibit no variation between different batches. Consequently, the correlation of results among different research groups is straightforward [2]. The mechanical properties at 20°c reported by the manufacturer of the PMMA sheets [4], which were used in this experimental work, are the following:

Tensile Strength	82.76 MPa
Flexural Strength	137.93 MPa
Shear Strength	75.86 MPa
Young's Modulus in Flexure	2.896 GPa
Poisson's Ratio	0.35
Density	1190 kg/m^3

The tensile strength was obtained at 1% s^{-1} strain rate. It must be borne in mind that the mechanical properties depend on the temperature at which they are measured and on the strain rate.

[a]Perspex is a trade mark of ICI.

3.3 Fabrication of the Specimens.

The specimens have been produced with transparent acrylic sheets of PMMA manufactured by the Plastics Division of Imperial Chemical Industries Limited. They are 1850 mm long, 1250 mm wide and 3 mm thick. Besides, they are shipped with a plastic cover from the factory. Thus, the development of defects, which would degenerate in fissures, is unlikely during transport. Nevertheless, before making the specimens, the sheet was checked to be free from defects.

In the first step of the manufacture process of the specimens, the plates were machined in accordance with the dimensions established in section 2.2, following the recommendations of the material manufacturer [5]. Figure 3.1 shows one of the specimens.



Figure 3.1 Notched specimens made of PMMA.

Through thickness cracks were produced with a fine fretsaw, which is shown in figure 3.2. It is 0.85 mm wide and 0.2 mm thick. A straight cutting of the notches and a longer working life of the blades were ensured by using a set of steel blade guides, which are shown in figure 3.3. Each guide is 60 mm long, 8 mm wide and 8 mm thick. The gap between the guides is adjusted with a screw system.

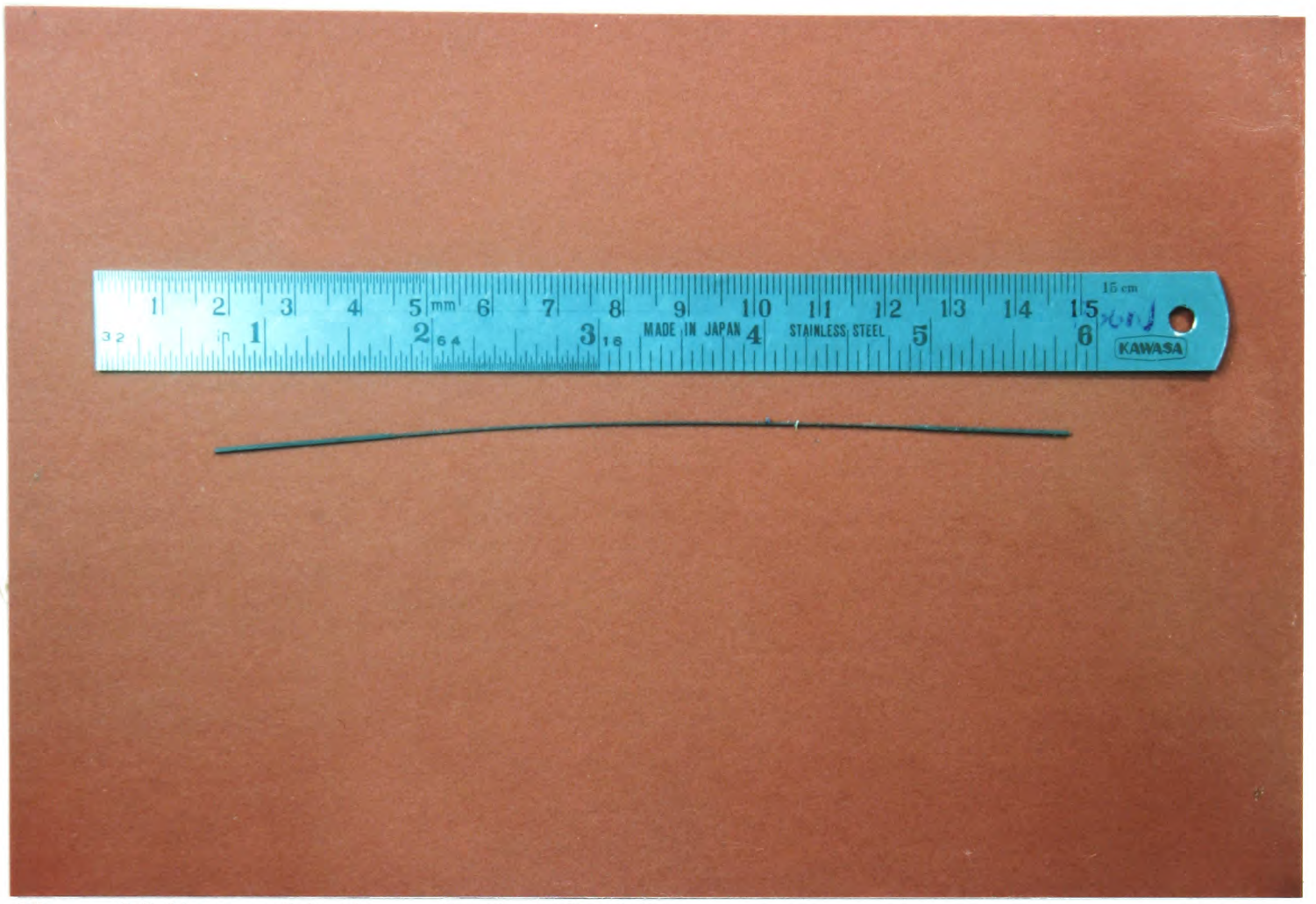


Figure 3.2 Saw used in the production of notches.

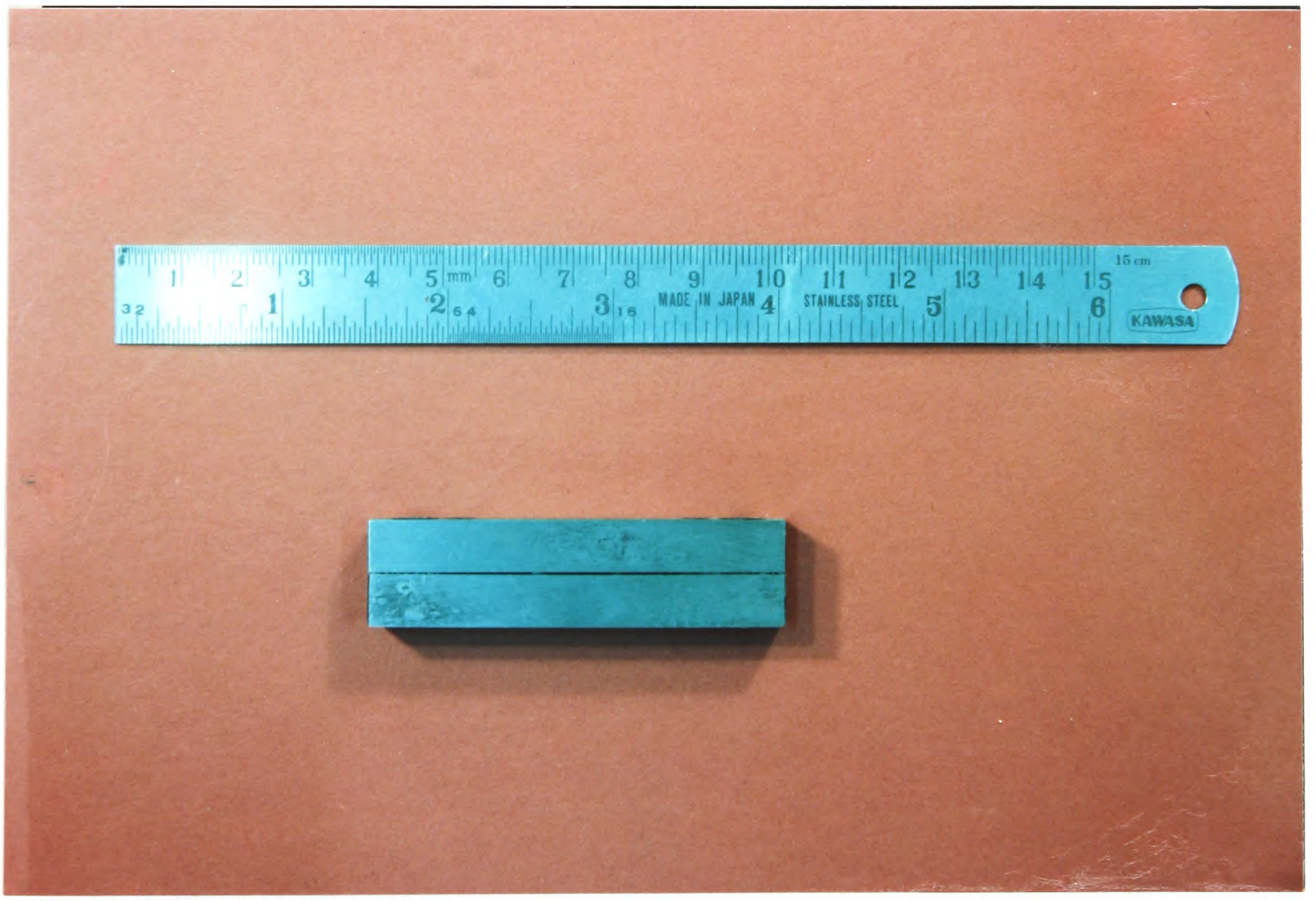


Figure 3.3 Steel blades guides.

A hole of 1 mm diameter at the centre was drilled to leave the required space for cutting the notch. The guides were then firmly attached at the centre of the specimen with adhesive tapes. Then, the specimen was clamped to the table of a drilling machine, using rectangular pieces of wood of the same thickness, which were put between the specimen and grip surfaces. This set up, which is shown in figure 3.4, was chosen because the plate is firmly attached without inducing unwanted stresses. Furthermore, the central hole of the table facilitates the guided saw operation. Figure 3.5 illustrates a detail of the notch cutting. All the notches were carefully cut either side of the central hole. The crack size range is restricted by the process of fabrication. In particular, the dimension of the blade guides defines the maximum notch length, which is 25 mm.



Figure 3.4 Set up for notch production.

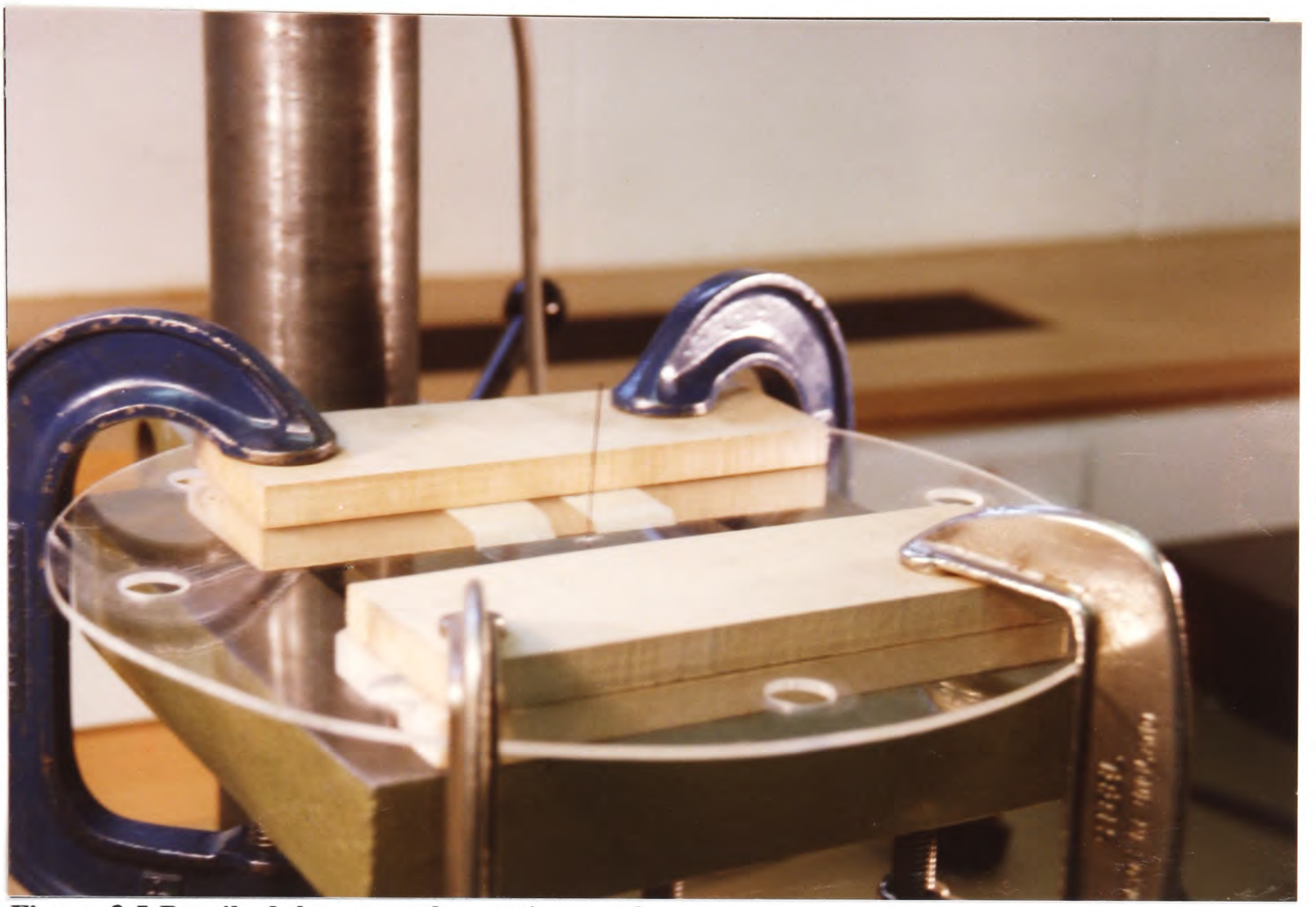


Figure 3.5 Detail of the set up for cutting notches.

In the case of instrumented specimens, strain gauges were bonded as close as possible to the crack tip. The FLE-I-23 type, produced by Tokyo Sokki Kenkyujo Co., Ltd., was selected, whose gauge dimensions are 1 mm length and 1.2 mm width. The sensing element is a foil made from copper and nickel and it is mounted on an epoxy base carrier, which is 5 mm x 2 mm. The gauges are supplied with leads.

Finally, the length and width of all the notches were measured with an optical comparator Mitutoyo PV-600. This apparatus has been designed to measure, inspect and trace sharply defined and magnified images of large workpieces. All these analyses are carried on a circular screen of 600 mm diameter, in which the screen glass is fine ground with cross hairs and it can rotate 360° with a vernier reading to 1'. All the measurements are carried on with a digital micrometer, in which the minimum reading is 0.001 mm. The cross travel of the micrometer stage is 100 mm x 500 mm and the stage size is 300 mm x 240 mm. In addition, the magnification factors are 5x, 10x, 20x, 50x and 100x and the accuracy of the contour magnification factor is less than 0.1% of the nominal magnification.

3.4 Effect of the Notch Shape in the Evaluation of the Stress Intensity Factor.

The notch width of the specimens, reported in tables 3.1 and 3.3, is within the range 0.2 mm and 0.33 mm. Clearly, the crack tip behaviour is simulated with artificial notches of finite radius. Therefore, it is important to determine whether the notch shape affects the evaluation of the SIF.

From a series of photoelastic tests, Pearson [6] found that the geometrical irregularities of the crack tip influence the stress field very near to the crack tip. Phang [7] reached similar conclusions when he evaluated the SIF with the same experimental technique. He considered that blunting, finite rotations and deformations at the crack tip arise from the existence of high stresses, the presence of a triaxial stress field and the steep stress gradient at the crack tip, as well as the artificial sharp notch effect.

In relation with the crack geometry, Smith et. al. [8] studied with mapping functions four different configurations to model real cracks, namely elliptical, rectangular, rhombus and blunted triangular. The stress distributions at the crack tip of each model were compared with the solution for an infinitely sharp crack. The results showed that any notch can be used to simulate a crack provided, that the crack length is bigger than the root radius and that the measurements are taken sufficiently far from the crack tip.

With respect to the error in the calculation of the SIF, Bowie and Neal [9] showed that for notch length-to-root radius ratios greater than two, it is at most 2 %. Similarly, Weiss and Yukawa [10] established that the difference between the stress distribution for sharp cracks and for finite root radii notches differs at distances less than 0.25 times the root radius from the crack tip. Smith and associates [11-13] also analyzed this problem with the theory of plane strain small deformation plasticity and estimated that the onset of nonlinearity would occur at $(r/a)^{1/2} \sim 0.173$.

Following an experimental approach, Hashemi et. al. [14] studied the crack tip sharpness effects on five different polymers, namely PMMA, PVC, PA, Nylon and PP. A series of tests were performed in three-point bending specimens and the tip radius varied from 13×10^{-6} m up to 1 mm. In the case of PMMA, a wide range of initial notch values converged to the exact

evaluation. Thus, specimens with notch radius lower than 0.30 mm are considered acceptable for fracture mechanics analysis.

Fraser et. al. [3] studied the fracture behaviour of notched specimens of PMMA for a wide range of geometries in Charpy impact tests and in tensile and slow bend fracture tests. The notch tip radii of the specimens varied from 0.3 to 1.5 mm. In addition, sharp notches were obtained by pushing razor blades. In the case of small notch tip radii (<0.35 mm), the fracture toughness evaluated is almost constant.

In brief, all these findings establish that the crack tip nonlinearities due to geometry of the notch front are extremely local and the stresses at the far field will not be influenced. The notch radius of the present specimens are within the range in which a convergence to exact solution has been observed by others. Furthermore, it falls within the limits found for valid fracture toughness measurements, as ascertain by static and dynamic tests.

3.5 Description of Crack Initiation Tests under Dynamic Loading Pressure.

The crack initiation analysis under dynamic conditions has been undertaken with two series of impact tests at room temperature. The main objectives of the first series were the evaluation of the chamber pressure required to initiate the crack and the establishment of the main characteristics of the fracture surfaces. For these purposes, failure and no-failure tests were performed with five specimens, whose crack length range is between 4 mm and 19 mm. Any strain gauges were bonded at their crack tip and the procedure, described in section 2.2.1, was followed in each test.

Initially, each specimen was loaded with a pressure wave which is generated with a pressure equal to 0.75 bar. Then, in the following tests, the pressure was increased until crack growth was observed. In all these tests, the output parameter is the chamber pressure that generated crack initiation, which will be defined as the "burst pressure".

The aim of the second series of tests was the evaluation of the crack initiation load and the strain rate during the specimen loading. Thus, after the range of the burst pressure that initiates the crack was established, three specimens were tested, whose crack length is within

the range between 4.8 mm and 14.7 mm. The strain history that showed crack initiation was registered.

In the final part, the strain and pressure histories, which were observed during crack initiation, were combined in a single graph. In all these cases, the dynamic calibration obtained in the analysis of the elastic response of the specimens (section 2.4.3) was considered and the crack initiation load was obtained.

3.6 Experimental Results of Crack Initiation under Dynamic Loading Pressure.

The chamber pressure required to initiate the crack in both series of tests, as well as the crack dimensions of the specimens are reported in Table 3.1. Besides, the results of the first series of tests are shown in the diagram crack length vs burst pressure, in figure 3.6, in which two well defined regions are observed. One of them is formed with the results of those tests in which there was no crack propagation, while the second is generated by those tests in which crack propagation was observed. A curve, that separates both regions, has been drawn.

TABLE 3.1
SPECIMENS TESTED UNDER DYNAMIC PRESSURE LOADING

SPECIMEN	CRACK LENGTH (mm)	CRACK WIDTH (mm)	CHAMBER PRESSURE AT CRACK INITIATION (bar)	REMARKS
25	4.761	0.226	1.50	(1)
27	19.141	0.331	1.15	(1)
29	10.362	0.207	1.25	(1)
32	14.461	0.223	1.20	(1)
34	4.932	0.259	1.40	(1)
36	4.862	0.285	1.25	(2)
37	9.694	0.302	1.25	(2)
38	14.745	0.330	1.00	(2)

(1) Without strain gauges (first series of tests).
(2) With strain gauges (second series of tests).

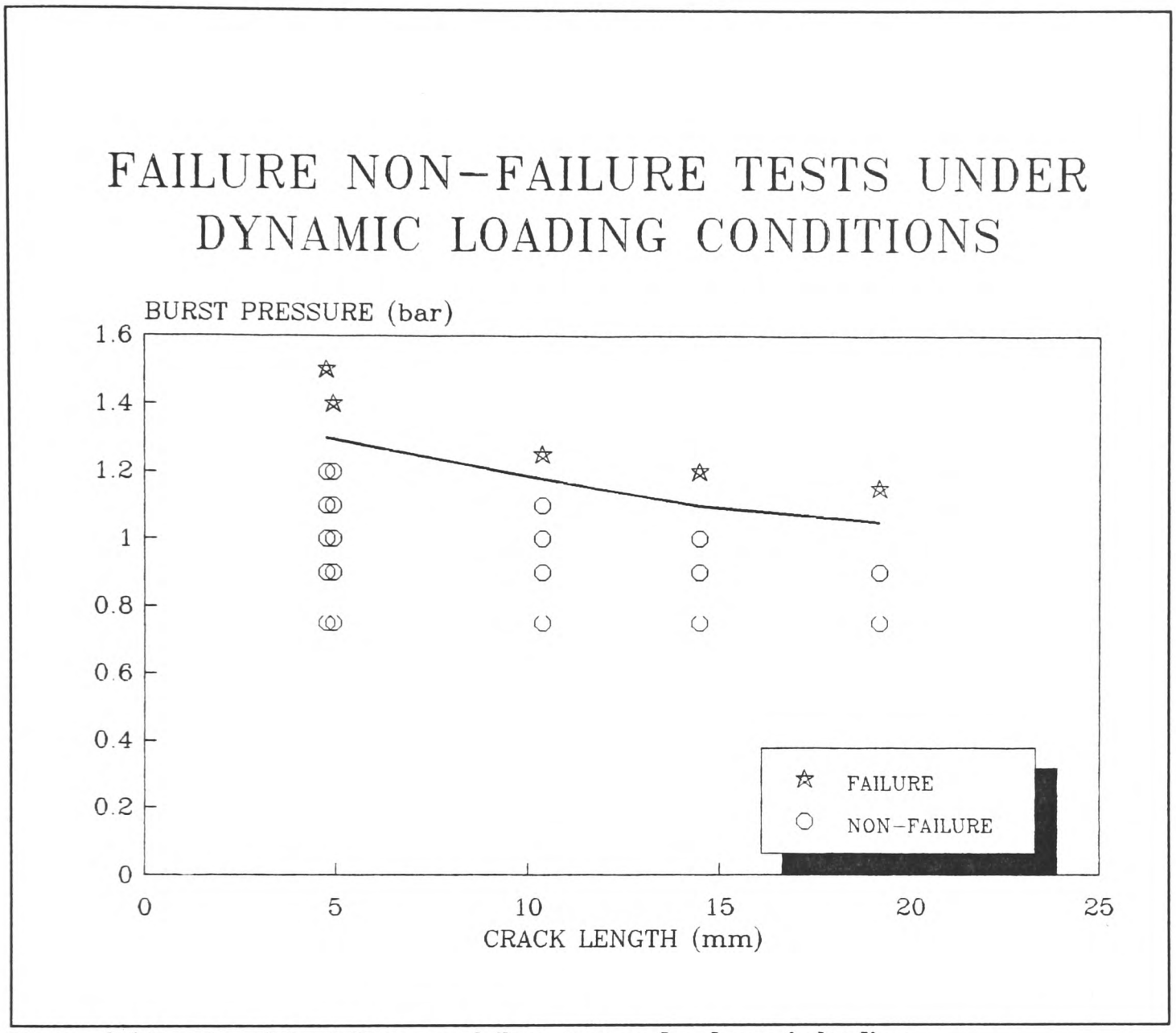


Figure 3.6 Results of the failure non-failure tests under dynamic loading.

The trend shows that for those specimens, whose crack length is greater than 15 mm, the burst pressure tends to a fixed value (1.1 bar). By contrast, the required load for crack initiation increases rapidly as the size of the crack diminishes.

These results demonstrate that crack initiation is likely when the specimens are loaded with blast waves generated with a bursting pressure in the range between 1.0 and 1.5 bar. No specimen fragmentation was found, which allows a postmortem analysis.

The analysis of the fracture surfaces showed that, in all cases, a state of bending stress was developed because their shapes are semi-elliptical, in which the major axis coincides with the plane of maximum tensile stress. Besides, the cracks always propagated close to the original crack plane. A typical resultant crack is illustrated in figure 3.7. This suggests that a state of plane strain may be considered in the evaluation of the fracture toughness.

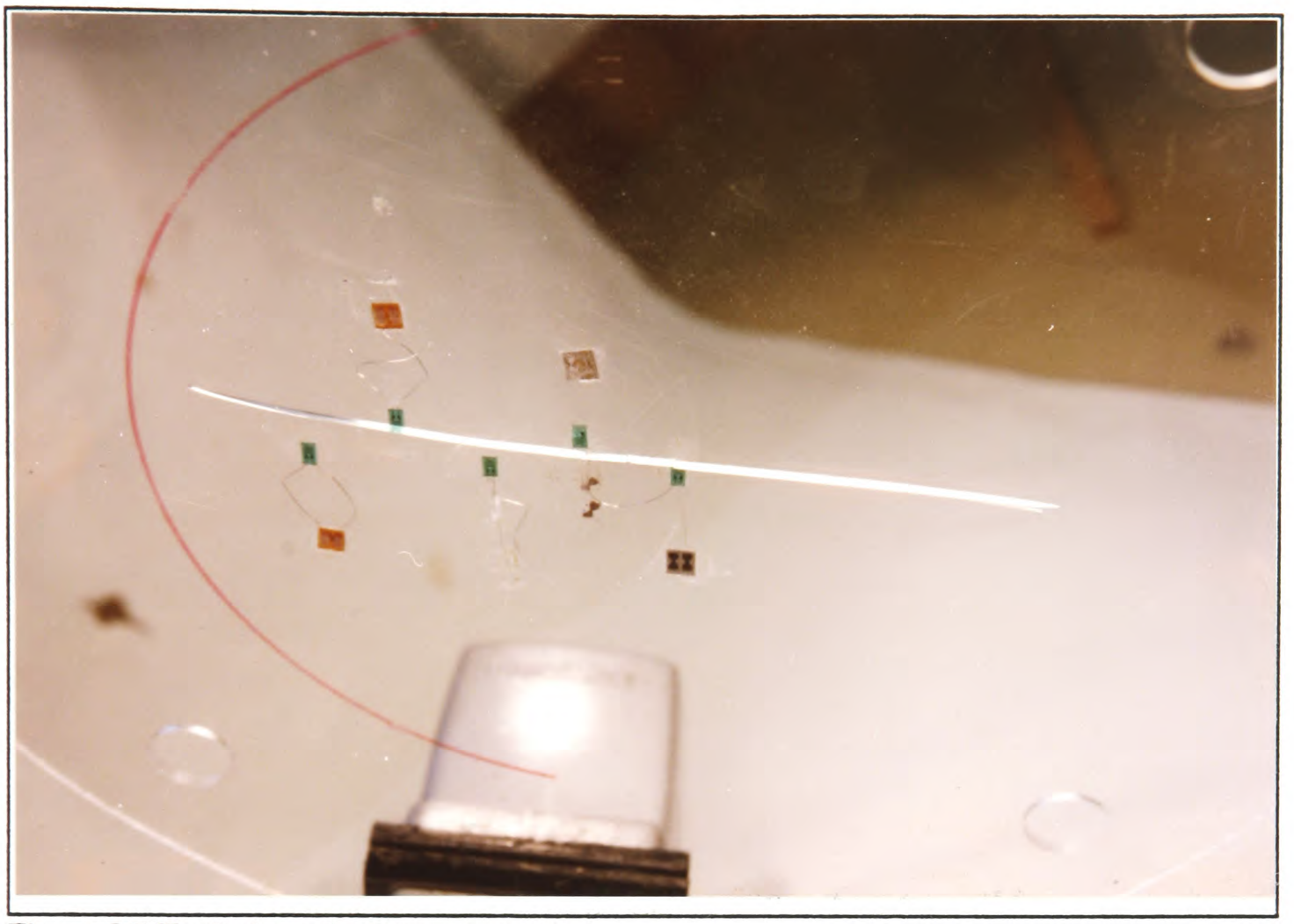


Figure 3.7 Typical crack after propagation.

In the second series of tests, once the required chamber pressure range is known, the membrane strain history traces, that indicate crack initiation, were recorded. Specimens 36, 37 and 38 were instrumented with strain gauges at the crack tip. Figures 3.8, 3.9 and 3.10 show the position of the gauges with respect to the crack tip for each specimen. They were loaded with the pressure waves which are generated with chamber pressures equal to 1.0 bar and 1.25 bar and the membrane strain histories traces were registered every $5x10^{-6}$ s. Thus,

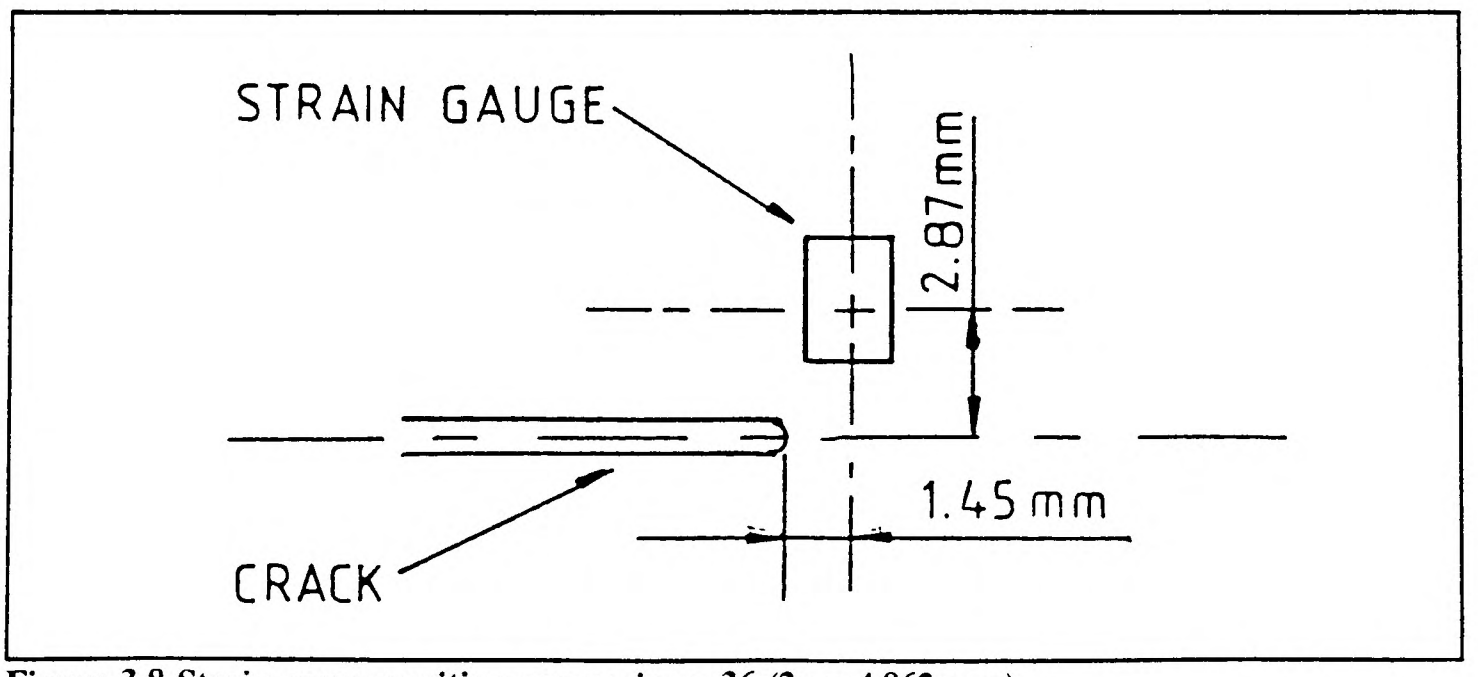


Figure 3.8 Strain gauge position on specimen 36 (2a = 4.862 mm).

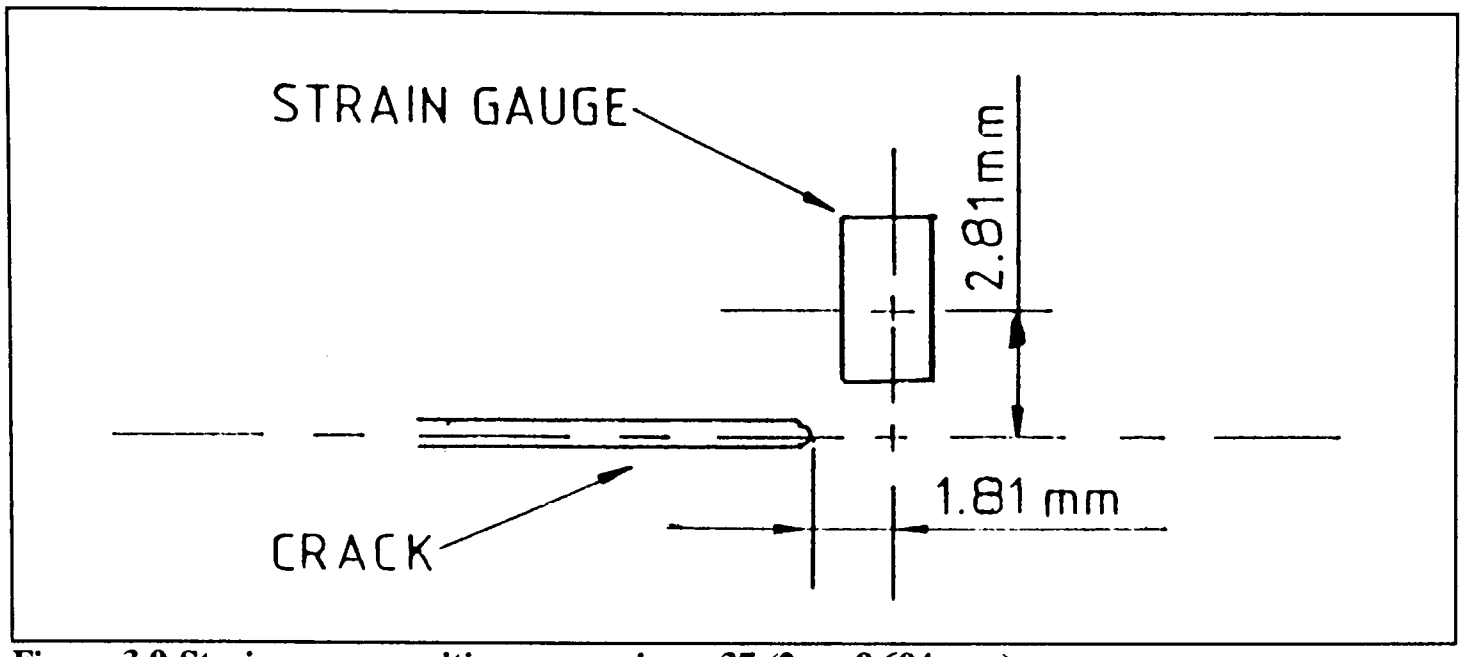


Figure 3.9 Strain gauge position on specimen 37 (2a = 9.694 mm).

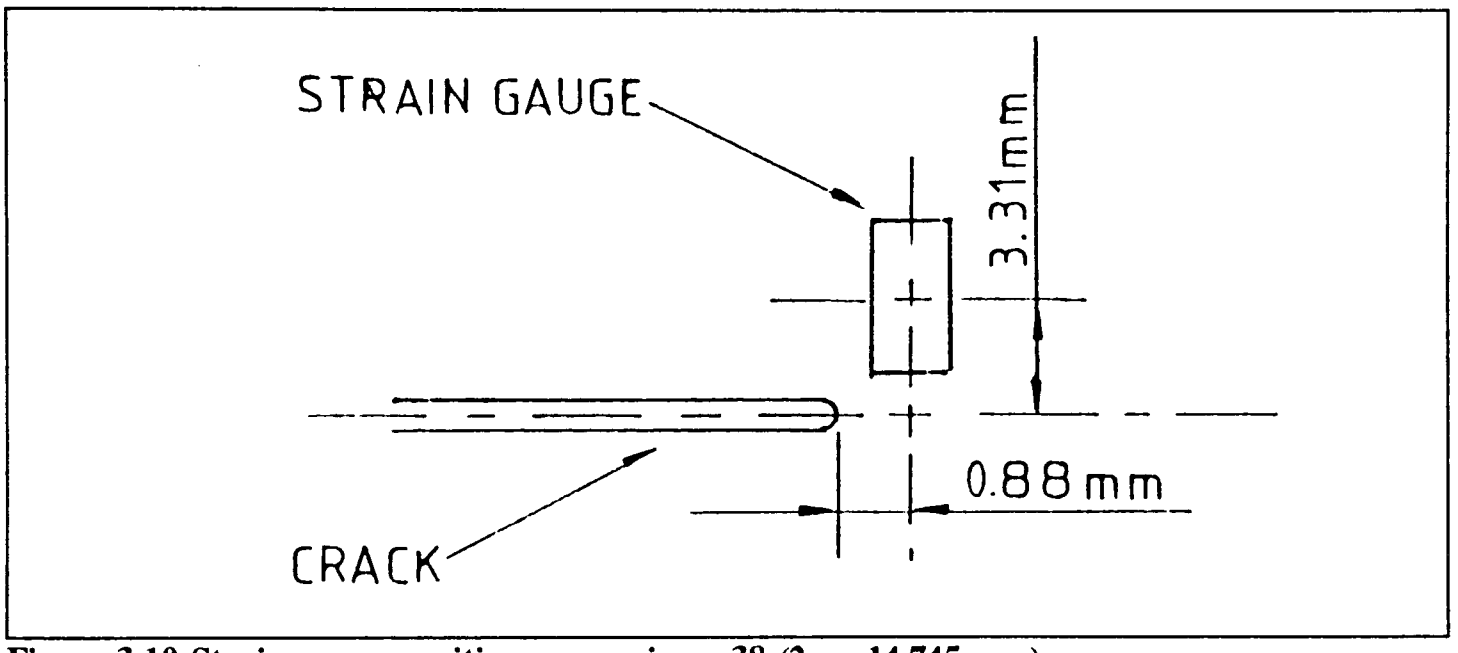


Figure 3.10 Strain gauge position on specimen 38 (2a = 14.745 mm).

they can be compared with the pressure histories, which were recorded with the same frequency.

The main characteristics of the membrane strain signals are the following. As soon as the load is applied, there is a transition phase in which the strain-rate changes from zero to a state of constant rate of increase. This trend continues until the crack starts to propagate. At this point, a sudden decrease in the signal is noticed, generating a peak point, which is sharply defined. A typical result is shown in figure 3.11 and no signs of stress waves reflection were observed.

The strain rate is evaluated from these curves. In each case, the slope of the curve before the

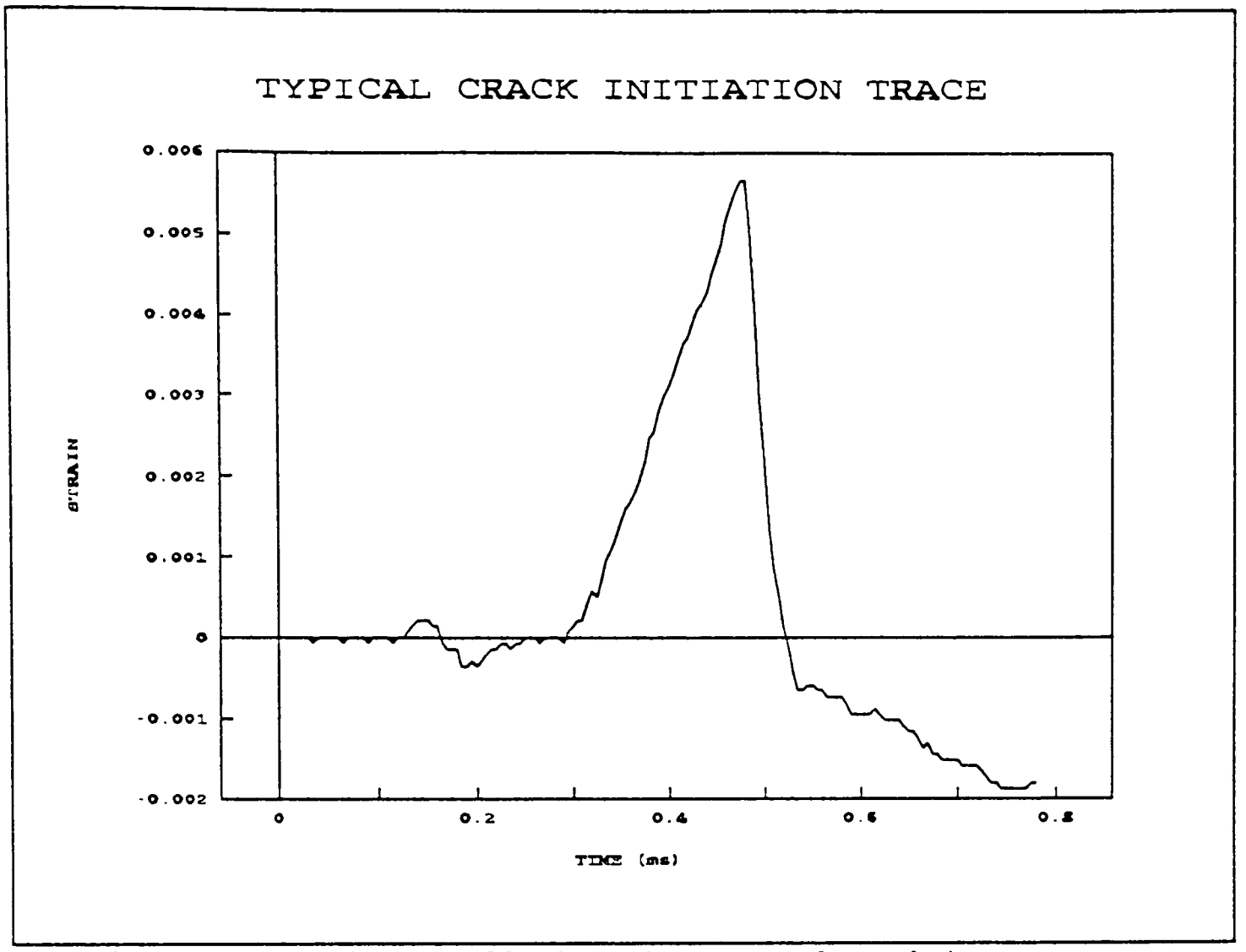


Figure 3.11 Typical signal registered by the strain gauges at the crack tip.

crack initiates is measured and the results are reported in table 3.2. Clearly, these are average evaluations at the neighbourhood of the crack tip. In theory, the strain rate is infinite at the crack tip.

TABLE 3.2
RESULTS OBTAINED FROM THE CRACK INITIATION ANALYSIS UNDER DYNAMIC PRESSURE LOADING

SPECIMEN	CRACK LENGTH (mm)	CHAMBER PRESSURE AT CRACK INITIATION (bar)	PRESSURE AT CRACK INITIATION (bar)	STRAIN RATE (s^{-1})
36	4.862	1.25	0.56	34.2
37	9.694	1.25	0.49	35.7
38	14.745	1.00	0.30	21.0

In order to make a comparison of the of the pressure and membrane strain histories, they were plotted in a voltage-time diagram, which are the common parameters to both series of tests. The cases studied are in figures 3.12, 3.13 and 3.14.

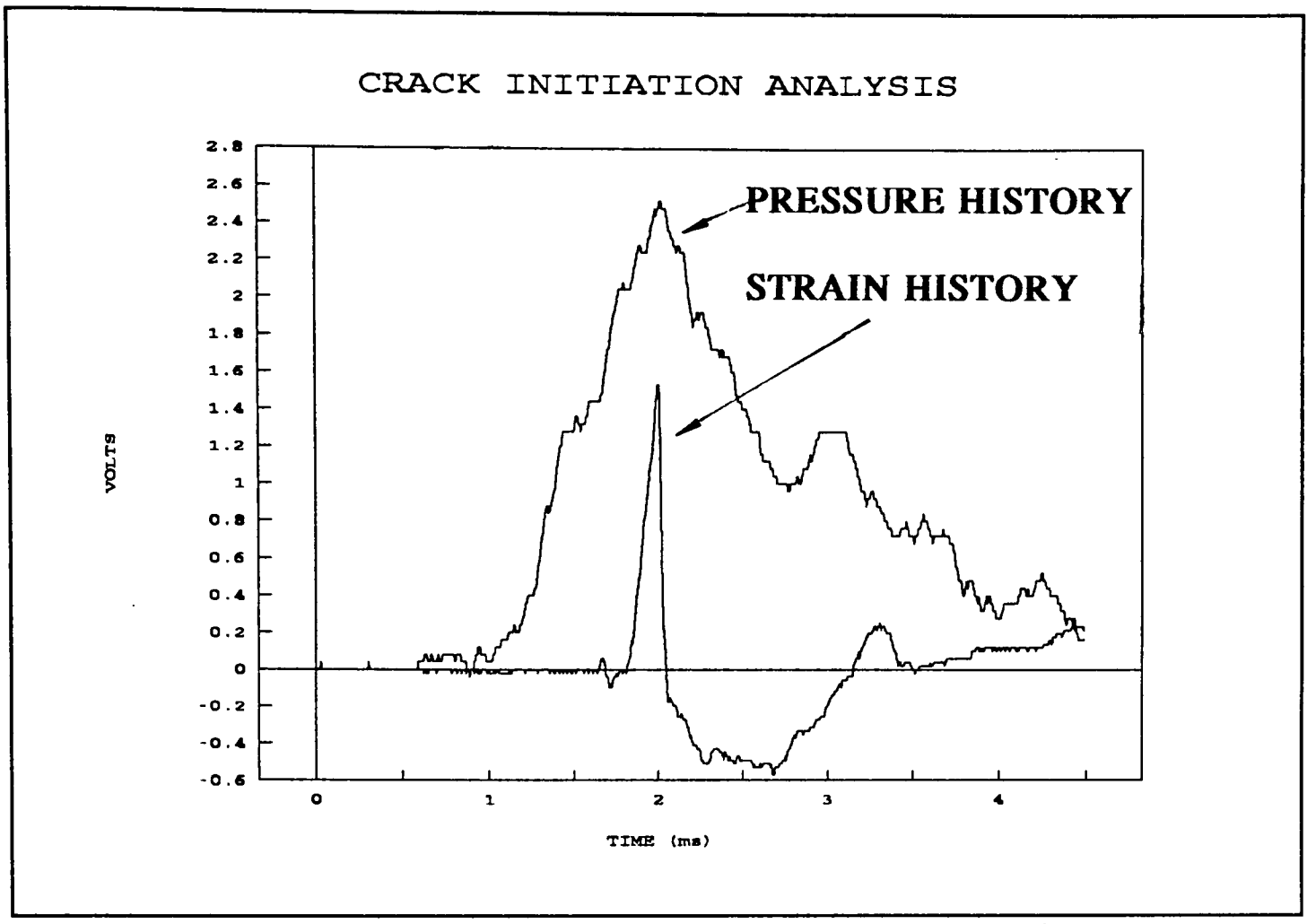


Figure 3.12 Comparison of the strain and pressure histories of specimen 36 at crack initiation (Pressure history envelops strain gauge signal).

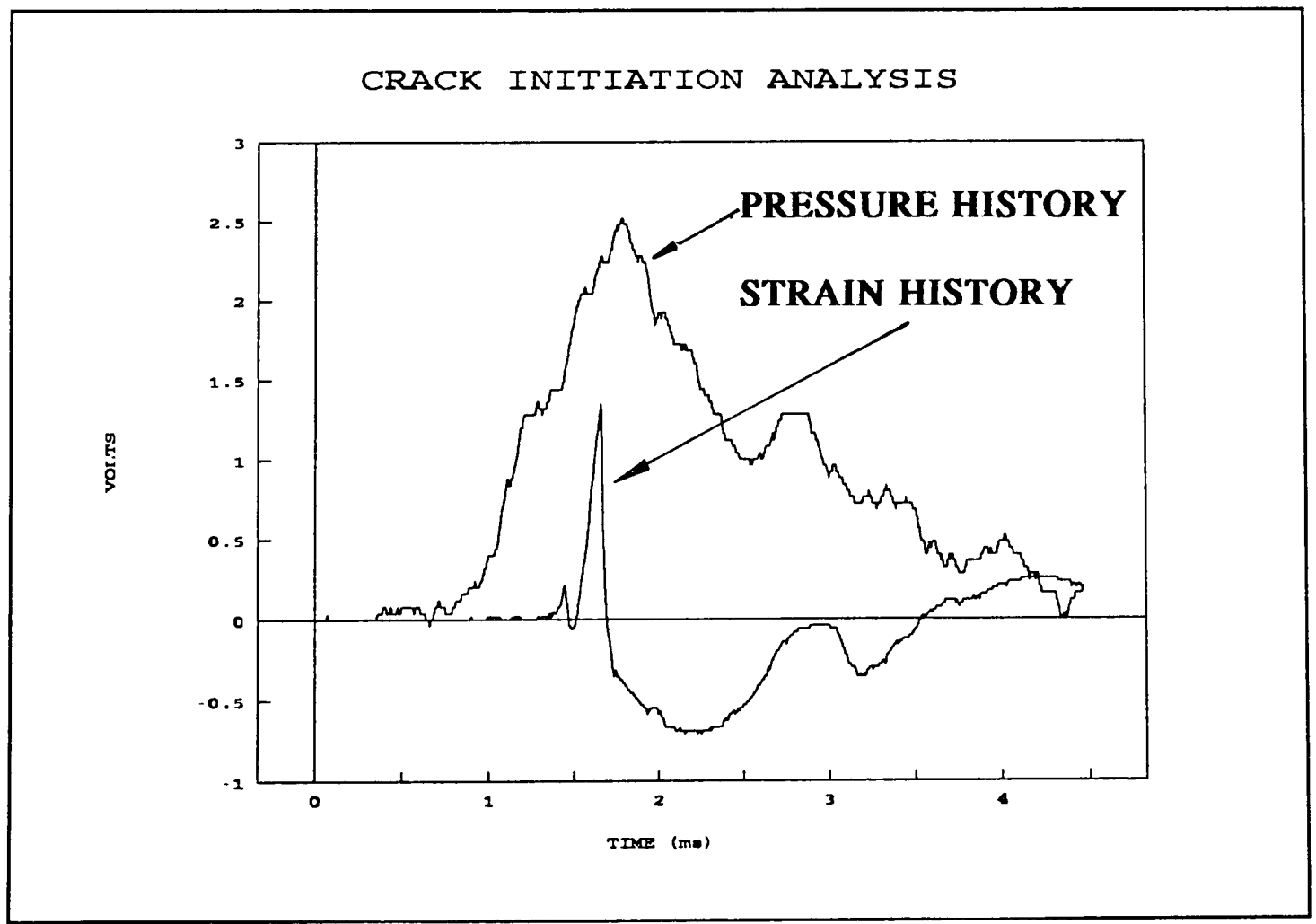


Figure 3.13 Comparison of the strain and pressure histories of specimen 37 at crack initiation (Pressure history envelops strain gauge signal).

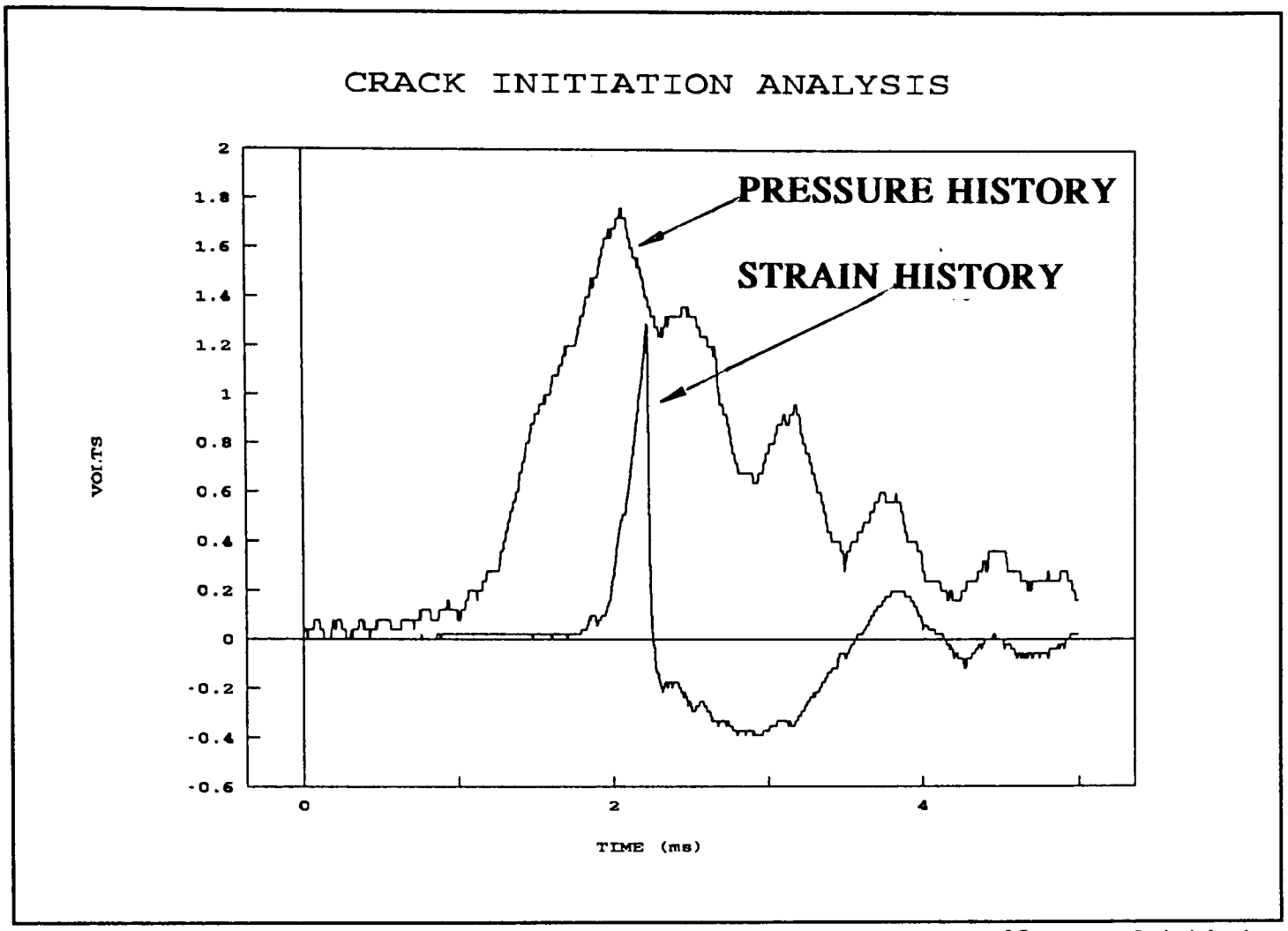


Figure 3.14 Comparison of the strain and pressure histories of specimen 38 at crack initiation (Pressure history envelops strain gauge signal).

These graphs were constructed with the LOTUS code in accordance with the following procedure. Firstly, the pressure history was plotted in a diagram time vs. voltage. Then, the strain history was plotted, considering the lag time observed between the pressure and strain histories in section 2.4.3. After the peak value of the strain history was identified, a vertical line was drawn from this point and its intersection with the pressure history curve was defined. The ordinate of this point is the voltage increment registered by the pressure transducer. Finally, the pressure at crack initiation was calculated with the appropriate calibration factor reported in table 2.1. The results obtained are shown in the table 3.2.

3.7 Description of Crack Initiation Tests under Static Loading Pressure.

Two series of tests have been done at room temperature. In both cases the impact test apparatus was operated in quasi-static conditions following the procedure described in section 2.2.2, in which the testing rig becomes a pressure vessel. Consequently, a leak through the specimen crack during the test has to be avoided. Thus, after the notch is produced, it is sealed

on the bottom surface of the specimen, with a tape made of Polytetrafluoroethylene (PTFE). This material deforms easily with very low loads, without splitting and separating from the specimen. In this way, forces that oppose the crack opening are unlikely. The recording system, which was used in the dynamic tests, was not employed, because the only output parameter is the pressure at crack initiation and is detected with the "pop" sound that is generated when the crack starts.

The aim of the first series of tests was to evaluate the crack initiation load and to observe the main characteristics of the crack surfaces. Thus, four specimens were loaded very slowly until crack initiation was detected. The range of the nominal crack length is between 3 mm and 19 mm.

The purpose of the second series of tests was to check the repeatability of the results obtained in the first series and, at the same time, to assess the effect of the load history on the fracture process, by loading and unloading the specimens several times before the crack is initiated. Hence, two specimens were loaded with a series of load cycles. In the first, the pressure was increased very slowly to 0.25 bar and, then, the rig was completely depressurized. In the subsequent loading cycle, this loading procedure was repeated and the peak pressure was increased 0.05 bar every time until crack propagation was detected.

3.8 Experimental Results of Crack Initiation under Static Loading Pressure.

The results of the tests with specimens 26, 31, 33 and 35, which were tested in the first series of tests, are shown in table 3.3. They are also plotted in figure 3.15, in which crack length and crack initiation pressure are associated. Similarly, the test results of the specimens 28 and 30, which were tested in the second series of tests, are shown in table 3.3 and plotted on the same diagram. In fact, there are small differences, but all the results practically superpose over the same curve, implying that the material is not affected by the load history.

The trend of the failure curve shows that for specimens with cracks longer than 15 mm, the crack initiation pressure tends to a constant value, 0.5 bar. On the contrary, specimens with smaller cracks require higher pressure for their initiation. Besides, it has been considered that the pressure is proportional to the applied stress. Hence, this behaviour suggests that the crack

TABLE 3.3
SPECIMEN TESTED UNDER STATIC LOADING PRESSURE.

SPECIMEN	CRACK LENGTH (mm)	CRACK WIDTH (mm)	PRESSURE AT CRACK INITIATION (bar)	REMARKS
26	8.651	0.221	0.80	(1)
28	8.349	0.212	0.70	(2)
30	19.043	0.249	0.55	(2)
31	18.749	0.225	0.50	(1)
33	2.959	0.300	1.45	(1)
35	4.881	0.208	1.05	(1)

(1) Pressure increase very slowly in a single step.
(2) Final pressure was reach in several steps.

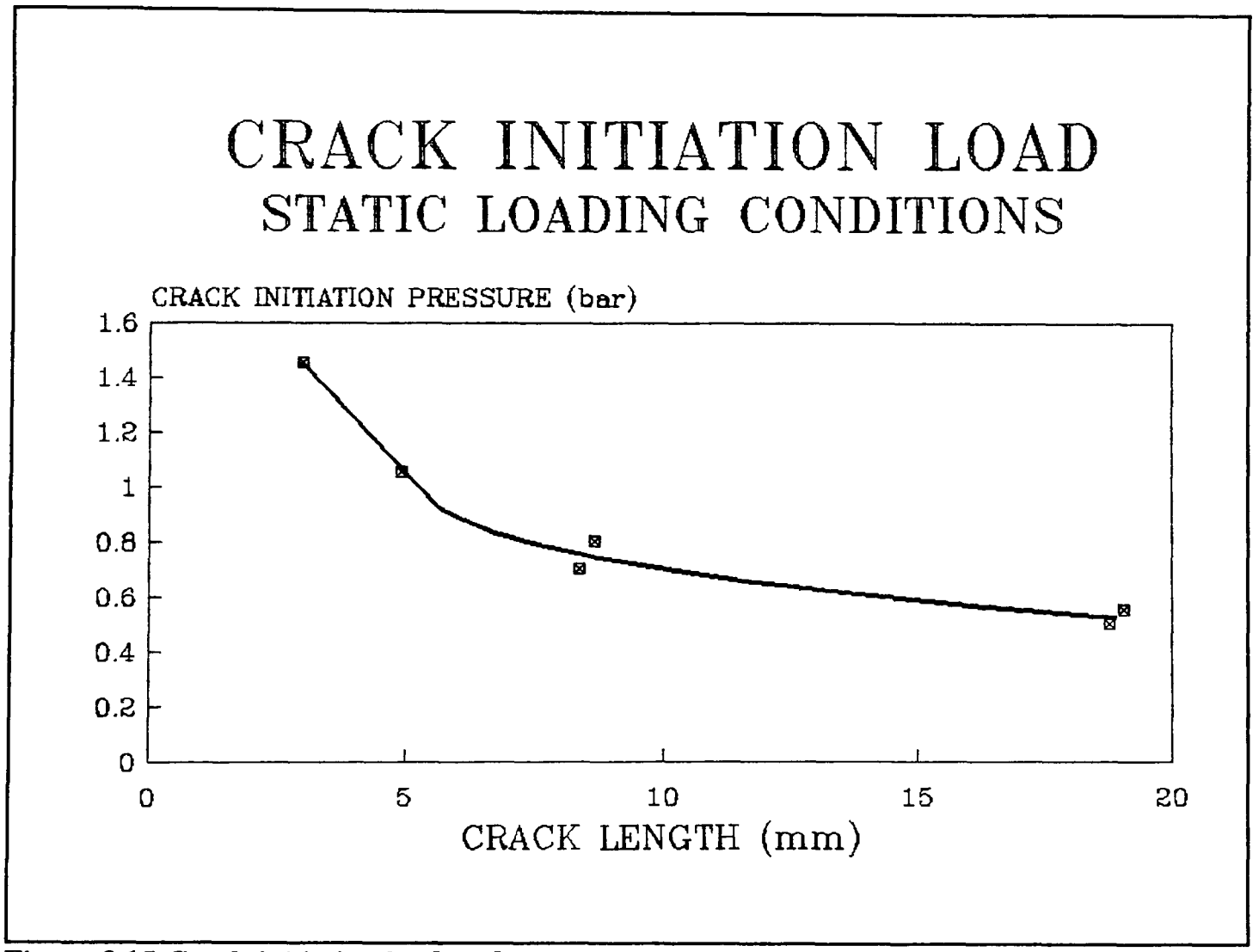


Figure 3.15 Crack initiation load under static pressure load.

initiation load varies linearly with the square root of the crack length. Plotting the inverse of crack length square root vs. crack initiation pressure in figure 3.16 and making a linear

regression analysis, a straight line, which intersects the vertical axis at -0.10 bar, is obtained. Its regression coefficient r^2 is 0.97. In theory, this line should intersect the origin. However, it has to be considered that the crack initiation loads were rounded. Thus, this line is shifted from the origin. The errors are not serious and the fracture behaviour can be explained with Griffith's theory.

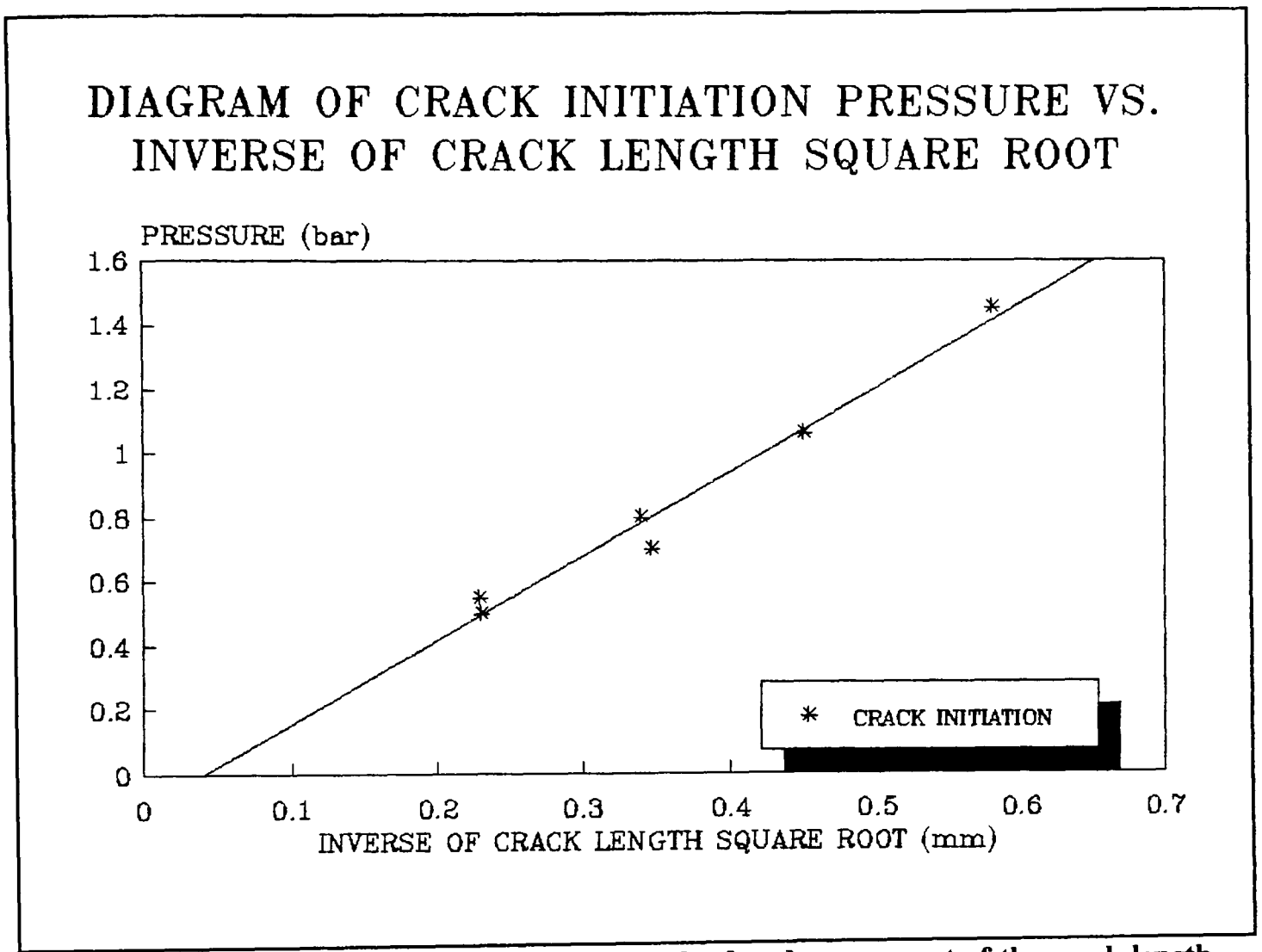


Figure 3.16 Relationship between crack initiation load and square root of the crack length.

With the exception of specimen 33, fragmentation was not observed and the resultant cracks propagated along the plane of the original crack. Their shape is elliptical and its major axis coincides with the plane of maximum tension stresses. Moreover, there are no signs of shear lips. So, plane strain conditions may be assumed in the evaluation of the fracture toughness.

3.9 Discussion of the Results.

A comparison among the loads required for crack initiation under quasi-static loading with those under dynamic loading and the bursting pressure is presented in the failure diagram (figure 3.17).

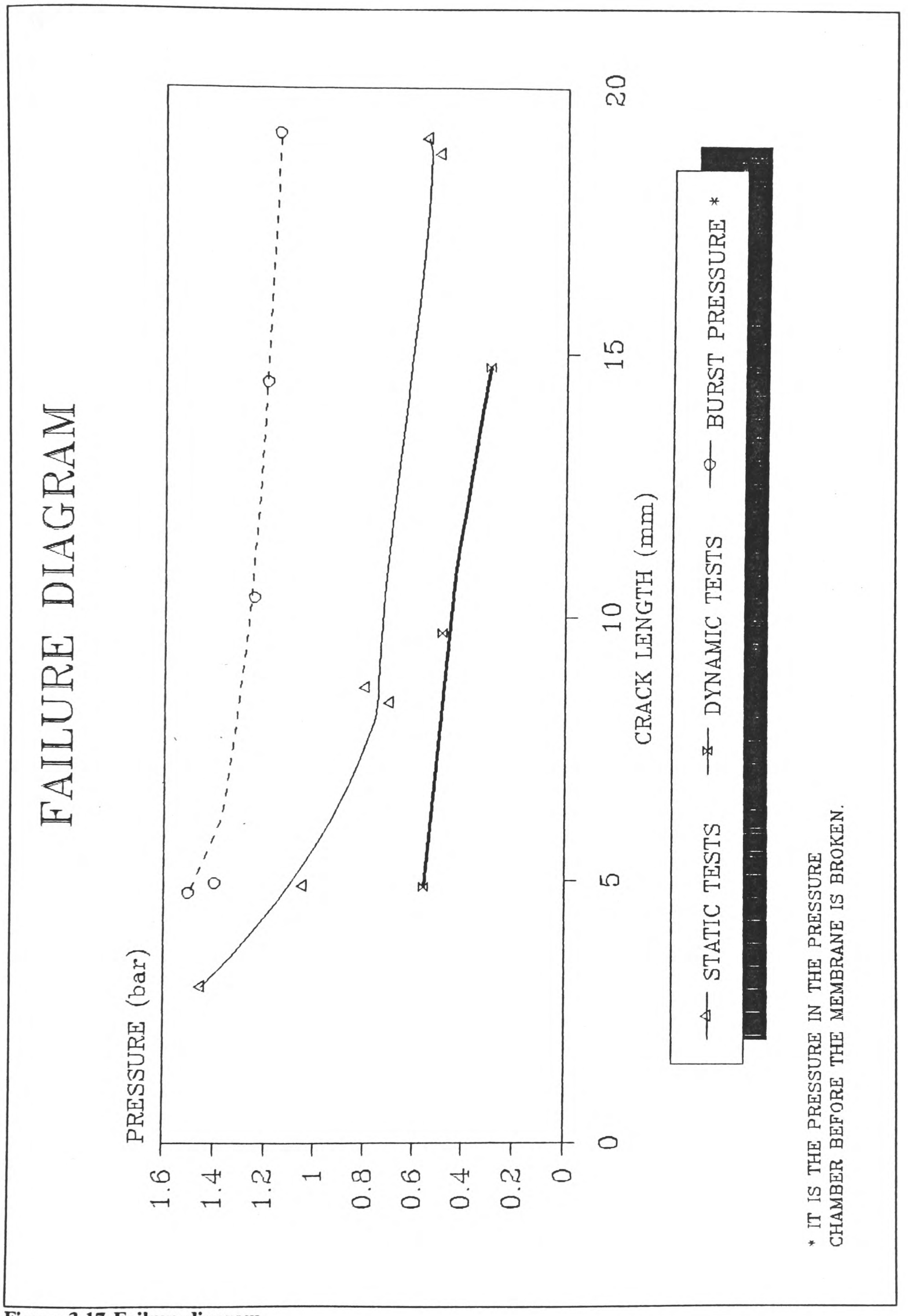


Figure 3.17 Failure diagram.

While static failure would seem to follow the traditional fracture mechanics rules, i. e., the pressure required to initiate fracture is inversely proportional to the square root of the crack length, dynamic failure follows totally different rules. The first question that arises is, which is the pressure at crack initiation?. Two values have been identified: the pressure of the chamber at the instant when the diaphragm bursts (burst pressure) and the pressure at crack initiation deduced from the strain gauges traces. Of the two values, it is clear that the second is the only one to be meaningful. In figure 3.17, both have been plotted. The pressure at crack initiation under dynamic conditions is much lower than the burst pressure and than the pressure under static conditions. Strain rate effects and inertial loads may account for the difference. A detailed investigation to find the reasons for this difference needs a numerical stress analysis and further experiments. They will be covered in the next chapters.

3.10 Summary.

The findings show that crack initiation under dynamic loading for those specimens, whose notches are within the range between 5 mm and 15 mm, is developed at strain rates lower than 35.7 s^{-1}, which are generated with burst pressures in the range between 1.0 bar and 1.25 bar. In this conditions, the crack initiation load is between 0.30 bar and 0.56 bar. Besides, the strain gauges at the crack tip showed that stress waves reflection does not occur. In the case of the quasi-static tests, the crack initiation pressure is within the range between 0.5 bar and 1.45 bar, when the crack length is between 3 mm and 19 mm.

The postmortem analysis of the fracture surfaces of the specimens tested under static and dynamic loading showed brittle behaviour, which was developed under a state of bending stresses. Besides, the crack propagated along the original plane of the crack, without showing signs of shear lips. This suggests a state of plane strain is developed. Hence, the numerical evaluation of the fracture toughness may be made with these data.

REFERENCES

1. Williams, J. G. *Fracture Mechanics of Polymers*, John Wiley and Sons-Ellis Horwood Limited, Chichester (1987).

2. Kinloch, A. J. and Young R. J. *Fracture Behaviour of Polymers*, Elsevier Applied Science (1990).

3. Fraser, R. A. W. and Ward, I. M. The fracture behaviour of notched specimens of polymethylmethacrylate. *J. Mater. Sci.* 9(1974)1624-1630.

4. The properties of "Perspex" acrylic materials. *Imperial Chemical Industries Limited*, Plastic Division, Welwyn Garden City, Herts, England (1971).

5. "Perspex" acrylic materials. Machining. *Imperial Chemical Industries Limited*, Plastics Division, Welwyn Garden City, Herts, England (1971).

6. Pearson, G. Fracture Mechanics Applied to Pressure Vessels, D. Phil. Thesis, Oxford University (1978).

7. Phang, Y. P. Stress Intensity Factors for Interacting Cracks, D. Phil. Thesis, Oxford University (1983).

8. Smith, C. W. and Schroedl, M. A. A study of near and far field effects in photo-elastic stress intensity determination, *Eng. Fracture Mech.* 7(1975)341-345.

9. Bowie, O. L. and Neal, D. M. The effective length of an edge slot in a semi-infinite sheet under tension, *Int. Journ. of Fracture*, 3(1974)111-119.

10. Weiss, V. and Yukawa, S. Critical appraisal of fracture mechanics, *Fracture Toughness Testing and its Applications*, ASTM STP 381 (1965).

11. McGowan, J. J. and Smith, C. W. A finite deformation analysis of near field surrounding the tip of a crack like elliptical perforations, *Int. Journ. of Fracture*, 11(1975)977-987.

12. McGowan, J. J. and Smith, C. W. A plane strain analysis of blunted crack tip using small deformation plasticity theory, *Advances in Engng. Sci.* 2(1976)585.

13. Smith, C. W., McGowan, J. J. and Peters, W. H. A study of crack tip nonlinearities in frozen stress field, *Exp. Mech.* 18, 8(1978)309-314.

14. Hashemi, S. and Williams, J. G. Crack sharpness effects in fracture testing of polymers, *J. Mater. Sci.* 20(1985)922-928.

CHAPTER 4

NUMERICAL ANALYSIS OF CRACK INITIATION UNDER DYNAMIC PRESSURE LOADING

4.1 Introduction.

The strain rate affects the mechanical properties and the fracture behaviour of materials. In consequence, several methodologies have been developed to evaluate the dynamic fracture toughness in which the analysis of the problem is simplified. In the case of linear elastic cracked bodies, which are loaded in mode I, the following fracture criterion has been proposed

$$K_I(t) = K_{Ic}(\dot{K}_I, T)$$

where the rate of change of stress intensity factor is

$$\dot{K}_I = \frac{K_{Ic}}{t_f}$$

t_f is the time to fracture and T is the temperature. Mines [1] considers that it is simplistic,

because it takes no account of history effects and the requirements of a finite material damage time.

Another way to tackle this problem is with the development of the dynamic fracture toughness models, which evaluate the strain rate sensitivity of K_{Ic}. Klepackzo [2] has proposed a relation among the rate of change of the stress intensity factor, the strain rate and the size of the plastic zone

$$\dot{K}_I = \dot{\epsilon} E \left(\frac{K_{Ic}}{\sigma_y}\right)$$

There have been some efforts to improve these models, as in [3], combining the static crack tip stress field, the fracture stress, the yield stress and the work hardening of the material. However, they are dependant on the knowledge of the state of stress and strain at the crack tip at failure and of the failure mode. Besides, the relation of microscopic parameters -crack tip stress field- to micro-mechanical properties -critical stress or strain- are required and no attention is given to the inertial effects [1].

An alternative solution to this problem is linear fracture mechanics, whose energetic approach has been used to evaluate the dynamic fracture toughness. In the case of impact testing with polymers, Williams [4] has proposed the lumped mass-spring model, which evaluates the energy release rate and takes into account the dynamic effects observed in impact tests. Nevertheless, the analysis of this problem is intricate, because the plastic deformation developed during the specimen loading gives energy dissipation. Besides, the spherical and cylindrical contact points give non-linear contact stiffness. A correction can be incorporated in the model as some form of damping in conjunction with the contact stiffness, but this increases the complexity of the analysis.

Summarising, these criteria show that the evaluation of the dynamic fracture toughness is not straightforward, because there are many factors, which are related with the variation of the mechanical properties of the material at the observed strain rates. Besides, a clear understanding of the inertial effects of the impact testing machine and the dynamic behaviour of the specimen is required.

The experimental results of the present research, reported in the earlier chapters, has shown that the crack initiation analysis has been simplified with the proposed impact testing technique. Consequently, the dynamic fracture toughness can be evaluated following two different procedures, in which standard solutions are applied or the fracture energy is calculated with a numerical method. Both methods are equivalent and they present advantages and limitations.

4.2 Evaluation of the Fracture Toughness.

4.2.1 The J-Integral Concept.

The J-Integral is a generalization of the energy fracture analysis to non-linear elastic materials, which considers the linear elastic behaviour as a particular case. It was introduced by Rice [5] and its theoretical background is based on an energy balance analysis. This fracture parameter has been interpreted as a rate of decrease of the potential energy of a cracked body when its crack increases.

$$J = -\frac{\partial \Pi}{\partial a} \qquad 4.1$$

With this definition, an equivalence with other fracture criteria can be established.

Regarding linear-elastic materials, the crack initiation conditions can be obtained from the theory of Griffith [6], which postulates that during an increment of crack extension, in an ideal brittle material, there is no change in the total energy. In other words, the sum of the variations of the potential energy of deformation Π and the surface energy S is equal to zero [7].

$$dE = d\Pi + dS = 0$$

In the case of a two-dimensional central cracked body, which is infinite and of unit thickness, the parameter S may be expressed in function of the surface energy density per unit area γ. Thus, the change of the surface energy for the extension of both crack tips is

$$dS = 2\gamma\, da$$

Besides, the energy release rate at crack initiation is

$$G = 2\gamma$$

Hence, the energy release rate in function of the potential energy of deformation is

$$G = -\frac{d\Pi}{da} \qquad 4.2$$

In consequence, the energy release rate in linear elastic conditions is equal to the rate of decrease of the potential energy when the size of the crack increases, which is the same meaning as the parameter J defined in equation 4.1.

Turning to the SIF, Irwin [8] has established that its relation with the energy release rate is

$$G = \frac{K^2}{E'} \qquad 4.3$$

where E' = E for plane stress and E' = $E/(1-\nu^2)$ for plane strain.

Considering equations 4.1, 4.2 and 4.3, a fracture criterion may be established, which relates all the J, G and K

$$J_c = G_c = \frac{K_{Ic}^{\ 2}}{E'} \qquad 4.4$$

These approaches are equivalent. Notwithstanding, the energetic approach offers several advantages. The most important is that the analysis is simplified. As a result, it can be

implemented in computing programs easily and can be used for the three dimensional fracture structure with different loading and boundary conditions, which would be intractable with a mathematical analysis.

With respect to the evaluation of the parameter J, consider a two-dimensional nonlinear elastic body of unit thickness. Then, this fracture parameter can be calculated with the following contour integral along a closed path around the crack tip, as shown in figure 4.1

$$J = \int_{\Gamma} (W dy - T \frac{\partial u}{\partial x} ds)$$

where W is the strain energy density, the y direction is taken normal to the crack line, T is a traction vector perpendicular to the path of integration and u is the displacement vector. The integration path is an arbitrary contour Γ, which starts from the lower crack face and extends counterclockwise around the crack tip to a point on the upper face. The crack surfaces are traction free [7].

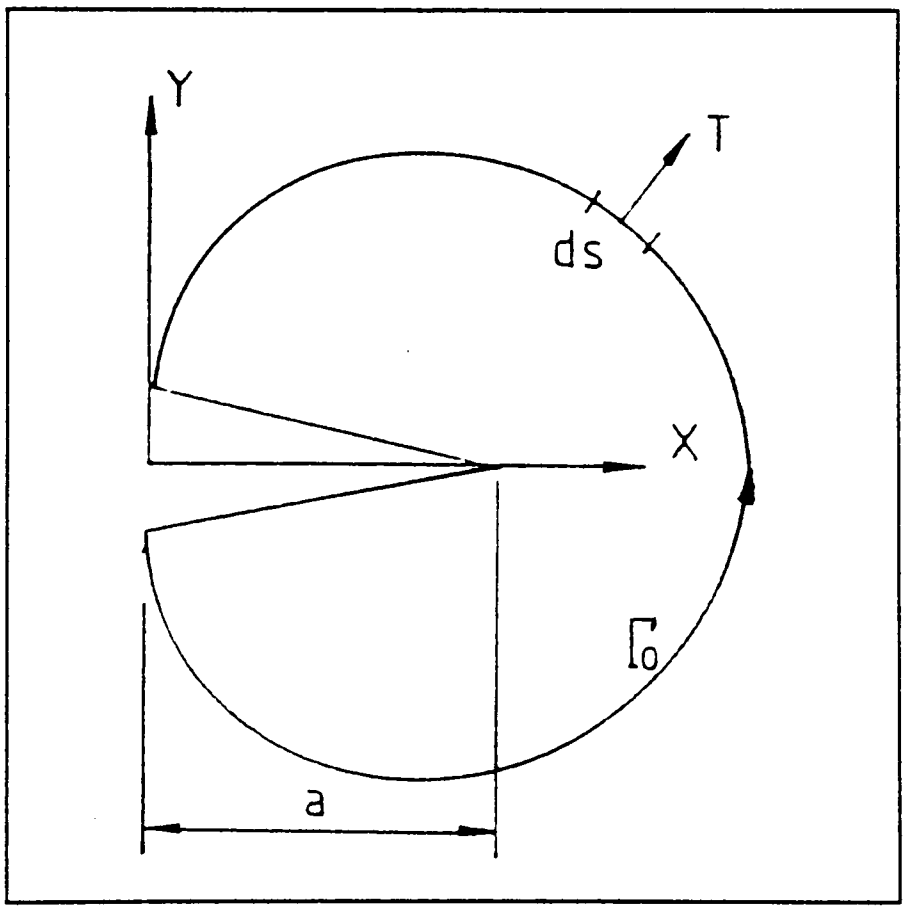


Figure 4.1 Dominion of definition of the J-Integral.

The first term of the right member of the equation represents the change in the elastic strain energy caused by the introduction of the crack in the body and the second is related with the work performed by external forces per unit of crack extension.

The main characteristic of this mathematical model is that it is path independent and is valid under quasi-static loading. In addition, it may be applied in those cases where small plastic zones are developed at the crack tip, provided that no unloading takes place. Accordingly, J is evaluated along a remote contour from the crack tip in such way that only elastic loads and

displacements are considered. Moreover, one of the advantages of this parameter is that it is relatively easy to evaluate in different structures with finite element programs [9], which can handle the crack tip singularity. In consequence, this method is very attractive.

4.2.2 The $\hat{J}$-Integral concept.

Kishimoto et. al. [10] extended the J-Integral to the case of a steady crack which is dynamic loaded. Based on an energetic approach, they proposed the path independent $\hat{J}$-Integral. In the absence of body forces, this contour integral takes the following form for a two dimensional cracked body

$$\hat{J} = \int_{\Gamma}(W_e n_1 - T_i \frac{\partial u_i}{\partial X_1})d\Gamma + \int\int_{A} \rho \ddot{u}_i \frac{\partial u_i}{\partial X_1} dA \qquad 4.5$$

where W_e and ρ are the elastic strain energy and the material density respectively. In accordance to figure 4.2, n_1 is a unit outward normal, T_i is the surface traction, u_i is the displacement and Γ is an arbitrary contour that surrounds the area A at the crack tip.

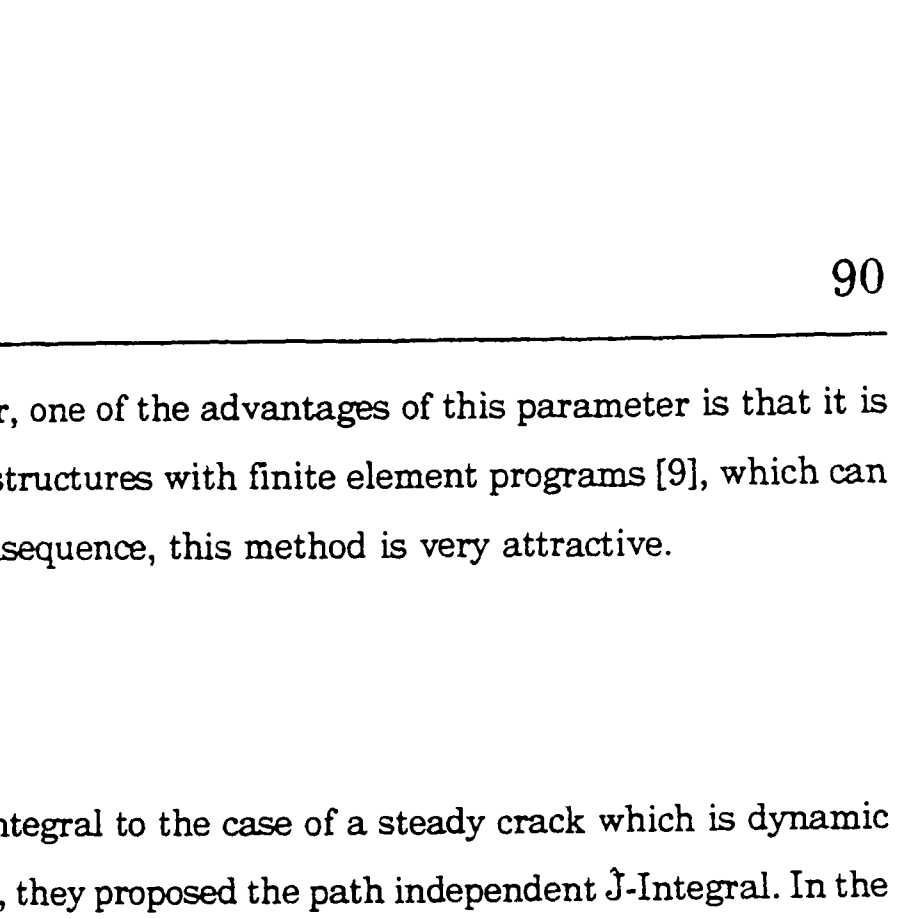


Figure 4.2 Dominion of definition of the $\hat{J}$-Integral.

The double integral of this equation represents the material inertia, which is neglected in the case of a quasi-static analysis. Thus, the equation is reduced to the J-Integral. On the contrary, when the crack is extending under dynamic loading, this equation becomes more complicated, because the term associated with the kinetic energy has to be taken into consideration.

The Ĵ-Integral has been interpreted as the rate of energy dissipated in the fracture process region corresponding to crack growth per unit of area. The authors have assumed that the fracture process region is independent upon body and crack geometries and loading conditions.

4.2.3 Numerical Evaluation of the J-Integral.

The J-Integral is calculated with the finite element method in the code ABAQUS. Before discussing the algorithm followed in the calculation of this parameter, a brief examination of the finite element method, as it affects the determination of dynamic fracture parameters, is presented in the following section.

4.2.3.1 Basic Principles of the Finite Element Method.

The finite element method is based on the assumption that a loaded structure can be divided into a finite number of elements, in which the state of stress is analyzed since an energetic point of view. Then, all the resultant equations are assembled and the loading and boundary conditions of the real structure are introduced to the system of equations in order to evaluate the nodal displacements. After the calculation of these parameters, the stresses and strains are obtained.

Following Zienkiewicz [11], consider that the displacements at any point within a finite element are defined by the column vector $\{f\}^a$, which is the product of general functions of position [N] and the nodal displacements $\{\delta\}$

$$\{f\} = [N]\{\delta\} = [N_1 \;\; N_2 \;\; \ldots \;\; N_n]\begin{Bmatrix}\delta_1\\ \delta_2\\ \cdot\\ \cdot\\ \cdot\\ \delta_n\end{Bmatrix} \qquad 4.6$$

where $\{\delta_i\}$ represents the displacements along each degree of freedom of each element node.

---

[a]Through this section, the convection that identifies column vectors with { } and row vectors with [ ], will be used

The resultant functions of position are

$$\{f\} = \begin{Bmatrix} u(x_1,x_2,...) \\ v(x_1,x_2,...) \end{Bmatrix}$$

Once the displacements at every point of the element are known, the strains can be obtained by the appropriate derivation of the matrix [N]

$$\{\epsilon\} = [B]\{\delta\} \qquad 4.7$$

The relation between stresses and strains, when general elastic behaviour is assumed, is the following

$$\{\sigma\} = [D](\{\epsilon\}-\{\epsilon_0\}) \qquad 4.8$$

in which $\{\varepsilon_0\}$ includes all the initial strains.

Now, assume that the potential energy of the system is expressed as

$$\phi = U + W$$

where the strain energy U is always positive and is the strain energy of the structure under a system of distributed loads {p} per unit of volume and concentrated loads {R}. W is the external work, which can take up positive or negative values.

The total potential energy of a finite element model is the sum of the potential energies contained within individual elements ϕ^e and the potential energy of the loads.

$$\phi = \sum \phi^e - \{R\}^T\{\delta\} - W_p$$

The minimum potential energy principle, which states that among all displacement configurations that satisfy internal compatibility and kinematic boundary conditions, those that also satisfy the equations of equilibrium make the potential energy a stationary value. If the stationary value is a minimum, the equilibrium is stable [12].

$$d[\phi] = 0$$

This expression is minimized with respect to the nodal displacements treated as variable parameters

$$\frac{\partial(\phi)}{\partial\{\delta_i\}} = 0$$

Then, the differentiation of the total potential energy is

$$\frac{\partial(\phi)}{\partial\{\delta_i\}} = \sum \frac{\partial(\phi^e)}{\partial\{\delta_i\}} - \{R_i\} - \frac{\partial W_p}{\partial\{\delta_i\}} \qquad 4.9$$

Considering equation 4.8, the strain energy within the element per unit of volume is

$$U^e = \frac{1}{2}\{\epsilon\}^T[E]\{\epsilon\} + \{\epsilon\}^T\{\sigma_0\} \qquad 4.10$$

and the energy due to the distributed loads per unit of volume is

$$W_p = \int [N]^T\{P\}\, d\,(vol)\{\delta_i\} \qquad 4.11$$

Equation 4.7 is substituted in 4.10 and with 4.11, differentiated with respect to the nodal displacements to obtain the minimized of the energy of an element e

$$\frac{\partial(\phi)^e}{\partial\{\delta_i\}} = \left(\int [B]^T[D][B]d(vol)\right)\{\delta\}^e - \int [B]^T[D]\{\epsilon_0\}d(vol) - \int [N]^T\{P\}d(vol)$$

The right term of this equation may be written in the following way

$$[k]^e\{\delta\}^e - \{F\}^e_{\epsilon_0} - \{F\}^e_p$$

for each finite element of the mesh, where $[k]^e$, $\{F\}_{\epsilon_0}^e$ and $\{F\}_p^e$ are the stiffness matrix, the nodal forces due to initial strain and the nodal forces due to distributed loads for each element. The resultant expression for the whole system is obtained with equation 4.9

$$\sum\left([k]^e\{\delta\}^e - \{F\}^e_{\epsilon_0} - \{F\}^e_p\right) - \{R_i\}$$

where, the vector $\{R_i\}$ represents the external concentrated forces.

The resultant system of equations of the whole system is expressed with the following simplified equation

$$[K]\{\delta\} = \{R\} + \{F\}_p + \{F\}_{\epsilon_0} = \{P\}$$

in which [K] is the stiffness matrix of the system, {δ} the column vector of the nodal displacements and {P} is the column vector of the external loads.

Turning now to the formulation of the finite element equations required for the dynamic analysis, the resultant dynamic force which acts on a node and in the absence of external forces, is

$$\{R_i\} = -M_i\frac{d^2f}{dt^2} = -M_i\{\ddot{\delta}_i\}$$

If the mass per unit of volume is ρ and assuming that it is distributed throughout the element, this inertial vector is

$$\{i\} = -\rho \frac{d^2 f}{dt^2} = \rho\{\ddot{f}\}$$

In accordance with equation 4.6, {f} can be expressed in terms of nodal displacements

$$\{i\} = -\rho [N]\{\ddot{\delta}\}$$

The inertial force of all the element is

$$\begin{aligned} \{F\}_i^e &= -\int [N]^T \{i\} d(vol) \\ &= -\left\{\int [N]^T \rho [N] d(vol)\right\} \{\ddot{\delta}\}^e \\ &= -[m]^e \{\ddot{\delta}\}^e \end{aligned}$$

Applying the d'Alambert principle, the general equation of dynamic "equilibrium" of the system is

$$[K]\{\delta\} = -[M]\{\ddot{\delta}\} + \{P\}$$

Regarding to the analysis of free vibrations, any external force is applied to the system. So, the last equation is reduced to the following form

$$[K]\{\delta\} = -[M]\{\ddot{\delta}\} \qquad 4.12$$

In this case, all the points of the system move in phase. So, the displacement is

$$\{\delta\} = \{\delta_0\} \sin \omega t$$

the second time derivative is

$$\{\ddot{\delta}\} = -\omega^2\{\delta\}\sin\omega t$$

when the last equation is substituted in 4.12, the typical eigenvalue relation of the natural frequency is obtained

$$\left([K]-\omega^2[M]\right)\{\delta_0\} = 0 \qquad 4.13$$

If the size of the matrices [K] and [M] are n x n, there will be n different values of the natural frequency, which are associated with a particular mode.

When viscous damping is included, the general equation is written in the following form

$$[M]\{\ddot{\delta}\}+[C]\{\dot{\delta}\}+[K]\{\delta\} = \{P\}$$

The term associated with the viscous damping may be interpreted as a force proportional to the velocity or to the first-time derivative of the displacements, which opposes to the motion. It has to be considered that this sort of damping is by no means the only type liable to develop. However, it is easy to introduce in the calculations and it can be considered as an approximation.

4.2.3.2 Evaluation of the J-integral with ABAQUS.

ABAQUS evaluates the J-Integral with the virtual crack extension method of Parks [13]. It is based on the energy comparison of two slightly different crack lengths in a cracked body, whose crack configuration is altered by changing nodal point positions. The initial balance of energy is obtained for the initial cracked structure and the energy of the case of the propagated crack is extrapolated.

Assuming that the evaluation of the potential energy can be obtained with the finite element model

$$P = \sum \int_{V_i} W dV_i - [T(X)]^t U$$

where the first term represents the sum of the strain energy density of all the finite elements in the mesh considered. Furthermore, T is the vector of nodal forces (obtained from consistent distribution of the prescribed traction and/or body forces), and X and U are the vectors of nodal point coordinates and displacements respectively. The last expression may also be expressed as

$$P = \sum W_i(X,U) - [T(X)]^t U$$

W_i depends on the nodal coordinates and displacements. Similarly, the nodal force vector depends on nodal coordinates through the shape functions.

The virtual crack extension of the crack is obtained by moving a distance δl all the nodes within the contour Γ_0 in the direction x, as shown in figure 4.3 The nodes between Γ_0 and Γ_1 are advanced by appropriately reduced amounts so as to maintain proper element geometry in the new configuration.

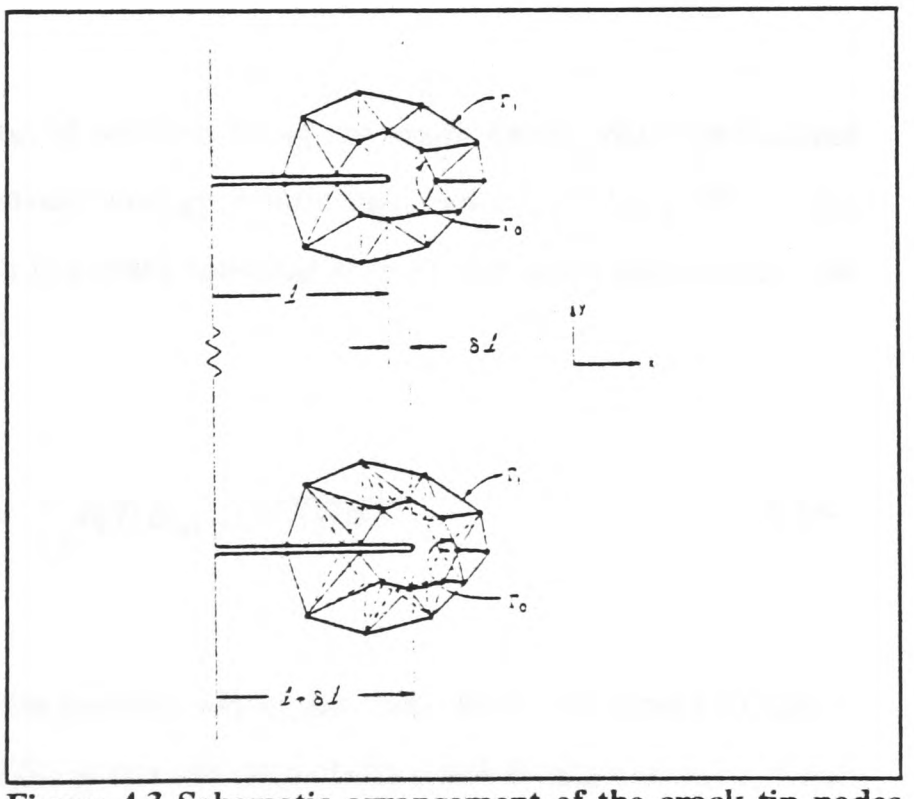


Figure 4.3 Schematic arrangement of the crack tip nodes after a virtual crack extension δl. After Parks [13].

The variation of the potential energy of the system due to the virtual crack extension is sum of the variation of the potential of each element of the resultant mesh.

$$\delta P = \sum \left[\left(\frac{\partial W_i}{\partial X} \right)^t \delta X + \left(\frac{\partial W_i}{\partial U} \right)^t \delta U \right] - T^t \delta U - U^t \left(\frac{\partial T}{\partial X} \right) \delta X$$

$$\delta P = \left[\sum\left(\frac{\partial W_i}{\partial U}\right)^t - T^t\right]\delta U + \left[\sum\left(\frac{\partial W_i}{\partial X}\right)^t - U^t\left(\frac{\partial T}{\partial X}\right)\right]\delta X$$

Considering that the displacements δU and the variation of the nodal forces T are very small, the first term vanishes and the second term is reduced. Besides, J is defined as the decrease of the potential energy.

$$-\delta P = -\left(\frac{\partial P}{\partial l}\right)\delta l = J\delta l = -\sum\left(\frac{\partial W_i}{\partial X}\right)^t \delta X$$

A generalization of the last expression is

$$-\delta P = \int_S J(S)\,\delta l(S)\,dS = -\sum\left(\frac{\partial W_i}{\partial X}\right)^t \delta X$$

In ABAQUS, J is interpreted as a function of position along the crack front, which calculates the decrease in total potential energy (strain energy minus load potential) $\Delta_{(VCE)}$ (P) of the loaded structure caused by an increase in the crack opening area at the same position on the crack front with the following expression

$$-\Delta_{VCE}(P) = \int_S J(S)\,\Delta_{VCE}(l(S))\,dS \qquad 4.14$$

where S is a coordinate which identifies the position along the crack front, as shown in figure 4.4, J(S) is the J-integral value and Δ_{VCE}(l(S)) is the advance of the crack front, normal to itself and in the plane of the crack at a certain point.

An evaluation is made at each node of the crack front. Hence, a set of linear equations is obtained, which relate the total potential energy changes caused by crack advance at each front nodal position to the J-integral values at the original crack front.

The J-integral may be evaluated by moving either the crack tip nodes or all the nodes within

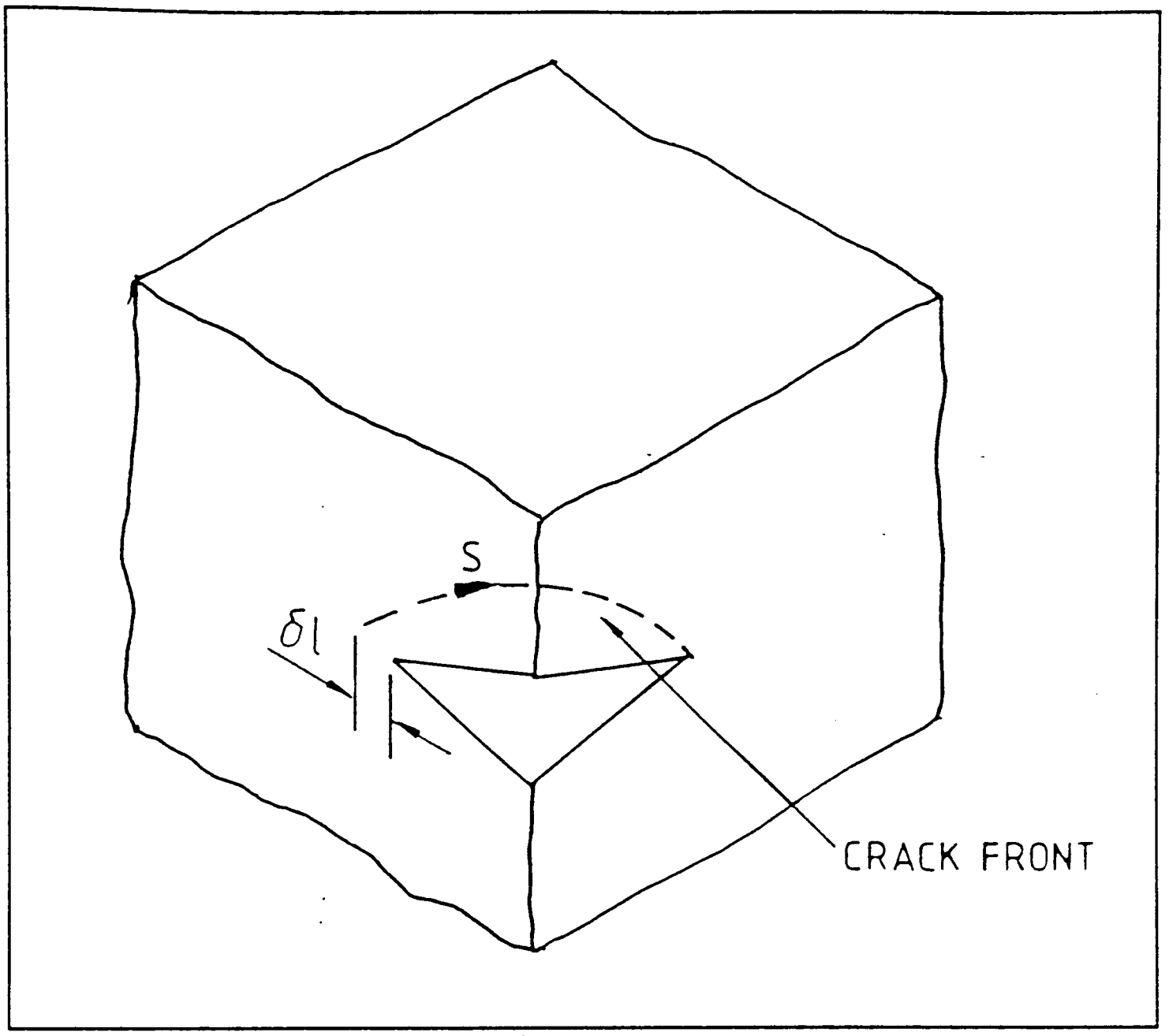


Figure 4.4 Virtual crack advance. After [9].

some closed contour around the crack tip in a section of the mesh corresponding to a particular crack front nodal position. Such multiple contour evaluation is provided automatically within the code and, in accordance with [14], accurate results are obtained in the last case. Agreeing with the recommendations in [15], the second contour gives the most accurate evaluation.

The accuracy of the J-Integral evaluation with ABAQUS was studied with the analysis of a rectangular plate, which has a through thickness central crack. It is under tensile stress (5 MPa) and its dimensions are shown in figure 4.5. The direction of the applied stress is perpendicular to the crack plane. For this purpose, the whole plate was modelled with a coarse mesh of 54 finite elements, as shown in figure 4.6.

Two solutions with different elements were obtained. In the first analysis, the mesh was filled with C3D20 elements, which are brick elements with full integration. In the second case, the reduced integration elements C3D20R were used. It has to be noted that those elements that

are along the longest axis of symmetry are thin. However, numerical singularities are unlikely.

Each time the crack tip was modelled with two rings of eight elements and the mechanical properties assigned to this model are those that correspond to PMMA reported in section 3.2. A detail of the crack tip elements is shown in figure 4.7. Regarding with the boundary conditions, the symmetry of the geometry and load was considered. Thus, those nodes, which are in the intersection of the longest lateral surfaces and the crack plane were fixed.

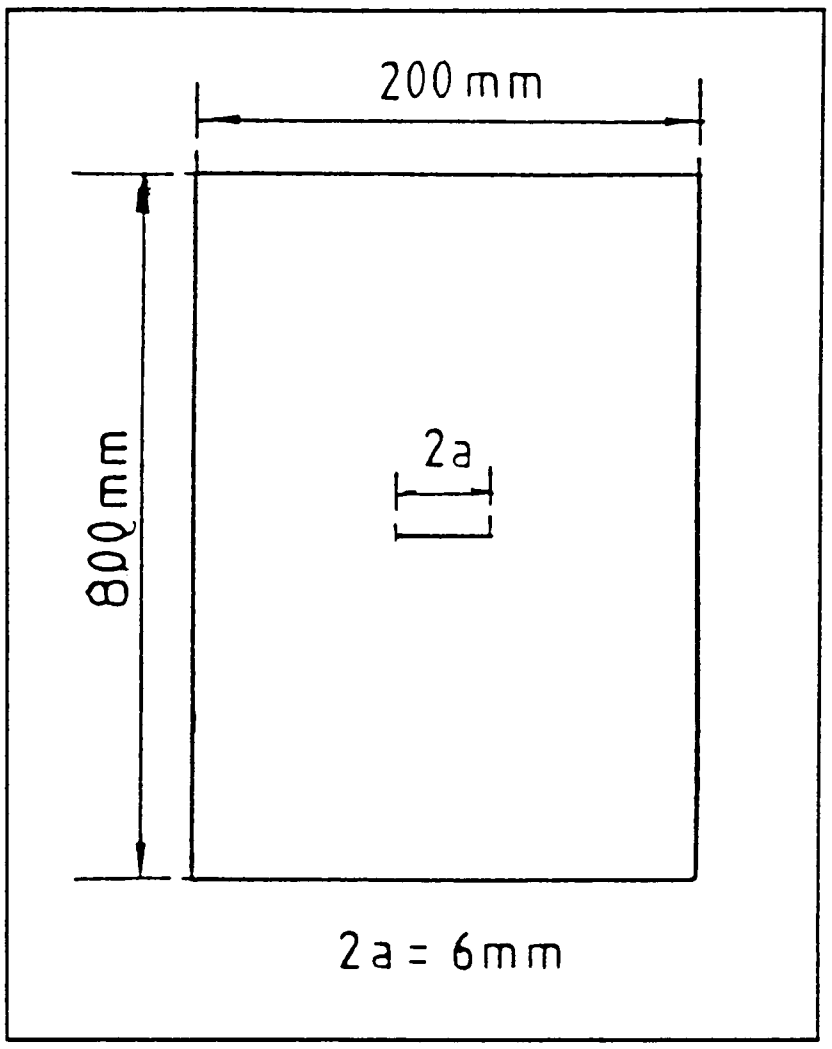


Figure 4.5 Cental cracked plate (thickness = 3 mm).

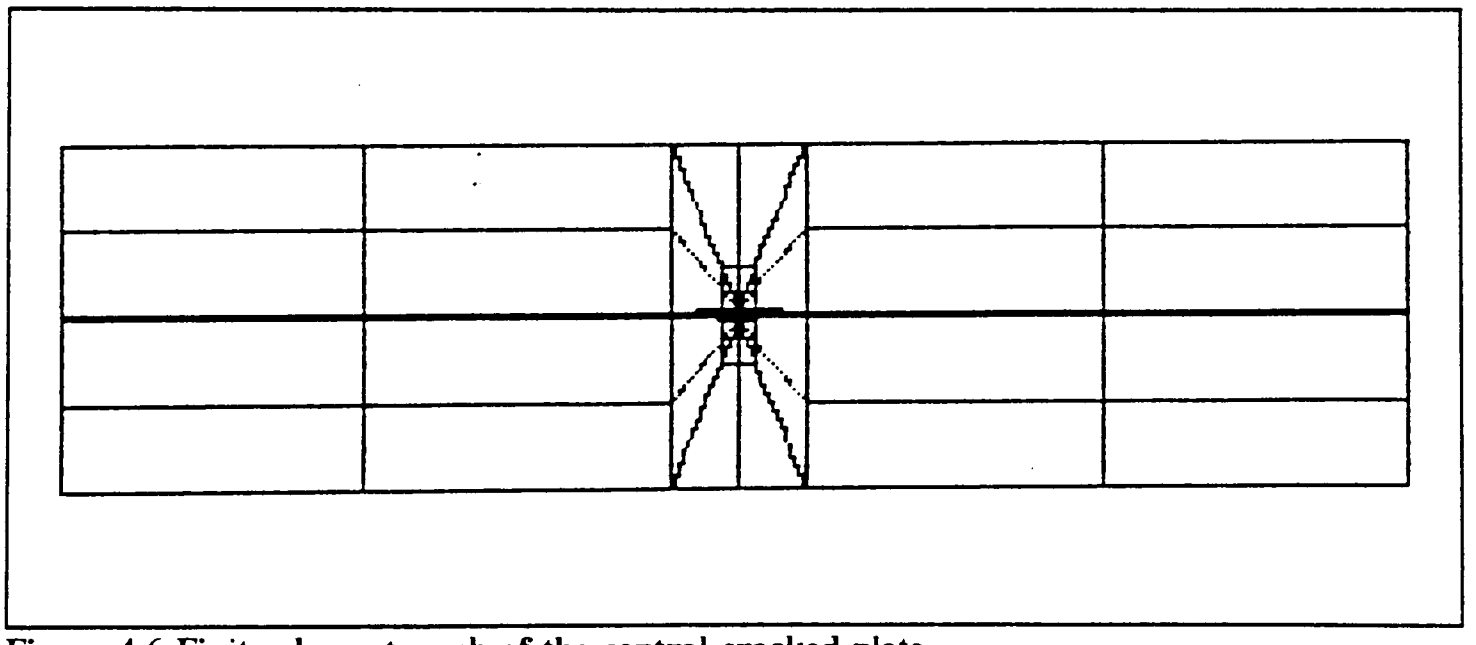


Figure 4.6 Finite element mesh of the central cracked plate.

The results obtained have been compared with the three analytical solutions proposed in [9] for the case shown in figure 4.8, in which the geometrical factor Y is evaluated with the relations discussed in [9] and proposed by Brown

$$Y = 1 + 0.256(\frac{a}{W}) - 1.152(\frac{a}{W})^2 + 12.200(\frac{a}{W})^3$$

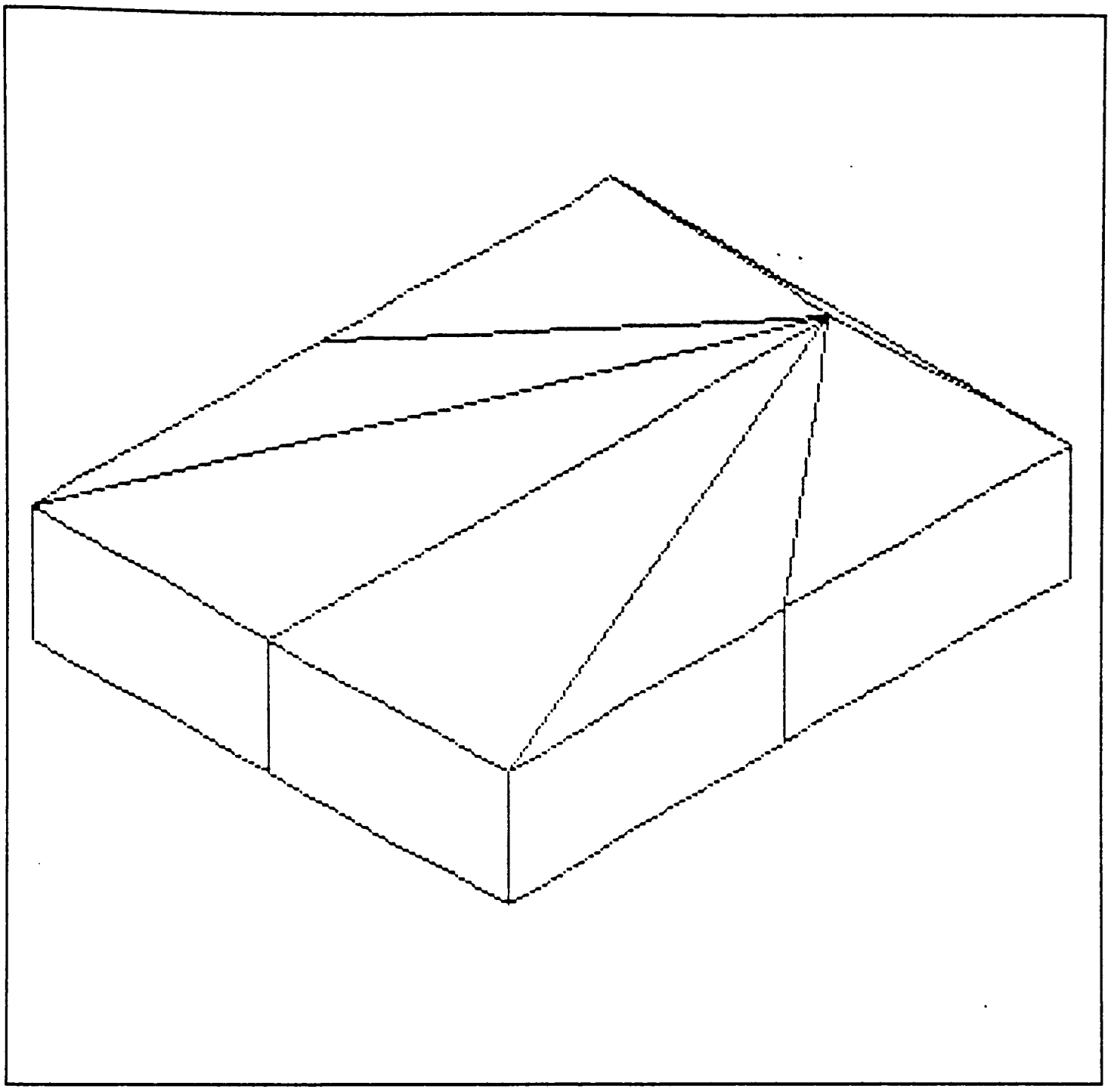


Figure 4.7 Detail of the crack tip elements.

Feddersen,

$$Y = \sqrt{\sec\frac{\pi a}{W}}$$

and Dixon

$$Y = \frac{1}{\sqrt{1-(\frac{2a}{w})^2}}$$

Regarding the ABAQUS solution, a state of plane strain was assumed and the SIF was calculated with equation 4.4. The following table compares all the evaluations.

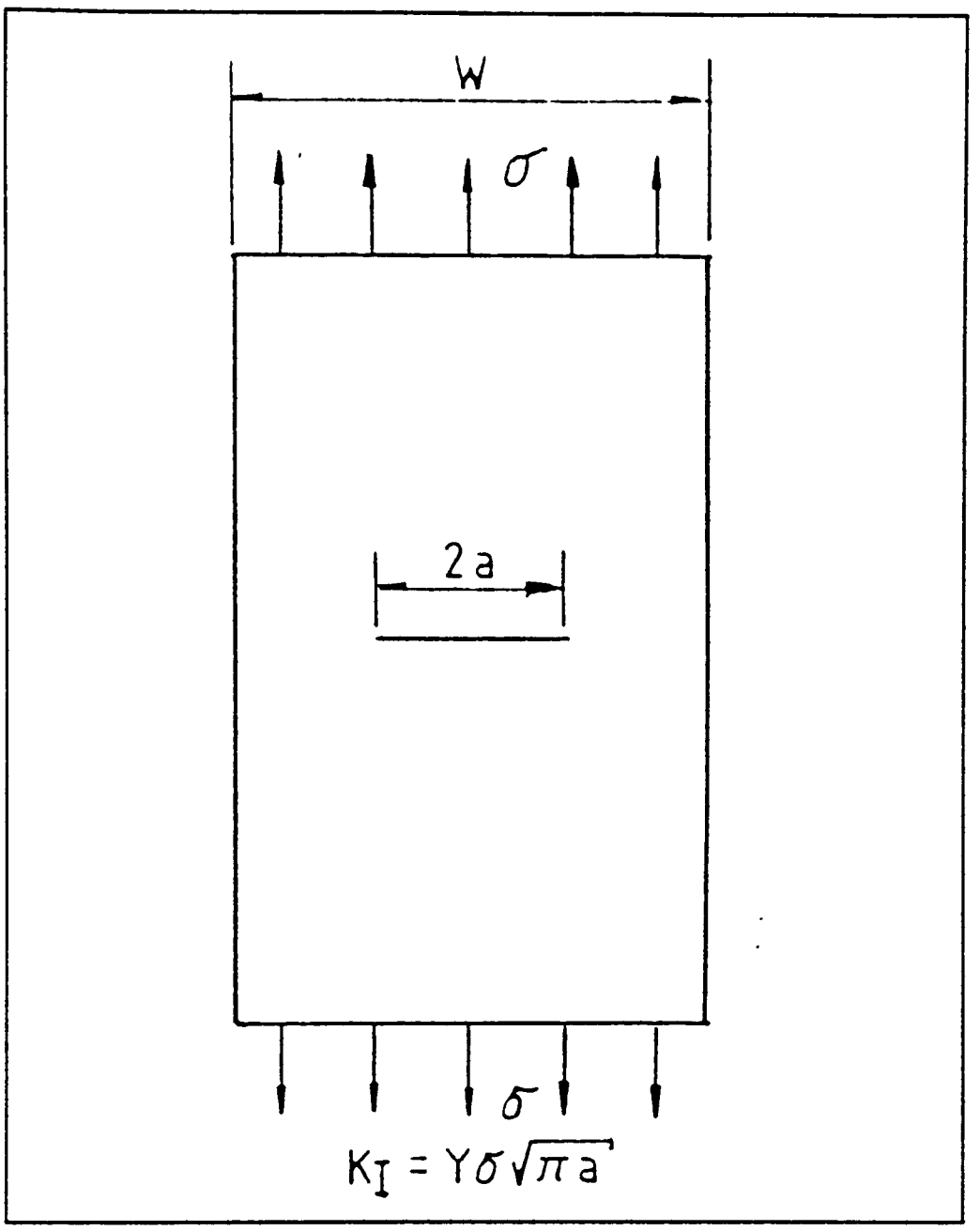


Figure 4.8 Rectangular central cracked plate under uniform tension stress.

TABLE 4.1
COMPARISON OF THE SIF EVALUATED WITH FINITE ELEMENT METHOD AND STANDARD SOLUTIONS

METHOD OF CALCULATION	K (MPa $(m)^{1/2}$)
ABAQUS with C3D20 elements (1st contour)	0.389
ABAQUS with C3D20 elements (2nd contour)	0.536
ABAQUS with C3D20R elements (1st contour)	0.723
ABAQUS with C3D20R elements (2nd contour)	0.539
Geometrical factor proposed by Brown	0.511
Geometrical factor proposed by Feddersen	0.485
Geometrical factor proposed by Dixon	0.509

The SIF evaluated with the standard solutions is around 0.5 MPa $m^{1/2}$, while the evaluation of ABAQUS along the second contour is 0.53 MPa $m^{1/2}$. However, an underestimated result is obtained with the first contour using C3D20 elements. Alternatively, the result with a grid of C3D20R is overestimated. Thus, the calculation of the SIF along the second contour gives the best solution.

4.3 Analysis of the Standard Solutions to the Problem of a Central Cracked Plate under Uniform Bending.

The SIF characterizes the stress field at the crack tip in a linear-elastic body with brittle behaviour. Consequently, the evaluation of the singular stress field at the crack tip is required. As pointed out by Gdoutos [16], it can be calculated mathematically from three basic methods, namely, the semi-inverse, the eigen-function expansion and the complex potentials. The first was developed by Westergaard [17,18] and is based on a complex representation of the Airy stress function. The second method was introduced by Williams [19] and the third was developed by Muskhelishvili [20]. With these methods, closed-form solutions have been established for a limited number of problems, which are related with infinite plates. Nonetheless, when the size of the crack is small compared to other dimensions of the body, these analytical solutions may be used. Their great disadvantage is that in the analysis of finite cracked bodies, the satisfaction of the boundary conditions is difficult and in the case of three dimensional bodies, their application becomes intractable.

Regarding the analysis of infinite cracked plates with a central crack through thickness, two bending theories have been used to study the stress field at the crack tip, namely, the Kirchhoff and Reissner theories.

4.3.1 Evaluation of the Stress Intensity Factor with the Theory of Kirchhoff.

Williams [21] based his analysis on the Kirchhoff-Poisson theory of thin plates and obtained the asymptotic behaviour of the bending stresses at the crack tip, of an infinite central cracked plate under bending, using the method of eigenfunction expansion.

According to figure 4.9, an infinite plate of thickness h with a trough crack has been considered. Its front is along the oz direction and the xy plane bisects the plate thickness. The

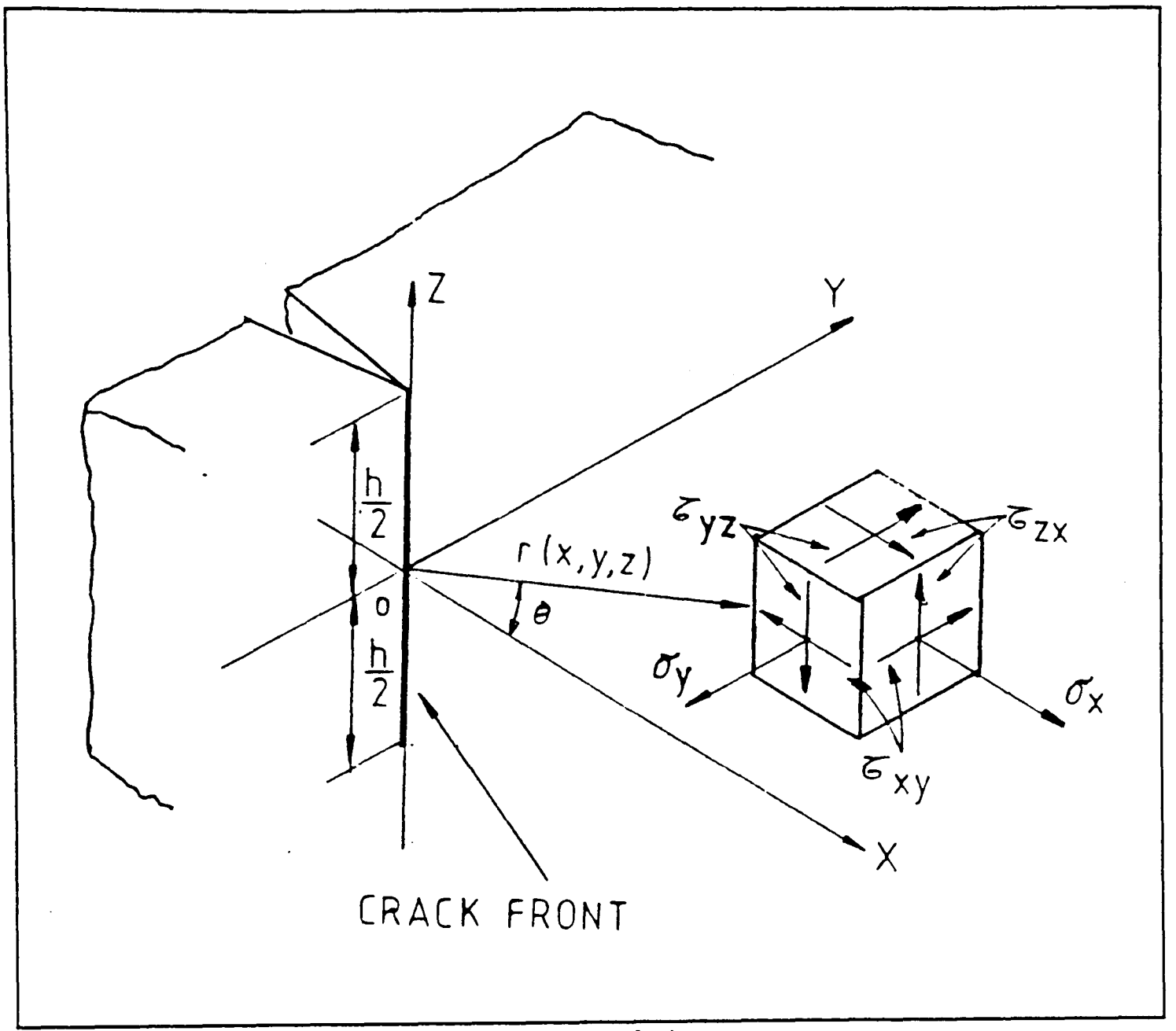


Figure 4.9 Stresses on an element close to the crack tip.

in-plane stresses σ_x, σ_y and τ_{xy}, which act on an element, are assumed that vary linearly along the thickness, while the shear stresses τ_{xz} and τ_{yz} change parabolically with z coordinate.

The boundary conditions along the crack plane are

$$M_y(x,0) = M_{xy}(x,0) = Q_y(x,0) = 0$$

However, the effect of the transverse shear deformation is neglected and the last two boundary conditions are replaced by a single one

$$Q_y(x,0) + \frac{\partial M_{xy}(x,0)}{\partial x} = 0$$

A set of equations that contained two unspecified constants was obtained. Later, they were defined by Sih et. al. [22] in terms of bending and shear stress intensity factors, which were calculated with a complex variable formulation.

The same problem was treated by Sih [23] who found that the stress field is given by

$$\sigma_x = -\frac{1-\nu}{2(3+\nu)}\frac{K_I z}{h\sqrt{2\pi r}}\left[3\cos\frac{\theta}{2}+\cos\frac{5\theta}{2}\right] + \frac{1-\nu}{2(3+\nu)}\frac{K_{II} z}{h\sqrt{2\pi r}}\left[\sin\frac{5\theta}{2}-\left(\frac{9+7\nu}{1-\nu}\sin\frac{\theta}{2}\right)\right]+O(r^{o})$$

$$\sigma_y = +\frac{1-\nu}{2(3+\nu)}\frac{K_I z}{h\sqrt{2\pi r}}\left[\cos\frac{5\theta}{2}+\left(\frac{11+5\nu}{1-\nu}\right)\cos\frac{\theta}{2}\right] + \frac{1-\nu}{2(3+\nu)}\frac{K_{II} z}{h\sqrt{2\pi r}}\left[\sin\frac{\theta}{2}-\sin\frac{5\theta}{2}\right]+O(r^{o})$$

$$\sigma_z = 0$$

$$\tau_{xy} = -\frac{1-\nu}{2(3+\nu)}\frac{K_I z}{h\sqrt{2\pi r}}\left[\sin\frac{5\theta}{2}+\left(\frac{7+\nu}{1-\nu}\right)\sin\frac{\theta}{2}\right] + \frac{1-\nu}{2(3+\nu)}\frac{K_{II} z}{h\sqrt{2\pi r}}\left[\frac{5+3\nu}{1-\nu}\cos\frac{\theta}{2}-\cos\frac{5\theta}{2}\right]+O(r^{o})$$

$$\tau_{yz} = -\frac{1}{2(3+\nu)}\frac{(h^2-4z^2)\pi}{h(2\pi r)^{3/2}}\left[K_I\sin\frac{3\theta}{2}+K_{II}\cos\frac{3\theta}{2}\right]+O(r^{-1})$$

$$\tau_{xz} = \frac{1}{2(3+\nu)} \frac{(h^2-4z^2)\pi}{h(2\pi r)^{3/2}} \left[-K_I \cos\frac{3\theta}{2} + K_{II} \sin\frac{3\theta}{2} \right] + O(r^{-1})$$

where K_I and K_{II} are bending stress intensity factors that depend on the load and geometry.

Erdogan et. al. [24], based on the analysis of Williams [21], have proposed the following relation for the evaluation of the SIF in an infinite flat plate under cylindrical bending.

$$K_I = \frac{6M_0}{h^2}\sqrt{a}\sin^2\beta$$

where $6M_0/h^2$ is the bending stress on the surface of the plate at infinity and, in accordance with figure 4.10, the angle β defines the direction of the crack plane, which is 90° for the present analysis.

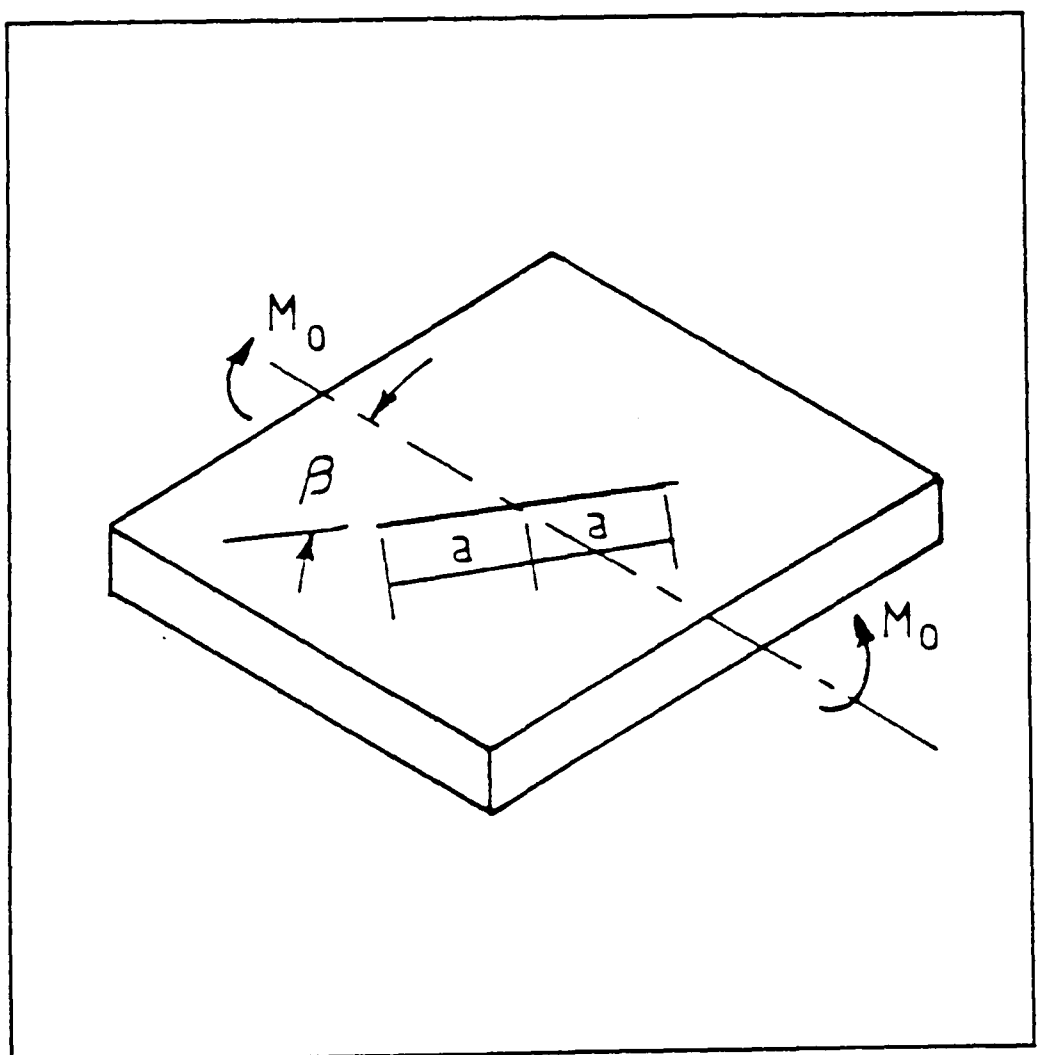


Figure 4.10 Infinite cracked plate under uniform bending.

Alternatively, Gdoutos [16] has proposed the following equation for the same case

$$K_I = \frac{6M_0}{h^2}\sqrt{\pi a} \qquad 4.15$$

The main difference between the last two equations is the constant $\pi^{1/2}$. To this respect, Kanninen [7] has mentioned that this factor has been incorporated artificially in the definition of the SIF, in order to simplify the calculation of energy release rate. So, both equations are equivalent. For consistency and following the generally accepted convention, equation 4.15 will be used.

Turning to the equations that evaluate the stress field at the crack tip, Gdoutos [16] has observed that

- The in-plane stresses σ_x, σ_y and τ_{xy} depend on the Poisson's ratio.

- The transverse shear stresses τ_{yz} and τ_{xz} have a singularity of the order $r^{-3/2}$, which is inconsistent with the singularity $r^{-1/2}$.

- The normal stress σ_z is everywhere zero, while along the crack front in most of the interior region, except near the surface, it should satisfy the plane strain condition.

- For symmetrical loading ($K_I = 0$) the ratio of the stresses σ_x and σ_y along the crack plane is $-(1-\nu)/(3+\nu)$. In the extensional case this relation is equal to the unity. Williams [21] concluded that more yielding might be expected as the percentage of bending to extension stress at the crack increases.

Consequently, an approximate evaluation of the SIF is made with these equations.

4.3.2 Evaluation of the Stress Intensity Factor with the Theory of Reissner.

Another mathematical analysis has been carried by Hartranft et. al. [25] for the problem of a central cracked plate under uniform bending. In fact, it is a generalization of the results of Knowles et. al. [26], who evaluated the SIF of an infinite plate, whose thickness is vanishingly

small. In both cases, the solution is based on the sixth-order theory of Reissner and the stress free crack surface conditions are completely satisfied. Another advantage, over the solution of Williams [21], is that in [25] the effect of the crack size and thickness over the SIF is evaluated.

The resultant stresses at the neighbourhood of the crack tip are the following

$$\sigma_x = \frac{K_I}{\sqrt{2\pi r}}\cos\frac{\theta}{2}\left(1-\sin\frac{\theta}{2}\sin\frac{3\theta}{2}\right) - \frac{K_{II}}{\sqrt{2\pi r}}\sin\frac{\theta}{2}\left(2+\cos\frac{\theta}{2}\cos\frac{3\theta}{2}\right)+O(1)$$

$$\sigma_y = \frac{K_I}{\sqrt{2\pi r}}\cos\frac{\theta}{2}\left(1+\sin\frac{\theta}{2}\sin\frac{3\theta}{2}\right) + \frac{K_{II}}{\sqrt{2\pi r}}\sin\frac{\theta}{2}\cos\frac{\theta}{2}\cos\frac{3\theta}{2}+O(1)$$

$$\sigma_z = 2\nu\left[\frac{K_I}{\sqrt{2\pi r}}\cos\frac{\theta}{2} - \frac{K_{II}}{\sqrt{2\pi r}}\sin\frac{\theta}{2}\right]+O(1)$$

$$\tau_{xy} = \frac{K_I}{\sqrt{2\pi r}}\sin\frac{\theta}{2}\cos\frac{\theta}{2}\cos\frac{3\theta}{2} + \frac{K_{II}}{\sqrt{2\pi r}}\cos\frac{\theta}{2}\left(1-\sin\frac{\theta}{2}\sin\frac{3\theta}{2}\right)+O(1)$$

$$\tau_{xz} = -\frac{K_{III}}{\sqrt{2\pi r}}\sin\frac{\theta}{2}+O(1)$$

$$\tau_{yz} = \frac{K_{III}}{\sqrt{2\pi r}}\cos\frac{\theta}{2} + O(1)$$

where K_I and K_{II} are the moment intensity factors and K_{III} is the shear force intensity factors. It is important to observe that all the stress equations are affected by $r^{-1/2}$ singularity.

Hartranft and Sih [25] have proposed that K_I can be evaluated with the following algebraic expression

$$K_I = \Phi(1)\,\sigma_0\sqrt{a}$$

where σ_0 is the bending stress, a is the half crack length and $\Phi(1)$ is the solution of the Fredholm integral equation at the crack tip. The last parameter takes into account the effect of the plate thickness and has been evaluated numerically in [25] for different values of Poisson's ratio. Figure 4.11 shows a graph in which the numerical solution of this integral is related with the dimensionless parameter λ, that associates the half crack length with the thickness of the plate.

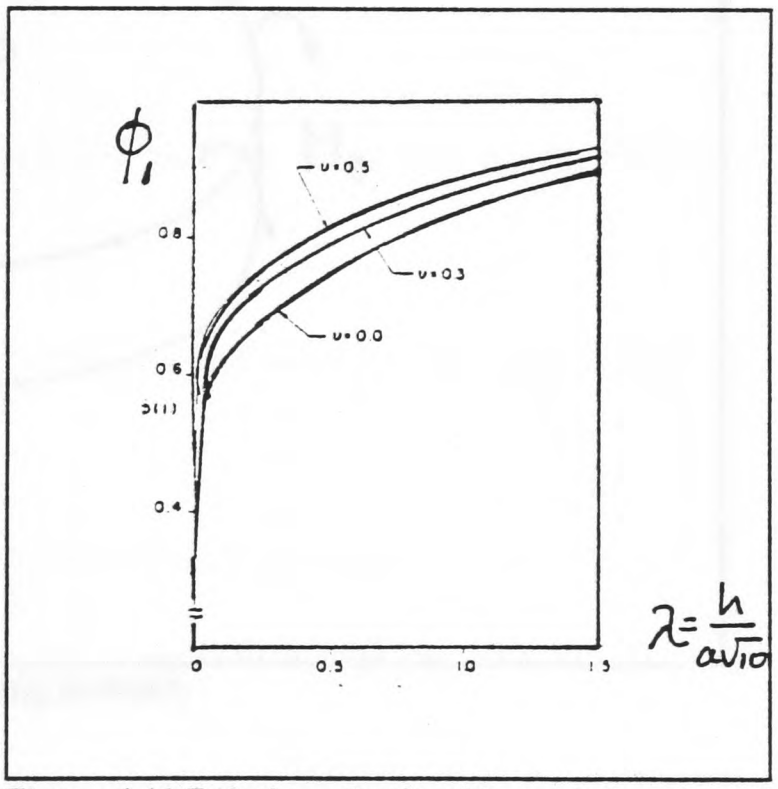


Figure 4.11 Relation of $\phi(1)$ with crack length and thickness of an infinite plate under bending. After Hartranft et. al. [25].

In the analysis of this graph, it is found that in the limit, when the thickness → 0, $\Phi(1) \rightarrow (1+\nu)/(3+\nu)$, which is the value of the geometrical parameter obtained in [26]. Alternatively, when the thickness of the plate increases, providing that the crack size remains constant, $\Phi(1)$ increases.

In the open literature, the bending SIF for a plate under uniform bending has been quoted with the equation evaluated in the lower limit, as in [27], which considers the case of a rectangular plate, which is centrally cracked and loaded under uniform bending. This situation is also observed in [28], in which the following equation is proposed for the evaluation of the

stress intensity factor of a cracked plate subjected to a uniform bending moment as shown in figure 4.12,

$$K_I = \left(\frac{1+\nu}{3+\nu}\right)\sigma\sqrt{\pi a} \qquad 4.16$$

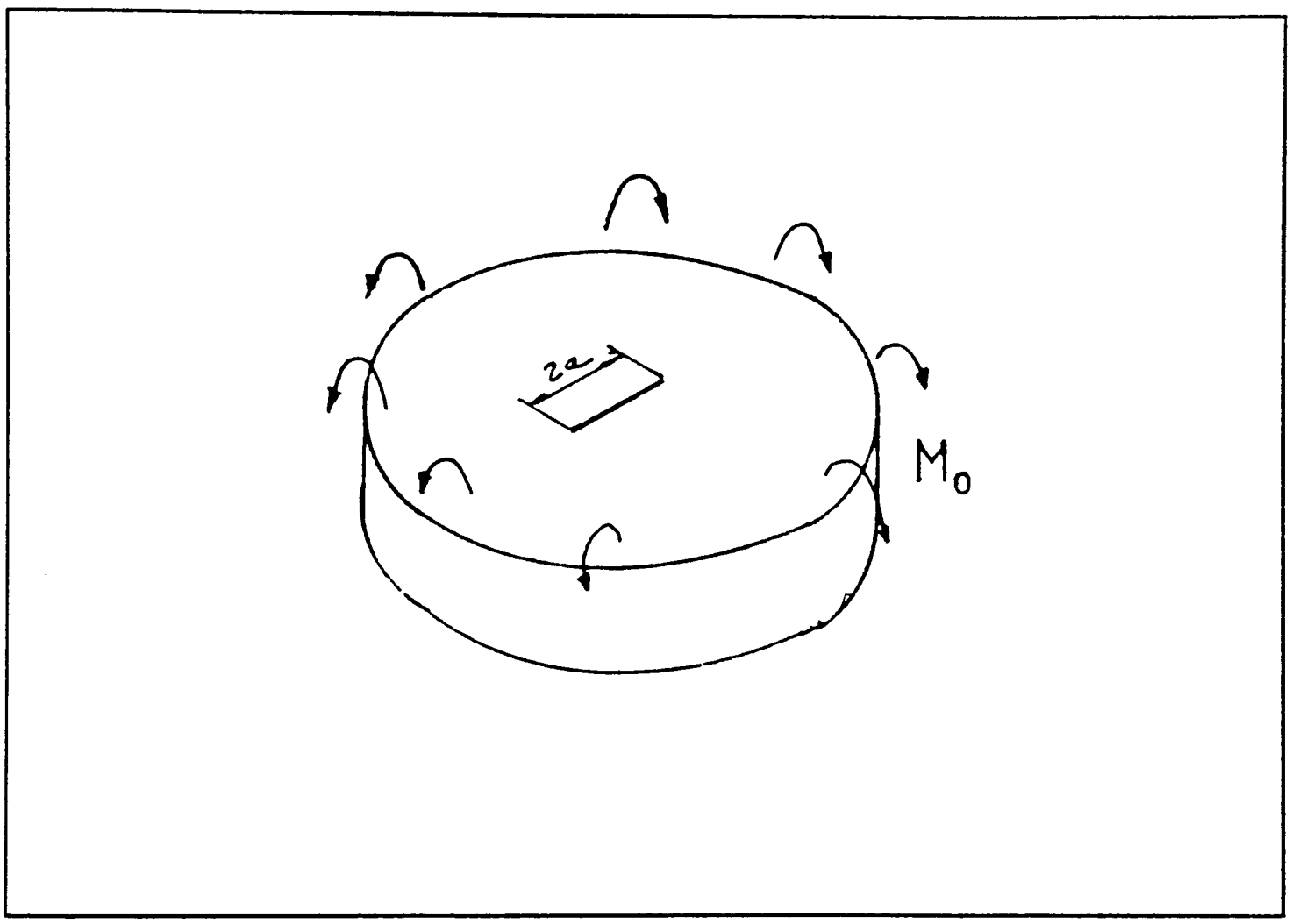


Figure 4.12 Cracked plate under uniform bending moment.

which, in fact, is evaluated at the limit, namely, when the plate thickness → 0. This equation may be corrected, by changing the constant coefficient with the value of the parameter $\Phi(1)$. The resultant equation is the one proposed in [25] multiplied by $\pi^{1/2}$. So, the new expression is

$$K_I = \Phi(1)\,\sigma\sqrt{\pi a} \qquad 4.17$$

4.4 Applications to the Problem in Hand.

The fracture toughness of the crack initiation tests under dynamic loading conditions has been calculated with three different procedures, namely

Case I	Dynamic stress analysis using the modal superposition method in conjunction with standard solutions.
Case II	Quasi-static evaluation of the J-Integral considering only the crack initiation load.
Case III	A complete dynamic analysis following the J-Integral and the dynamic direct integration methods.

while for those cases in which the specimens were tested under static conditions, the following procedures were followed

Case IV	Static stress analysis using the finite element method in conjunction with standard solutions.
Case V	Static stress analysis following the J-Integral method.

4.4.1 Analysis of a Plate without a Crack.

The dynamic elastic response of a circular plate has been analyzed by simulating the variation of its membrane strains at the centre when it is impacted with the loading cases selected in section 2.4.2. This evaluation has been done with the modal superposition dynamic analysis, which is implemented within the code ABAQUS. Its fundamental concept is based on the fact that the response of the structure is expressed in terms of a relatively small number of eigenmodes of the system [14]. The orthogonality of the eigenmodes uncouple the system, generating a set of independent equations for each mode of vibration. When each mode response has been determined, they are superimposed and the displacements are obtained. Only a few modes are required in order to get an accurate estimate, making this procedure computationally inexpensive. Finally, the stresses and strains are evaluated directly from the

displacements [29].

At first glance, the geometry of the plate and the distribution of the loads suggest that the problem can be analyzed with a mesh that models only one quarter of the plate with shell elements, like the one illustrated in figure 4.13.

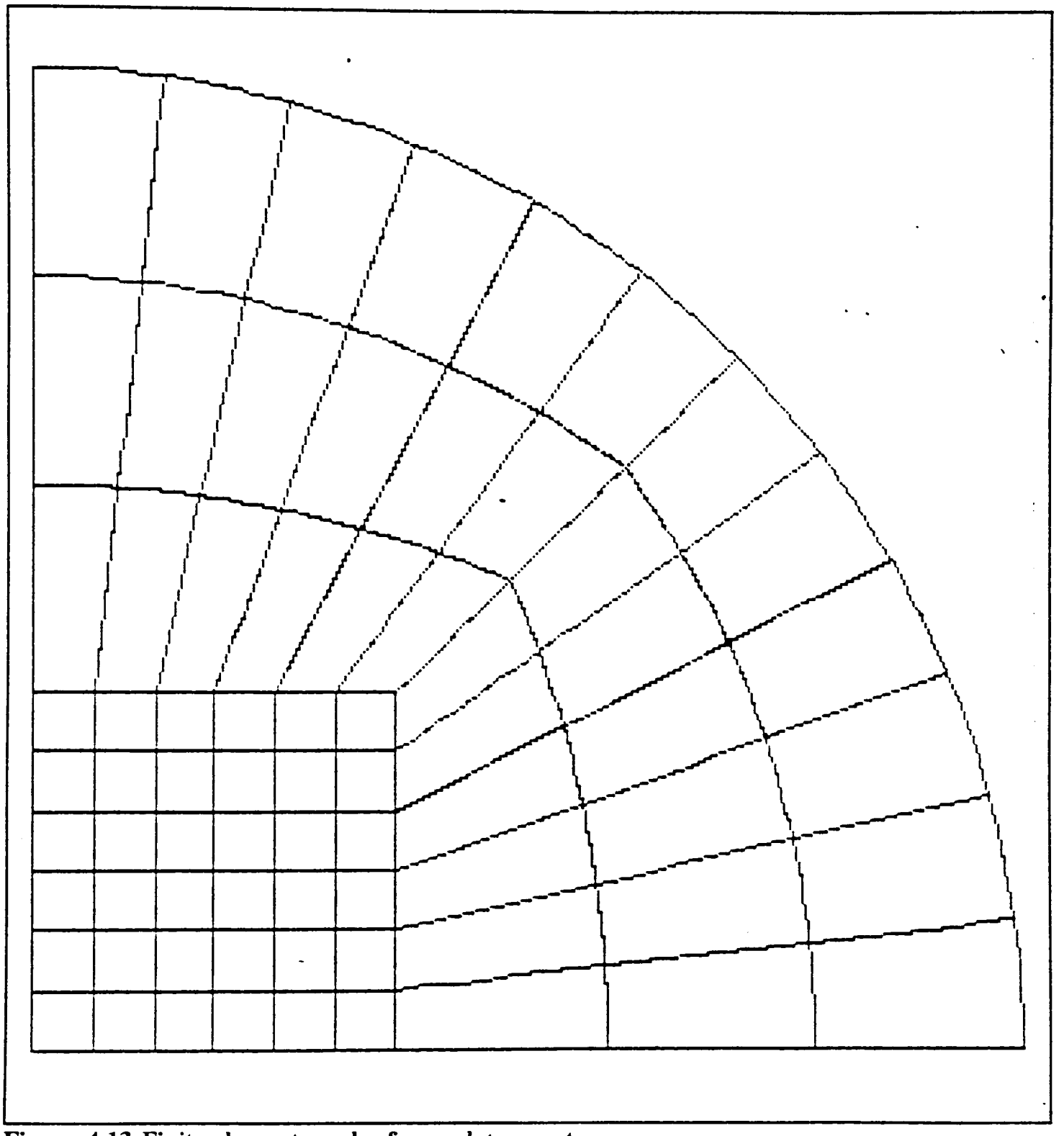


Figure 4.13 Finite element mesh of one plate quarter.

This grid was used in the preliminary analyses and four main conclusions were obtained. Firstly, this mesh is a stiff model, because the imposed boundary conditions that simulated the effect of the symmetrical parts affects the response of the plate. The improvement of the solution was unlikely when the number of finite elements was increased or the time increment

was reduced. On the contrary, the computing time was increased. Thus, this situation was improved when the whole plate was analyzed. Secondly, the boundary conditions strongly affect the results obtained. So, a systematic analysis, based on experimental evidence, is required in order to select the proper boundary conditions. Thirdly, ABAQUS does not perform fracture mechanics analysis when a mesh of shell elements is loaded over its principal plane with pressure loading. In consequence, the advisable alternative is to use brick elements. Finally, in order to avoid numerical problems, the mesh should be made with well shaped brick elements in critical regions. According to [14], there is the risk of introducing constraint variables, when tetrahedron and wedge elements are used in these areas.

The library of solid elements within ABAQUS has isoparametric elements of first and second order of interpolation. The first order elements are essentially constant strain elements, while the second order elements, which is the highest order available, model linear strain field and are recommended in the analysis of relatively thin members subjected to bending.

With respect to the fracture mechanics analysis, the second order isoparametric can be degenerated, in such way that the $r^{-1/2}$ singularity of the stress field at the crack tip is obtained through the use of the quarter point technique, which requires that the mid-side nodes are displaced at 1/4 of the distance along the side from the node at the singularity. Considering these arguments, the C3D20 brick elements of 20 nodes was selected.

All the finite element calculations have been performed in a CONVEX C220 computer, which has a 128 Mb main memory and its operating system is CONVEX OS version 8.1. This vectorizing mini-supercomputer is virtual-memory and is good for fast processing of DO loops in FORTRAN and C programs, which are computational-intensive or with large memory requirements.

4.4.1.1 Characteristics of the Finite Element Mesh.

The analysis of the whole specimen implies the introduction of the contact effect among the specimen, the external flange and the bolts on the calculation, making the evaluation more complex because the use of contact elements is required. It was assumed that the strain field in the central region is not affected by this edge conditions. So, the finite element analysis was simplified by modelling only the section of the specimen, which is inside the internal circle of

the external flange. As a result, a grid of 96 elements which represents a plate of 165 mm diameter and 3 mm thick was obtained, as shown in figure 4.14. In all these analysis, the physical and quasi-static mechanical properties of PMMA, which are reported in section 3.2, were considered.

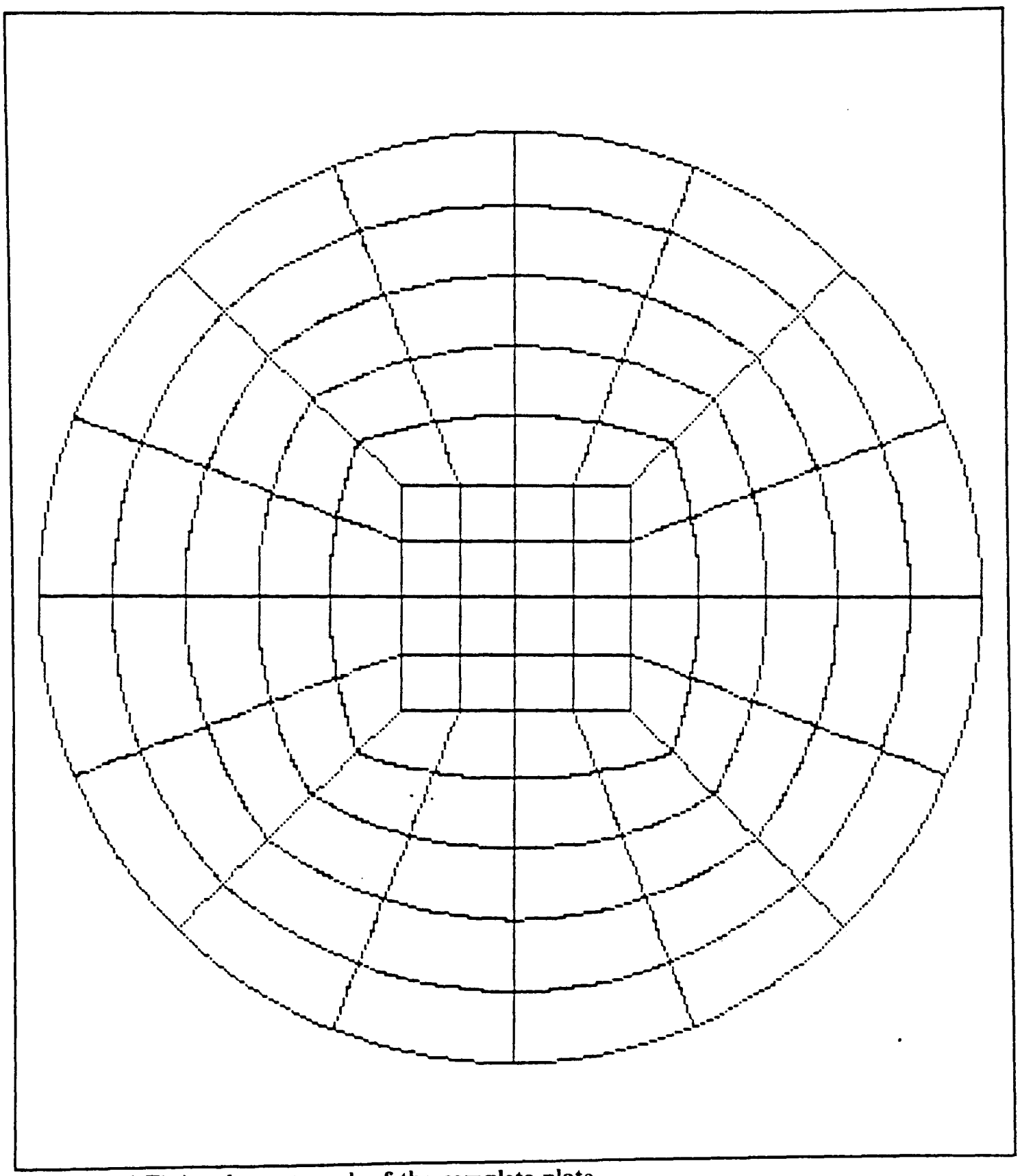


Figure 4.14 Finite element mesh of the complete plate.

In order to avoid problems in the numerical evaluation, the central part was modelled with 16 well shaped elements and out of this region, the geometry of the elements was affected gradually. So, the external row of elements conform with the circular boundary of the plate.

4.4.1.2 Selection of the Boundary Conditions of the Finite Element Model.

The specimens, in the dynamic tests, are fixed to the impact testing apparatus in such way that they are neither simple supported nor clamped. As a result, the selection of the boundary conditions is not straightforward. In consequence, an analysis was carried on to identified a parameter that change with the boundary conditions. It was noticed that the natural frequency is sensitive to the edge conditions. This situation was confirmed with the study of the analytical evaluation of the natural frequency of plates of constant thickness made of materials which are perfectly elastic, homogeneous and isotropic [30]. Furthermore, this dynamic parameter can be measured experimentally.

Accordingly, a procedure for the selection of the boundary conditions was established based on experimental analysis. Initially, the natural frequency of the specimens fixed onto the impact testing apparatus was evaluated experimentally. Then, this parameter was calculated numerically with the finite element grid described above varying its boundary conditions. Finally, both evaluations were compared and the model which gives the most accurate results was selected. The same procedure was followed with the specimens tested in static conditions.

4.4.1.2.1 Experimental Evaluation of the Natural Frequency of the Specimens.

A circular plate, 3 mm thickness and made of PERSPEX, was fixed onto the impact testing apparatus in the same way as the cracked specimens when tested under dynamic conditions. Then, an accelerometer Brüel & Kjær model 4344 was installed at the centre of the specimen and connected to a Tektronix 2211 oscilloscope.

The specimen was struck with a small hammer. As a result, it oscillated at its natural frequency. The accelerometer picked up the plate vibration and emitted a signal which triggered the set-up. The data was registered and the resultant wave was displayed on the scope screen. Its frequency was measured from the trace with the scope cursor. After the repetition of the results was confirmed, several readings were taken. Finally, an average value of 196 Hz was obtained.

The same procedure was repeated for a clamped specimen between the top flanges of the testing rig, which are the specimen conditions for a static analysis. The average natural

frequency measured was 362 Hz. It is close to the analytical result for a clamped circular plate, which is 397 Hz.

4.4.1.2.2 Numerical Evaluation of the Natural Frequency of the Specimens.

The analysis of the specimen behaviour during a dynamic test shows that the external flange of the rig restricts the vertical movement of the specimen edge, when the pressure wave expansion takes place. However, it can rotate freely. This is ensured by making round all the flange edges. So, the boundary nodes of the mesh, on the top perimeter, are impeded to move along the vertical direction. Furthermore, in order to avoid numerical singularities in the finite element calculations, the rigid body movement was restricted by fixing some points of the grid. Thus, four equidistant nodes of the boundary top layer were clamped, in such way that the symmetry of the strain field at the centre of the specimen is not affected.

With these conditions, the natural frequency of the finite element model was calculated with the natural frequency extraction procedure of ABAQUS, in which the frequencies of the current system are obtained by eigenvalue techniques. The natural frequency calculated was 192.4 Hz. Turning to the specimen tested under static loading, all the boundary nodes of the model were clamped and the natural frequency calculated was 360 Hz.

Both numerical evaluations compare well with the experimental results. Hence, these are the boundary conditions selected for all the finite element calculations discussed in this chapter.

4.4.1.3 Results Obtained.

Initially, the numerical solution was calibrated with the experimental results obtained in 2.4.3, in which the variation of the strains at the centre of the plate were studied. The loading resulted from blast waves generated with burst pressures equal to 1.0 bar, 1.25 bar and 1.5 bar, which are identified as cases A, B and C respectively. These evaluations were restricted to the initial load ramps of the pressure histories, because crack initiation is likely during this period. The duration of these dynamic events is around 1 ms and they have been recorded with approximately 200 points. Consequently, the loading data of the finite element model has been approximated by a piecewise linear representation.

In the first series of calculations, the elastic response of the structure without damping was obtained, considering the first seven modes of vibration. In case A, the numerical strain history shows a negative phase that lasts 1.1 ms and then it increases sharply, as shown in figure 4.15, where it is compared with the experimental evaluation. The analysis of the experimental results in the same interval show that during the first 0.8 ms negative membrane strains are unlikely. Then, the strains increase. Moreover, the strain rate registered in the experimental tests is lower than the numerical counterpart.

The numerical results of case B, which are compared with the experimental counterpart in figure 4.16, have a similar pattern. The initial negative phase lasts around 0.9 ms, which is nine times bigger than the one observed experimentally. Besides, the differences between the minimum strain values is significant and the strain rates are slightly different.

A similar comparison is displayed in figure 4.17 for the case C, in which it can be observed that the initial part of the numerical strain history is negative. So, the positive and negative phase, which are observed in the experimental results during the same interval, are not reproduced, although, the strain rates after this time are similar.

It is important to observe that in all the numerical cases, the ramps of the strain histories occur at the same instant that was registered experimentally. Consequently, the lag observed between the experimental strain and the pressure histories was obtained in all the calculations. Besides, the positive phase is similar. Another characteristic of all the numerical solutions, is that the numerical results continue increasing after the experimental peak strain has been reached.

These facts suggest that the results may be improved by reducing the negative phase, which can be done by introducing the damping properties of the specimen in the calculations. Nevertheless, their evaluation is impracticable. Hence, a viable alternative is to adjust the numerical results by varying the critical damping factors of each mode of the system. This method has no physical basis in the finite element model, so, it is a purely mathematical concept introduced in association with the eigenmodes of the system and cannot be extended to those cases in which the natural frequencies of the system are constantly changing [14].

In general terms, when different values of damping were applied, the negative phase in the

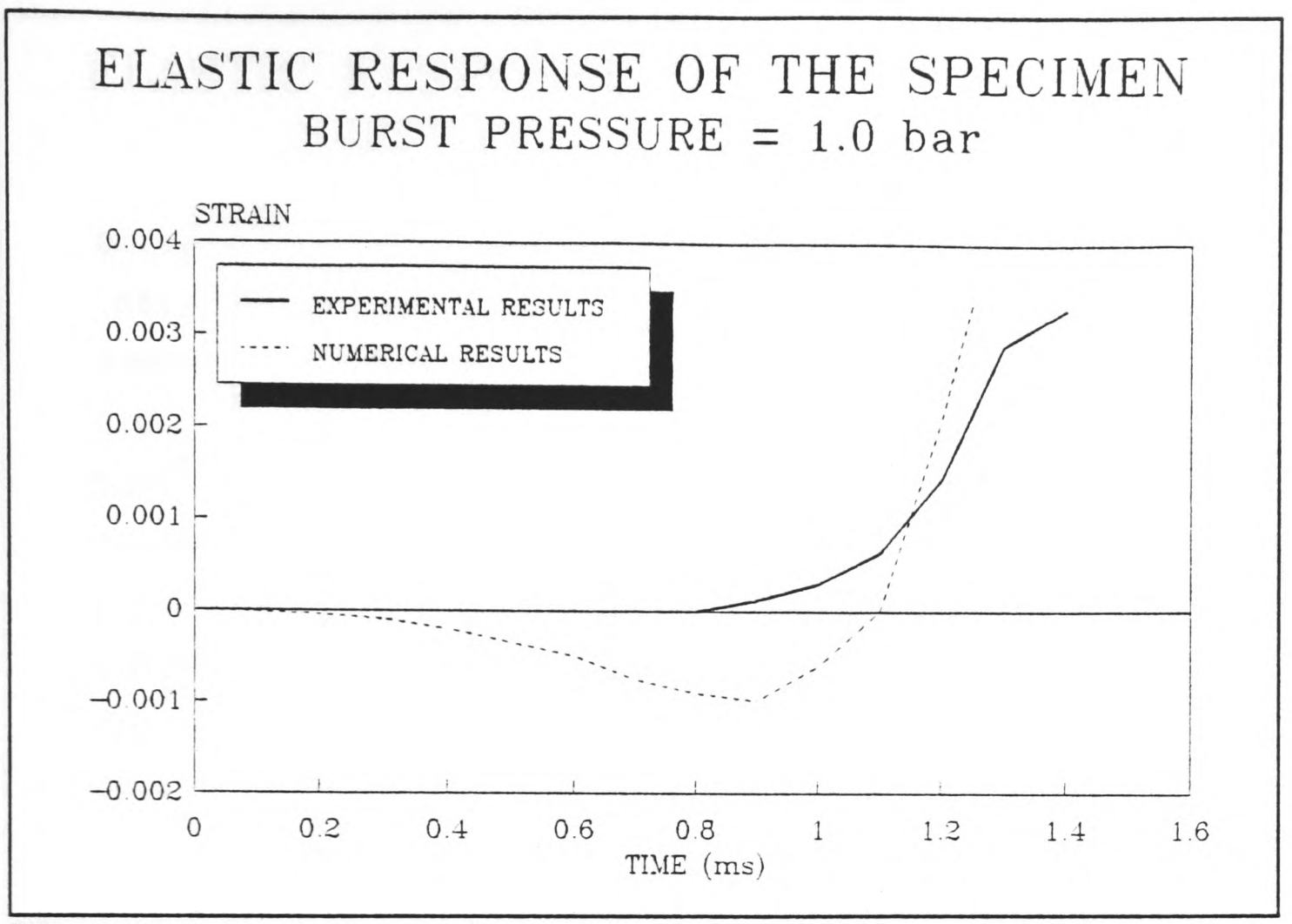


Figure 4.15 Comparison between the experimental and undamped numerical evaluations (burst pressure = 1.0 bar).

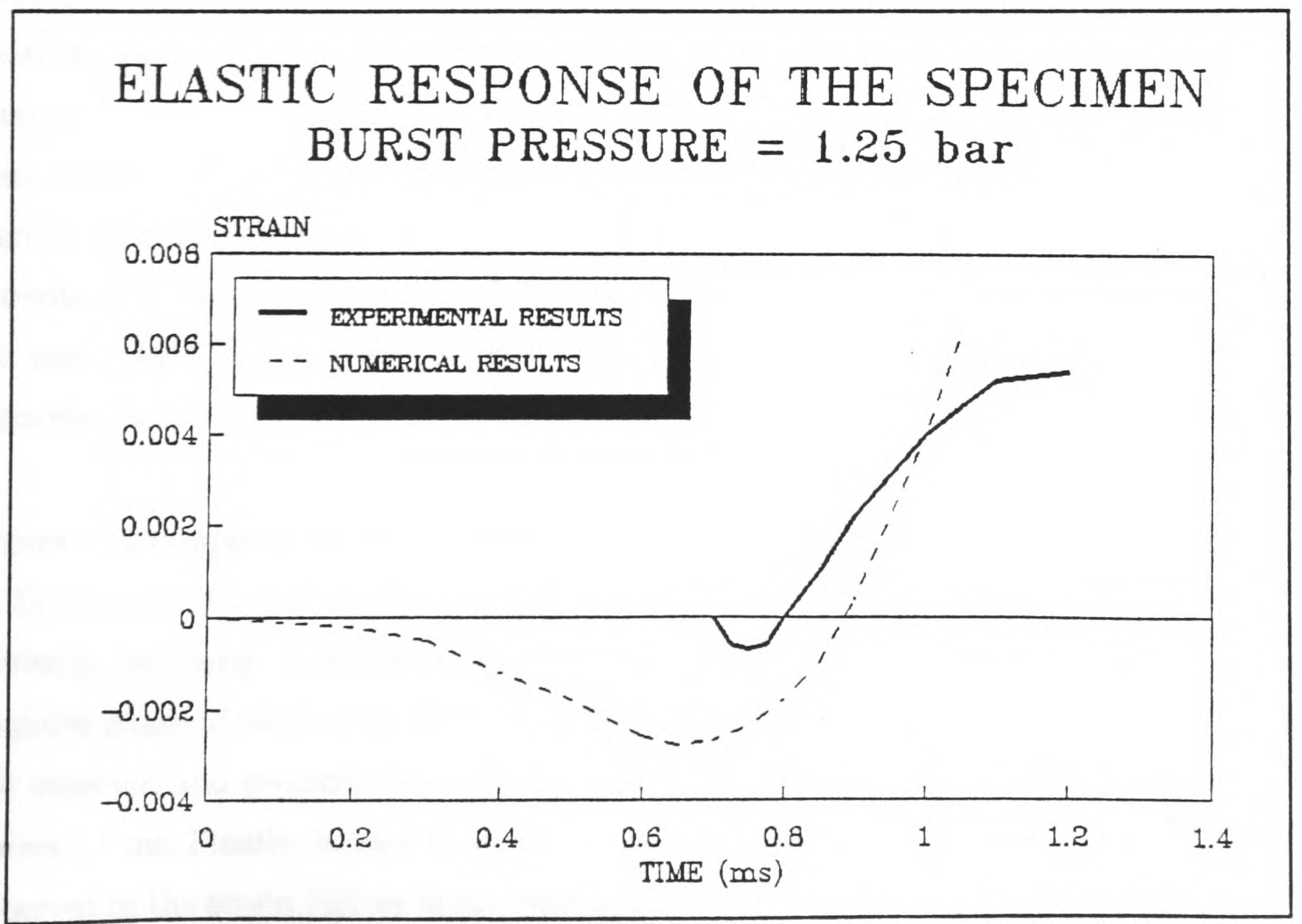


Figure 4.16 Comparison between the experimental and undamped numerical evaluations (burst pressure = 1.25 bar).

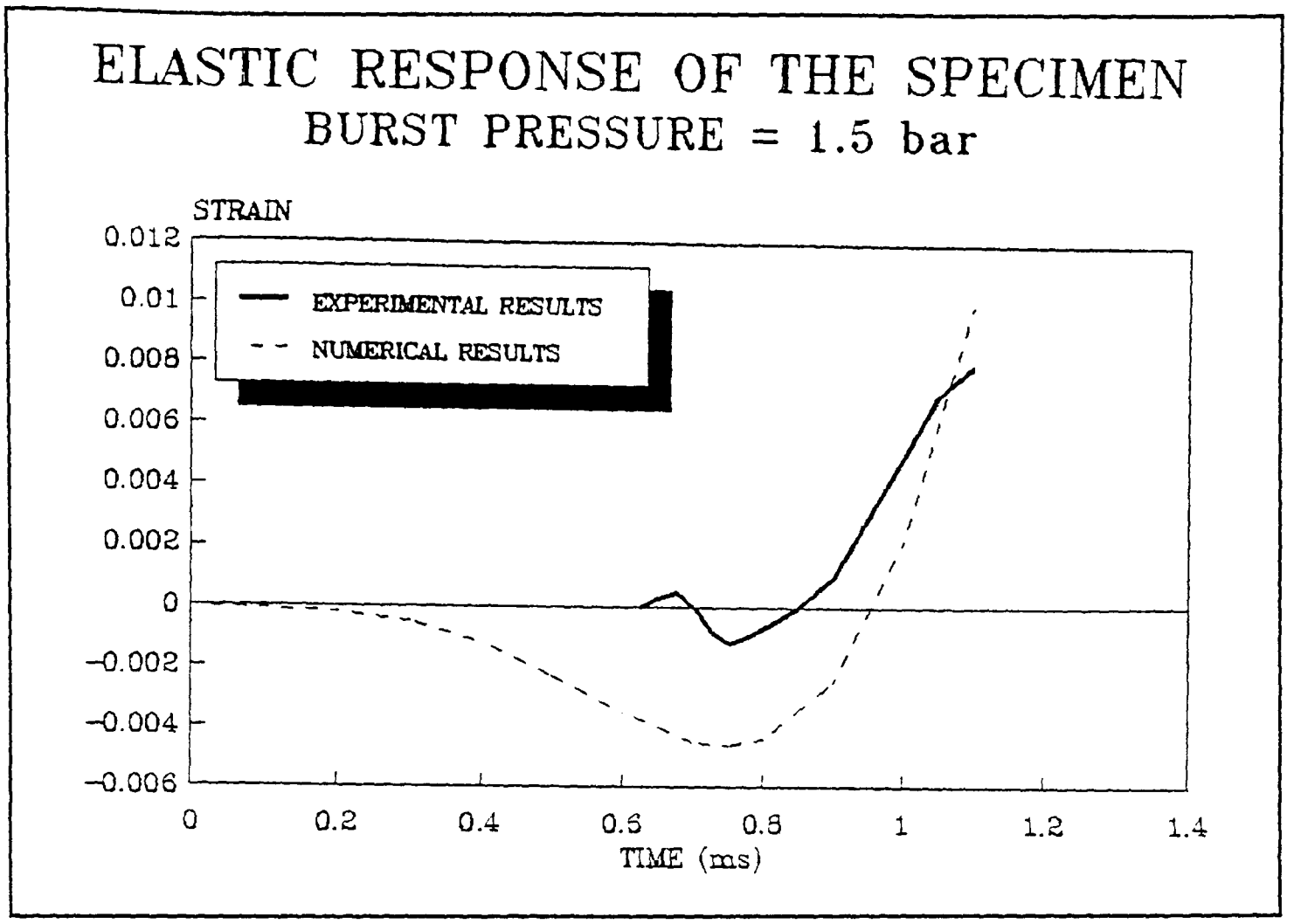


Figure 4.17 Comparison between the experimental and undamped numerical evaluations (burst pressure = 1.5 bar).

numerical results was reduced and the ramp strain rates calculated were closer to those observed during each test. So, the criterion, that was adopted for the calibration of the numerical solution, was that the ramps of the experimental and numerical strain histories were similar and the minimum values of the negative phase were in the same range. The best simulation of the strain history was obtained when a critical damping factor equal to 1.0 was introduced in the calculations, which corresponds to the condition when the system returns to its static equilibrium state as rapidly as possible, without any oscillation, after any disturbance.

Figure 4.18 compares the experimental and numerical results with this assumption for case A. In the first 0.9 ms, negative strains were calculated and after 1 ms, both solutions are virtually the same. A similar comparison is presented for the case B in figure 4.19. The negative phase of the numerical strain-history is reduced to the first 0.7 ms and after 0.8 ms the observed and predicted strain rates increase at the same rate. This situation is likely before 1.1 ms. Finally, in case C, which is presented in figure 4.20, the initial positive phase observed in the strain history is not reproduced. However, after 0.8 ms, both curves have the same rate of increase.

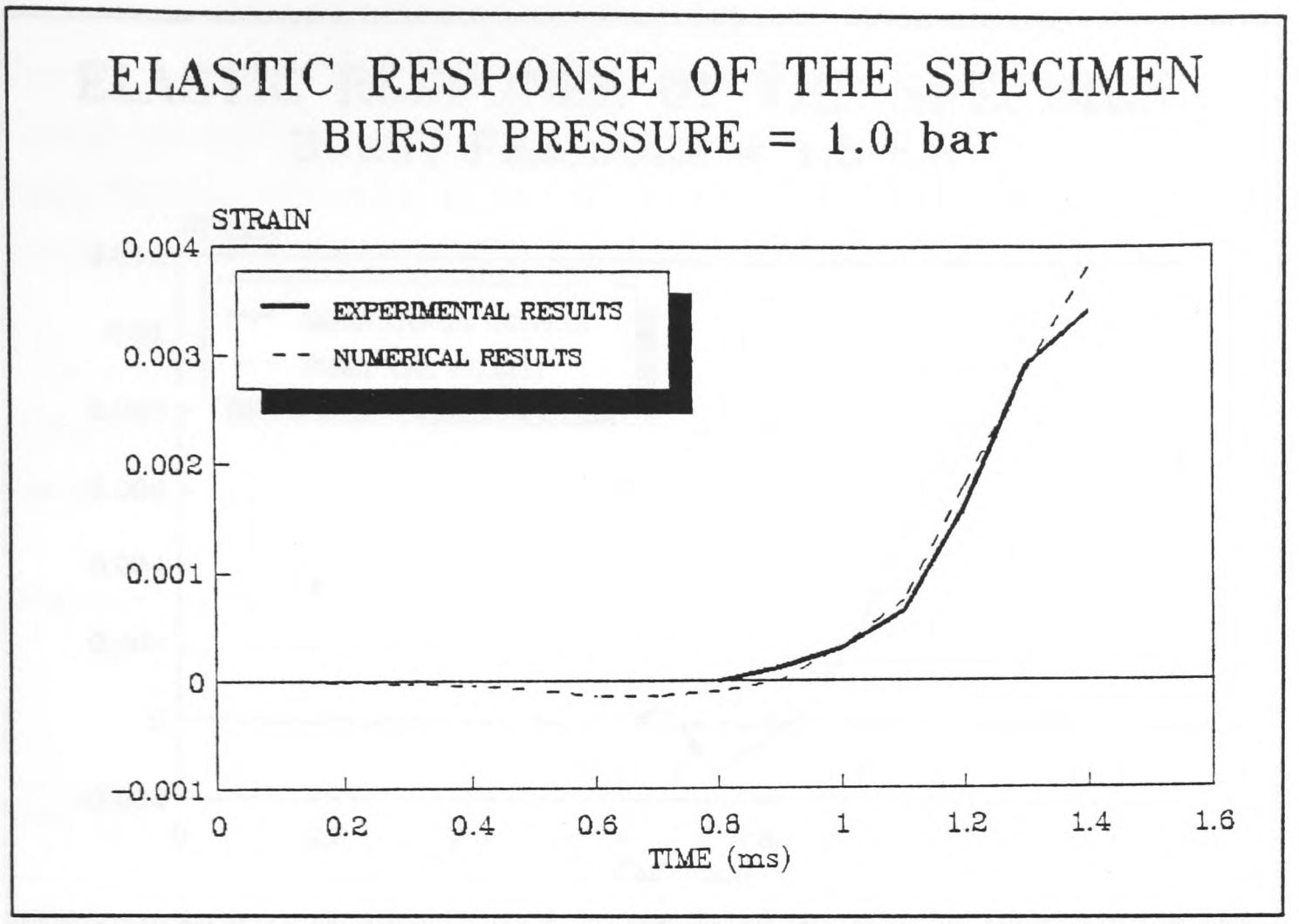


Figure 4.18 Comparison between the experimental and numerical evaluations (burst pressure = 1.0 bar).

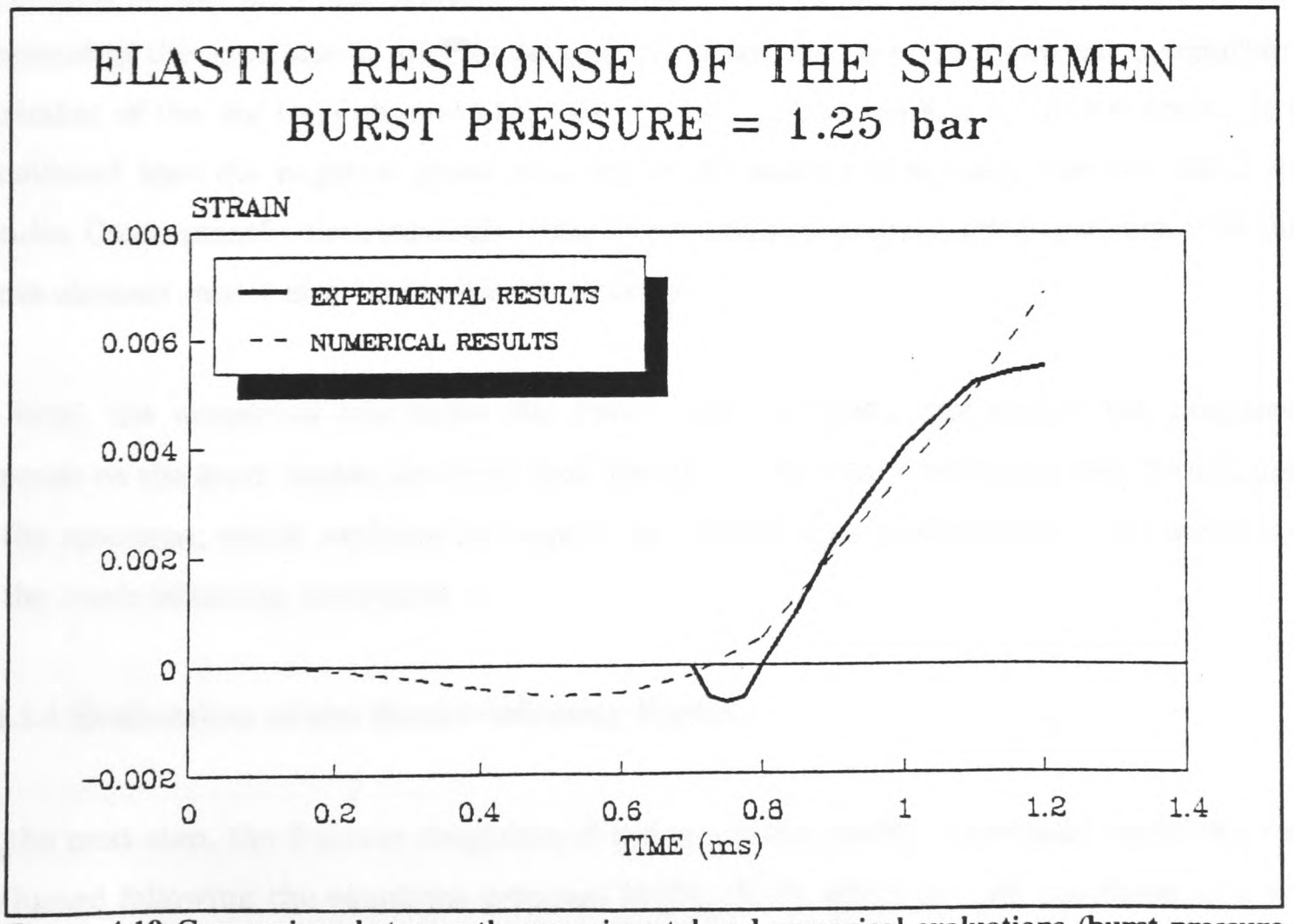


Figure 4.19 Comparison between the experimental and numerical evaluations (burst pressure = 1.25 bar).

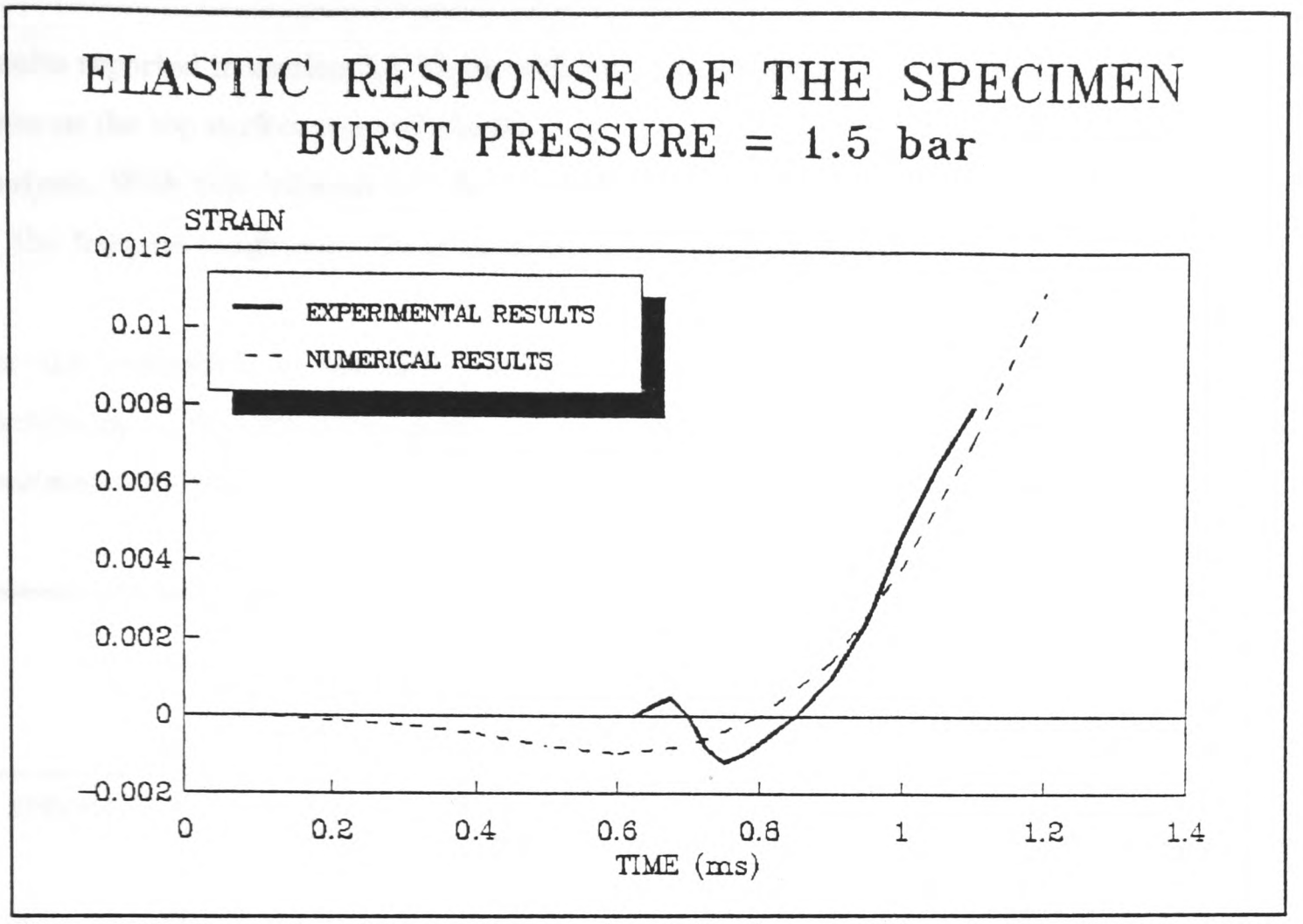


Figure 4.20 Comparison between the experimental and numerical evaluations (burst pressure = 1.5 bar).

In general terms, the common characteristic observed in these solutions is that the predicted response of the specimen is slightly delayed. However, this does not represent a significant variation of the lag time observed between the load and strain history. Furthermore, It is considered that the negative phase observed in the numerical solution does not affect the results. Consequently, the evaluation of the stress field at the centre of the specimen with this finite element model may be considered accurate.

In brief, the numerical evaluation has shown that the elastic response of the specimens depends on the exact evaluation of the load history, the boundary conditions and the damping of the specimen, which confirms the importance of the dynamic calibration in the evaluation of the crack initiation conditions.

4.4.1.4 Evaluation of the Stress Intensity Factor.

In the next step, the fracture toughness of the specimens tested in dynamic conditions was evaluated following the equations proposed in [24,25,28], which are the equations 4.15 and 4.17. For this purpose, the instant of crack initiation was obtained from the experimental

results reported in section 3.6. Then, with the calibrated model, the stress at the centre of the plate on the top surface was calculated at the instant of crack initiation with a modal dynamic analysis. With this information the dynamic SIF was evaluated at the instant of fracture, i. e., the fracture toughness. These calculations correspond to case I.

For the evaluation of the SIF with equation 4.17, the coefficient $\Phi(1)$ was selected in accordance to the graph of figure 4.11, considering the crack length and thickness of the specimens. All the results obtained are shown in table 4.2.

TABLE 4.2
FRACTURE TOUGHNESS EVALUATED WITH STANDARD SOLUTIONS
(DYNAMIC TESTS)

SPECIMEN	CRACK LENGTH (mm)	STRESS AT CRACK INITIATION (MPa)	K_c IN ACCORDANCE WITH EQUATION 4.15 (MPa $m^{1/2}$)	CORRECTION FACTOR Φ (1)	K_c IN ACCORDANCE WITH EQUATION 4.17 (MPa $m^{1/2}$)
36	4.862	23.2	2.02	0.83	1.68
37	9.634	11.2	1.37	0.76	1.04
38	14.745	10.6	1.61	0.73	1.17

The results of equations 4.15 and 4.17 are compared in figure 4.21. It can be observed that the lowest values of fracture toughness are obtained with the last equation. However, both curves show similar increase of this parameter for specimens with cracks smaller than 10 mm.

For the static cases, a similar approach was followed, in which the stresses at the centre of the plate were statically calculated with the finite element mesh described above, considering the results of the static tests reported in table 3.3 and the boundary conditions established in section 4.4.1.2. As in the dynamic series of tests, the fracture toughness was evaluated with the relations 4.15 and 4.17 (case IV). The results obtained are shown in the following table with the correction factor $\Phi(1)$.

In particular, the results of the specimens 26 and 28, which have a similar crack length, are different. This discrepancy may be explained with the fact that the range of the accuracy in the measurement of the load is 0.05 bar and the readings are rounded to the next close figure. So, the readings are taken at the ends of 0.1 bar interval. A similar situation is observed with

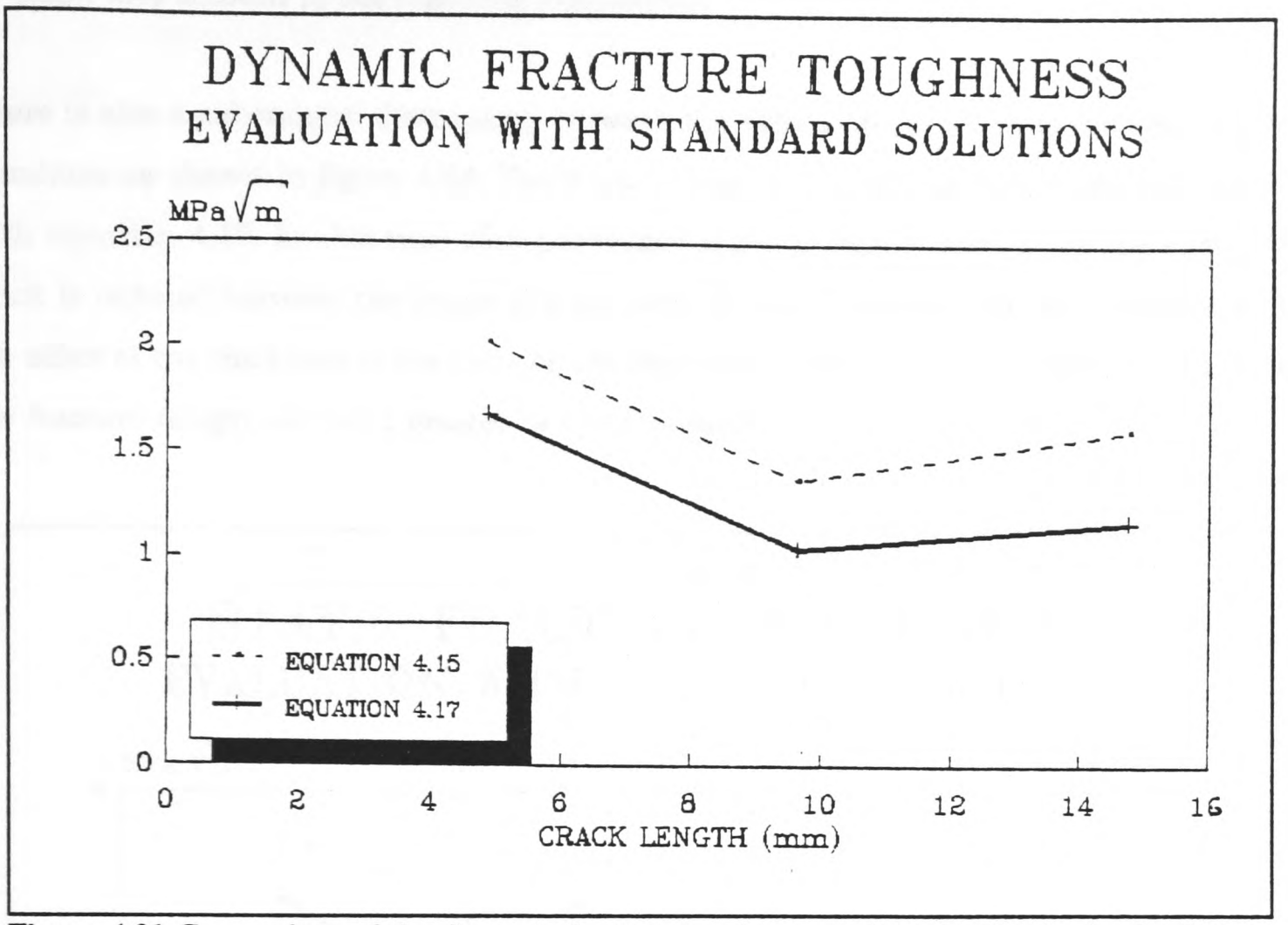


Figure 4.21 Comparison of the dynamic fracture toughness evaluated with standard solutions (case I).

TABLE 4.3
FRACTURE TOUGHNESS EVALUATED WITH STANDARD SOLUTIONS
(STATIC TESTS)

SPECIMEN	CRACK LENGTH (mm)	STRESS AT CRACK INITIATION (MPa)	K_c IN ACCORDANCE WITH EQUATION 4.15 (MPa $m^{1/2}$)	CORRECTION FACTOR Φ (1)	K_c IN ACCORDANCE WITH EQUATION 4.17 (MPa $m^{1/2}$)
26	8.651	30.0	3.49	0.79	2.76
28	8.349	26.2	3.00	0.79	2.37
30	19.043	20.6	3.56	0.72	2.56
31	18.749	18.7	3.21	0.72	2.31
33	2.959	54.3	3.70	0.90	3.33
35	4.881	39.4	3.45	0.83	2.86

the specimens 30 and 31, in which the load was evaluated within a 0.5 bar pressure interval. The observed differences may be reduced if the crack initiation load is measured with more precision. From this, it can be established that values obtained are at the ends of the range of accuracy and the middle point of this interval is the average result. This consideration will

be taken into account in the following evaluations.

There is also a substantial discrepancy between the values calculated from the two different equations as shown in figure 4.22. The lower values of the fracture toughness are obtained with equation 4.17. In this case, this parameter shows a steady increase as the size of the crack is reduced between the range of 8 mm and 19 mm. This situation can be explained by the effect of the thickness of the plate on the fracture process. For cracks smaller than 8 mm, the fracture toughness has a greater rate of increase.

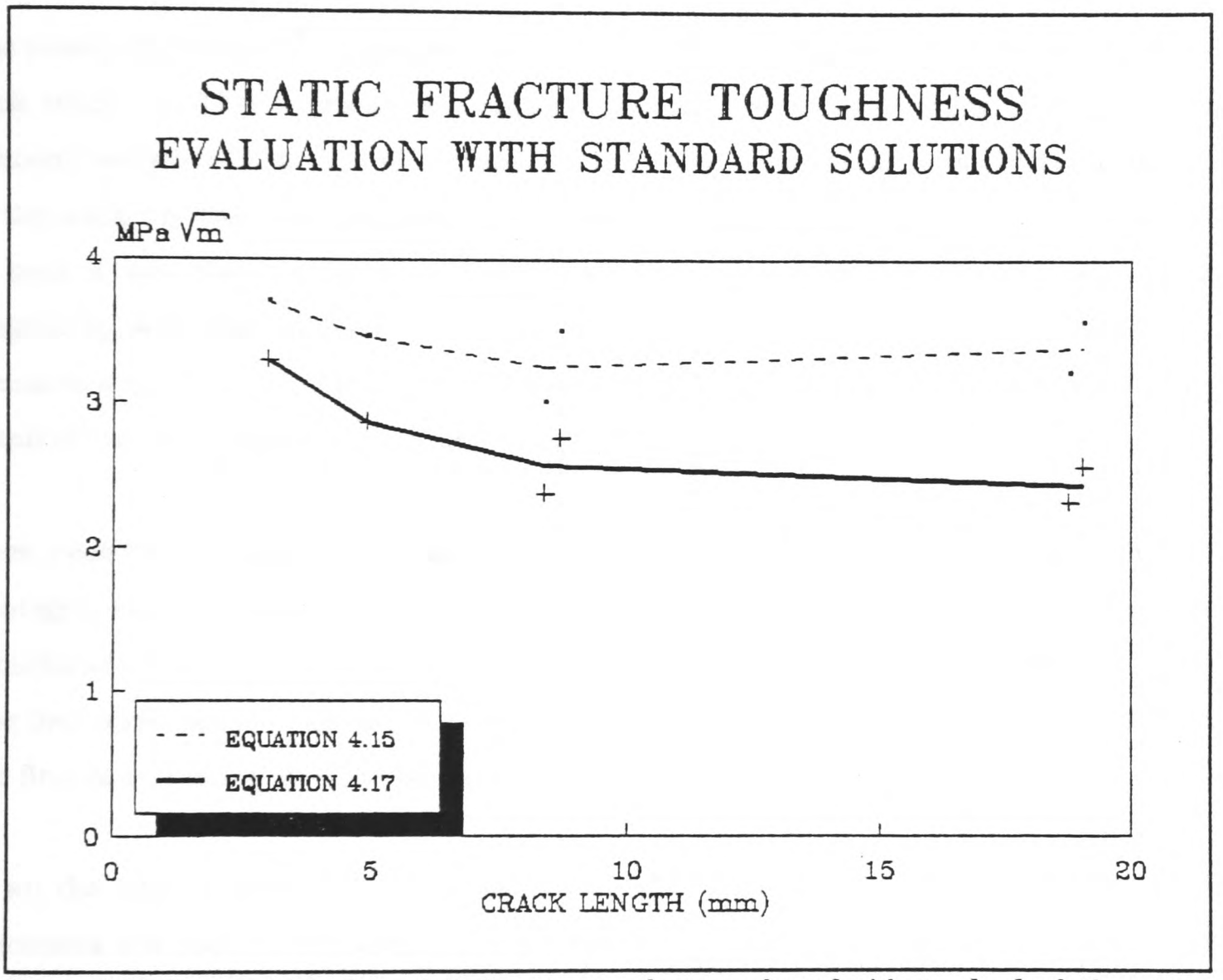


Figure 4.22 Comparison of the static fracture toughness evaluated with standard solutions (case IV).

Alternatively, the results obtained with equation 4.15 show that the fracture toughness within the range between 8 mm and 19 mm is almost constant, increasing for cracks lower than 8 mm. If these results are compared with those obtained with equation 4.17, it can be concluded that the equation 4.15 gives overestimated results.

4.4.2 Analysis of Cracked Plates.

4.4.2.1 Characteristics of the Finite Element Mesh for the Evaluation of the J-Integral.

The development of the finite element mesh of the cracked specimens is based on the same considerations that were taken into account for the mesh of a plate without crack. Consequently, a circular flat plate, which is 165 mm diameter and 3 mm thickness, was modelled with a mesh of 296 C3D20 second order isoparametric elements arranged in two layers, requiring 1884 nodes.

The mesh is focused at the crack ends, as shown in figure 4.23, in which 24 elements surround each crack tip. This approach was followed because the mid-side nodes of the crack tip elements are moved to the 1/4-point position, giving a square root singularity in the strain field at the crack tip. The remaining nodes of the elements that surround the crack tip, are spaced in such a way that the element size will grow as the square of the distance from the singularity, with their mid-side nodes exactly at their mid-sides. For this reason, the crack tip elements are very small and they can not be appreciate in the drawing of the whole mesh. A detail of the crack tip elements is shown in figure 4.24.

Each crack tip was modelled with three surrounding rows of eight elements. Consequently, the J-integral may be evaluated along four different contours. However, only the first two were considered based on the analysis of the accuracy of the evaluation discussed in section 4.2.3.2. The first corresponds to the set of nodes at the very crack tip, while the second path includes the first row of elements that enclose the crack tip.

In all the tests, a state of bending stress was developed. As a result, the top layer of the specimens was under the maximum tensile stress. So, the fracture toughness was calculated with the J-integral values obtained from the top layer of nodes.

4.4.2.2 Fracture Toughness Evaluation of the Dynamic Tests.

Initially, the evaluation of the fracture toughness was done with a static approach. For this purpose, the crack initiation load was obtained from the experimental results, which are reported in table 3.2. In addition, the boundary conditions established for dynamic tests in section 4.4.1.2 were integrated in the input data with the quasi-static mechanical properties

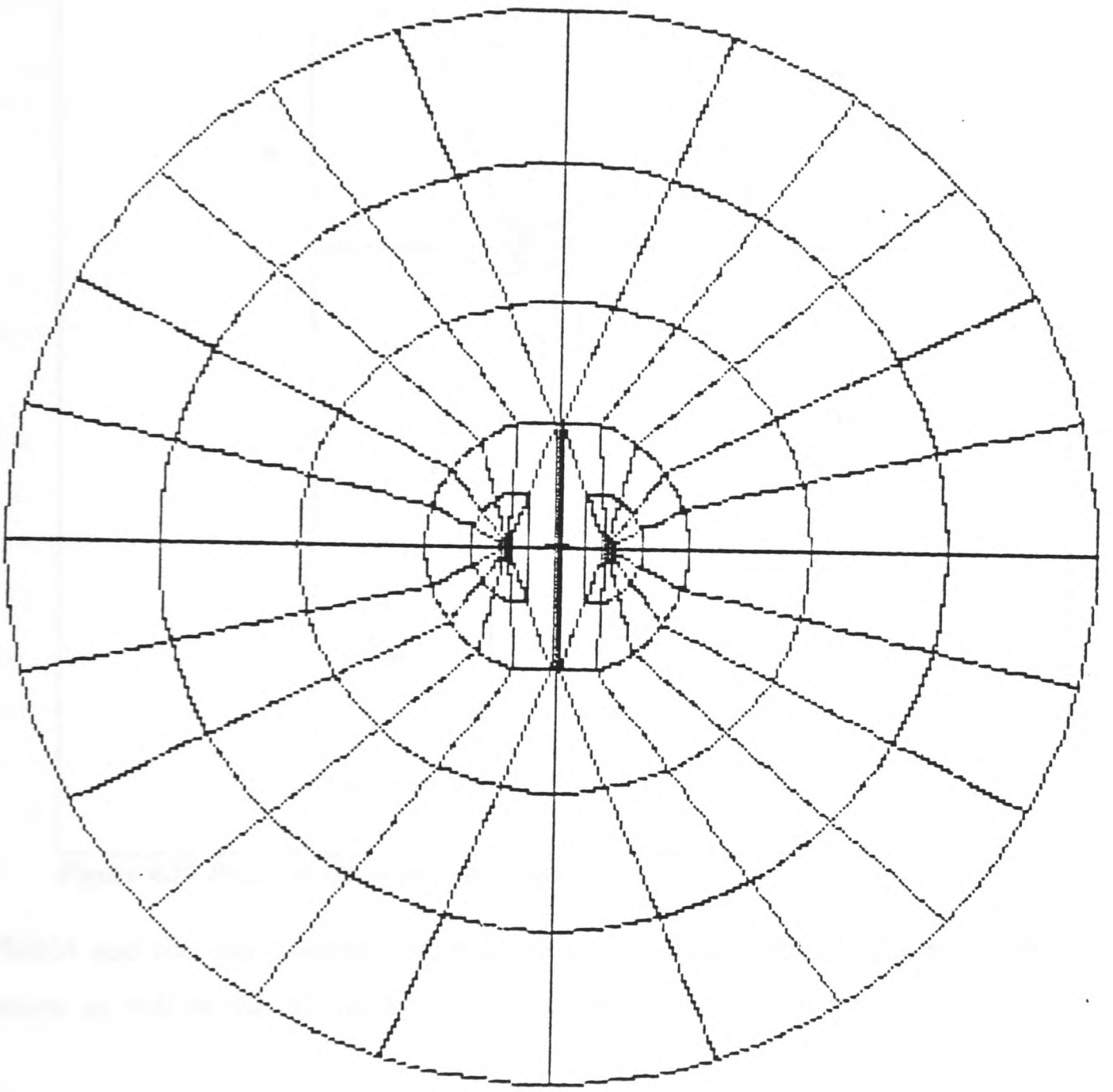


Figure 4.23 Finite element mesh of the central cracked plate.

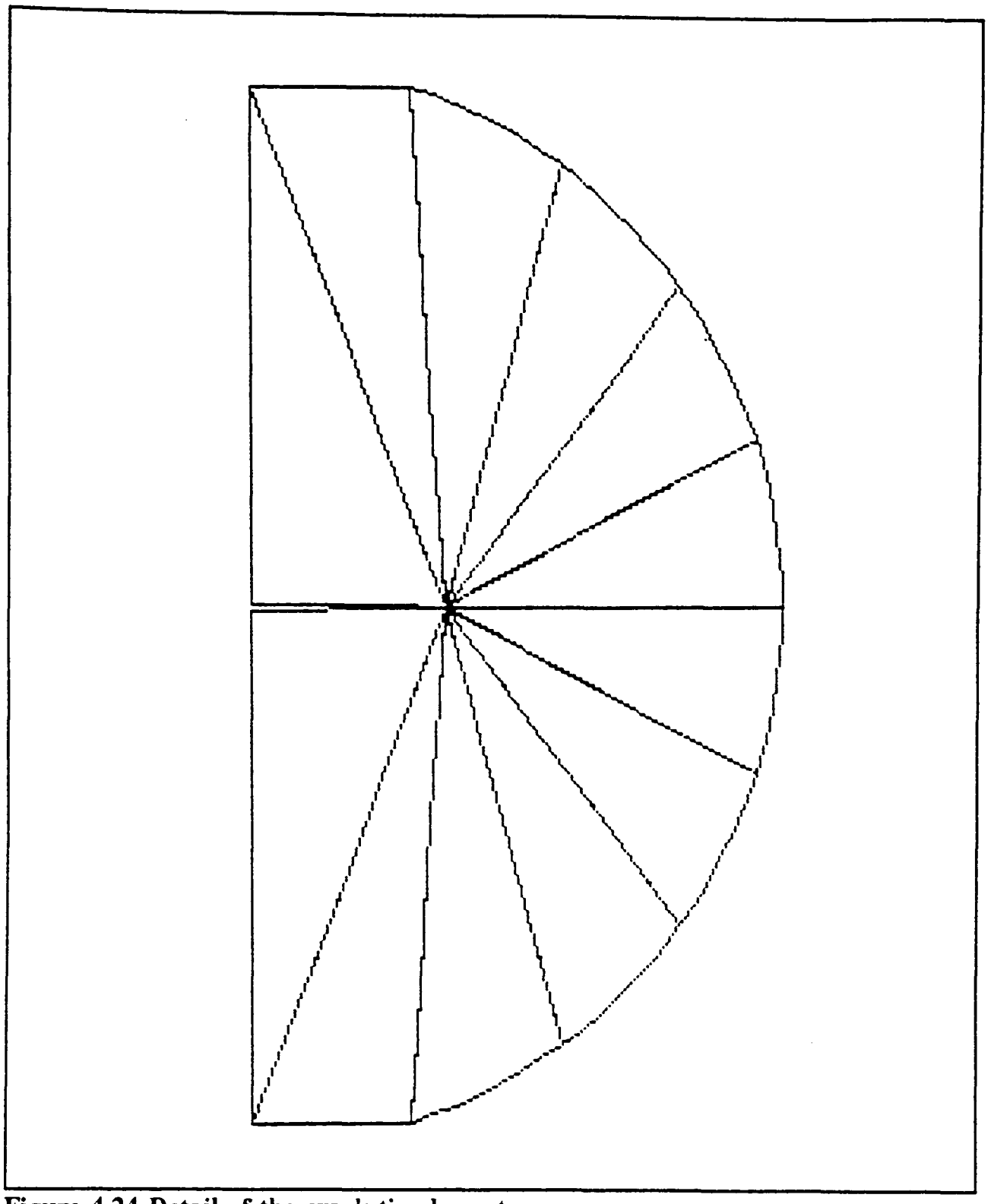


Figure 4.24 Detail of the crack tip elements.

of PMMA and the crack length. Table 4.4 show the value of the J-integral for the first two contours, as well as the calculated natural frequency for each specimen (case II).

The analysis of the results, show that the first contour always gives a smaller value than the second contour and the J-integral value decreases as the crack size increases.

In the case of specimen 38, the crack propagated after the pressure rise reached its peak value. However, the unloading of the specimen is not big and a good approximation may be obtained by calculating the J-integral with the peak pressure.

TABLE 4.4
J-INTEGRAL EVALUATION OF THE DYNAMIC TESTS
(STATIC ANALYSIS)

SPECIMEN	CRACK LENGTH (mm)	PRESSURE AT CRACK INITIATION (BAR)	J-INTEGRAL		FREQUENCY (Hz)
			1st CONTOUR (N/m)	2nd CONTOUR (N/m)	
36	4.862	0.56	2590	3136	195.21
37	9.694	0.49	2601	2919	194.29
38	14.745	0.30	1724	2108	193.23

With respect to the natural frequencies, this parameter varies slightly and it can be considered that it is not affected by the state of stresses. In consequence, the dynamic characteristics of the specimen and the boundary conditions are constant through the tests.

In the evaluation of the fracture toughness, it was observed that the crack propagated in a brittle condition and the development of shear lips was unlikely. In consequence, equation 4.4 was used with the results of the second contour, considering plane strain conditions. The results obtained are shown in table 4.5 for each specimen.

TABLE 4.5
FRACTURE TOUGHNESS OF THE DYNAMIC CASES
(STATIC ANALYSIS)

SPECIMEN	CRACK LENGTH (mm)	K_c (MPa $(m)^{1/2}$)
36	4.862	3.27
37	9.694	3.16
38	14.745	2.68

At first glance, the range of the results suggest that K_c is overestimated by comparison with the results given in table 4.2. In consequence a dynamic analysis was performed. The findings of the preliminary analysis showed, that the evaluation of J-Integral with the modal dynamic analysis, leads to the static results, which implies that the dynamic characteristics of the specimens were not taken into account in the dynamic analysis.

As a second step, this problem was analyzed with the dynamic method of direct integration, which is also implemented within ABAQUS (case III). This method is recommended for those

cases in which a sudden event initiates the dynamic problem -a vehicle crash, a pipe break, a bird strike, etc.- and the structural response involves very large amounts of energy dissipated. Furthermore, it is also advisable to be used with non-linear dynamic response problems. All the equations of motion of the system are integrated through the time. Hence, from a computational point of view, it is remarkably more expensive than the modal method.

The results obtained with a mesh of C3D20, show that the response of the specimen is stiff. Thus, the C3D20R elements, which are reduced integration brick elements, were used. In this case, eight integration points are required rather than the 27 points employed in the full integration element. As a result, the Gauss scheme, which is one order less than the "full" scheme, is used to integrate the internal forces and stiffness of the elements. These elements are recommended when the number of constraints introduced in mesh should be reduced. As in the case of internal constraints in the continuum theory being modelled, such as incompressibility, or the Kirchhoff transverse shear constraints in bending problems. In such applications fully integrated elements will "lock" and their response will be too stiff [14].

The boundary conditions for dynamic tests, described in section 4.4.1.2, the load history with its dynamic calibration, as established in section 2.4.3, and the data obtained from the crack initiation tests under dynamic loading, which is reported in table 3.2, were taken into account. The results obtained are shown in the following table.

TABLE 4.6
FRACTURE TOUGHNESS CALCULATED WITH THE DIRECT INTEGRATION METHOD

SPECIMEN	CRACK LENGTH (mm)	J-INTEGRAL (2nd CONTOUR) (N/m)	K_c (MPa $(m)^{1/2}$)
36	4.862	138.0	0.67
37	9.694	68.0	0.48
38	14.745	29.0	0.31

These results are compared in figure 4.25 with those obtained with a quasi-static approach (case II reported table 4.5). The difference between the results is very large, although both curves indicate that the fracture toughness increases as the size of the crack decreases. In order to explain this difference, the results have to be compared with the results of the static tests and the evaluations obtained with the standard solutions.

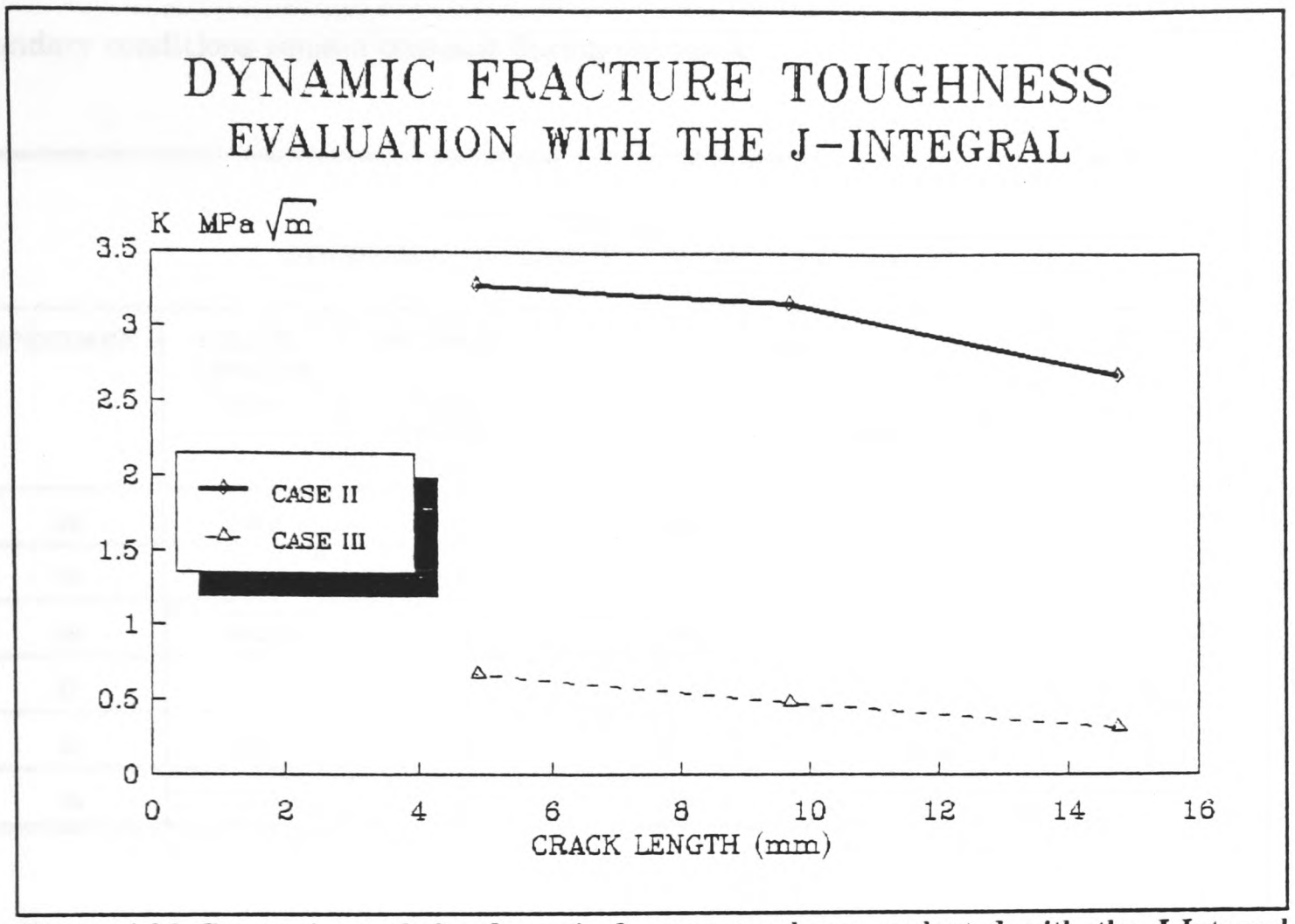


Figure 4.25 Comparison of the dynamic fracture toughness evaluated with the J-Integral following dynamic and static approaches.

4.4.2.3 Fracture Toughness Evaluation of the Static Tests.

The fracture toughness of the specimen tested in static conditions was evaluated with the mesh that is illustrated in figure 4.23, which was filled with C3D20 elements. For this purpose, the boundary conditions established in section 4.4.1.2 for those specimens tested under static conditions were considered. Besides, the pressure load measured at crack initiation and the crack dimensions, which are in table 3.3, were attached to the input data with the quasi-static mechanical properties of the material (case V).

The results obtained for each specimen are shown in table 4.7, in which the value of the J-Integral along the first two contours and the natural frequency are shown. In general terms, the J-Integral value decreases as the size of the crack increases, which is the same pattern observed in previous evaluation. Moreover, the J-integral evaluated at the crack tip is lower than the one calculated at the second contour. Regarding the natural frequency, it varies slightly when the state of stress changes and it may be regarded as constant. Thus, the

boundary conditions remain constant during the tests.

TABLE 4.7
J-INTEGRAL EVALUATION OF THE STATIC CASES

SPECIMEN	CRACK LENGTH (mm)	PRESSURE AT CRACK INITIATION (bar)	J-INTEGRAL		FREQUENCY (Hz)
			1st CONTOUR (N/m)	2nd CONTOUR (N/m)	
26	8.651	0.80	2252	2396	364.3
28	8.349	0.70	1689	1779	364.4
30	19.043	0.55	1869	2206	359.8
31	18.749	0.50	1528	1794	359.9
33	2.959	1.45	5806	8440	366.7
35	4.881	1.05	2933	3524	365.0

The fracture toughness was calculated with the evaluation of the J-Integral along the second contour. In all the static tests, the development of shear lips was unlikely and the crack propagated in a brittle manner. Thus, the SIF at crack initiation was calculated with equation 4.4 assuming plane strain conditions.

TABLE 4.8
FRACTURE TOUGHNESS OF THE STATIC CASES

SPECIMEN	CRACK LENGTH (mm)	K_c (MPa(m)$^{1/2}$)
26	8.651	2.86
28	8.349	2.48
30	19.043	2.75
31	18.749	2.48
33	2.959	5.37
35	4.881	3.47

The results obtained for each specimen are shown in table 4.8 and they are presented graphically in figure 4.26. It is observed, that the fracture toughness of those specimen with cracks larger than 8 mm decreases slightly as the size of the crack increases. However, this parameter increases sharply for those specimens with cracks smaller than 8 mm.

It should be borne in mind, for the interpretation of results, that in the case of specimen 33,

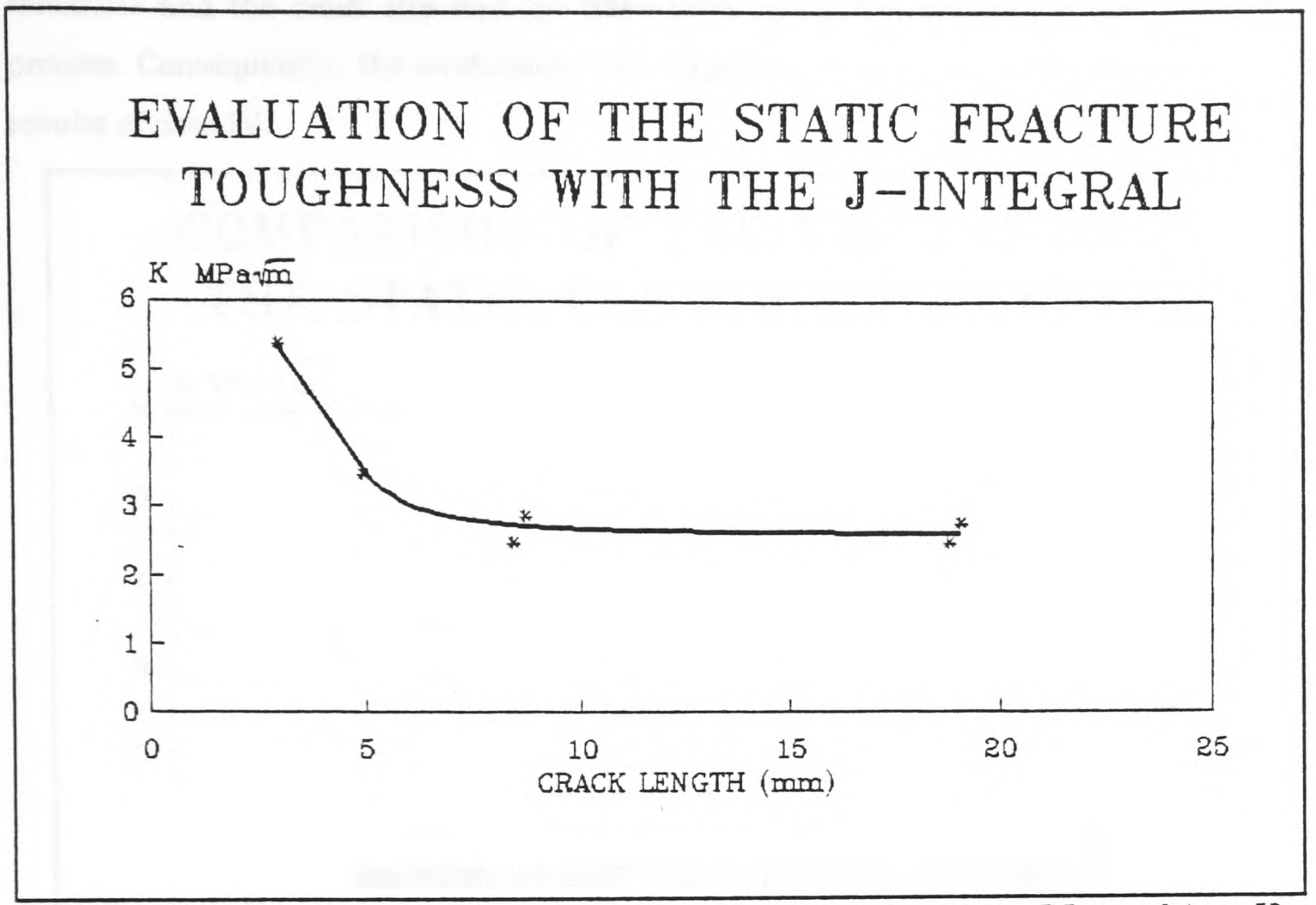


Figure 4.26 Evaluation of the fracture Toughness of the static tests with the J-Integral (case V).

the hole of 1 mm diameter, which was drilled before the crack was cut, and the crack length are in the same range of dimensions. Consequently, the fracture toughness is affected by this geometrical conditions. Rooke et al. [27] have compared the case of central crack in a finite width plate with the case of two cracks at the edge of a hole in a rectangular plate. In both cases, they are loaded with a uniform bending moment. For similar crack lengths, and when the diameter of the hole is in the same range of the crack dimensions, there is an increment in the fracture toughness, which is the situation observed.

4.5 Discussion of the Results.

The results obtained in the evaluation of the fracture toughness for the specimens tested under static conditions are compared in figure 4.27 (cases IV and V). For this purpose, only the analytical solution that includes the effect of specimen thickness -equation 4.17- is compared to the ABAQUS results. As it can be observed, both curves compare well, for those specimen with cracks longer than 8 mm. However, the FEM gives high values of fracture toughness in those specimens with cracks smaller than 8 mm. In this respect, it can be said, that the increment observed is due to two main factors, namely, the geometrical relation between the

thickness and the crack size and the effect produced by the initial hole over the fracture process. Consequently, the evaluation with equation 4.17 is going to be considered as the results of case IV.

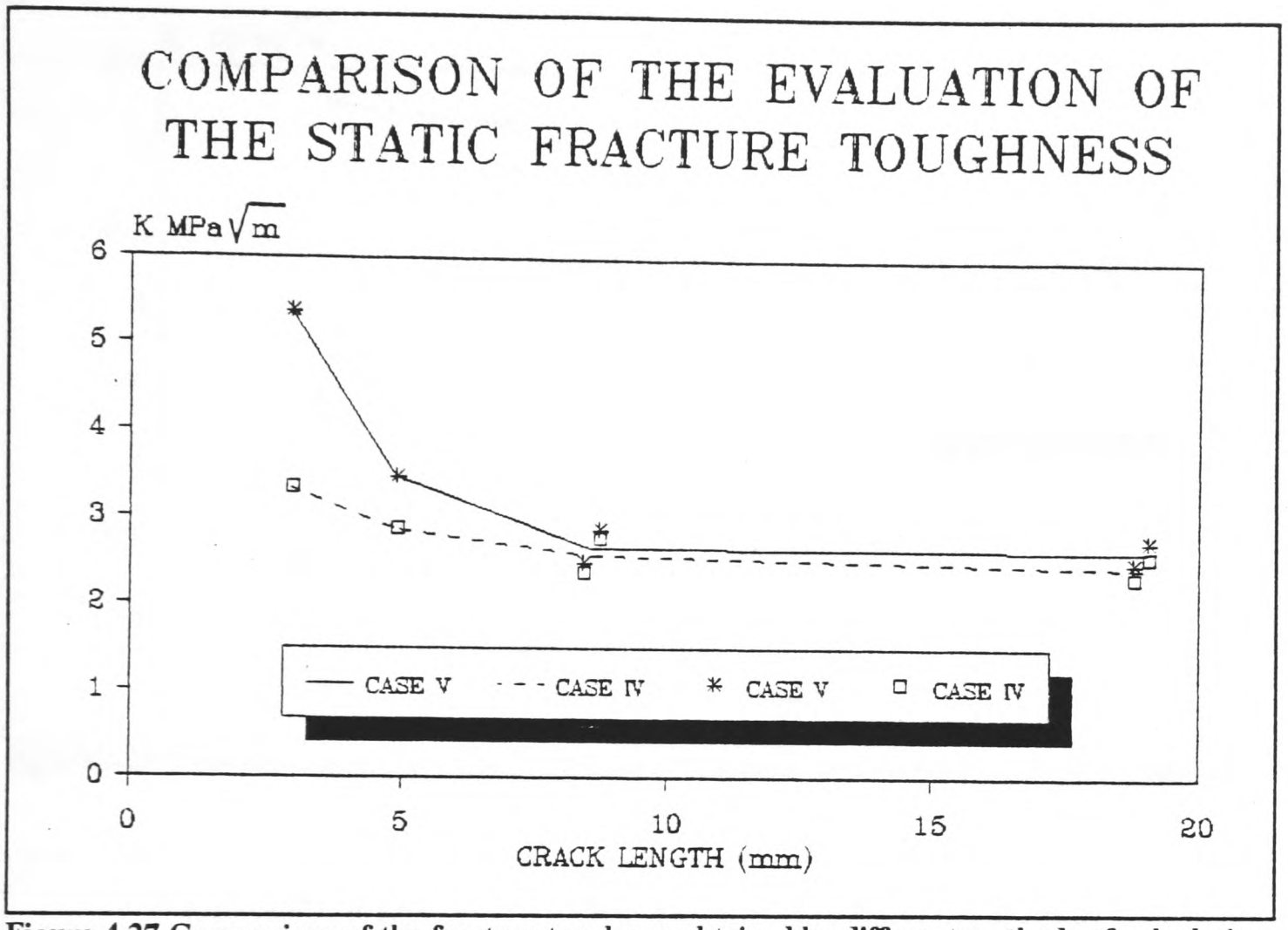


Figure 4.27 Comparison of the fracture toughness obtained by different methods of calculation.

A similar comparison is made in figure 4.28 with the results obtained in the evaluation of the fracture toughness of the specimens tested in the dynamic tests, namely cases I, II and III. For this purpose, it is only to be considered the results of equation of 4.17 in case I, because the analysis in figure 4.27 indicates that these results are accurate.

As it can be observed, the evaluation of the dynamic fracture toughness with the procedure of case II, gives higher values than the standard solutions. On the contrary, the results computed in case III are lower than those of case I. This suggests that the evaluation with a static approach overestimates this parameter. This consideration is based on the fact that the crack started at strain rates higher than 21 s^{-1} and on the assumption that in a brittle material, the fracture toughness is reduced as the strain rate is increased. Furthermore, a comparison between the results of the FEM evaluation of the static tests (case IV) with the dynamic fracture toughness calculated with a static approach (case II) is shown in figure 4.29, where it is observed that the results are within the same range.

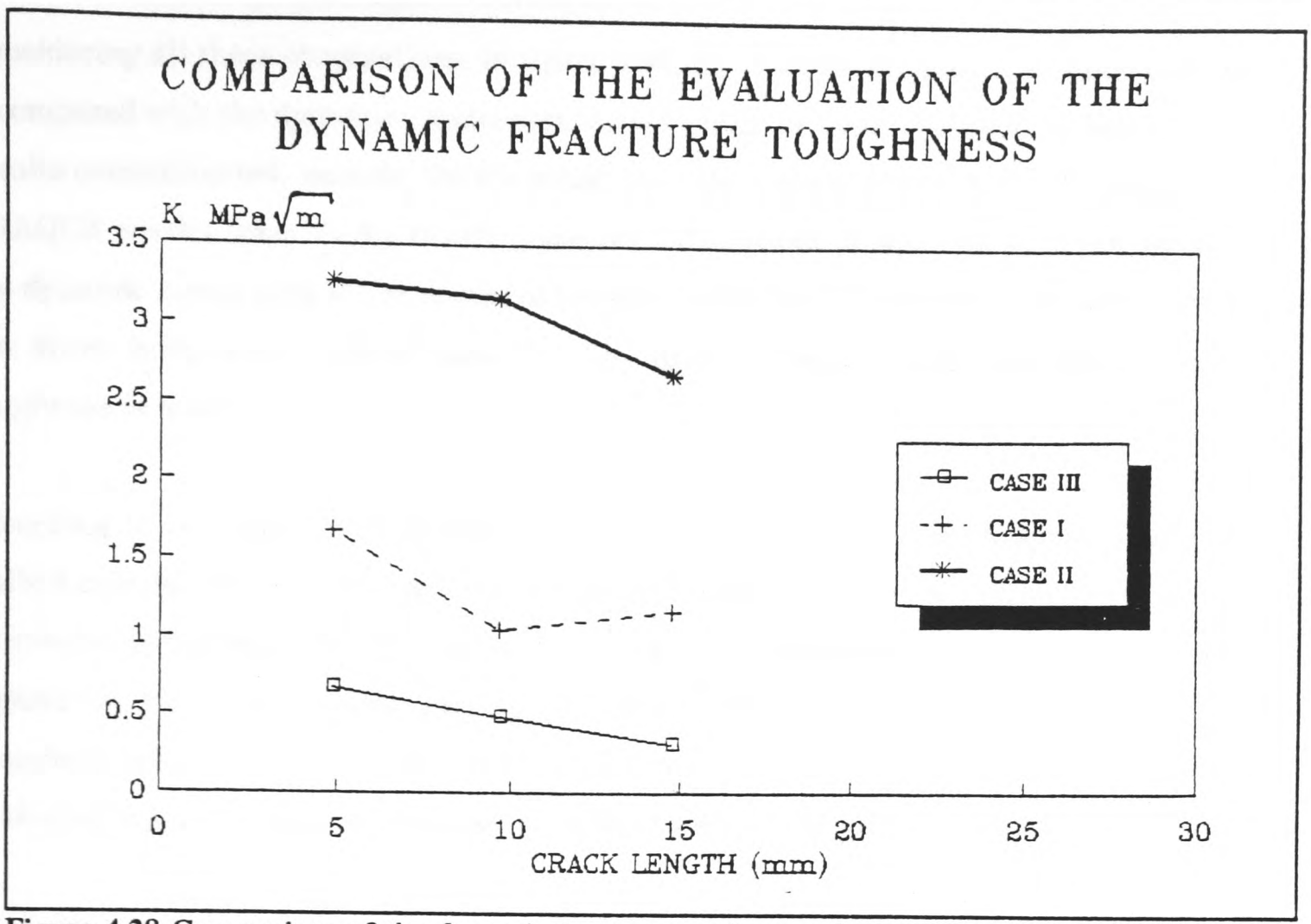


Figure 4.28 Comparison of the dynamic fracture toughness calculated by different methods.

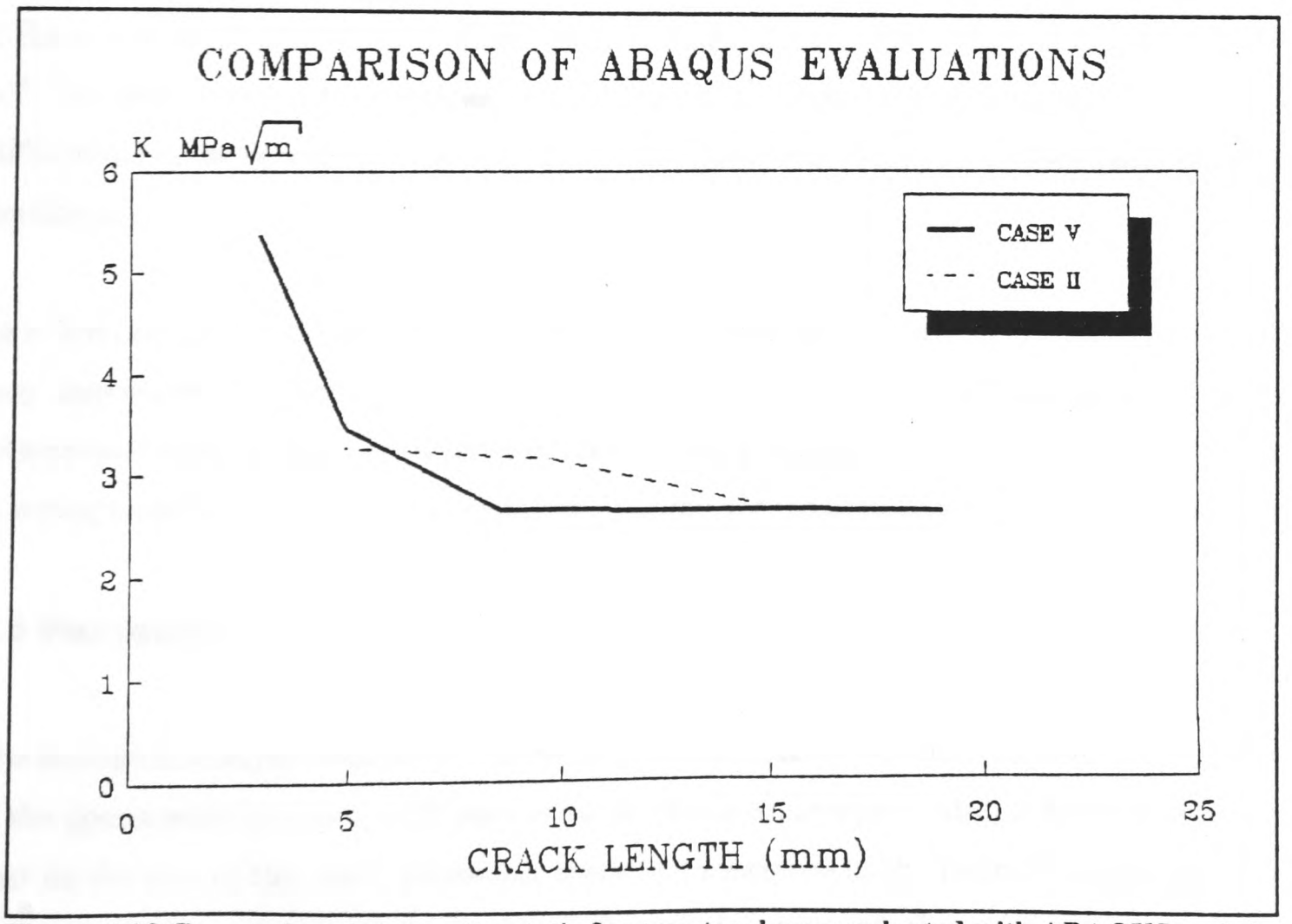


Figure 4.29 Comparison between the static fracture toughness evaluated with ABAQUS and the dynamic fracture toughness calculated with a static approach.

Considering all these observations, in figure 4.30, the fracture toughness in static conditions is compared with the dynamic counterpart, considering only those evaluations that do not give results overestimated, namely, for the static case, the results of equation 4.17 (case IV) and ABAQUS results (case V), for the dynamic case, the results of equation 4.17 evaluated with the dynamic stress field at the centre of the specimen (case I) and ABAQUS evaluation with the direct integration method (case III). The findings indicate that the dynamic fracture toughness is lower.

According to the analysis of Marshall et. al. [31], who compared the fracture toughness of PMMA calculated by several researchers with different techniques, the range of values of this parameter is between 0.63 MPa $m^{1/2}$ and 1.94 MPa $m^{1/2}$. They establish that the actual values depend on two main factors, namely, the strain rate at crack initiation and the errors associated with the experimental technique. As a result, the range of the fracture toughness evaluated with acceptable techniques is reduced within 0.76 MPa $m^{1/2}$ and 1.75 MPa $m^{1/2}$.

Regarding to the range of results for the dynamic tests, the range of the fracture toughness obtained is between 1.1 MPa $m^{1/2}$ and 0.5 MPa $m^{1/2}$. So, these results are in the bottom part of the range established in [31]. However, the range of the static results is around 2.6 MPa $m^{1/2}$. On this respect, the numerical and standard solutions were in agreement. Thus, this difference has to be explained based on more experimental analysis of the crack initiation conditions.

As a final remark, all these different procedures of evaluations have demonstrated that it is very important to select the proper method of calculation of the SIF and give the proper interpretation of the results. Otherwise, the diverse approximations and limitations may lead to wrong results. Furthermore, the static calibration of a dynamic test is intrinsically incorrect.

4.6 Summary.

The numerical analysis results have shown that under dynamic loading, the fracture toughness of the specimens decreases, with respect to the static counterpart. Also, it has been observed that as the size of the crack decreases, there is an increase of the fracture toughness under static and dynamic pressure loading. The explanation of these observations is not straightforward, because several factors are involved.

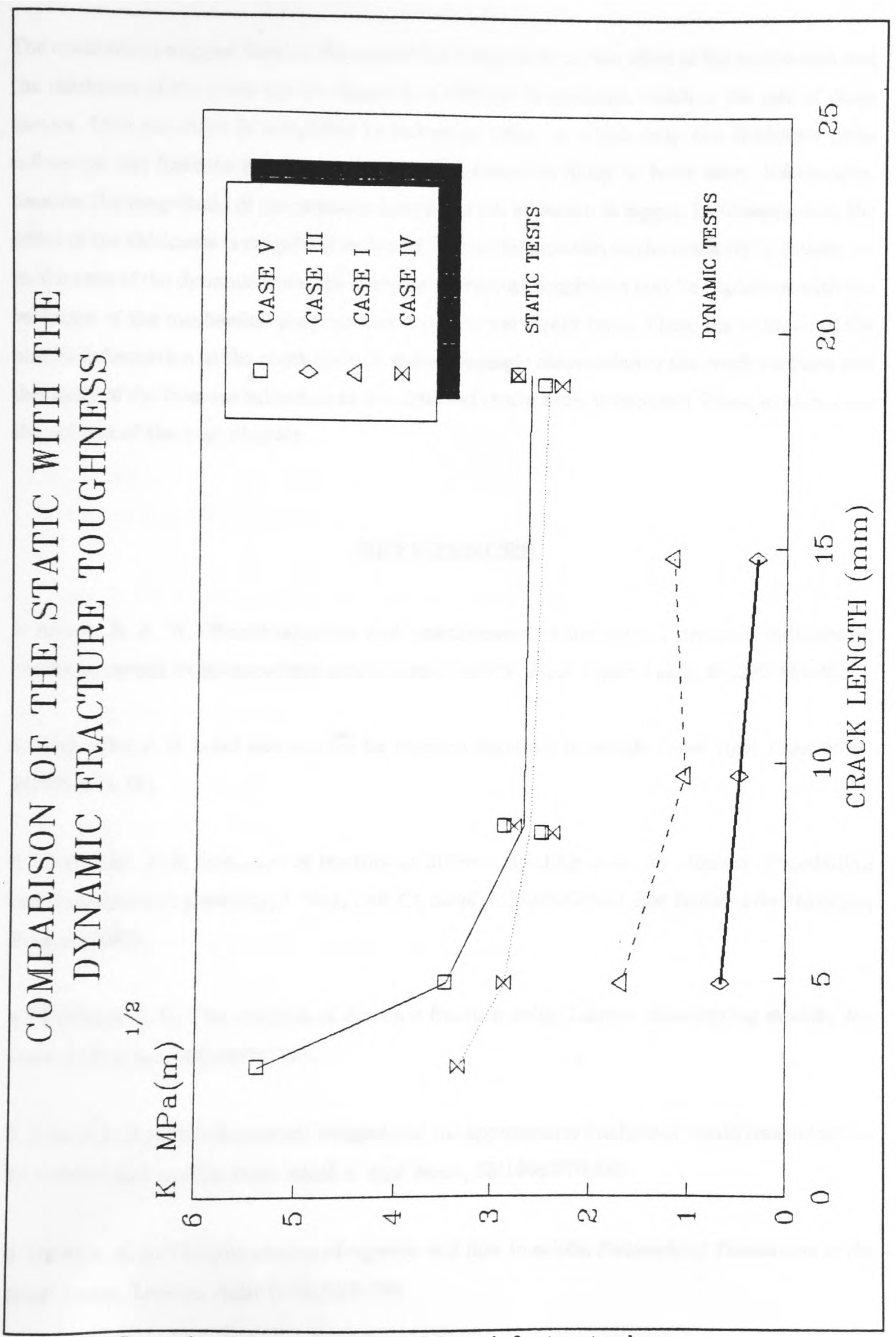


Figure 4.30 Comparison between the static and dynamic fracture toughness.

The conclusions suggest that, in the case of the dynamic tests, the effect of the strain rate and the thickness of the plate are combined. It is difficult to establish which is the role of these factors. This situation is simplified in the static tests, in which only the thickness plate influences the fracture process. Besides, the specimen is likely to have more deformation, because the magnitude of the pressure load for crack initiation is bigger. In consequence, the effect of the thickness is magnified and more plastic deformation at the crack tip is developed. In the case of the dynamic tests, the decrease in fracture toughness may be explained with the variation of the mechanical properties at the observed strain rates. Thus, the analysis of the plastic deformation at the crack tip with the microscopic observation of the crack surfaces and the study of the fracture behaviour at the observed strain rates is required. These analyses are the subject of the next chapter.

REFERENCES

1. Mines, R. A. W. Characterization and measurement of the mode I dynamic initiation of cracks in metals at intermediate strain rates-a review. *Int. J. Impact Engng*, 9(1990)441-454.

2. Klepaczko, J. R. Load rate spectra for fracture initiation in metals. *Theor. Appl. Fract. Mech.* 1(1984)181-191.

3. Klepaczko, J. R. Initiation of fracture at different loading rates: an attempt of modelling based on dynamic plasticity, *J. Phys., Coll. C5, Suppl. 8* C5245-C5250. Les Editions de Physique, France (1985).

4. Williams, J. G. The analysis of dynamic fracture using lumped mass-spring models, *Int. Journ. of Fracture*, 33(1987)47-59.

5. Rice, J. R. A path independent integral and the approximate analysis of strain concentration by notches and cracks, *Trans. ASME J. Appl. Mech.*, 35(1968)379-386.

6. Griffith, A. A. The phenomena of rupture and flow in solids, *Philosophical Transactions of the Royal Society*, London, A221 (1921)163-198.

7. Kanninen, M. F. and Popelar, C. H. *Advanced Fracture Mechanics*, The Oxford Engineering Science Series, Oxford University Press (1985).

8. Irwin, G. R. Structural aspects of brittle fracture, *Appl. Mats. Res.* 3(1964)65-81.

9. Ewalds, H. L. and Wanhill, R. J. H. *Fracture Mechanics*, Edward Arnold and Delftse Uitgevers Maatschappij publishers, London (1989).

10. Kishimoto, K. Aoki, S. and Sakata, M. On the path independent integral $\hat{J}$, *Engng Fracture Mech.* 13(1980)841-850.

11. Zienkiewicz, O. C. and Cheung, Y. K. *The Finite Element Method in Structural and Continuum Mechanics*, McGraw-Hill, London, 1967.

12. Cook, R. D. *Concepts and Applications of Finite Element Analysis*, John Wiley and Sons (1974).

13. Parks, D. M. The virtual crack extension method for nonlinear material behaviour, *Comp. Meth. in Appl. Mech. and Engng.* 12(1977)353-364.

14. Hibbitt, D., Karlsson, B. I., Sorenson, P. *ABAQUS Theory Manual*, version 4.8, Hibbitt, Karlsson & Sorenson, Inc., Rhode Island (1989).

15. Hibbitt, D., Karlsson, B. I., Sorenson, P. *ABAQUS User's Manual*, version 4.8, Hibbitt, Karlsson & Sorenson, Inc., Rhode Island (1989).

16. Gdoutos, E. E. *Fracture Mechanics Criteria and Applications*, Kluwer Academic Publishers, Dordrecht, The Netherlands, (1990).

17. Westergaard, H. M. Stresses at a crack, size of the crack and the bending of reinforced concrete, *Proceedings of the American Concrete Institute*, 30(1934)93-102.

18. Westergaard, H. M. Bearing pressures and cracks, *Trans. ASME J. Appl. Mech.* 6(1937) A.49-A.53

19. Williams, M. L. On the stress distribution at the base of a stationary crack, *Trans. ASME J. Appl. Mech.* 24(1957)109-114.

20. Muskhelishvili, N. I. *Some Basic Problems of the Mathematical Theory of Elasticity* (transl. from the Russian by J. R. M. Radok) 2nd ed. Noordhoff Int. Publ., The Netherlands (1975).

21. Williams, M. L. The bending stress distribution at the base of a stationary crack. *Trans. ASME J. Appl. Mech.,* 28(1961)78-82.

22. Sih, G. C., Paris, C. and Erdogan, F. Crack-tip stress intensity factors for plane extension and plate bending problem, *Trans. ASME J. Appl. Mech.* 29(1962)306-310.

23. Sih, G. C. Flexural problems of cracks in mixed media, *Proceedings of the First International Conference on Fracture*, (eds. T. Yokobori, T. Kawasaki and J. L. Swedlow), Sendai, Japan, 1(1965)391-409.

24. Erdogan, F., Tuncel, O. and Paris, P. C. An experimental investigation of the crack tip stress intensity factor in plates under cylindrical bending, *Trans. ASME J.of Basic Engng.*, (1962)542-546.

25. Hartranft, R. J. and Sih, G. C. Effect of plate thickness on the bending stress distribution around through cracks, *J. Math. and Phys.*, 47(1968)276-291.

26. Knowles, J. K. and Wang, N. M. On the bending of an elastic plate containing a crack, *J. Math. and Phys.,* 39(1960)223-236.

27. Rooke, D. P. and Cartwright, D. J. *Compendium of Stress Intensity Factors*, Procurement Executive, Ministry of Defence, Her Majesty's Stationary Office, London (1976).

28. Williams, J. G. *Fracture Mechanics of Polymers*, Ellis Horwood Limited, Chichester, England (1987).

29. Clough, R. W. and Penzien, J. *Dynamics of Structures*, McGraw-Hill Book Company (1975).

30. Reismann, H. *Elastic Plates, Theory and Application*, John Wiley & Sons (1988).

31. Marshall, G. P. and Williams J. G. The correlation of fracture data for PMMA, *J. Mater. Sci. Letters*, 8(1973)138-140.

CHAPTER 5

INTERPRETATION OF THE RESULTS

5.1 Introduction.

The analysis of the experimental results has demonstrated that lower pressure loads are required to initiate a crack in dynamic than in static conditions, although in both cases the cracks propagated under brittle conditions. Likewise, the fracture toughness under static conditions is higher than under dynamic conditions.

In the dynamic crack initiation tests, the data collected with strain gauges at the crack tip has shown that the fracture process occurs at different levels of strain-rate. In other words, the graph 3.11 indicates that before the crack initiates, the strain rate is constant. Furthermore, from a theoretical point of view, the strain rate can be considered almost infinite just before the crack initiates. However, it can be assumed that this period is small and some yielding is developed at the crack tip, limiting the strain rate. Hence, crack initiation is likely to be affected only by the initial strain rate which in the tests is below 40 s^{-1}.

In brief, the last part of the evaluation of the fracture toughness in dynamic conditions requires the assessment of several factors, namely, the analysis of the variation of the mechanical properties at the observed strain rates, the analysis of the crack surfaces at the crack tip and the evaluation of the accuracy of the numerical solution. With all this information, a complete picture of the fracture process can be established and the differences

observed between the static and dynamic results can be explained.

5.2 Evaluation of the Mechanical Properties of PMMA at Different Strain Rates.

5.2.1 Description of the Testing Rig.

Preliminary tests showed that the evaluation of the PMMA mechanical properties in tension with a universal testing machine is limited to a low range of strain rates, because the cross-head speed is low and the gauge length of the specimens is relatively large. In consequence, the hydraulic universal rapid-load test machine, which was developed by Cooper and Campbell [1], was chosen. It is capable of testing at crosshead velocities up to 1 m/s and the strain rate range obtained in tension tests is up to 100 s^{-1}. A schematic arrangement and a photograph of the machine and associate recording equipment are shown in figures 5.1 and 5.2 respectively.

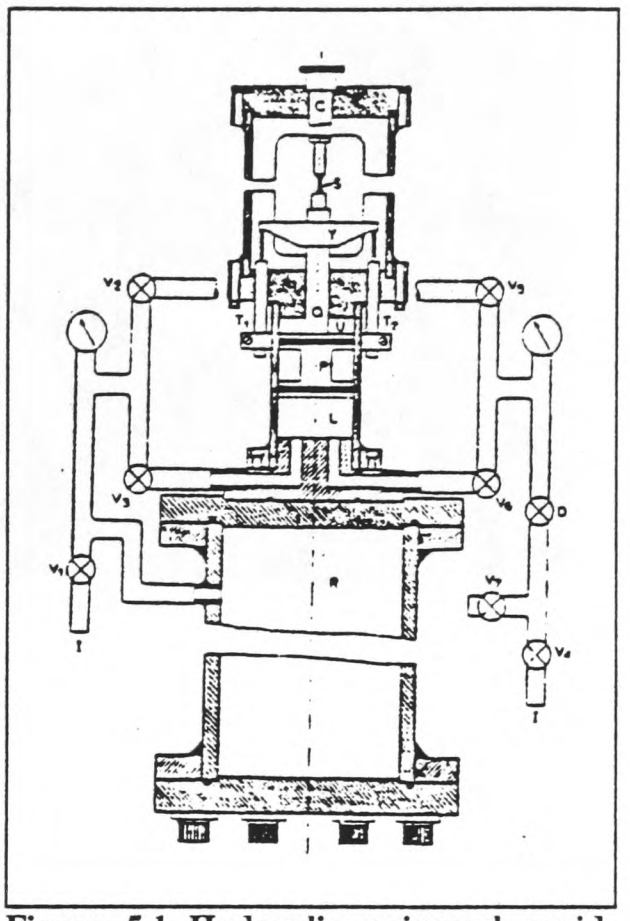


Figure 5.1 Hydraulic universal rapid-load test machine. After Cooper et. al. [1].

This testing machine is operated in the following way. Oil is supplied at a pressure of up to 13.8 MPa at the inlet pipes I and is used to pressurize the reservoir R, through the valve V_1. The upper cylinder U and the lower cylinder L are connected with either the opening valves V_2 and V_3. The pressure applied to one side of the piston P is counteracted by the pressure applied to its other side through valves V_4 and V_5 or V_6. The specimen S, which is connected between the piston rod Q and the load cell C, is under no load or under any desired static preload.

The load is applied by operating, by means of a solenoid, the quick-acting release valve V_7. This permits oil to flow out to the outlet pipe, through valves V_5 or V_6, and the damping unit D, whose orifice size determines the nominal strain rate in a given test. For this purpose, a circular plate pierced by six holes of different sizes is incorporated and it may be rotated, so as to bring any of these holes into line with the oil pipe.



Figure 5.2 Hydraulic universal testing machine and associate equipment.

The opening of the release valve V_7 also triggers the recording system, which registers the information with a DL902 Datalab transient recorder. It is a digital instrument designed to capture a single shot or low repetition events and present them for a continuous display on the screen of an oscilloscope. This instrument features two independent signals inputs each of which can digitise and store waveforms at a maximum sample rate of 1 MHz per channel. Each signal is recorded simultaneously in a 2048 sample memory or, alternatively, the signal at input 1 can be recorded in one memory, whilst samples from a previous sweep are retained in the second. A plug-in card position is incorporated in the unit for the inclusion of a microcomputer.

The information is displayed on a CS-1021 Trio oscilloscope, which is a dual trace, for an analysis of the test quality. Its vertical sensitivity range is from 1 mV/div to 5 V/div and the high sweep speed is 50 ns/div (x10 MAG). The data is saved with an IBM PC with the code TRANS, which has been especially written for this purpose.

5.2.2 Fabrication of the Specimens.

The design considerations of specimen took into account several factors. Firstly and most important, the specimens have to be made from the same sheets of PMMA that were used for the fabrication of the cracked specimens. Secondly, the gauge length of the specimens has to be as small as possible and thirdly, special grips are required for fixing the specimens with the loading devices of the testing machine.

The specimens were machined to the dimensions shown in figures 5.3. Steel grips, shown in figure 5.4, were bonded to the specimens with a cyanoacrylate adhesive, which is a relative low viscosity fluid based on acrylic monomer and characterized by extremely fast rates of cure. Its ability to fill gaps is limited by its cure mechanism. So, it will not cope with gaps bigger than 0.125 mm. The junction was designed to carry shear load, following the recommendations of Lees [2], namely, that the range dimension of the overlap is between 12 mm and 25 mm, that the design of the joint should minimise peel or cleavage forces and that the thickness of the adhesive within the joint line should be as thin as possible.

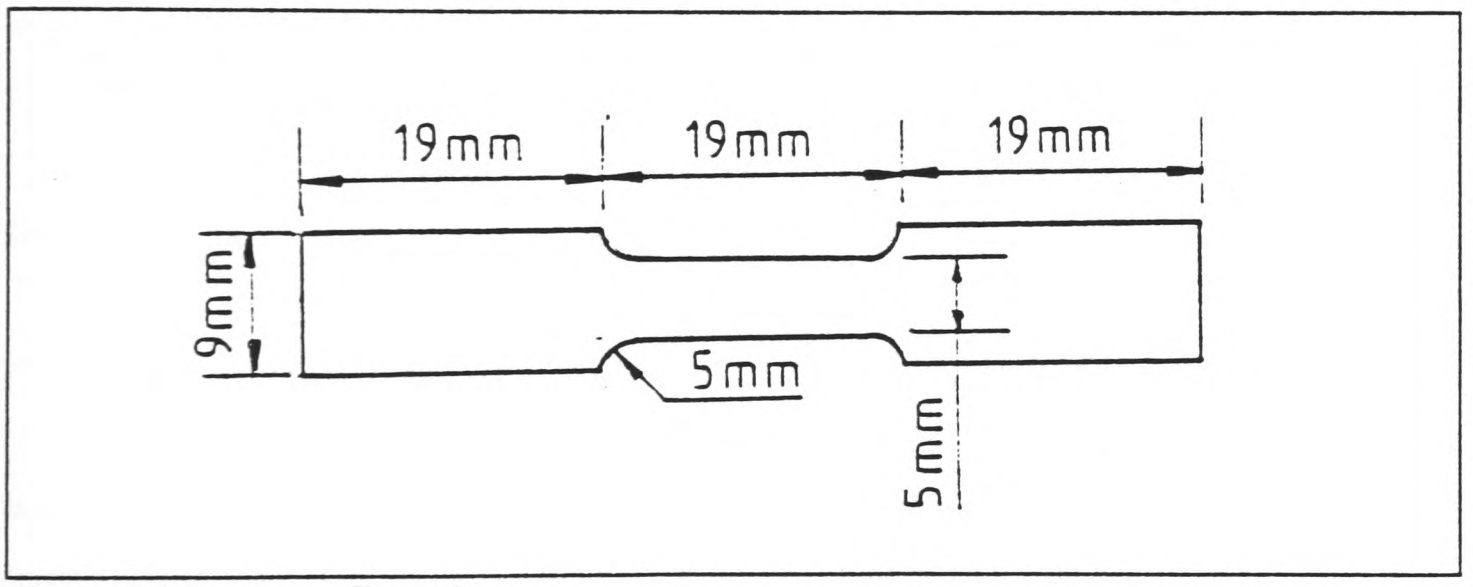


Figure 5.3 Specimen dimensions.

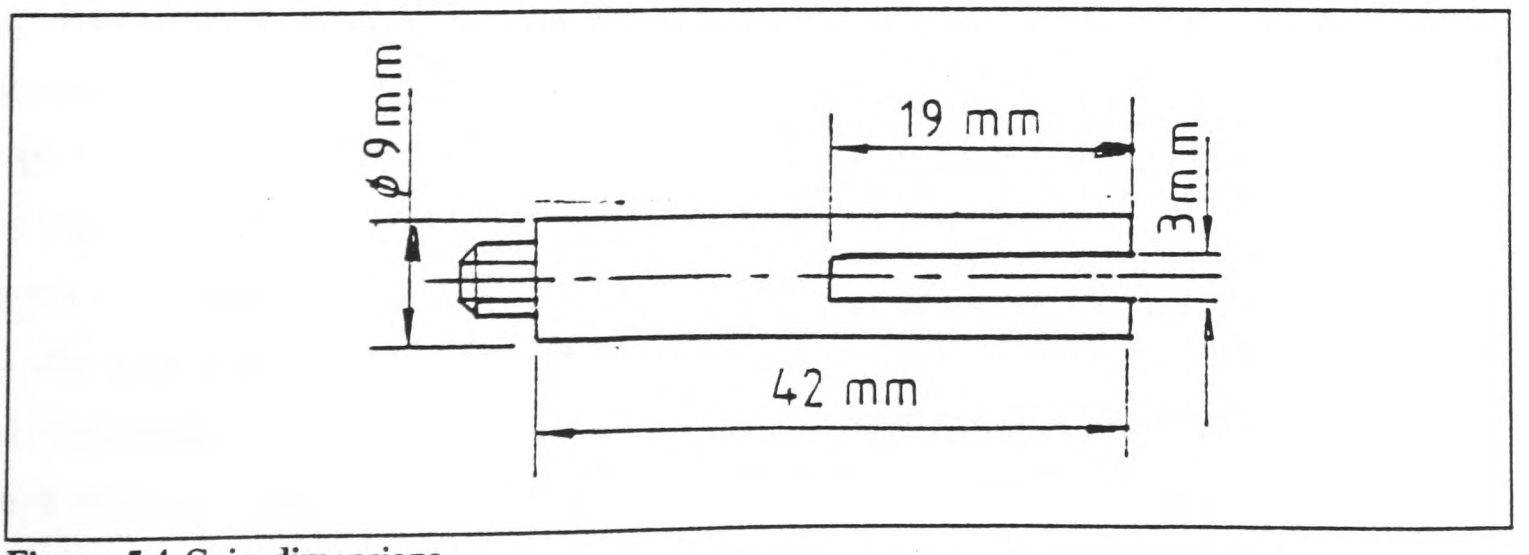


Figure 5.4 Grip dimensions.

In order to ensure that the specimen and the grips were aligned, the steel jig shown in figure 5.5 was used. It is a rack, in which the specimens with both of their grips are put between a couple of inclined surfaces, after the adhesive was applied. Then, both joints are pressurized with screws, which are accommodated on steel strips, that are clamped at their ends, until the glue set. Figure 5.6 shows the resultant assembly for the tension tests.

5.2.3 Description of the Test.

The procedure that was followed in all these tension tests, and in accordance with figure 5.1, consists of the following steps. Initially, the tension load cell C and its platen are fitted and the required orifice of the damping unit is fixed. Then, the valves V_2 and V_6 are opened, while valves V_3 and V_5 are closed. Afterwards, the specimen is positioned centrally on the loading platen by means of a split centring ring and the knurled nut on the tensile load cell is left quit slack in order to eliminate the possibility of any unintentional preloading. Once the specimen is in position, the pressure is increased on both sides of the piston by adjusting the valves V_1 and V_4. When the required cylinder pressure is reached, the valves V_1 and V_4 are shut. Finally, the valve V_7 is operated, loading the specimen and the data registered by the transducers is recorded.

In this series of tests, the top grip was attached to a load cell, which is instrumented with four Micro-Measurements CEA-06-125UN-120 strain gauges. They are polyimide-encapsulated Constantan gauges and are primarily used for general-purpose static and dynamic stress analysis. Their output has been calibrated in order to obtain the applied load.

The bottom grip of the specimen was joined to the moving crosshead and both elements were instrumented with a TRANS-TEK linear variable differential transformer (LVDT) series 100. Its principle of operation is based on magnetic induction. So, the output voltage is directly proportional to the relative velocity over its working range, which is 12.5 mm. Its maximum velocity is limited by the output voltage of the velocity transducer, which is 500 V. Besides, it has zero hysteresis and no excitation is required. In the case of the tension tests, the output was integrated, therefore, the deformation across the specimen was measured. The resultant strain rates, stresses and strains were calculated, when the data was processed with the code LOTUS.

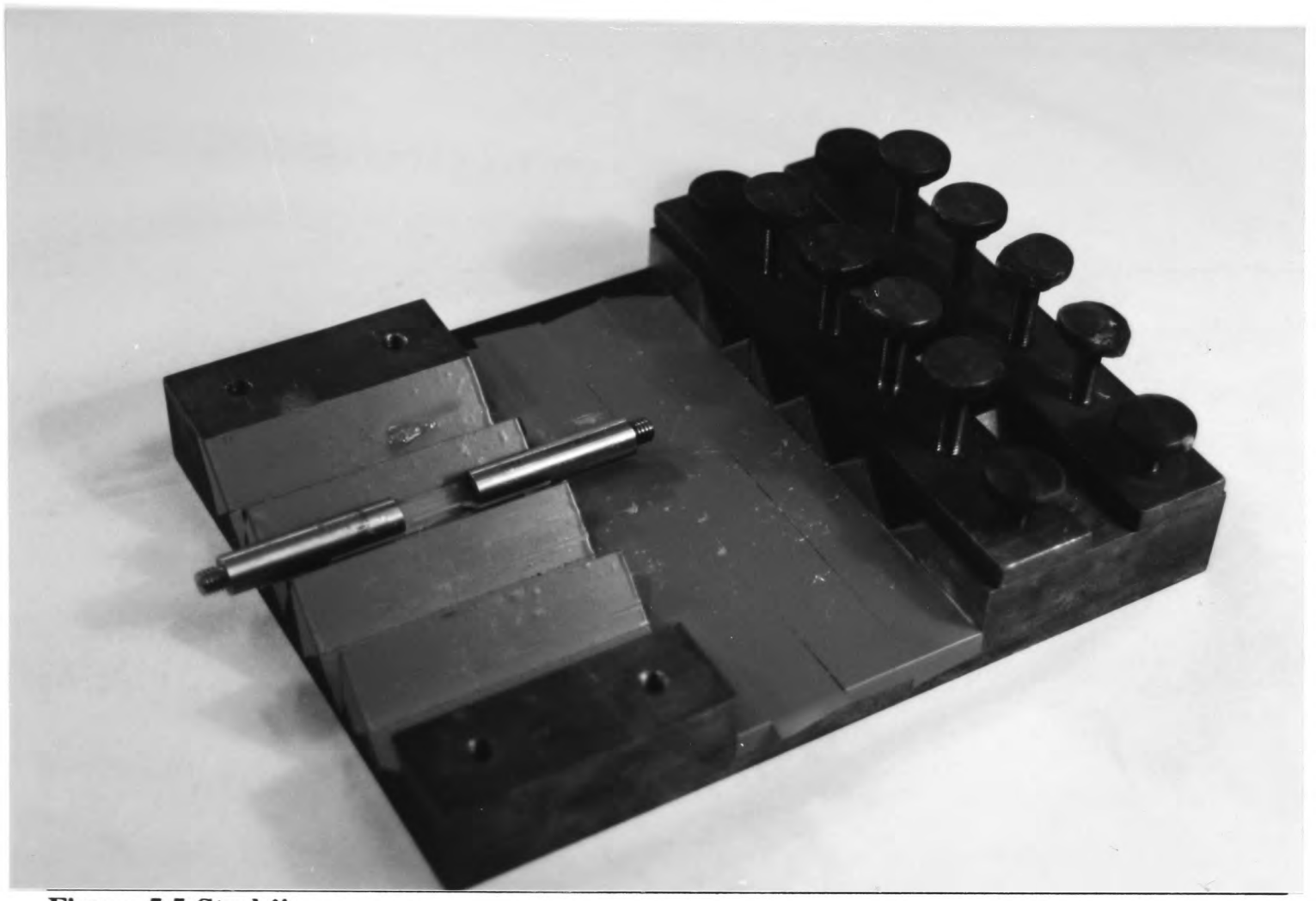


Figure 5.5 Steel jig.

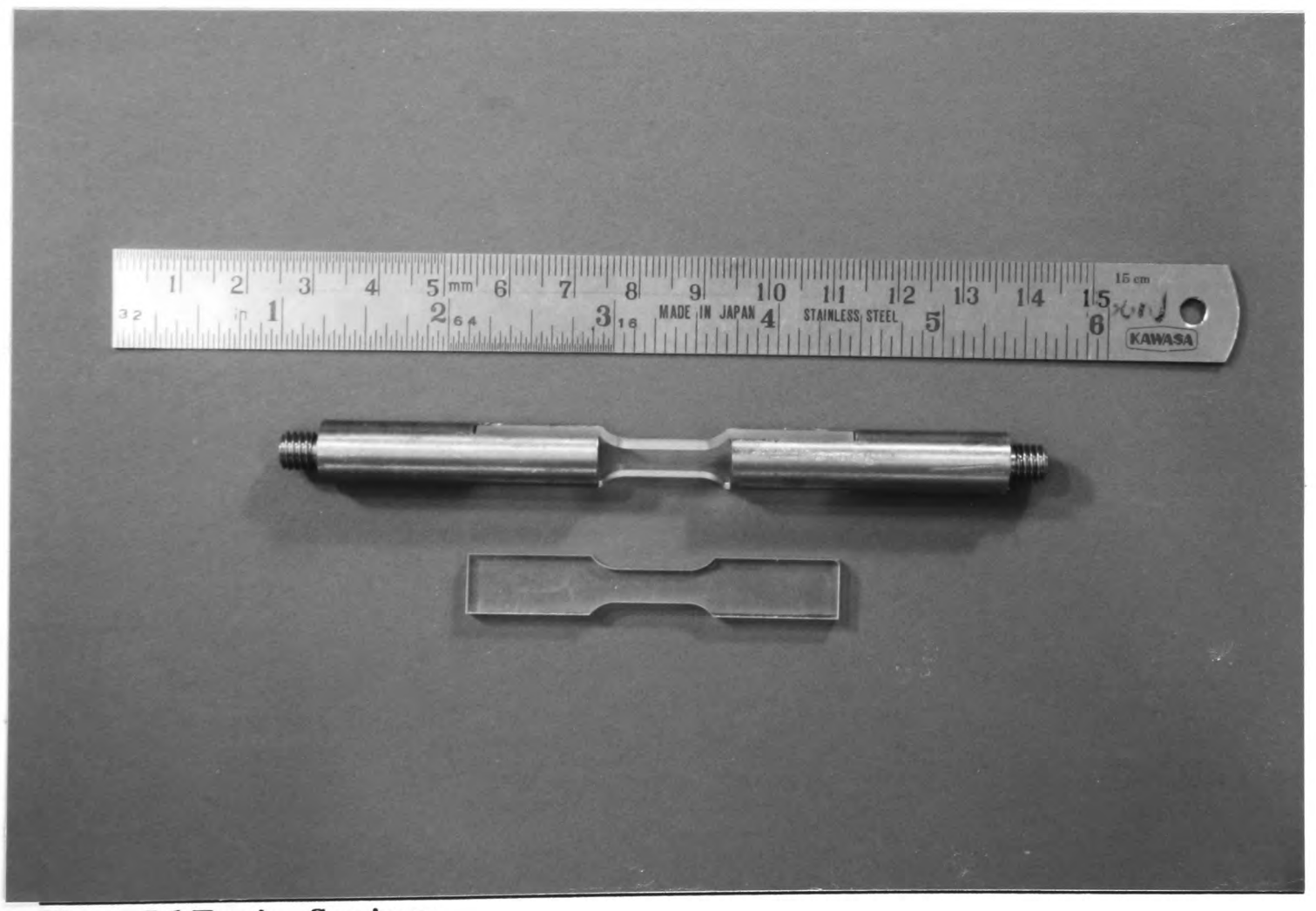


Figure 5.6 Tension Specimen.

This instrumentation was selected because the main interest was the evaluation of the variation of the modulus of elasticity and the tensile strength with respect to the strain rate. In this case, the load and deformation can be measured until the specimen is broken. An alternative procedure is to measure the specimen strains with strain gauges bonded on the specimen. However, it is unclear if the gage defoils or the specimen fails at the end of each test.

A fact taken into consideration is that the deformation measured includes the compliance of the specimen and grips. Nevertheless, large loads are unlikely and the steel grips are considerably stiffer than the specimens. Thus, the error in the strain evaluation is reduced.

5.2.4 Results Obtained.

Three test were carried on with different cross-head velocities and an additional test, in which the width of the specimen gauge length was reduced to 3 mm, was performed in order to get results with a higher strain rate. Figure 5.7 shows a typical strain history of the first two tests, which were virtually performed at constant strain rate. However, in the other two, the strain rate varied from zero to a maximum value. In these situations, the slope of the curve gives the strain rate at a specific instant. Typical results are shown in figure 5.8.

The resultant stress-strain relation of the last two cases shown are in figures 5.9 and 5.10 respectively, in which the failure of the specimen is denoted by the vertical line at the end of each curve. Table 5.1 summarizes the test results.

TABLE 5.1
RANGE OF STRAIN RATES

TEST	STRAIN RATE RANGE (s^{-1})	FRACTURE STRESS (MPa)	FRACTURE STRAIN
1	0.15	58.4	0.0219
2	2.0	78.0	0.0239
3	0 - 20.0	85.0	0.0238
4	0 - 35.0	120.3	0.0270

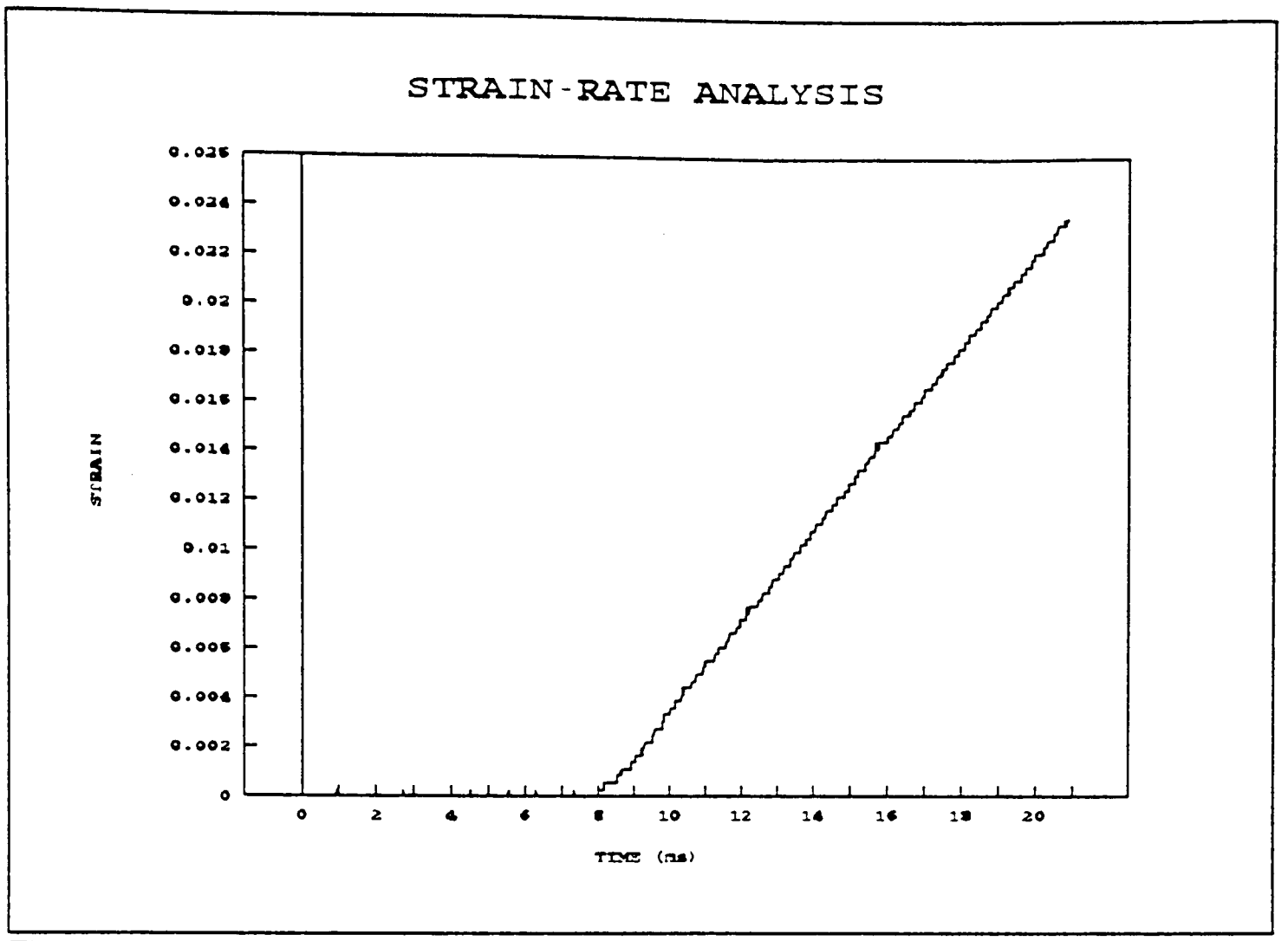


Figure 5.7 Strain-rate curve of test 2.

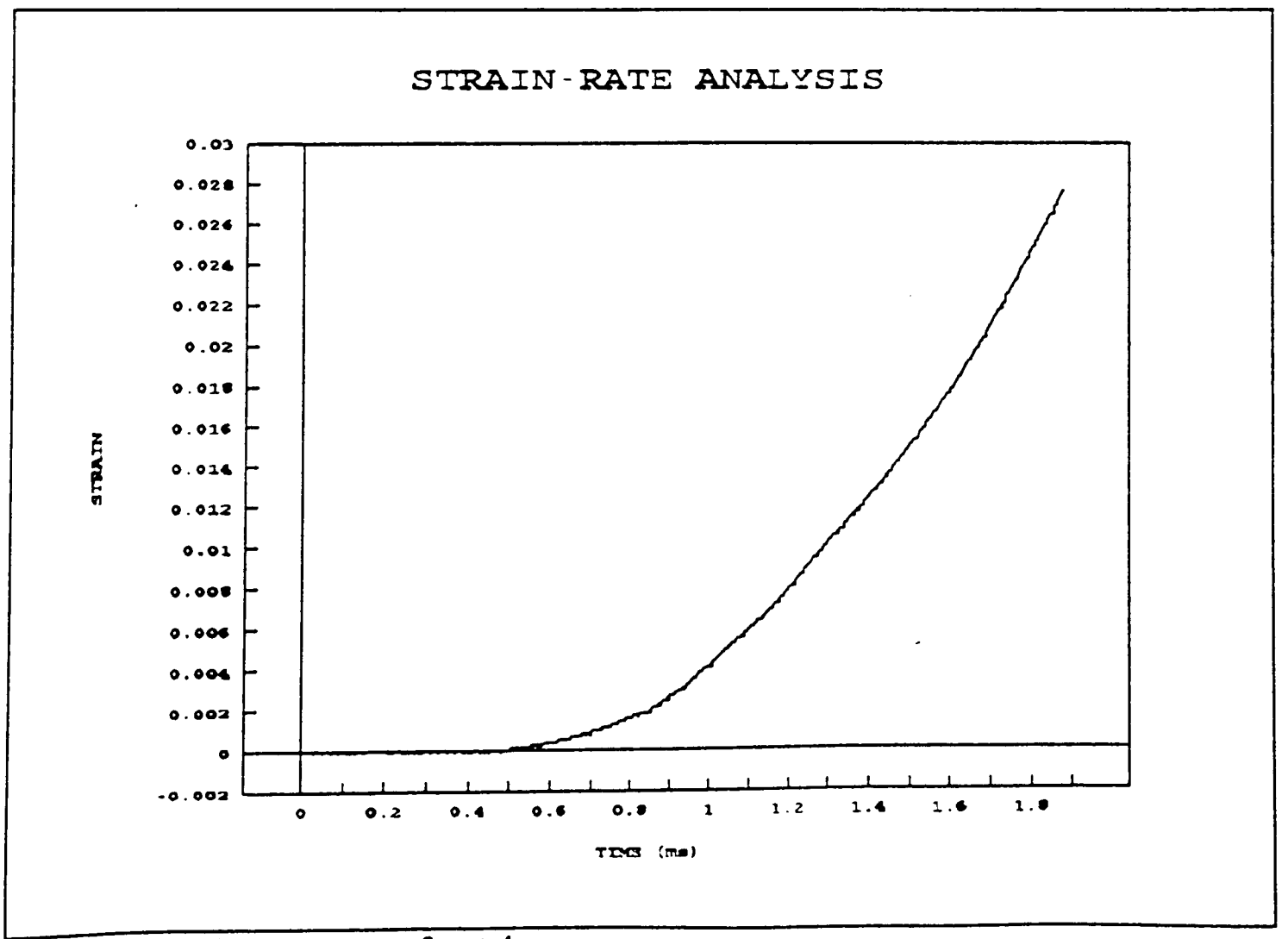


Figure 5.8 Strain rate curve of test 4.

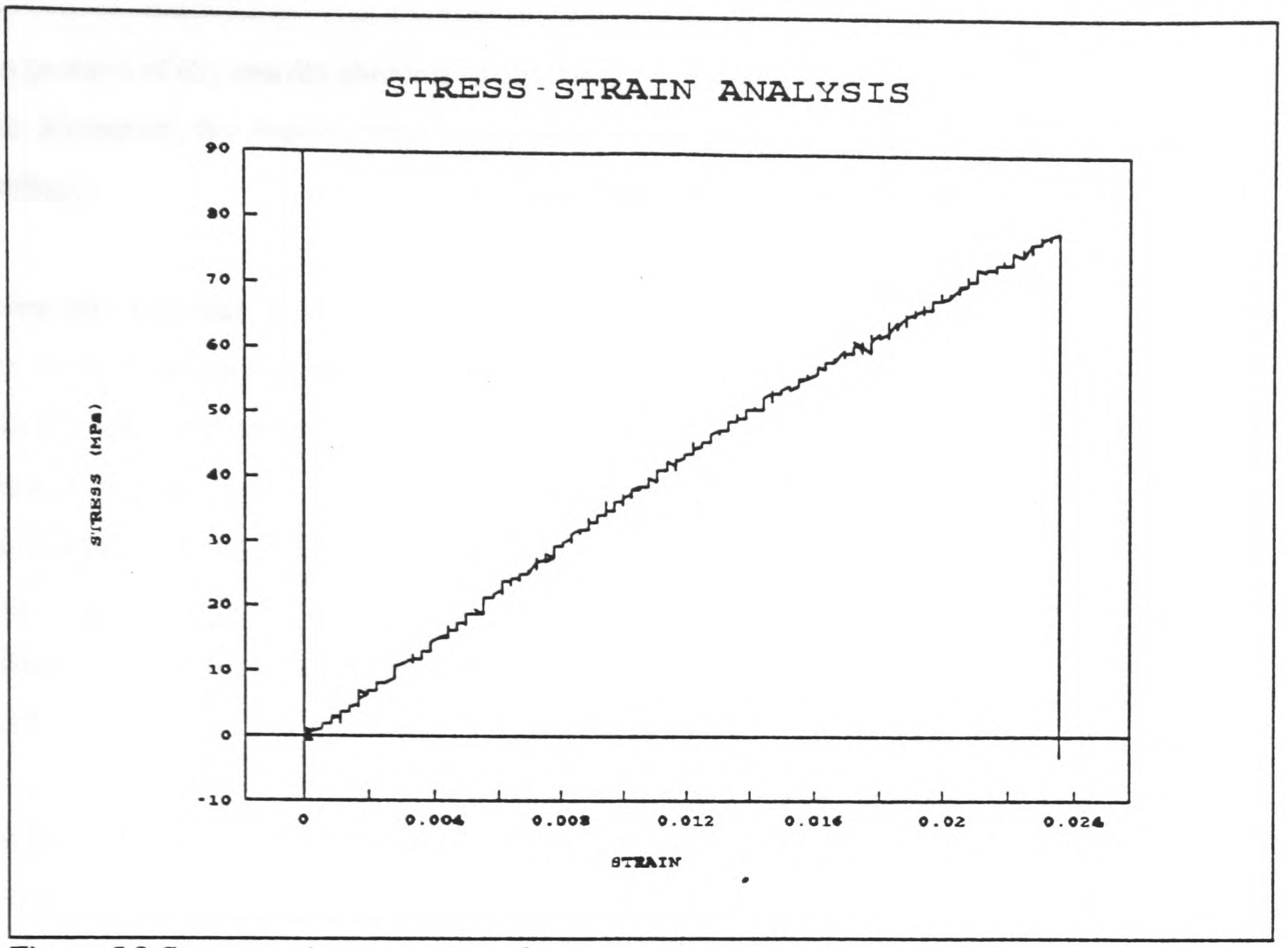


Figure 5.9 Stress-strain curve of test 2.

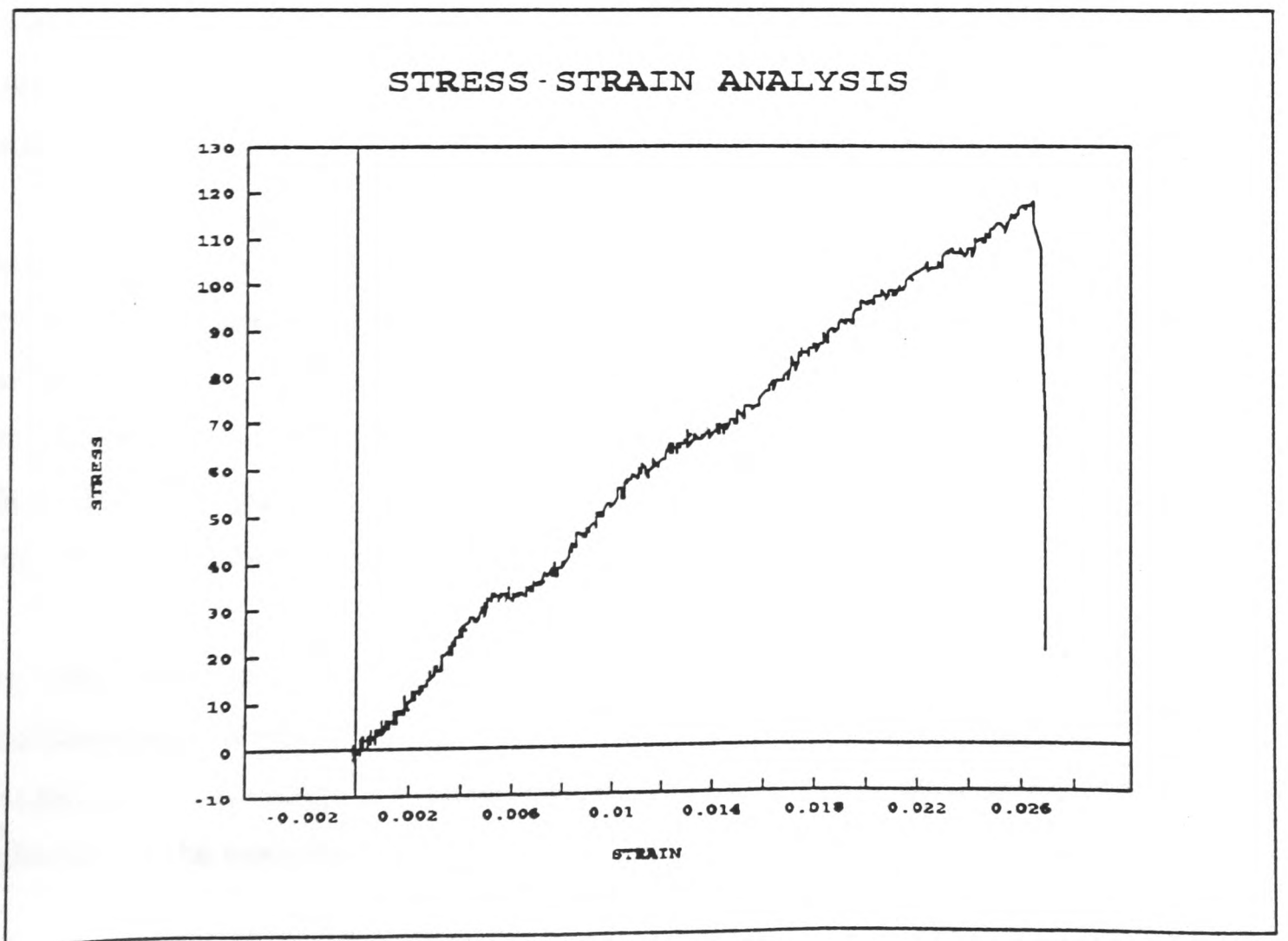


Figure 5.10 Stress-strain curve of test 4.

The pattern of the results shows that the fracture stresses and strains increase with the strain rate. Moreover, the post-mortem analysis of all the specimens showed that they failed without yielding.

Stress-strain relations at constant strain rate were constructed from the recorded data by selecting points in all the curves which have the same slope. The curves obtained are shown in figure 5.11 and this data is summarized in table 5.2, which relates the Young's modulus with the strain rate.

TABLE 5.2
MODULUS OF ELASTICITY AT DIFFERENT STRAIN RATES

STRAIN RATE (s^{-1})	MODULUS OF ELASTICITY (GPa)
0.15	2.9
2.0	3.2
20.0	3.8
35.0	4.3

The experimental data related with the evaluation of the mechanical properties of PMMA at different strain rates and at room temperature is not abundant in the open literature. In particular, in table 5.3 are compared the value of the modulus of elasticity obtained with the information reported by Kobayashi et. al. [3], the manufacturer of the specimen material [4], Beadmore [5] and Katsamanis et. al. [6].

Kobayashi et. al. [3] evaluated the mechanical properties for the three lowest strain rates reported with an Instron-type tensile tester UTM-1, made by Tokyo-Baldwin. In the case of the test at 48 s^{-1}, a UTM-5, which is originally designed to fit elastomers showing large deformations, was employed. Therefore, a "slack-grip" was installed to eliminate transient effects. The breaking load was measured with the load cell in all cases and no special grips were used with UTM-1 tensile tester.

The information given by the manufacturer of the PMMA sheets [4] indicates that the specimens were extended at a constant rate and the load and extension were measured simultaneously. An extension gauge was attached to the specimen gauge length for the evaluation of the modulus.

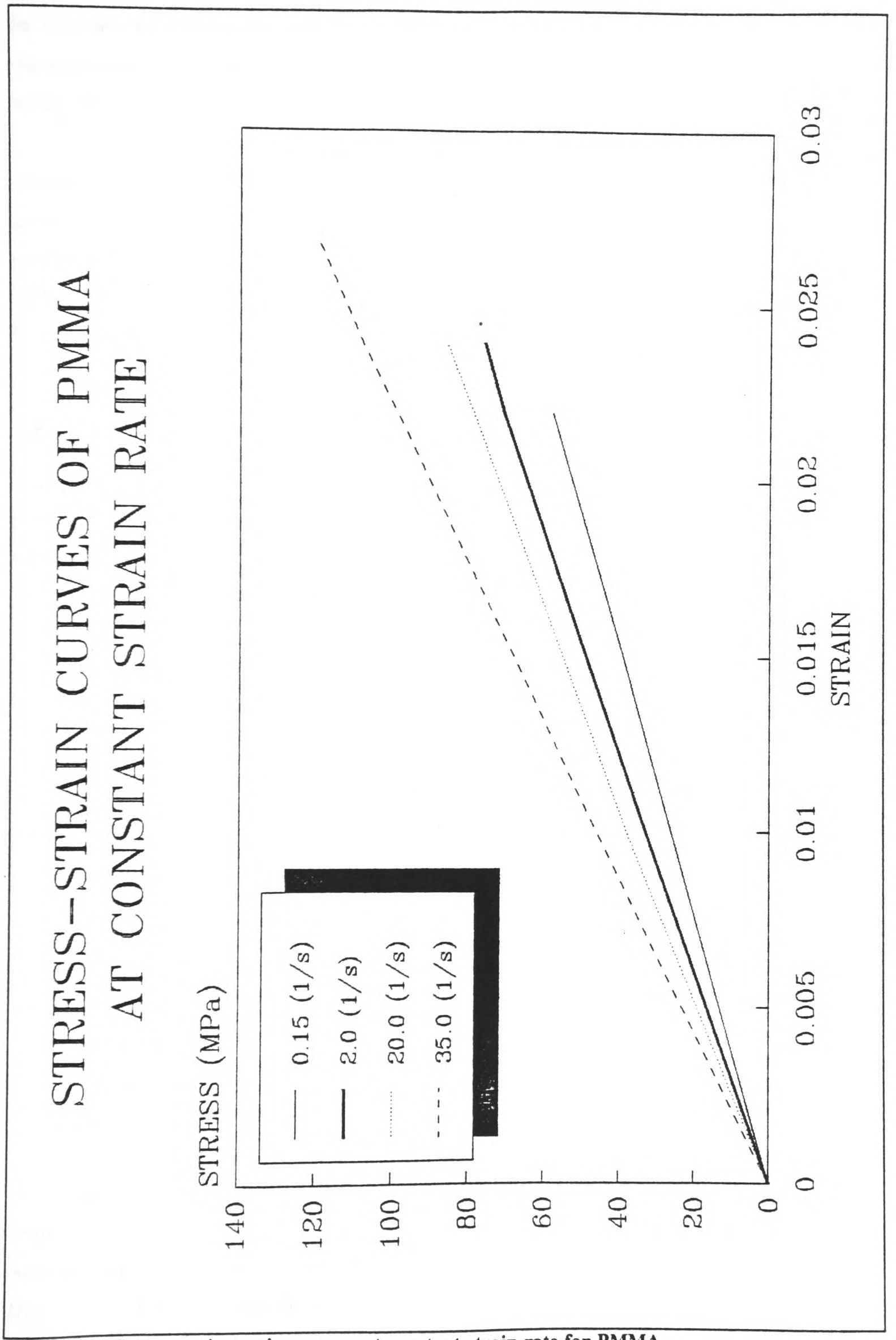


Figure 5.11 Stress-strain tension curves at constant strain-rate for PMMA

In relation with the tensile tests performed by Beardmore [5], it has only been reported that the specimens were tested in an Instron testing machine and the temperature was carefully controlled.

Katsamanis et. al. [6] evaluated the modulus of elasticity with a Hopkinson bar, using a strain gauge technique for the measurements of the strains and loads. This bar was impacted by a projectile fired from the air-gun.

TABLE 5.3
COMPARISON OF THE MODULUS OF ELASTICITY OF PMMA AT VARIOUS STRAIN RATES

STRAIN RATE (s^{-1})	MODULUS OF ELASTICITY (GPa)	TESTING TECHNIQUE	REFERENCE
2.6×10^{-7}	1.0	Instron-type tensile test at constant rate	Kobayashi et. al. [3]
0.00001	2.6	Specimen extended at constant rate	ICI [4]
0.0001	2.9	Specimen extended at constant rate	ICI [4]
0.0007	1.9	Instron-type tensile test at constant rate	Beardmore [5]
0.001	3.1	Specimen extended at constant rate	ICI [4]
0.01	3.3	Specimen extended at constant rate	ICI [4]
0.026	2.0	Instron-type tensile test at constant rate	Kobayashi et. al. [3]
0.15	2.9	Hydraulic universal rapid-load test	This work
2.0	3.2	Hydraulic universal rapid-load test	This work
20.0	3.8	Hydraulic universal rapid-load test	This work
35.0	4.3	Hydraulic universal rapid-load test	This work
48.0	4.0	Instron-type tensile test at constant rate	Kobayashi et. al. [3]
100.0	5.5	Hopkinson bar	Katsamanis et. al. [6]

For the comparison of these data, it has to be borne in mind that, according to the testing information available, the compliance of the testing set up in [3] and [5] is higher than in [4], in which the deformations were measured from the gauge length. In consequence, the modulus of elasticity obtained in the former two cases tends to be lower than in the last one.

With respect to the testing evaluations performed in this work, special care was taken to reduce the compliance of the system specimen-testing machine. Nevertheless, the deformations were not evaluated on the gauge length of the specimen. Thus, the results tend to be smaller than those of [4]. In general terms, the results obtained in this work can be considered

acceptable, in range and reflect the sensitivity of the mechanical properties to the strain rate.

Finally, the comparison of the results with those obtained at a greater strain rate [6], confirms that the elasticity modulus increases with the strain rate.

A similar analysis was carried on table 5.4, using some of the information discussed above. In particular, the fracture stresses at different strain rates are compared with the data reported in [4] and [5].

TABLE 5.4
COMPARISON OF THE FRACTURE STRESS OF PMMA AT VARIOUS STRAIN RATES

STRAIN RATE (s^{-1})	FRACTURE STRESS (MPa)	TESTING TECHNIQUE	REFERENCE
0.00001	56.0	Specimen extended at constant rate	ICI [4]
0.0001	69.0	Specimen extended at constant rate	ICI [4]
0.0007	69.0	Instron-type tensile test at constant rate	Beardmore [5]
0.001	81.0	Specimen extended at constant rate	ICI [4]
0.01	89.0	Specimen extended at constant rate	ICI [4]
0.15	58.4	Hydraulic universal rapid-load test	This work
2.0	78.0	Hydraulic universal rapid-load test	This work
20.0	80.3	Hydraulic universal rapid-load test	This work
35.0	120.3	Hydraulic universal rapid-load test	This work

As it can be seen, the results reported in [4] tend to be higher than those obtained in this work. This difference can also be explained with the compliance of the testing set-up. Generally speaking, the increasing pattern of the fracture stress with the strain rate is observed. So, it can be considered that the results of this work are acceptable.

5.3 Analysis of Crack Surfaces.

A survey in the open literature shows that several microscopic techniques have been used to study the characteristics of the fracture surfaces. Among them, the scanning electron microscopy (SEM) and transmission electron microscopy (TEM) have widely been utilized to study the relationship between the crack surface geometry and the crack propagation velocity

mainly. In the case of the present research, this situation is well beyond its scope. On the other hand, the microscopy with low levels of magnifications allows to make general observation of the crack surface, which is the purpose of this analysis. Thus, it was done with an Ultraphot II camera microscope made by Carl Zeiss, which has a 90 mm x 120 mm photo head that is interchangeable with 35 mm photo head or projection head.

5.3.1 Description of the Procedure of Analysis.

The observations were made with an objective which gives x20 magnifications and the specimens were mounted onto a stage, which is circular rotating, centring mechanical with two verniers for perpendicular measurements and suitable for observations with transmitted light. The specimens were carefully cut from the cracked plates, in such a way that rectangular strips were obtained. Their dimensions depend on two factors, namely, the intensity of the transmitted light beam and the space available between the lens of the microscope and the stage. Thus, one of its longest edges is the crack surface and, in order to avoid problems with the microscopic observations, the other longest side was cut parallel at a distance of 10 mm from the crack surface. In fact, it was easy, because the cracks always propagated along the crack plane and a preparation of the observation surface is not required.

All the specimens were mounted on a stage, in such way that their crack surfaces were perpendicular with the observation axis. Then, the areas of interest near the crack tip were spotted and analyzed. In the last part of this procedure, the images of interest were photographed. So, the observed area was projected on the focusing screen of the photo head. Subsequently, the holder for 90 mm x 120 mm film pack was installed with 55 Polaroid film, which is an instant sheet film ISO 50/18° for black and white prints and negatives. Finally, the automatic exposure system was switched on and the picture was taken.

5.3.2 Analysis of the Crack Surfaces of the Specimens Tested under Dynamic Loading.

Typical observations of the crack surfaces of the specimens tested under dynamic loading are shown in figures 5.12, 5.13, 5.14 and 5.15 which correspond to the specimens 25, 29, 32 and 27 and their crack lengths are 4.76 mm, 10.36 mm, 14.46 mm and 19.14 mm respectively. In all those pictures, the left side corresponds to the specimen plane that was under maximum

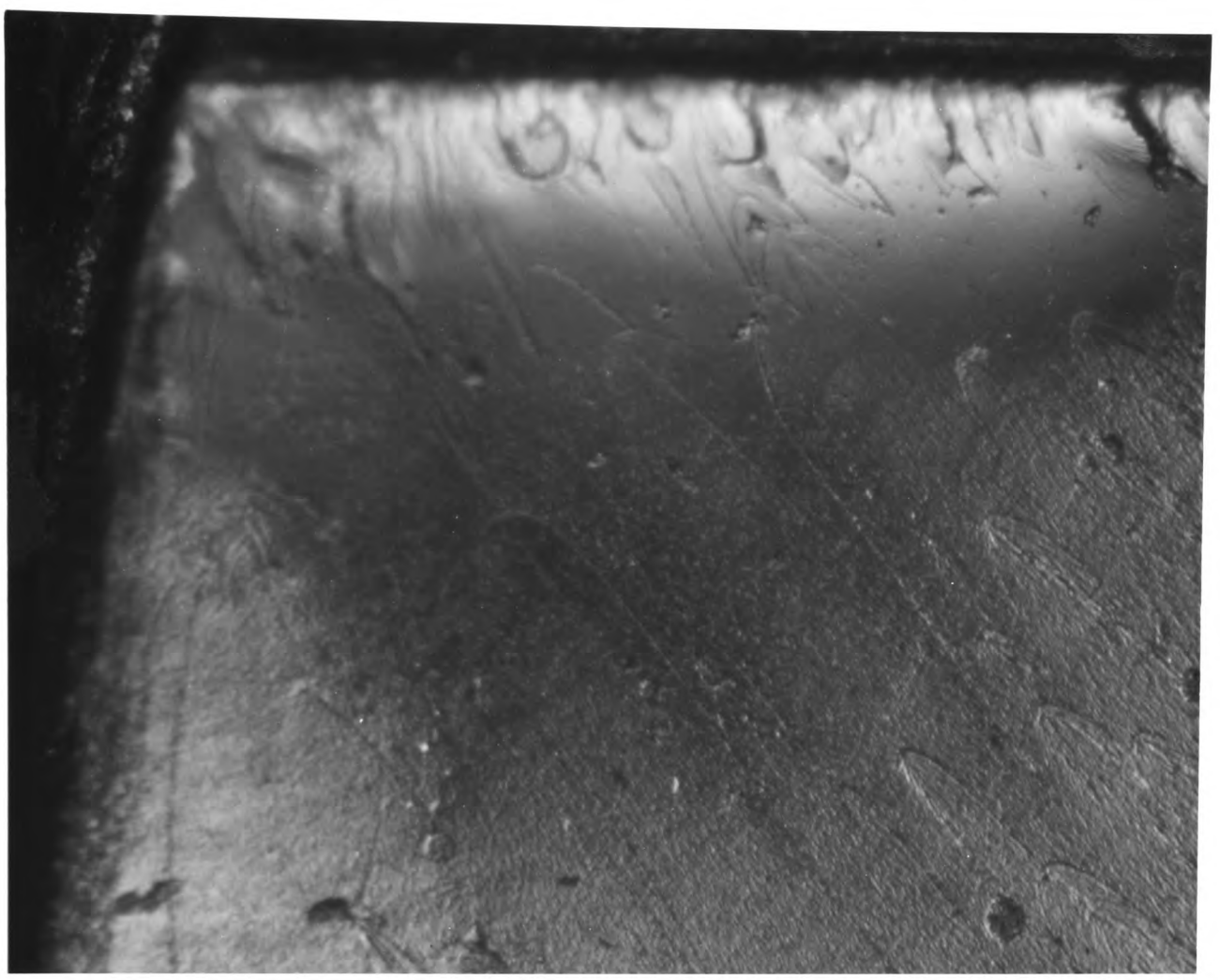


Figure 5.12 Specimen 25 tested under dynamic loading (2a = 4.76 mm).

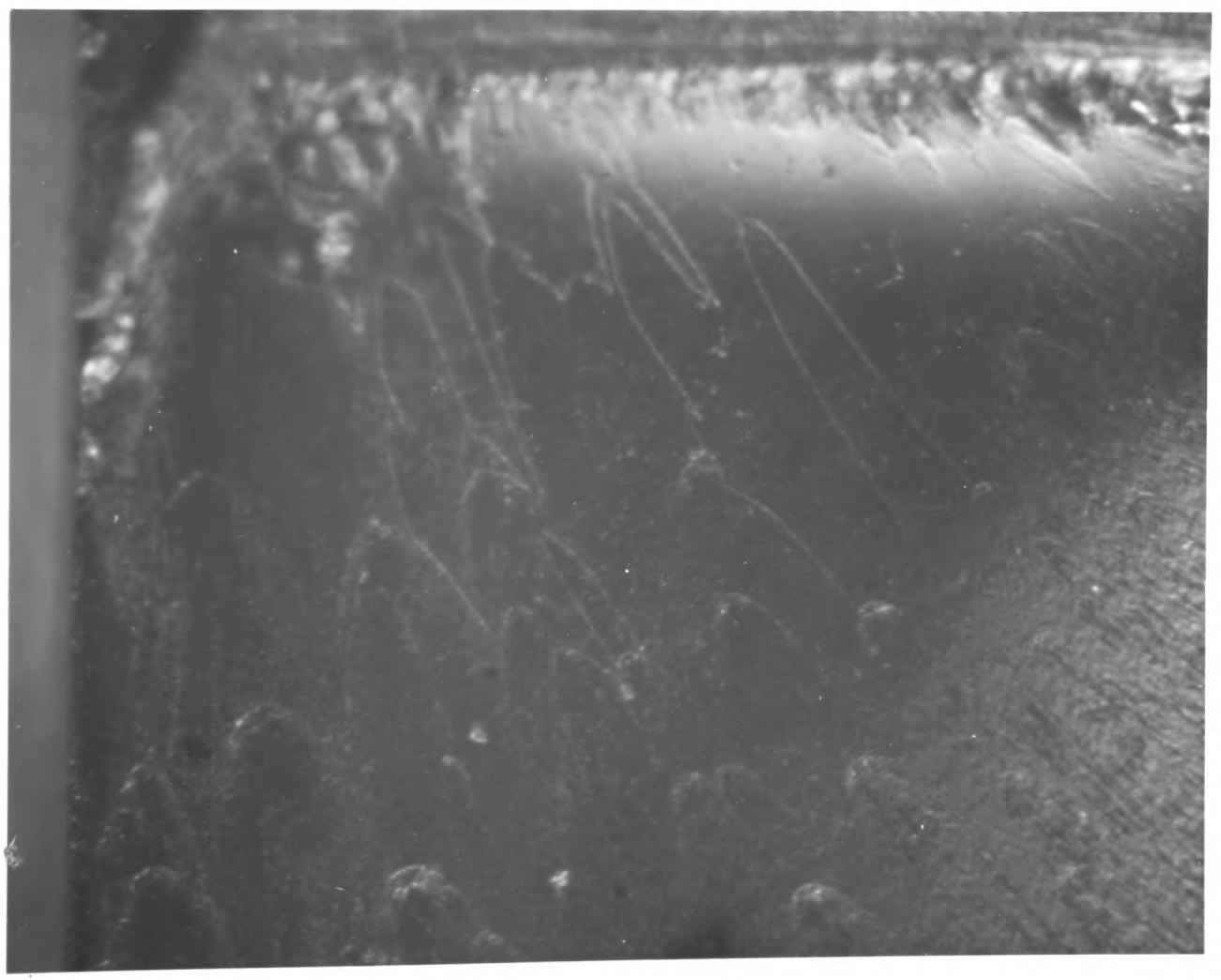


Figure 5.13 Specimen 29 tested under dynamic loading (2a = 10.36 mm).

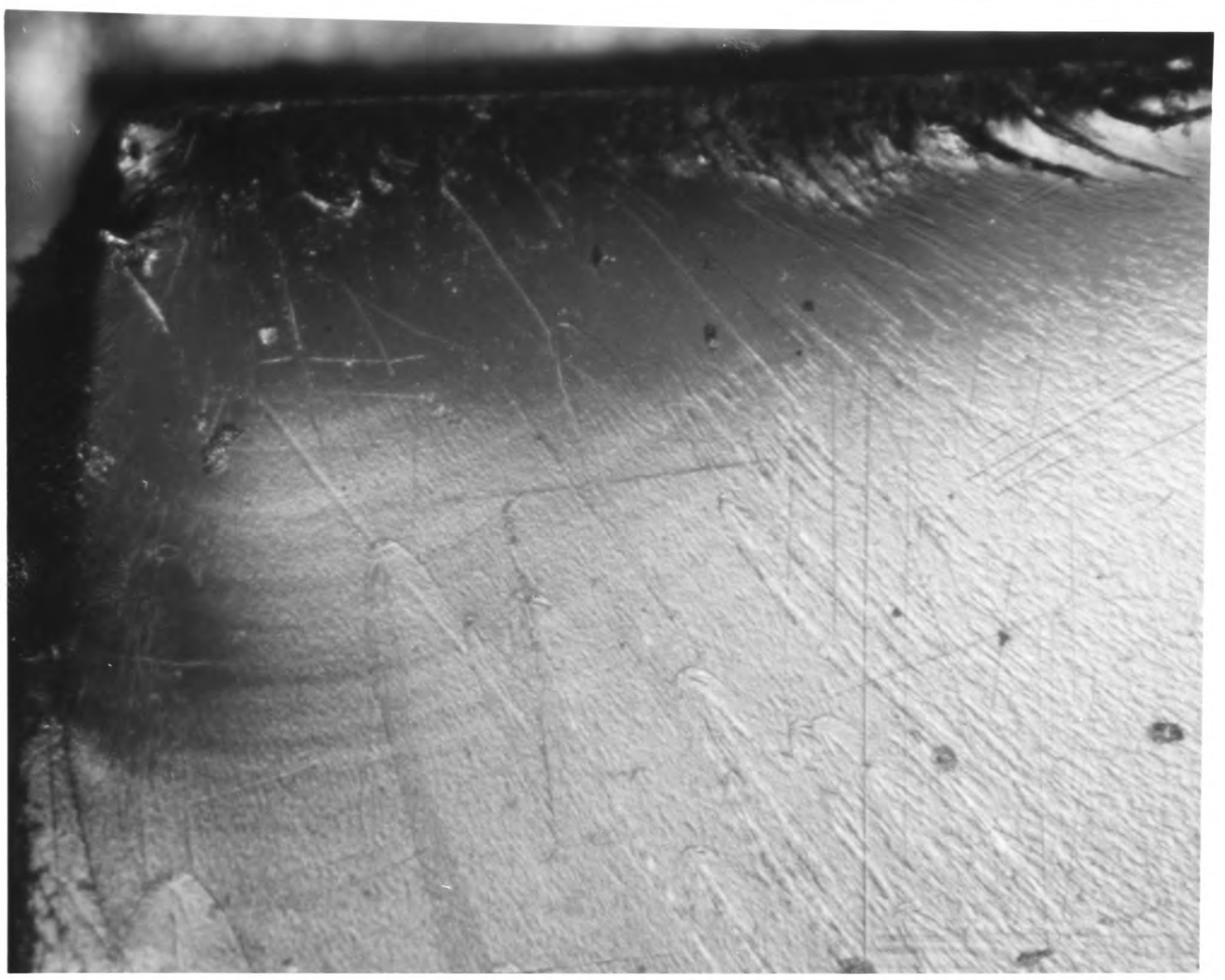


Figure 5.14 Specimen 32 tested under dynamic loading (2a = 14.46 mm).

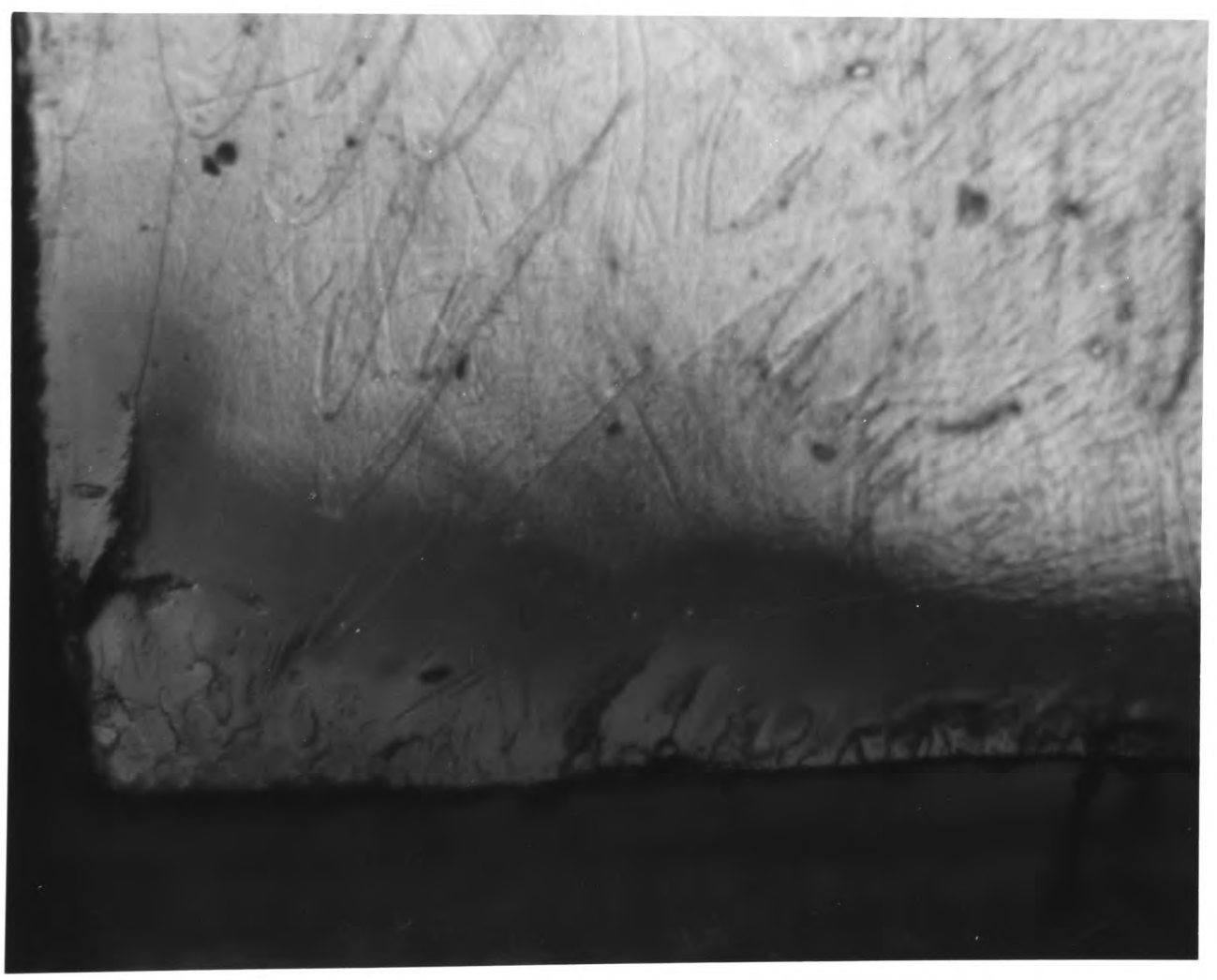


Figure 5.15 Specimen 27 tested under dynamic loading (2a = 19.14 mm).

state of tension. Furthermore, the original crack front is the boundary between the sawed surface, which is identified by the horizontal marks left by the tool, and the crack surface, which has different sort of marks. The testing conditions of these specimens are described in section 3.5.

In all cases, the characteristics of the fracture surfaces are consistent. The pictures show a black spot at the crack tip, which indicates that the cracks initiate in different plane than the one of the crack surface. However, at close distance, the crack surface is aligned with the original crack plane where three main regions have been identified. The first has parabolic marks and it is around the corner where the plane of maximum tensile stress and the crack front intersect. All the axis of the parabolas are heading to such intersection, indicating that the crack initiates from such point. The second is formed by small flaws which are along the top part of the original crack front. Their initial direction is parallel to the specimen surfaces. However, after a short distance, they deflect and tend to align with the crack front and the third is a rough area that bounds the two bright regions mentioned before.

From this data the following fracture mechanism is proposed to explain crack propagation. Before the crack starts, a series of microvoids develop around the top end of the original crack front, which is an area under tensile stress. Then, the crack propagates with an elliptical front from the top end of the notch. Its axis of symmetry coincides with the notch front and the top surface of the specimen. All the voids are intersected and parabolic marks are left on the crack surface. In addition, tensile stresses are developed parallel to the original crack front, which generate some fissures along its top end.

These observations are in accordance with the fracture process suggested in [7], which establishes that a thin layer of material is expanded to form a craze. Then, the crazed layer is extended to its breaking point, propagating the crack. Kinloch et. al. [8] have claimed that crazes are initiated when an applied tensile stress causes microvoids to nucleate at points of high stress concentration in the polymer, created by scratches, flaws, cracks, dusts particles, molecular heterogeneities, etc. The microvoids develop in a plane perpendicular to the maximum principal stress but do not coalesce to form a true crack since they become stabilised by fibrils of plastically deformed, oriented polymeric material spanning the craze. When the crack initiate and grow, the fibrillar structure in a craze is brake. Likewise, this mechanism is frequently a precursor to brittle fracture, because, although considerable plastic deformation

and local energy adsorption are involved in the whole process, this micromechanism is often highly localised and confined to a very small volume of material. The craze zone is generally developed in front of the crack tip and it can be modelled with the Dugdale line plastic-zone model [9].

All the crack pictures are in accordance with the observation in [10], in which the crack growth takes place by breakdown of the craze along its centre line, leaving a relatively smooth fracture surface. In consequence, the assumption that the cracks propagated under a state of plane strain is confirmed. It has also to be remarked that the crack surfaces of those specimens, which were loaded several times before crack initiation, did not show any difference with those loaded only one time.

5.3.3 Analysis of the Crack Surfaces of the Specimen Tested under Static Loading.

Typical observations of the crack surfaces of the specimen tested under static conditions are shown in figures 5.16, 5.17 and 5.18, which correspond to the specimens 28, 31 and 26 respectively. Their crack lengths are 8.35 mm, 18.75 mm and 8.65 mm and their testing conditions are described in section 3.7. In all these pictures, the top plane was under tension.

The cracked surfaces can be classified in two groups. In the first, which was observed in most of the static tests, the crack surface at the crack tip has a complex geometry. Typical results are shown in figures 5.16 and 5.17. In the former case the load was applied by increasing pressure steps, while in the last case, the pressure was applied in a single step. In these situations the load history did not make any difference on the surface geometry.

The observations show an area with two sets of ribs at the crack tip, that has an abrupt transition into a smooth surface. The first is aligned in concentric quarter of ellipses with respect to the point of crack initiation, surrounding the crack tip and revealing in which way the crack front propagated. Kusy et. al. [11] made a qualitative analysis of the fracture surfaces that were created under bending loading. They observed parabolic marks and ribs around the point of initiation and concluded that the ribs were formed only in cases where loading conditions resulted in a tensile stress field ahead of the crack tip. Moreover, their width and spacing increased as the crack traversed the specimen into zones of increasing tensile stress.



Figure 5.16 Specimen 28 tested under static loading (2a = 8.35 mm).



Figure 5.17 Specimen 31 tested under static loading (2a = 18.75 mm).

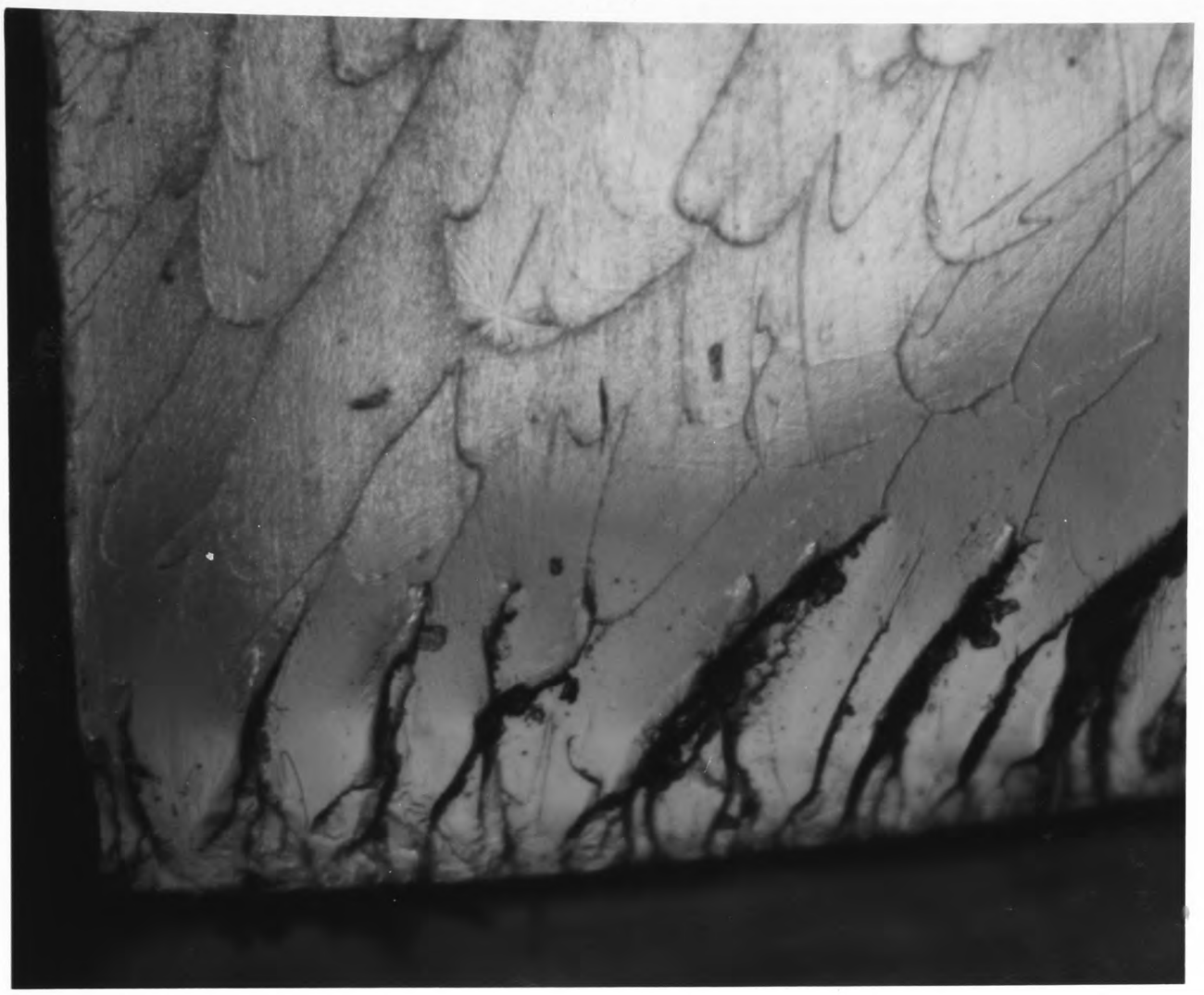


Figure 5.18 Specimen 26 tested under static loading (2a = 8.65 mm).

The second set of ribs originate from the point of crack initiation and their trajectory is perpendicular to the first set of marks. In this respect, Kusy [12] has established that these dark bands, which run parallel to the direction of crack propagation, represent small changes in elevation between fracture planes and they are caused by different degrees of elastic distortion of the material, that result from local variations in crack velocity or crack front displacement.

In general terms, these crack surfaces have the characteristics of a rapidly moving crack, whose rib markings are regularly spaced perpendicular to the direction of crack propagation [11,12,13] and their transition with a smooth surface is abrupt [14]. Kusy and coworkers [11] have claimed that the origin of the rib features is somewhat uncertain although it would appear to be related to a type of stick-slip propagation due to either crack bifurcation or the effect of stress waves interaction.

The analysis of the second group of crack surfaces obtained in the static tests shows that small cracks are originated along the original crack front and over 2.5 mm from the top surface of

the specimen. They are perpendicular to the crack front and after a short distance their direction is deflected toward the compression side. The rest of the surface appears with some parabolic marks heading to the point of crack initiation. It is important to notice that this pattern occurred a couple of times and only in one crack end, while the other extreme of the crack showed the characteristics observed in the first group. A typical result is shown in figure 5.18.

In this respect Van Noort et. al. [15] established that the fracture surface of PMMA is by no means universal. From their observations, they concluded that there is no "conventional" fracture surface of PMMA, since its topography is highly dependent on the design of the tests-piece and the type of test performed. Thus, they recommend great caution when attempting to interpret the fracture topography. The same conclusion was obtained by Dearth [16], who analyzed the fracture surfaces of a single-edge notched samples of PMMA under wedge loading and his observations were not in agreement with those of Kusy et. al. [11] obtained in similar tests.

Summarizing, the comparison of the fracture surfaces of the specimens tested under dynamic loading with those of the first group of the static tests shows that in the last case more fracture energy is required, because of the plastic deformation. With regard to the crack surfaces of the second group, they are similar to those obtained under dynamic conditions. However, the fissure density at the crack front is higher in the static case, which indicates that more fracture energy is consumed as well. In consequence, less fracture energy was required for crack propagation under dynamic loading.

5.4 Analysis of the Numerical Results.

At first glance, the acceptance of the numerical evaluations of the dynamic fracture toughness, reported in figure 4.30, is debatable, because, both procedures lead to different results. Nevertheless, several factors have to be considered in their final acceptance.

In the case of the calculation of the stress intensity factors with standard solutions, the numerical evaluation of the stress field at the centre of a plate without any crack was calibrated with the experimental results. It could, therefore, be argued that the results obtained by applying the conventional static calibration of Williams to the actual dynamic

stresses should be corrected. On the other hand, this approach ignores the effect of stress waves reflected at the free surfaces of the crack, a factor that is considered when calculating the dynamic J-Integral using ABAQUS.

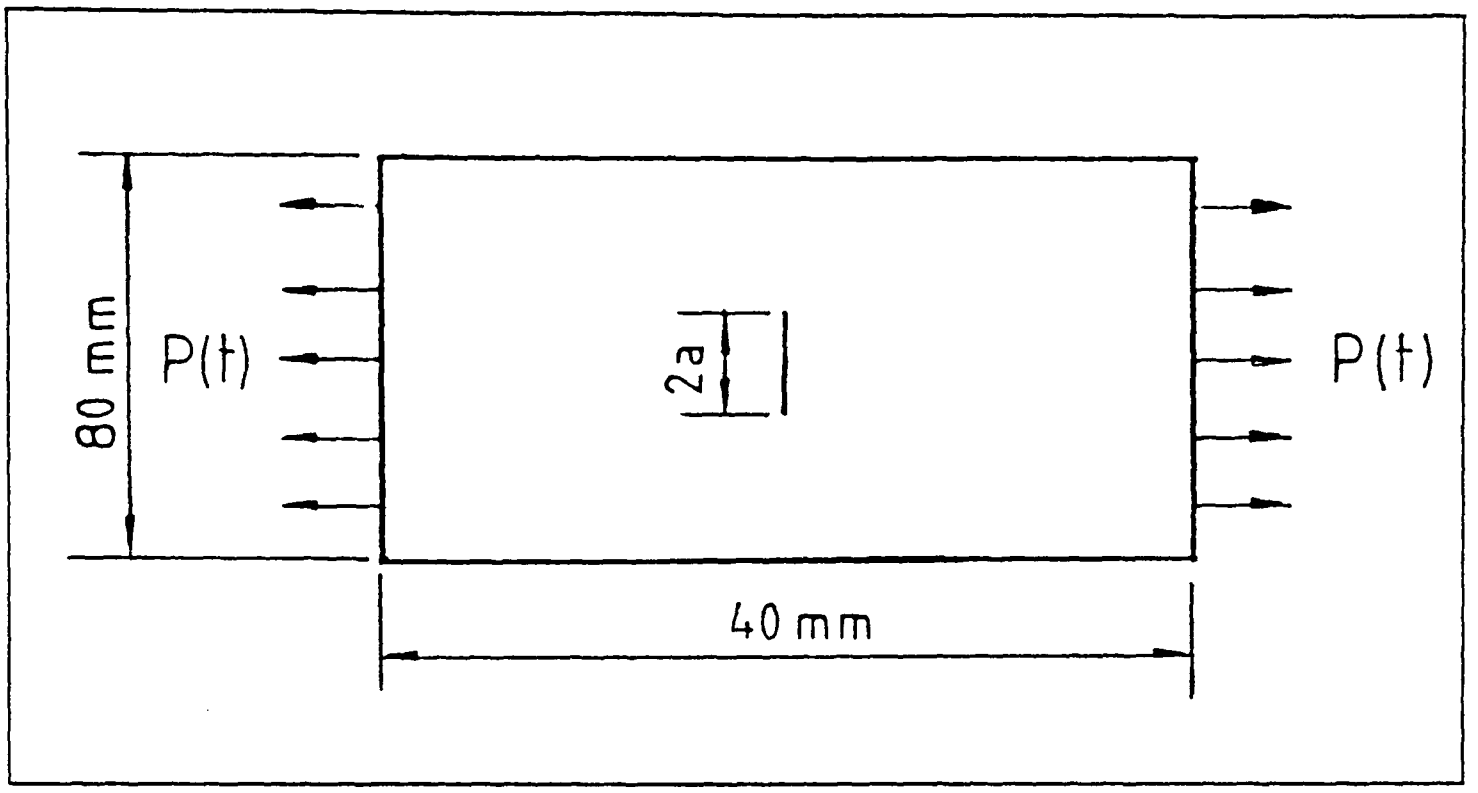


Figure 5.19 Dimensions of the cracked plate analyzed in the Chen's problem (2a=4.8 mm).

In order to assess the validity of the ABAQUS calculations a benchmark was chosen. This was the problem originally treated by Chen [17] which consists in the evaluation of the dynamic SIF in a rectangular plate with a centrally located crack, as shown in figure 5.19. The plate is loaded dynamically in the axial direction by a uniform tension P(t) with Heaviside-function time dependence, as shown in figure 5.20, under plane strain conditions. Furthermore, the material is linear elastic with the following characteristics

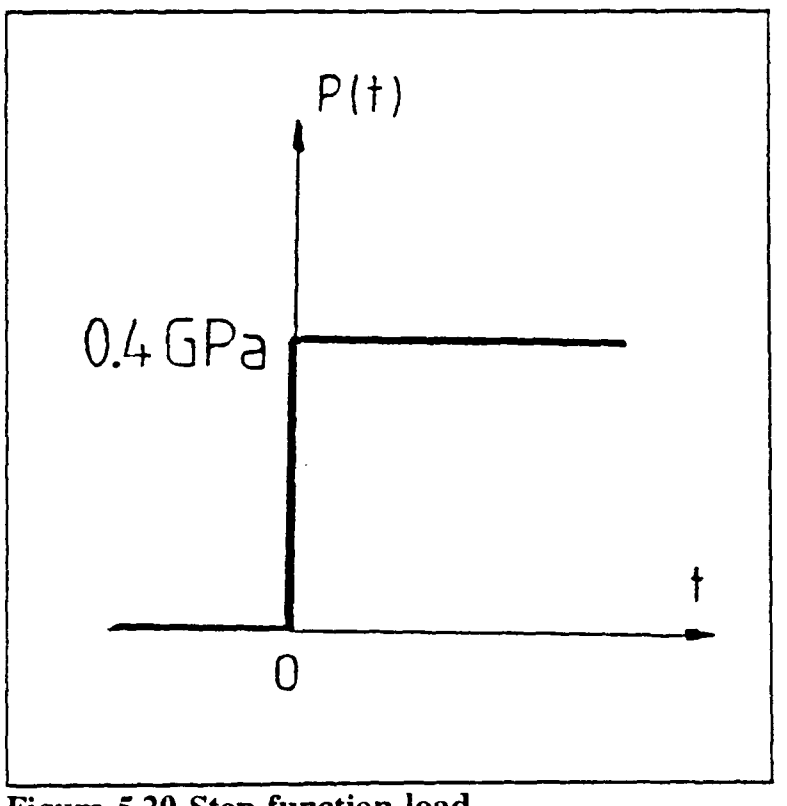


Figure 5.20 Step-function load.

Shear Modulus μ= 76.923 GPa
Bulk Modulus K = 166.667 GPa
Poisson's ratio ν = 0.3
Density = 5 Mg/m^3

Chen used the two-dimensional version of HEMP 3D program, which was developed to solve

problems ranging from dynamic plasticity to gas dynamics, including fracture mechanics, using explicit finite difference methods with second order accuracy to solve the equations of continuum mechanics in three space dimensions and time. The program uses a Lagrange grid that moves with the material and whose zones, in general, are cubic shapes. However, the grid can be generated with distorted cubes [18].

The solution obtained is shown in figure 5.21, which has the following interpretation. During the time I_1, the incident longitudinal wave travels from the plate ends to the crack. Then, in the time interval (R_1 - I_1), the Rayleigh wave generated by the initial incident waves, travels between both crack tips. Besides, during (P_1 - I_1), the scattered longitudinal wave, generated by the initial incident waves as well, moves from a crack tip to the nearest boundary surface of the plate and back to the same tip. Similarly, (S_1 - I_1) corresponds to the scattered transverse wave. At the time I_2, the incident longitudinal has travelled the length of the plate, reflected from the boundary surface on the opposite side, and then, returned to the crack. In an analogous way, the time intervals (R_2 - I_2), (P_2 - I_2) and (S_2 - I_2) may be interpreted with respect to the secondly incident longitudinal waves. This solution is also compared with the static evaluation and the effect of the stress waves over the time history of the SIF can be observed easily.

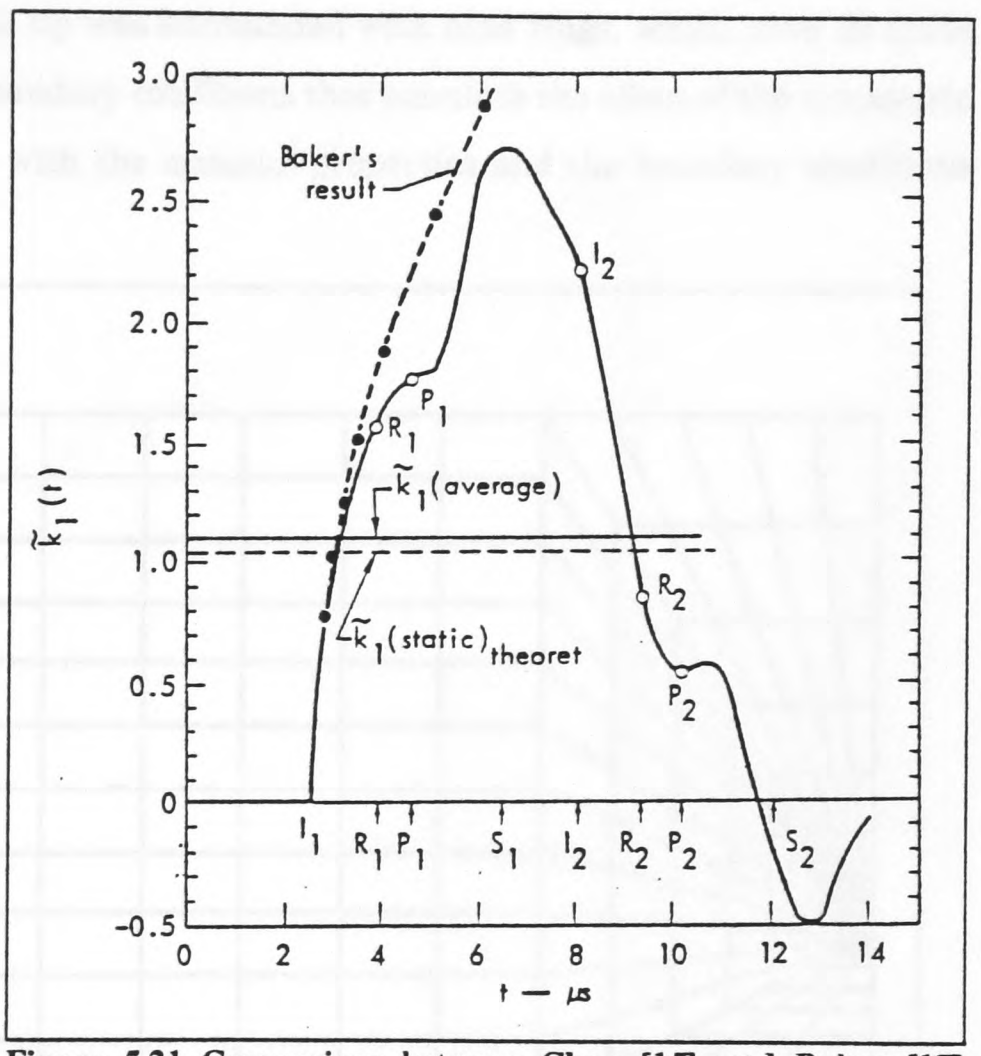


Figure 5.21 Comparison between Chen [15] and Baker [17] solutions. After Sih [16].

This numerical solution is also compared with the results of Baker [19] in the same graph, who analyzed the case of a semi-infinite crack which suddenly appears and grows at constant velocity in a stretched infinite elastic body. The analytical solution has been worked out by transforms methods including the Weiner-Hopf and Cagniard techniques. As it can be observed

in figure 5.21, the numerical and analytical solutions are in agreement before the stress wave reflections take place.

An analysis of this problem was carried on with ABAQUS. For this purpose, the symmetry of the loading and the plate was considered and only one quarter was modelled with the grid shown in figure 5.22. It requires 281 CPE8 elements, which are biquadratic plane strain elements of eight nodes. The crack tip was surrounded with nine rings, which have 19 finite elements each one. Besides, the boundary conditions that simulate the effect of the symmetric parts were imposed to the model with the material properties and the boundary conditions mentioned above.

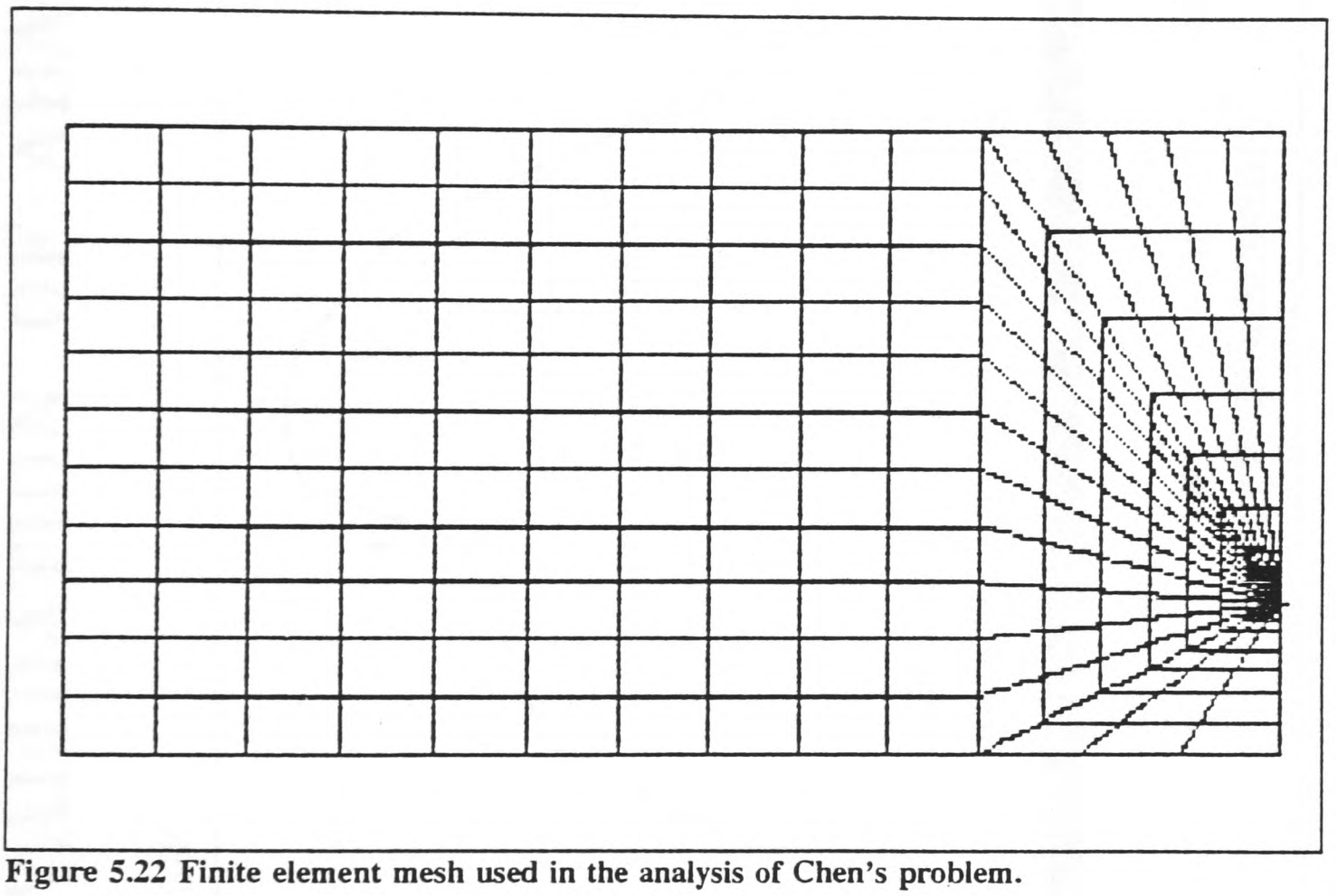


Figure 5.22 Finite element mesh used in the analysis of Chen's problem.

ABAQUS solution is compared with the solution of Chen [17] and Brickstad [20], who analyzed this problem with finite element approach, in figure 5.23. Good agreement has been found when the crack is opening. Thus, ABAQUS is capable to evaluate the effect of the interaction of the stress waves with the crack surfaces and boundaries in the evaluation of the fracture surface, when a static crack is loaded dynamically.

Xia [21] has established that ABAQUS version 4.8, which has been used in the all the numerical calculation reported in the present work, only takes into account the first integral

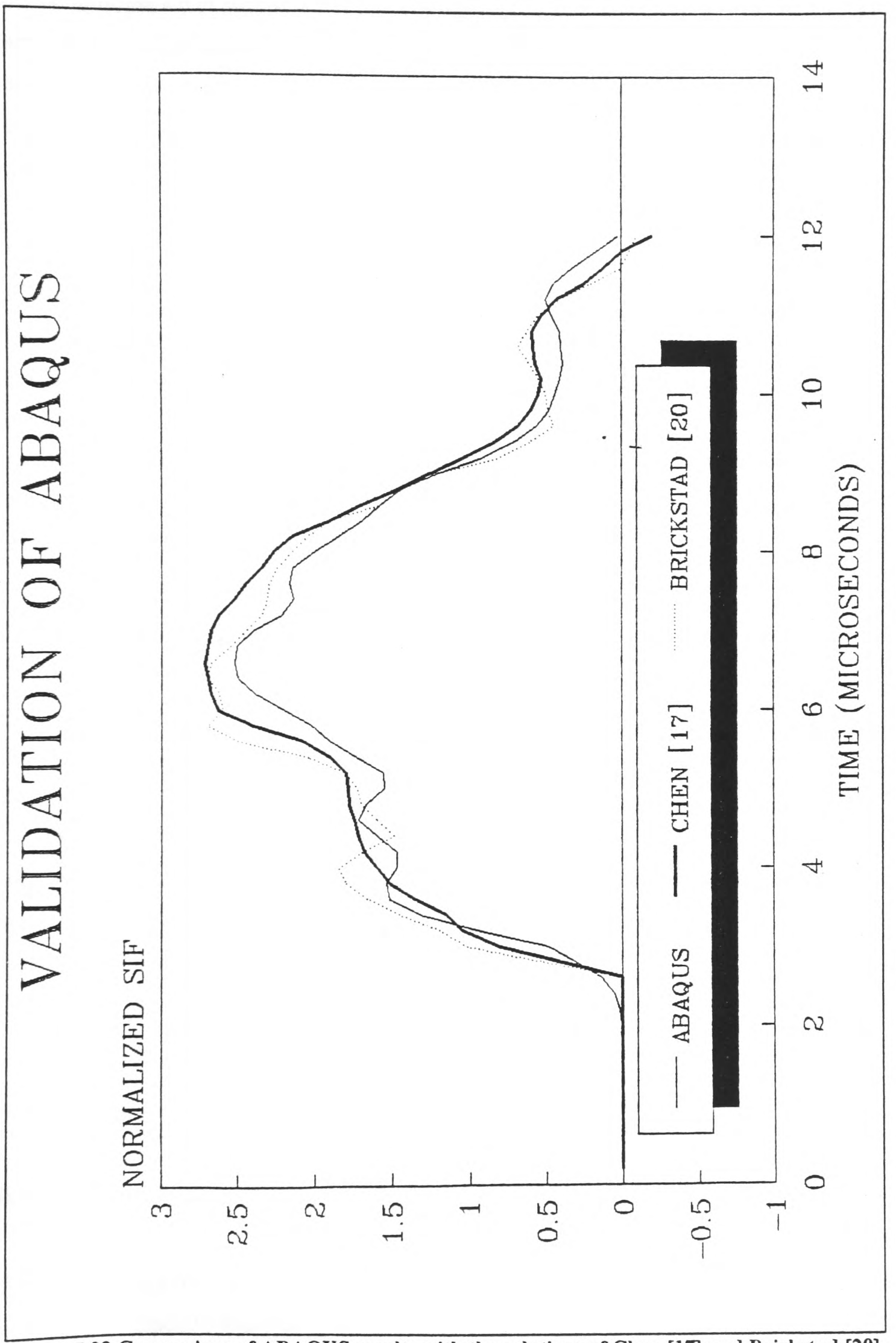


Figure 5.23 Comparison of ABAQUS results with the solutions of Chen [17] and Brickstad [20].

of the equation 4.5 of section 4.2.2. and the stress field and strain energy around the crack tip are calculated dynamically. Hence, the only error comes from the inertia term, which is the double integral of equation 4.5. He recognized that the integral becomes path dependent. Nonetheless, it is a good parameter as long as its value is calculated along several paths and the convergence of the results are observed.

Xia et. al. [22] compared the ABAQUS solutions of the dynamic evaluation of J of a two layered beam with an interface crack with the results of the theoretical model proposed in [23]. Rigid bonds were assumed in front of the crack tip, simplifying the problem. In all cases, ABAQUS solutions compared well with the theoretical evaluation, as shown in figure 5.24. It can therefore be concluded that the results obtained by ABAQUS by the dynamic direct integration method can be accepted as an accurate indication of the dynamic J-Integral. It also follows that the stress intensity factor deduced from the J-Integral, or the corresponding fracture toughness, will be equally accurate since the transformation,

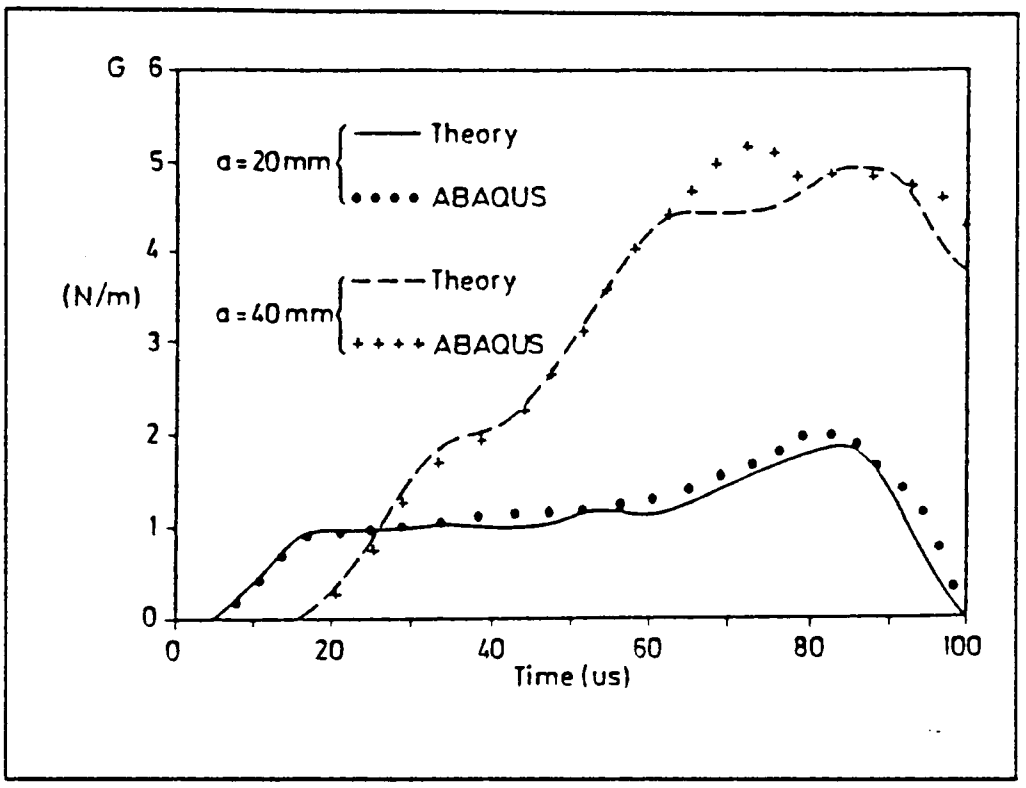


Figure 5.24 Comparison of the energy release rate calculated with ABAQUS and theory. After Xia [23].

$$K = \sqrt{E'J}$$

is always applicable.

5.5 Conclusions.

Referring to figure 4.30 and in general terms, the results of the PMMA test have shown to have a static fracture toughness of 2.6 MPa $m^{1/2}$ and a dynamic fracture toughness of 0.5 MPa $m^{1/2}$ under bending stresses. This reduction is reflected in the fact that considerably less plastic deformation is developed at the crack tip of those specimens tested under dynamic loading

conditions. Likewise, the crack surface geometry of the specimen tests in static conditions is very complex and it is not possible to establish as clearly the fracture mechanism as in the dynamic counterpart. Nevertheless, it can be assumed that a similar mechanism is developed. Thus, it can be supposed that this process is developed in more stable conditions and in a larger volume of material. As a result a tougher response is observed.

Finally, it must be borne in mind that all the calculations were done with the quasi-static value of the modulus of elasticity, although, the tensile tests in the hydraulic universal rapid-load test machine have demonstrated that this parameter increases with the strain rate. In the cases of the numerical evaluation of the dynamic stress field at the centre of the specimen and the J-Integral with the dynamic direct integration method, the error introduced in the calculation is not serious. Besides, the integration of the rate of variation of this elastic property in the finite element model will make the calculations and evaluation of results complex.

In the case of the crack initiation event, it occurs at a definite strain rate, which is the left slope at the peak point in the strain-history registered by the strain gauges at the crack tip - figure 3.11-. At this instant the modulus of elasticity has a value, which is higher than in quasi-static conditions. So, a corrected value of the dynamic fracture toughness due to the effect of the strain rate have to be calculated. For this purpose, the information of tables 3.2, 4.6 and 5.2 is considered and these data and the new results are summarized in the following table.

TABLE 5.5
DYNAMIC FRACTURE TOUGHNESS CORRECTED DUE TO THE EFFECT OF THE STRAIN RATE

SPECIMEN	CRACK LENGTH (mm)	J-INTEGRAL (N/m)	STRAIN RATE (s^{-1})	MODULUS OF ELASTICITY (GPa)	K_c (MPa $(m)^{1/2}$)
36	4.862	138.0	34.2	4.3	0.82
37	9.694	68.0	35.7	4.3	0.57
38	14.745	29.0	21.0	3.8	0.36

These new values of the dynamic fracture toughness raise the bottom curve in figure 4.30. However, the difference observed between both evaluations of the dynamic fracture toughness remains and the conclusions discussed above are still valid.

REFERENCES

1. Cooper, R. H. and Campbell, J. D. Testing of Materials at Medium Rates of Strain, *J. Mech. Eng. Sci.*, No. 4 9(1967)278-284.

2. Lees, W. A. *Adhesives in Engineering Design*, The design Council, London. Springer-Verlang (1984).

3. Kobayashi, A., Ohtani, N. and Sato, T. Phenomenological aspects of viscoelastic crack propagation, *J. Appl. Polymer Sci.* 18(1974)1625-1638.

4. The properties of "Perspex" Acrylic Materials. *Imperial Chemical Industries Limited*, Plastics Division, Welwyn Garden City, Herts, England (1971).

5. Beardmore, P. Temperature dependence of yield and fracture in Polymethylmethacrylate, *The Philosophical Magazine*, 19(1969)389-401.

6. Katsamanis, F. G. and Delides, C. G. Fracture surface energy measurements of PMMA: a new experimental approach. *J. Phys. D* 21(1988)79-86.

7. Ward, I. M. *Mechanical Properties of Solid Polymers*, Wiley-Interscience a division of John Wiley, London(1971).

8. Kinloch, A. J. and Young, R. J. *Fracture Behaviour of Polymers*, Elsevier Applied Science, London(1990).

9. Dugdale, D. S. Yielding of steel sheets containing slits, *J. Mech. Phys. Solids*, 8(1960)100-104.

10. Brown, H. R. and Ward, I. M. Craze and fracture in poly(methylmethacrylate, *Polymer* 14(1973)469-475.

11. Kusy, R. P., Lee, H. B. and Turner, D. T. Rib formation in the fracture of polymethyl-

methacrylate, *J. Mater. Sci.* 11(1976)118-124.

12. Kusy, R. P. Effect of molecular weight on the fracture morphology of poly(methylmethacrylate) in cleavage *J Mater. Sci. Letters*, 11(1976)1381-1384.

13. Kusy, R. P. and Turner, D. T. Influence of the molecular weight of poly(methylmethacrylate) on fracture morphology in notched tension, *Polymer*, 18(1977)391-402.

14. Döll, W. A molecular weight dependant fracture transition in polymethylmethacrylate, *J. Mater. Sci.* 10(1975)935-942.

15. Van Noort, R. and Ellis, B. The fracture topography of poly(methyl methacrylate), *J. Mater. Sci. Letters*, 3(1984)1031-1034.

16. Dearth, R. S. The fracture topography of wedge-loaded samples of poly(methylmethacrylate), *J. Mater. Sci. Letters*, 7(1988)171-172.

17. Chen, Y. M., Numerical computation of dynamic stress intensity factors by a Lagrangian finite-difference method (The HEMP CODE), *Eng. Frac. Mech.* 7(1975)653-660.

18. Sih, G. C. (ed.) *Mechanics of Fracture, Vol. 4, Elastodynamic crack problems*, Noordhoff International Publishing, Leyden, The Netherlands (1977).

19. Baker, B. R. Dynamic stresses created by a moving crack, *Trans. ASME J. Appl. Mech.* 29(1962)449-454.

20. Brickstad, B. A FEM analysis of crack arrest experiments, *Int. Journ. of Fracture*, 21(1983)177-194.

21. Xia, Y. Dynamic applications of ABAQUS, *United Kingdom ABAQUS training course*, Manchester, 26 September 1990.

22. Xia, Y. and Ruiz, C. Transient shear deformation at interfaces of laminated beams, *Int. Journ. of Fracture*, 48(1991)205-218.

23. Xia, Y., Behaviour of a two-layered beam under impact loading, *Int. J. Impact Engng.*, 7(1988)415-428.

CHAPTER 6

GENERAL CONCLUSIONS AND PROPOSAL FOR FUTURE WORK

6.1 Research objectives.

The original brief of this research project was the development of a new impact testing method, in which the specimen is loaded uniformly with a pressure wave that raises steadily without violent oscillations and can be measured accurately. Besides, the dynamic and inertia effects are minimized.

The analysis of the current impact techniques, like the Charpy and the drop weight tests, which have been widely used among others, have shown that they are incapable to make an accurate evaluation of the load, because the interaction between the testing rig and specimen generates undesirable dynamic effects. It was concluded that this situation is eased when the specimen is loaded with a pressure wave and the specimen geometry is simplified. Thus, circular flat specimens were tested. They are loaded over one of their surfaces. In addition, the application of this impact testing technique to crack initiation problems was considered. So, the specimen material chosen was PMMA, which is brittle at room temperature. The problem of crack initiation under dynamic pressure loading has not been completely solved, since it has been studied mainly with cylindrical geometries, made of ductile materials. Some research areas were highlighted, namely,

- the development of the proposed impact technique, which involves the characterization of the load, the establishment of the range of application and analysis of the elastic response of the specimens,

- the analysis of crack initiation phenomenon under dynamic pressure loading and

- the extension of the fracture mechanics concepts to the evaluation of the fracture toughness in dynamic conditions, as well as its interpretation.

This project was divided in two parts. In the first, an impact testing rig was designed and, in the second, the proposed technique was applied to the analysis of crack initiation under dynamic pressure loading with an experimental-numerical procedure.

6.2 Conclusions.

6.2.1 Design of the Impact Testing Rig.

The experimental rig is a variation of a shock tube, which generates blast waves that load circular flat specimens under a dynamic bending state of stress. Moreover, fracture tests in static conditions are performed easily. These characteristics are amply desirable, because, the effect of the dynamic loading can be compared with the one developed under static conditions, simplifying the assessment of the dynamic fracture phenomenon.

The preliminary experiments showed that the observation period of the initial wave is less than 5 ms and the parameters that can be measured without affecting the phenomenon observed are strain and pressure, using strain gauges and piezo-electric pressure transducers. However, both parameters have to be evaluated separately, because the cracked specimens can not be instrumented with both transducers, because the installation of the pressure transducer on the specimen perturbs the stress field at the crack tip.

Extensive experimental work was performed, in order to evaluate the main characteristics of the loading wave. Initially, the expansion chamber was left open to the atmosphere. The findings established that the specimens are loaded with a blast wave, which has an initial

triangular pulse and its magnitude can be controlled and measured easily. Its initial ramp lasts less than 1.5 ms. Besides, it is well defined, increases steadily without violent oscillations and the results are highly repeatable.

By contrast, this situation is unlikely when the expansion takes place in close vessel conditions, in which the impact wave is magnified at the impact surface, making its evaluation complex. As a result, it was decided to load the specimen in open tube conditions.

Accordingly, the specimen was fixed onto the testing rig, leaving a gap between the specimen impact surface and the top flange of the expansion chamber, through which the pressure wave expands in the atmosphere. Hence, the characteristics of the resultant pressure wave were studied, varying the gap size.

The same pattern, that is obtained when the tests are performed with the expansion chamber open to the atmosphere, was observed in this series of tests, when the blast wave is generated with a burst pressure between 1.0 and 2.0 bar. Nonetheless, the initial point of the pressure wave trace is not well defined for certain gap dimensions.

In order to get a wider criterion for the selection of the loading cases for the impact tests, the membrane+bending and bending strain histories at the centre of an uncracked specimen, which is made of PMMA and 3 mm thickness, was studied. The quality and magnitude of the resultant traces were analyzed for the same loading and expansion conditions of the pressure tests mentioned above. The findings showed that the stress wave reflection is unlikely and when the expansion takes place through a gap of 4.2 mm, the best definition of the traces of the pressure, membrane+bending strains and bending strains is obtained. In consequence, in the selected loading case, the blast wave is generated with a burst pressure within the range between 1.0 bar and 1.5 bar and it expands through a 4.2 mm gap.

A complete picture of the blast wave was obtained with the analysis of the pressure front. For this purpose, a steel end plate was instrumented with a pressure transducer at its centre and another was installed at different points over the plate. Both transducers were connected to the same register system and triggered simultaneously. Several tests were performed varying the magnitude of the blast wave and the position of the second transducer. In all the cases, the traces superpose. Clearly, these results demonstrate that the front is plane and the

interference with the internal wall of the expansion chamber is unlikely. Therefore, the specimen is loaded uniformly.

The last analysis of the first part was related with the elastic response of the specimens to the dynamic load. Ergo, a test was designed to evaluate simultaneously pressure and strain. In this instance a pressure transducer was installed as close as possible to the centre of the impact surface of the specimen and it was loaded with the selected loading cases. A lag between the pressure and strain traces was observed. This situation was not influenced by the distance between the points of measurement. So, it was concluded that the analysis of the crack initiation problem should involve a dynamic calibration, demonstrating that the assumption of a quasi-static calibration, which has been widely considered in the current impact testing techniques, is wrong.

The conclusion of the first part of this project establishes that this impact testing technique is better than conventional impact testing and the crack initiation phenomenon can be studied with an experimental-numerical technique. The crack initiation load is obtained in the experimental part, while the fracture toughness is evaluated numerically. Finally, it is important to keep in mind that the crack tip is under bending stresses. Thus, this is not a standard plain strain material dynamic test.

6.2.2 Crack Initiation Analysis under Dynamic Pressure Loading.

In the second part, the evaluation of the dynamic fracture toughness was accomplished. For this purpose, a notch was sawed at the centre of PMMA plates, which are 3 mm thick. The notch length range is between 5 and 20 mm. Obviously, their tip radius is finite. However, the literature survey indicated that, in the case of PMMA, the crack behaviour may be observed in specimens with notch tip radius smaller than 0.3 mm. In the case of this research work, the tip radius of the specimens is well bellow this limit. In consequence, this cutting technique was considered good.

Initially, the magnitude of the dynamic loading required for crack initiation was determined and, at the same time, the consistency of the results was observed, by means of failure non-failure tests. In the following series of tests, cracked specimens were instrumented with strain gauges at the crack tip and they were loaded with the loading cases selected. The strain-

histories registered shows that they increase steadily up to a maximum value. Then, a sudden drop is observed that indicates the crack initiation. These data were analyzed in conjunction with the pressure history of the corresponding loading cases that initiated the crack, considering the dynamic calibration. Then, the pressure at crack initiation was obtained, as well as the strain rate.

In parallel, static tests were developed and a parabolic relationship between the crack size and the crack initiation load was found, implying that the Griffith theory is valid.

The comparison between the results of the dynamic and static tests demonstrate that lower loads are required in dynamic conditions. Moreover, in the static and dynamic cases, brittle fracture behaviour was observed and the shape of all the crack surfaces suggests that a state of plane strain was developed. Thus, it was concluded that the fracture mechanics principles can be extended to the case of dynamic loading.

In relation with the numerical work, the evaluation of the dynamic fracture toughness was done with the finite element code ABAQUS. In particular, three different procedures were followed for the analysis of the dynamic problems, namely, a quasi-static evaluation of the J-Integral considering only the crack initiation load, a dynamic stress analysis in conjunction with standard solutions and a complete dynamic analysis following the J-Integral method.

The preliminary analysis showed that all these calculations are not straightforward, because several factors have to be clarified. In the first instance, an appropriate finite element mesh was selected. Thus, the whole specimen was modelled, because, in the quarter plate model, the boundary conditions of the symmetrical parts leads to a stiff mesh.

The selection of the boundary conditions was based on an experimental analysis. For this purpose, the natural frequency of the specimens was measured for the fixing conditions of the specimen onto the testing rig in the static and dynamic tests. In parallel, they were calculated with the finite element mesh described above varying its boundary conditions. Finally, the boundary conditions, which bring the experimental and numerical results into agreement, were selected.

With this information, the numerical calibration of the model was done. For this purpose, the strain-history was evaluated with the loading cases selected. The findings showed that the reproduction of the experimental results with undamped models is unlikely. Ensuing, the best solution was obtained when a critical damping factor equal to one was included in the input data. The results showed that ABAQUS is capable to make an accurate analysis of the specimen strain field during the initial ramp of the blast wave. At the end of this numerical analysis, the finite element model required was obtained.

In the next step, it was found that there are two standard solutions that can be applied to the problem at hand. Thus, their theoretical basis was studied and it was concluded that one of them gives approximate results. It is based on the bending theory of Kirchhoff and has two main disadvantages. Firstly, the boundary conditions at the crack surfaces are not fully satisfied. As a result, the singularity $r^{-1/2}$ is not in all the stress field equations. Secondly, the effect of the specimen thickness is not considered. Alternatively, the exact solution, which is based on the bending theory of Reissner, satisfies completely the boundary conditions on the crack surfaces, the singularity $r^{-1/2}$ is in all the stress field equations and the effect of the specimen thickness is considered.

In order to assess the accuracy, the static results of both standard solutions were compared with ABAQUS solution. The findings demonstrate that the exact standard solution and ABAQUS results are in good agreement. By contrast, the approximate solution overestimates the fracture toughness.

With respect to the evaluation of the dynamic fracture toughness, it was calculated initially following a quasi-static approach with the finite element method. In this case, the crack initiation load was considered and the results obtained are overestimated.

Alternatively, the application of the exact standard solution combined with the dynamic evaluation of the stress field at the centre of the specimen, indicates that the dynamic fracture toughness is around 1.1 MPa $m^{1/2}$, which is in the range of the static fracture toughness evaluated by other researchers. With respect to the evaluation of the J-Integral with the dynamic direct integration method, the dynamic fracture toughness obtained is reduced to around 0.5 MPa $m^{1/2}$.

At this point, there were three main questions that had to be answered before the final acceptance of the results, namely, the factors that cause reduction of the fracture toughness in dynamic conditions, the effect of the observed strain rates over the mechanical properties of the material and the accuracy of the numerical solutions of the dynamic analysis. Consequently, additional experimental and numerical work was carried on to clarify these points.

A microscopical analysis of the crack surfaces was carried on with low levels of magnifications, because the main interest was the establishment of general characteristics of the crack surfaces. The findings showed that, in the case of the specimens tested under dynamic conditions, voids are developed in the area which is close to the intersection of the plane of maximum tensile stress and the notch front. They grow and coalescence. When the crack propagates from this point, an elliptical front is developed, which eventually intersects these discontinuities, leaving parabolic marks on the crack surface. Their vertex head toward the point of crack initiation. Moreover, small cracks are developed at the top end of the notch front. They are parallel to the to the specimen surfaces and, in a short distance, they deflect downward. Clearly, this revels that a tensile stress is developed parallel to the notch front. The rest of the surface is rough.

In the case of the static cases, the findings showed that there are two patterns. In the first, which is the common, plastic deformation is likely. In fact, a complex geometry was developed which is characterized by a network of two rib sets. The first indicates the position of the crack front during its propagation, while the second is perpendicular to the first, suggesting the direction of crack propagation. It is not possible to establish a fracture mechanism due to the complexity of the geometry. Nonetheless, it can be assumed that the same mechanism observed in the dynamic cases is developed in comparatively bigger volume of material. Alternatively, the second pattern is similar to the one observed in the dynamic tests and it is developed in a larger volume. Accordingly, both cases reflects that more fracture energy is required to initiate a crack in static conditions than in dynamic conditions. Therefore, this explains the increment in fracture toughness.

With respect to the evaluation of the mechanical properties, tensile tests at different strain rates were performed in a hydraulic universal rapid-load test machine. The specimens were taken from the same sheets of material that was used in the fabrication of the cracked

specimens. Although, special care was taken to reduce the compliance of the whole testing set-up, the results obtained tend to be smaller than those obtained when the elastic properties are evaluated from deformations measured at the gauge length of the specimen. It was concluded that the results are in line with those obtained by other authors. Furthermore, they showed that the modulus of elasticity and the fracture stresses increases with the rate. Consequently, the values of the fracture toughness were corrected, because the initial calculations were done with the quasi-static value of the Young's modulus. An increment in the dynamic fracture toughness was observed. However, the difference between the dynamic and static solutions remains.

With respect to the numerical evaluations of the dynamic fracture toughness, it must be observed that the disadvantage of the solution obtained with the exact standard solution in conjunction with the dynamic evaluation of the stress field, is that the effect of the stress waves over the crack surfaces is not taken into account, because the calculations are for a plate without crack. From a benchmark solution, it was found that ABAQUS can consider the interaction of the stress waves with the crack surfaces and specimen boundaries. So, it was concluded that the dynamic solution of ABAQUS is correct.

Recapitulating, the impact testing proposed has shown that it has several advantages. The principal is that the load increases steadily, without violent oscillations. Thus, an accurate evaluation of the loading conditions can be made, using conventional transducers and recording systems. Additionally, information such as strain rate can be obtained. Nevertheless, its range of application is limited by the strength of the pressure chamber and safety conditions. It is applicable to materials which have similar mechanical characteristics to PMMA.

Its application to the dynamic crack initiation problem in PMMA under dynamic pressure loading has simplified the analysis of the problem. The results show that the fracture toughness in static conditions and under a bending state of stress is around 2.6 MPa $m^{1/2}$. Similarly, under dynamic loading, it is 0.5 MPa $m^{1/2}$. Likewise, the need to use relatively large starter cracks has been demonstrated.

It is important to mention that the evaluation of the dynamic fracture toughness has to be based necessarily on a dynamic calibration and the analysis has to be accomplished with a experimental-numerical technique. The accuracy of the results depend on two main points.

Firstly, the precision of the evaluation of pressure load. Secondly, the ability of the numerical method to consider all the dynamic parameters involved.

Finally, the fracture toughness values calculated are not necessarily in plain strain, because bending stresses are developed at the crack tip. So, the results of this test cannot be compared directly with those in which the crack tip is in plane strain conditions. Nevertheless, the SIF calculated at crack initiation is a dynamic fracture toughness.

6.3 Proposal for Future Work.

Four main potentials research areas, in which the proposed impact testing can be used to develop further work, have been recognized, namely, study of crack growth, analysis of the effect of the notch front geometry over the fracture process, evaluation of the dynamic fracture toughness of other polymers and analysis of the strain rate effect on crack initiation.

With respect to the analysis of crack growth, exploratory work has been done, in which strain gauges were bonded along the crack propagation path. All these transducers were connected to the same recording system and triggered simultaneously. The experimental results with PMMA specimens indicated that when the crack passes close to each strain gauge, their strain-rate curve showed a sharp decrease. Likewise, when all the signals were plotted in a single strain-rate diagram, it was possible to deduce the average time in which the crack moves among the different points of measurement and the average crack propagation velocity is obtained considering these data and the distance between gauges. The crack propagation velocities measured with this technique are in agreement with similar results of other researchers. See appendix A.

Additionally, the relation of the crack surface geometry with crack propagation velocity can also be established in post-mortem analysis and, when the strain gauge traces are plotted in a single diagram with the pressure history, the magnitude of the load can be obtained accurately during the fracture event. This evaluation may be improved by using crack propagation gauges, because the distance among the transducers is reduced.

Another area explored was the analysis of the effect of the crack front geometry on the fracture process. In particular, preliminary work has already been done with specimens that have a

triangular crack front, which were tested under static and dynamic conditions. See appendix B.

Since the results with this impact testing technique have demonstrated that there has been a substantial improvement with respect to the current techniques, it is considered that it can be applied to other polymeric materials to obtain true values of the dynamic fracture toughness. In this case the scope of the technique becomes wider, because these materials have different fracture behaviour -brittle or ductile-. As a result, it is possible to study the impact fracture performance of these materials at different strain rates.

Finally, the findings of the present work have confirmed that the fracture toughness is strain rate dependent. Furthermore, the magnitude and duration of the pressure pulse can be varied easily. Consequently, a crack can be initiated under controlled strain rate. Thus, this impact testing technique can also be applied in the fracture characterization of materials at different strain rates.

APPENDIX A

EVALUATION OF THE CRACK PROPAGATION VELOCITY

The purpose of this series of tests is to explore the application of the impact testing method proposed in this research project to the measurement of the crack propagation velocity under dynamic pressure loading. The preliminary tests showed that the crack always propagates along its original plane, the specimen fragmentation was unlikely and crack initiation was clearly detected with the signal of a strain gauge bonded at the crack tip.

A.1 Description of the Experimental Technique.

The specimens 36, 37 and 38 were instrumented with four strain gauges, which were bonded along the path of crack propagation. A schematic arrangement is shown in figure A.1, in which

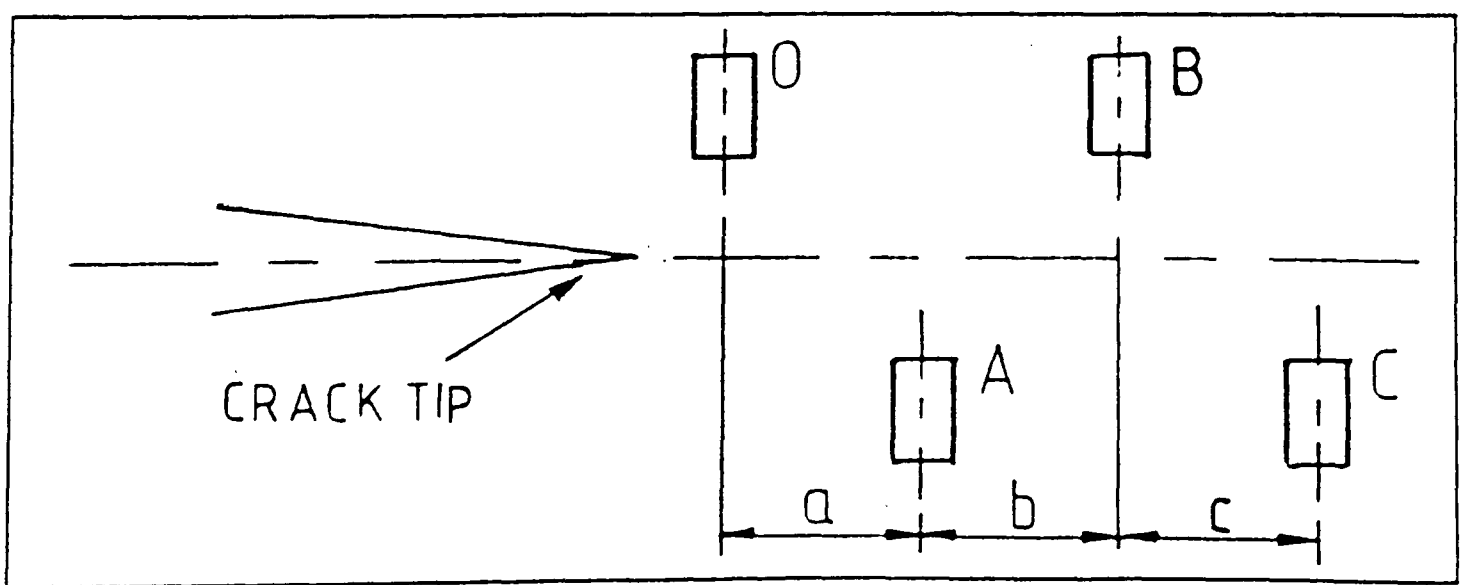


Figure A.1 Schematic arrangement of the strain gauges.

the strain gauge that is close to the crack tip is identified with the label O. Table A.1 indicates the distance among the strain gauges for each specimen.

TABLE A.1
STRAIN GAUGE SEPARATION

SPECIMEN	a (mm)	b (mm)	c (mm)
36	15.3	15.3	15.4
37	15.2	14.8	14.7
38	15.1	14.9	15.3

The distance between the crack tip and the nearest strain gauge is illustrated in figures 3.8, 3.9 and 3.10 for each specimen and the description of the tests and crack dimensions are in section 3.5 and 3.6 respectively.

All the strain gauges were connected to the data recording system described in section 2.2 and were triggered simultaneously. The test procedure is described in section 2.2.1.

A.2 Results Obtained.

All the traces obtained in each test were plotted in a single strain-time graph. Figure A.2 shows a typical case, which corresponds to the test results of specimen 37. In all the cases, the strain gauges pick up the typical variation of the strain that indicates crack initiation, as described in section 3.6. Hence, the maximum points of each curve were considered as the instant in which the crack tip was close to the strain gauge. The time required for the crack to move between the strain gauges was obtained from this graph and is given in table A.2.

TABLE A.2
CRACK PROPAGATION TIME

SPECIMEN	t_a (ms)	t_b (ms)	t_c (ms)
36	0.050	0.025	0.050
37	0.055	0.035	0.055
38	0.060	0.110	(1)

(1) Strain gauge failure.

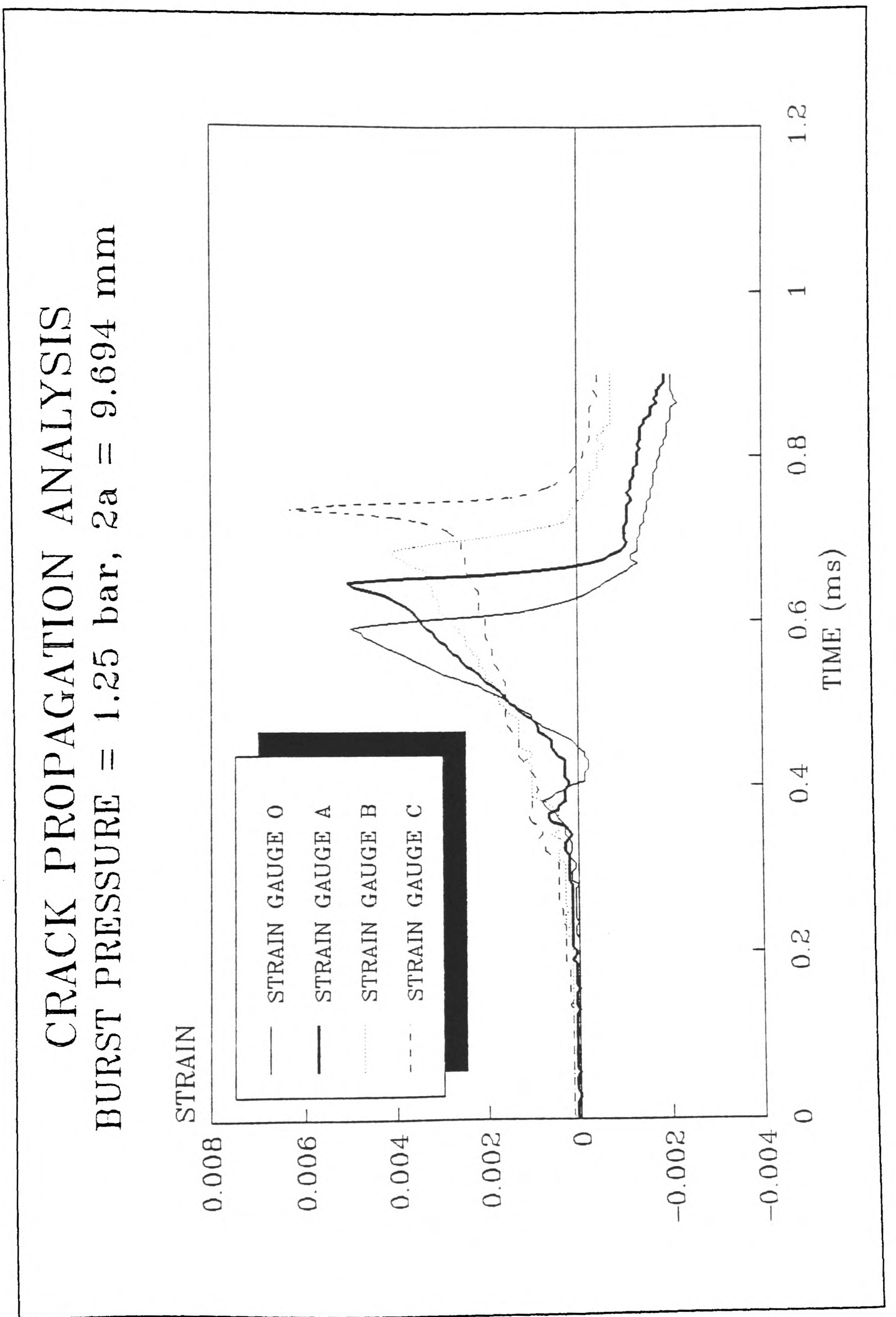


Figure A.2 Strain gauge signals registered during crack propagation.

Considering the data in table A.1 and A.2, the average crack propagation velocity was obtained. The results are given in table A.3.

TABLE A.3
AVERAGE CRACK PROPAGATION VELOCITY

SPECIMEN	V_a (m/s)	V_b (m/s)	V_c (m/s)
36	306	612	308
37	276	423	267
38	252	135	---

The analysis of the strain-rate curves shows that their initial ramp has two phases. In the first, there is a steady increase and it occurs over a relative long period of time, in some cases it can be approximated with a straight line. On the contrary, the second phase occurs in a short period and its slope is close to the vertical. This situation can be appreciated clearly with the signal of the strain gauge C in figure A.2. For the purpose of the evaluation of the strain rate, only the first phase was considered and the results obtained are in table A.4.

TABLE A.4
STRAIN RATE

SPECIMEN	$\dot{e}_a$ (s^{-1})	$\dot{e}_b$ (s^{-1})	$\dot{e}_c$ (s^{-1})
36	20	10	4.7
37	20	13	10
38	12.5	2.8	---

A.3 Discussion of the Results.

Bergvist [1] proposed the following equation for the evaluation of the terminal crack velocity in PMMA

$$V_T = 0.42\sqrt{\frac{E}{\rho}} \qquad \text{A.1}$$

in which E and ρ are the modulus of elasticity and density of the material respectively. In the case of the specimen 36, the maximum crack propagation velocity was measured along the distance b, in which the average strain rate is 15 s^{-1}. Considering the evaluation of the elastic properties at different strain rates obtained in section 5.2.4 and the physical properties reported in section 3.2, the limiting velocity is 730 m/s. The velocity measured (612 m/s) is below this theoretical limit.

The highest crack propagation velocities in PMMA, under low loading strain rates, reported in the open literature, are the following

Schardin [2]	655 m/s
Dulaney and Brace [3]	670 m/s
Cotterel [4]	670 m/s
Katsamanis et. al. [5]	670 m/s
Dahlberg [6]	700 m/s

In the case of high loading rates, Theocaris et. al. [7] reported velocities up to 850 m/s. In this respect, Rosakis [8] explained these differences arguing that PMMA is strain rate dependent. So, the modulus of elasticity increases with the strain rate. As a result, and in accordance with equation A.1, its limiting velocity increases under dynamic loading conditions. It can be concluded that the results reported in table A.3 are in line with the observation of other researchers.

Finally, the set of strain gauge traces of figure A.2 are compared with the pressure pulse that initiate the crack. All the curves are plotted in terms of volts, which is the common parameter and the calibration factor obtained in section 2.4.3 is taken into consideration. As it can be seen in figure A.3, the initial pressure pulse envelops all the strain gauge signals and the crack propagation event takes place around the peak of the pressure pulse. From this information, it is possible to deduce the magnitude of the load during the period of observation.

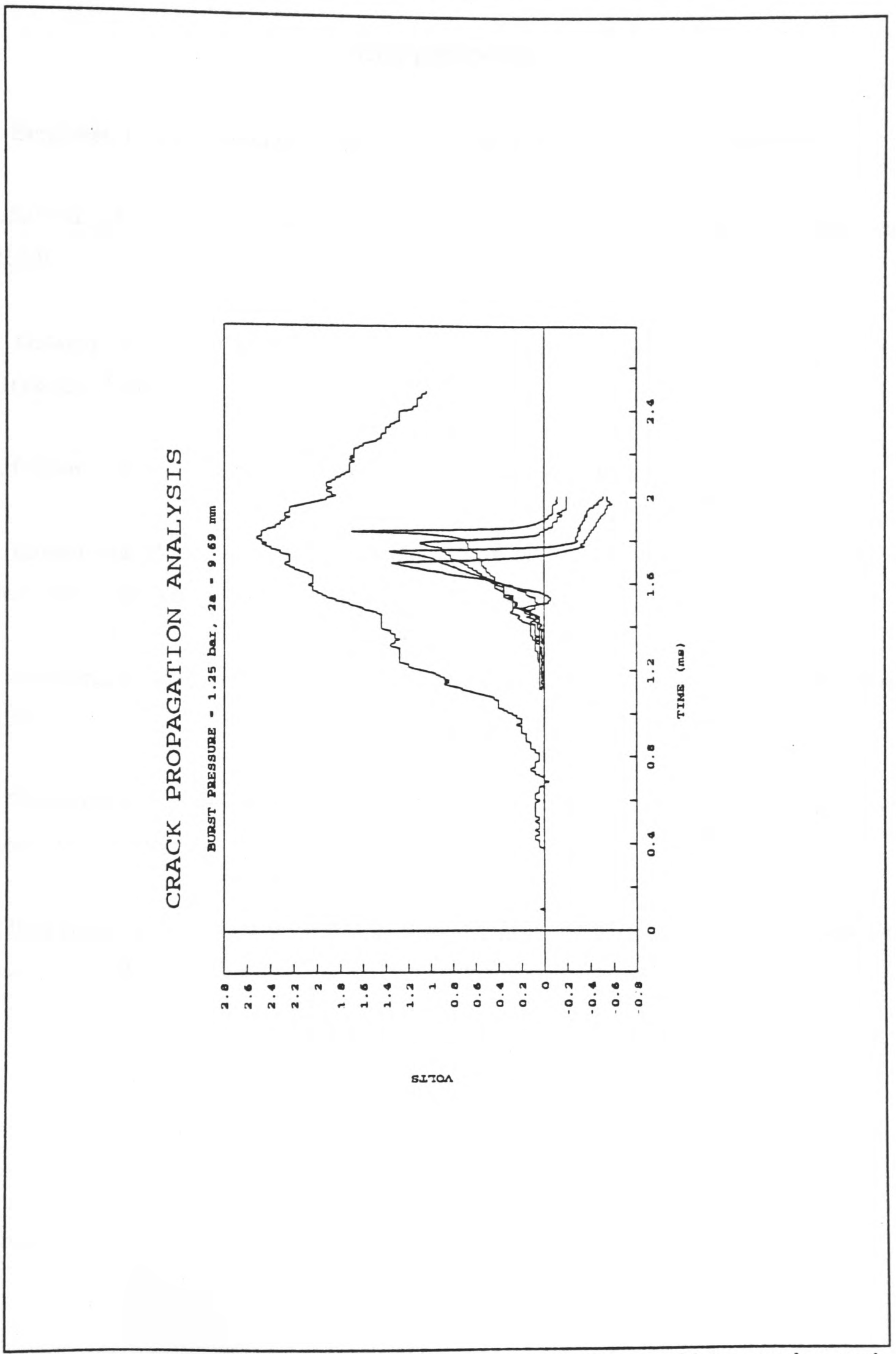


Figure A.3 Comparison between pressure and strain histories (Pressure history envelops strain gauge signals).

REFERENCES

1. Bergkvist, H. The motion of a brittle crack, *J. Mech. Phys. Solids*, 21(1973)299-339.

2. Schardin, H. Velocity effects in fracture, *Fracture*, Ed. B.L. Averback et. al., Wiley, New York (1959).

3. Dulaney, E. N. and Brace, W. F. Velocity behaviour of a growing crack, *J. Appl. Phys.* 31(12)2233-2236.

4. Cotterell, B. Velocity effects in fracture propagation, *Appl. Math. Res.* 4(1965)227-232.

5. Katsamanis, F., Raftopoulos, D. and Theocaris, P. S., The dependence of crack velocity on the critical stress in fracture, *Exp. Mech.*, 17(1977)128-132.

6. Dahlberg, L. Experimental studies of crack propagation in polymers, *R. Inst. Tech.*, Stockholm (1972).

7. Theocaris, P. S. and Katsamanis, F., Response of cracks to impact by caustics, *Engng Fracture Mech.*, 10(1978)187-210.

8. Rosakis, A. J. Analysis of the optical method of caustics for dynamic crack propagation, *Eng. Frac. Mech.*, 13(1980)331-347.

APPENDIX B

CRACK INITIATION ANALYSIS WITH SPECIMENS WITH A TRIANGULAR NOTCH FRONT

The fracture phenomenon has been explained with models that have perfect geometries (straight or elliptical). Nevertheless, real cracks are not as perfect as it is assumed in theoretical analysis. Thus, there are some differences between the theoretical and real crack tip stress fields. In consequence, it is not possible to identify accurately the crack initiation point and establish the position of the front during crack propagation. Accordingly, the purpose of this appendix is to give an in sight into the application of the proposed impact testing technique to the analysis of crack initiation in specimens that have a triangular front.

B.1 Experimental work.

B.1.1 Fabrication of the Specimens.

Circular plates of PMMA were cut in accordance with the dimensions established in section 2.2. Then, their centre on both surfaces was identified and material was carefully removed with a scalpel along a diametral direction as shown in figure B.1. This operation was carried out to half depth of the plate and was repeated on the other side of the specimen to produce a through crack. As it can be observed, the thickness of the specimen reduces evenly between the notch tip and the slot end, through a distance which is three times the crack size. The crack dimensions are given in table B.1 and B.2 for those specimens tested under dynamic and

static conditions respectively. It is important to observe that the nominal crack length is the distance between the apices of the crack tip.

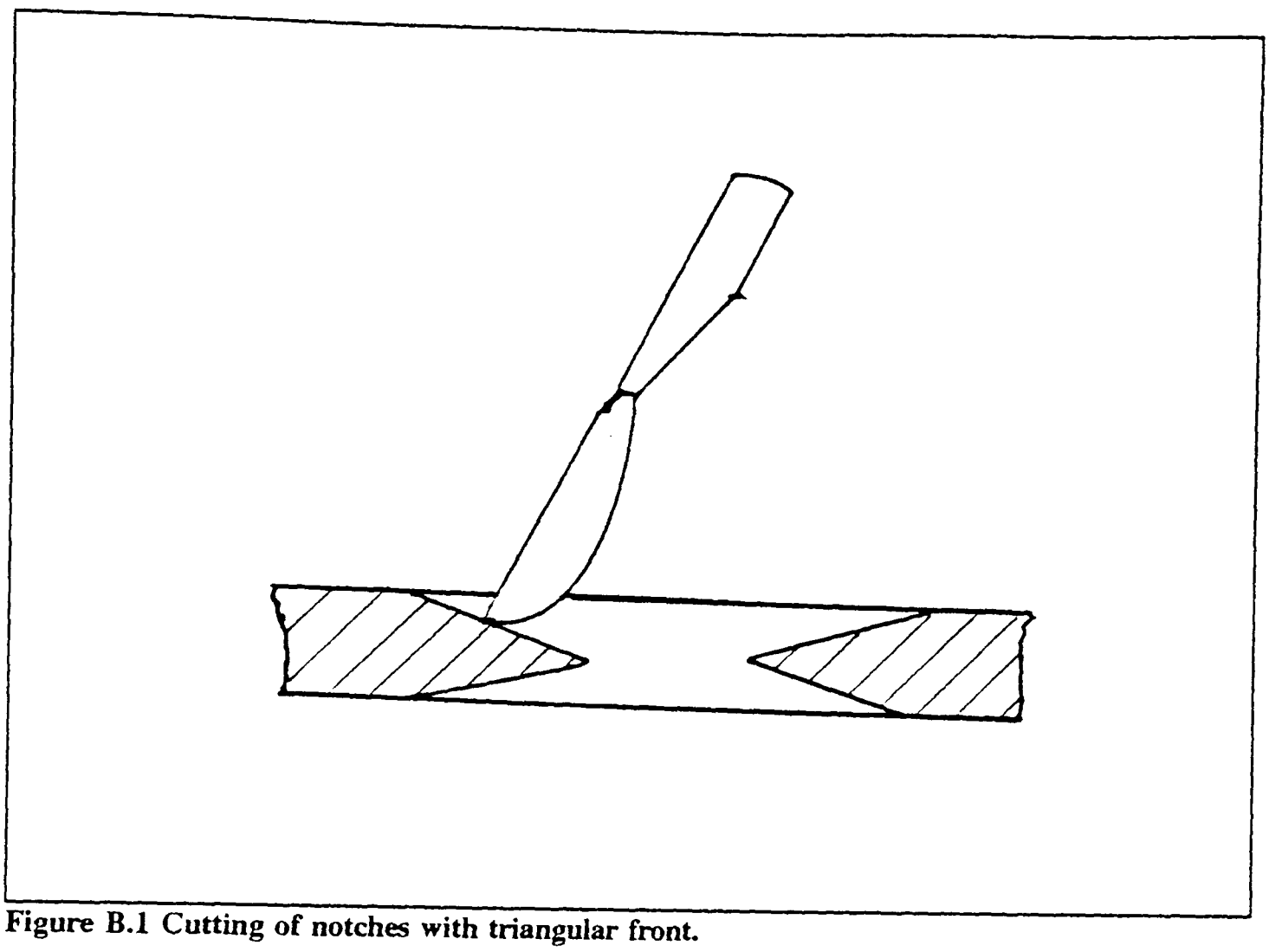


Figure B.1 Cutting of notches with triangular front.

B.1.2 Dynamic Tests.

Two series of tests were performed, following the procedure described in section 2.2.1. In the first, the magnitude of the burst pressure required for crack initiation was established with failure/non-failure tests. It was concluded that its range is within 1.0 bar and 1.5 bar.

In the second series, some specimens were instrumented with strain gauges at the crack tip. The purpose was to obtain the crack initiation instant, from the analysis of the strain-history. Furthermore, in conjunction with the pressure history of the blast wave and the dynamic calibration conditions given in 2.4.3, the crack initiation load was determined. In all these cases, the strain gauge traces obtained are similar to the typical one shown in figure 3.11 and described in section 3.6. The results of the second series are summarized in table B.1.

TABLE B.1
SPECIMENS TESTED UNDER DYNAMIC LOADING PRESSURE

SPECIMEN	NOMINAL CRACK LENGTH (mm)	CRACK WIDTH (mm)	BURST PRESSURE (bar)	CRACK INITIATION PRESSURE (bar)	STRAIN RATE (s^{-1})
1	9.96	0.311	1.00	0.19	1.6
3	4.97	0.321	1.25	0.42	2.5
4	3.95	0.350	1.25	0.47	5.6
5	3.11	0.376	1.50	0.64	8.0
6	0.92	0.320	1.50	0.74	11.0
7	1.70	0.299	1.50	0.68	12.0

B.1.3 Static Tests.

In static tests, the operational procedure described in section 2.2.2 was followed. Moreover, after the notch was produced, it was sealed on the bottom surface of the specimen with a Polytetrafluoroethylene (PTFE), in order to avoid leaks during the test. Then, the specimen was loaded with a pressure load, that was raised slowly and steadily, until crack initiation was detected by the "pop" sound. The results are given in table B.2.

TABLE B.2
SPECIMENS TESTED UNDER STATIC LOADING PRESSURE

SPECIMEN	NOMINAL CRACK LENGTH (mm)	CRACK WIDTH (mm)	CRACK INITIATION PRESSURE (bar)
15	1.384	0.277	1.60
16	2.811	0.269	1.10
17	5.079	0.358	0.70
18	7.423	0.330	0.60
21	3.680	0.384	0.85
22	19.775	0.405	0.45
23	15.741	0.351	0.50
24	13.209	0.302	0.55

B.2 Analysis of the Crack Surfaces.

A typical crack surface of a specimen tested under dynamic conditions is shown in figure B.2. The original crack front is the boundary of the brilliant triangular surface, whose apex is the crack tip. Two main features are observed. Firstly, there are parabolic marks, whose axes of symmetry are perpendicular to the edge that was subject under tensile stress. Besides, they are heading towards the tension side. Secondly, small cracks were developed perpendicular to the border that was under tension. The rest of the surface is brilliant. All the cracks always propagated along its original plane without the signs of shear lips, which suggests that plane strain conditions were developed.

From this information, it is not possible to establish conclusively which is the point of crack initiation as in the case of the specimens with straight front, in which parabolic marks were heading to a single point (figures 5.12 and 5.13), Nonetheless, the fracture mechanism described in section 5.3.2 is considered to be applicable and it can be said that the crack initiated along a segment of the crack front that is under tension and close to the crack tip. This situation may be clarified if observations with higher levels of magnification are undertaken.

With regard to the crack surfaces of the specimens tested under static conditions, they show the same characteristics in all the tests. Their geometry is complex and there are signs of plastic deformation, as shown in figure B.3. At the crack tip, there is a network of two sets of ribs. The first is formed by elliptical marks, which revel the position of the crack front during the propagation. Their major axis coincides with the edge crack that was under tension. The second set tends to be perpendicular to the first one and the ribs are originated from small cracks. Their alignment hints the direction of crack propagation. All this complex surface is bounded by a rough surface. In all the tests, the cracks always propagated along their original plane, suggesting that a state of plane strain was developed.

If figure B.3 is compared with figure 5.16 and 5.17, it can be observed that, in the specimens with triangular front, the first set of ribs is not concentric with the crack initiation point. Likewise, the second set of ribs does not generate from such point. So, it can be concluded that the crack initiated along a segment of the crack front that was under tension. As in the dynamic case, detailed study with greater levels of magnification is required to determine the

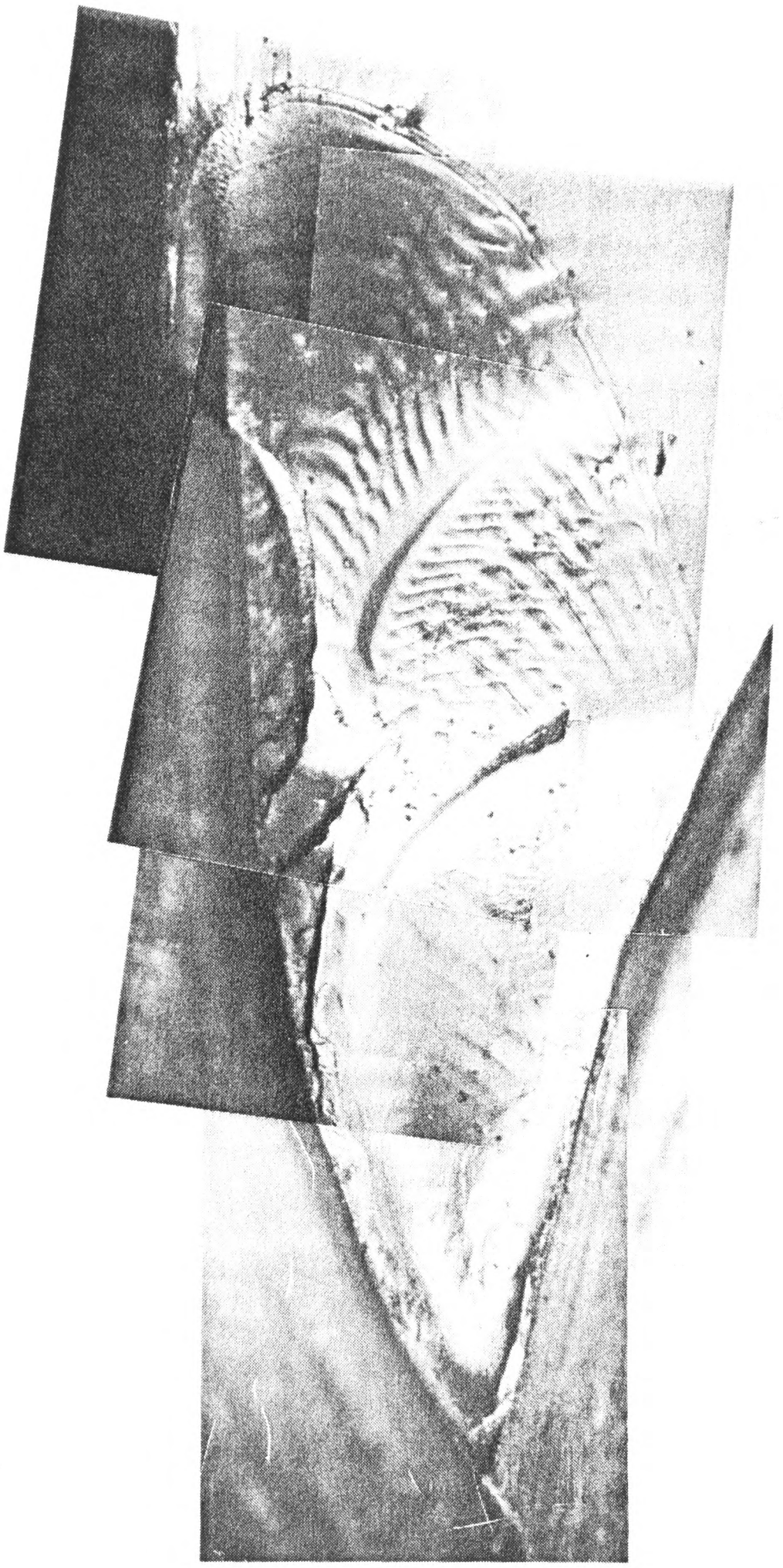


Figure B.2 Crack surface of a specimen tested under dynamic pressure loading.



Figure B.3 Crack surface of a specimen tested under static pressure loading.

point of crack initiation and establish the real crack length.

B.3 Discussion of the Results.

In order to compare the static and dynamic results, a failure diagram (figure B.4) was plotted in which the nominal crack length and the crack initiation pressure were related. Similar results to those obtained in chapter 3 (figure 3.17) were observed. In brief, a lower pressure load is required to initiate a crack in dynamic than in static conditions. Based on the analysis of the crack surfaces and on the conclusions obtained in chapter 5, it can be said that higher loads are required in static conditions, because some elastic energy is required for plastic deformation during the fracture phenomenon.

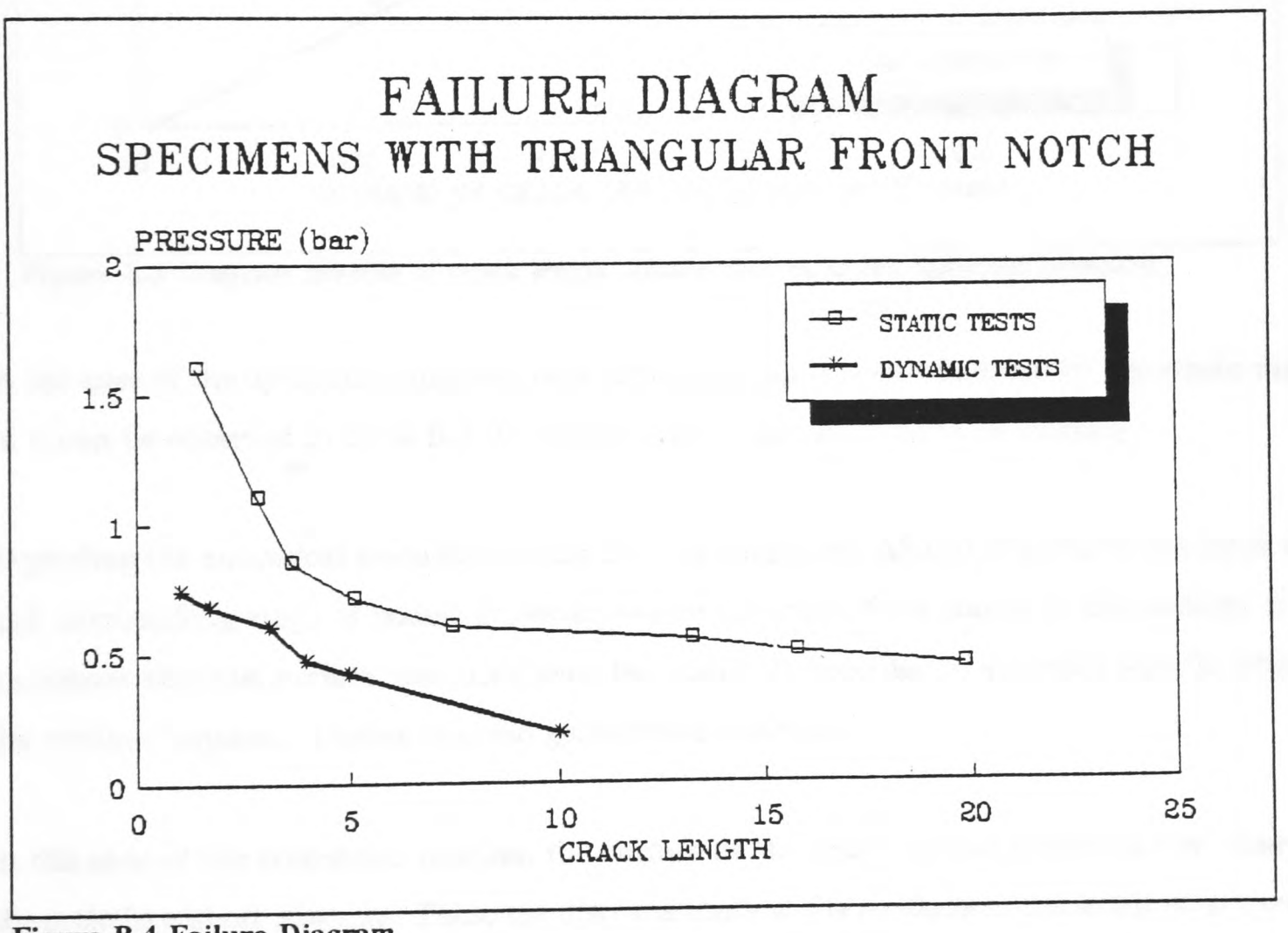


Figure B.4 Failure Diagram.

In order to assess the relationship between the crack length and static crack initiation pressure, a diagram, which relates the inverse of the nominal crack length square root with the crack initiation pressure (figure B.5), was plotted. Then, a linear regression analysis was performed and a straight line, which intersects the vertical axis at -0.02, was obtained. The regression coefficient r^2 is 0.97. Although, crack initiation was unlikely at the apex of the crack front, these results suggests that it is initiated closely to this point.

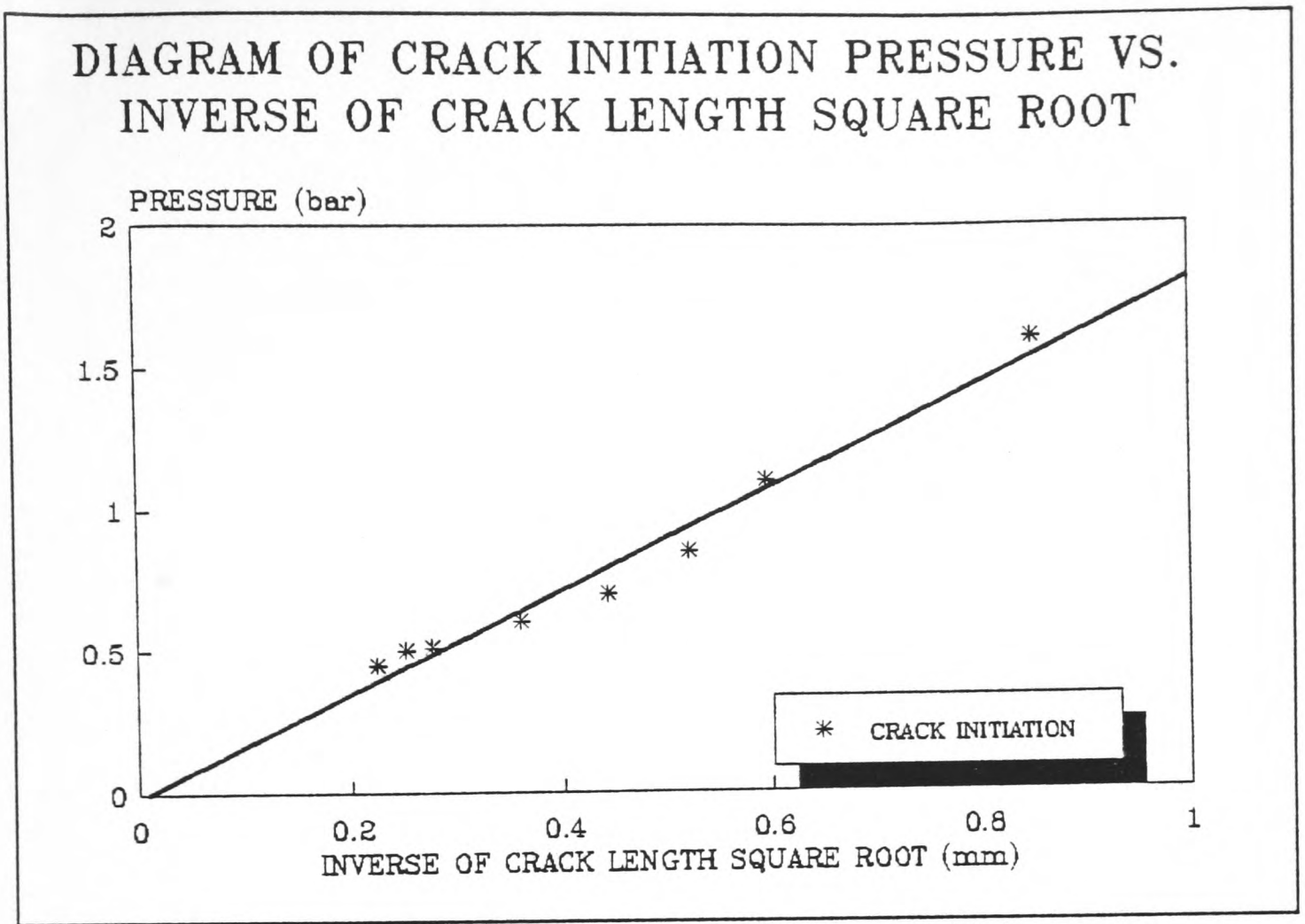


Figure B.5 Diagram inverse of crack length square root vs. crack initiation pressure.

In the case of the dynamic tests, the crack initiation load is also influenced by the strain rate, as it can be observed in table B.1. In consequence, a parabolic curve is unlikely.

Regarding the numerical evaluation of the fracture toughness, ABAQUS perturbs the crack tip and surrounding rings of nodes. However, where the crack front comes to the surface, it is important that the surface normals should be accurately specified at all nodes that lie within the contour request, in order to avoid geometrical distortion.

In the case of the triangular notches, the surface at the crack tip has gradients that change abruptly in a short distance. Thus, the displacements of the surfaces nodes is not as accurate as in the case of plane surfaces. Consequently, the J-Integral evaluation is approximate. An alternative to solve this situation is to generate a mesh with a large number of elements.

Finally, all these results have to be interpreted with caution, because the specimen thickness at the crack tip neighbourhood is not constant. The analysis of the SIF standard solutions for central cracked plates under uniform bending, has shown that the fracture phenomenon is greatly influenced by the geometric characteristics of the specimen (section 4.3).